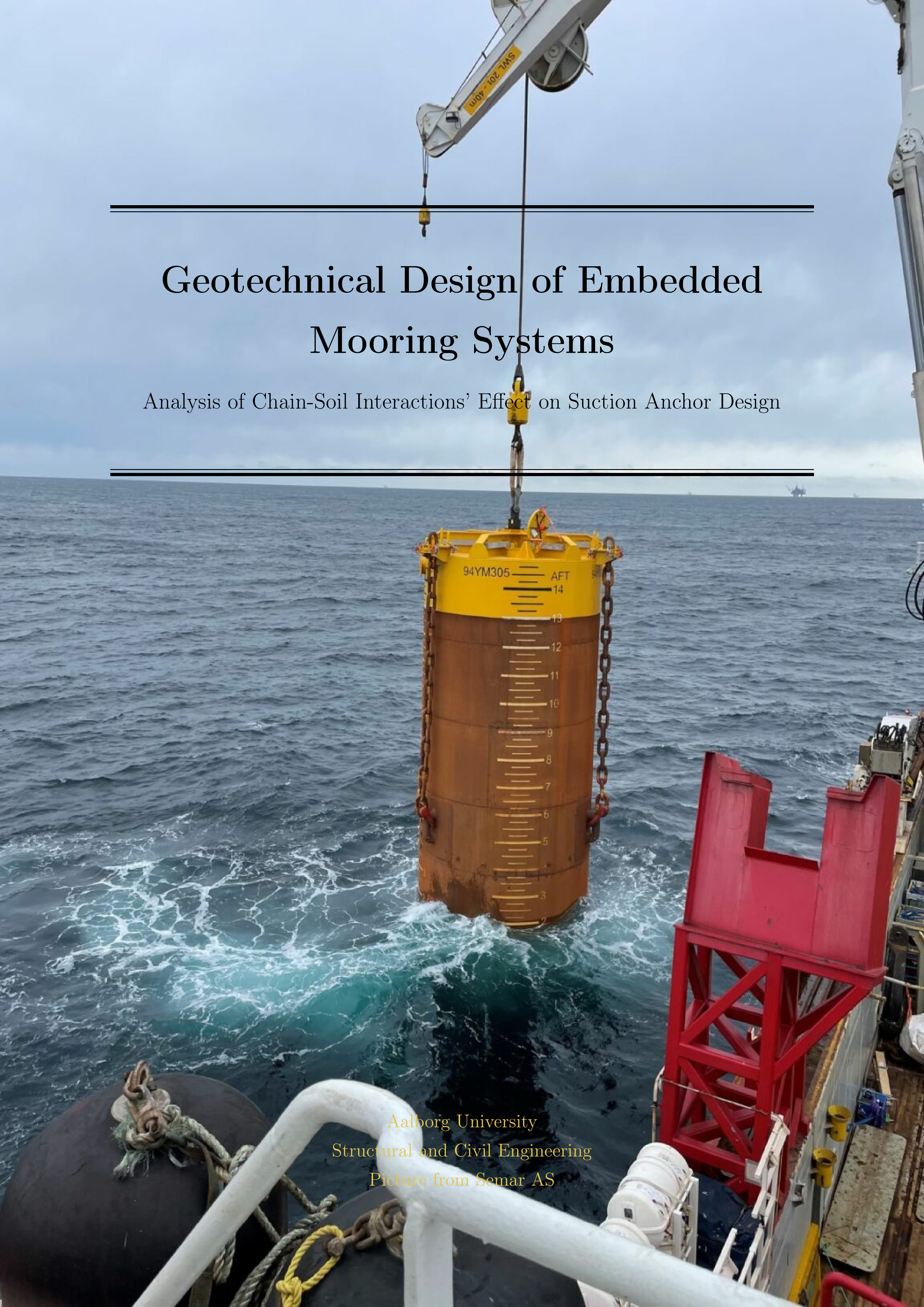

Geotechnical Design of Embedded Mooring Systems

Analysis of Chain-Soil Interactions' Effect on Suction Anchor Design

Aalborg University
Structural and Civil Engineering
Picture from Semar AS

THE FACULTY OF ENGINEERING AND SCIENCE
DEPARTMENT OF THE BUILD ENVIRONMENT
Thomas Manns Vej 23
9220 Aalborg Øst
https://www.build.aau.dk/

Title:
Geotechnical Design of Embedded Mooring Systems

Project:
Master Thesis

Project period:
Sept. 1, 2022 - June 9, 2023

Group members:
Christian Lykke Jensen
Stefan Rysgaard Houmann
Troels Juul Pedersen

Supervisor:
Lars Bo Ibsen

ECTS:
45 ECTS

Number of pages: 141

Abstract: This thesis investigates the geotechnical design of suction anchors and embedded mooring chains for floating wind turbines. The study addresses three questions regarding the embedded chain-soil interactions, the modelling of the pull-out capacity of suction anchors, and the optimisation of the combined mooring system. Regarding embedded chain-soil interactions, three approaches, Neubecker and Randolph [1995], Lee et al. [2014], and Mortensen [2015] were evaluated. Mortensen's method gave reasonable results in estimating chain configuration, load reduction, and the increase in loading angle. A series of FEA using PLAXIS 3D considered several aspects of modelling the pull-out capacity for different load configurations. The analyses concluded that the self-weight of the anchor should be modelled as this influences the displacement field. Furthermore, applying force-controlled loading provided reasonable results in contrast to displacement-controlled loading. The optimisation employed a surrogate-based approach, incorporating Mortensen's chain-soil interaction model and FEA. The optimisation minimised material consumption, revealing that increasing the skirt length is more beneficial than increasing the diameter. The padeye position of an optimised anchor was found to be 0-0.25 times the skirt length. The findings offer guidance for engineers in the optimisation of anchor design, considering the interaction effects with mooring chains. Implementing these insights can enhance overall load-bearing capacity, reliability, and cost-effective solutions for the entire mooring system of floating wind turbines.

Preface

This report is written in the period September 2022 to June 2023 by 4th-semester students, studying the Master's programme in Structural and Civil Engineering at Aalborg University (AAU). The report is conducted as a 45 ECTS masters thesis with a focus on the station keeping of floating offshore wind turbines. This involves the geotechnical aspects of the mooring line and the anchor.

The supervisor of the thesis has been Lars Bo Ibsen Professor at AAU. A special thanks to senior specialist Søren Dam Nielsen and leading specialist Søren Peder Hyldal Sørensen from COWI for their guidance and constructive feedback. The authors are grateful for the office space provided by COWI and for being a part of the offshore wind section during the last year of our education.

Reading Guide

This thesis presents three articles, all related to the station-keeping of floating wind turbines. Each article focuses on a different aspect within this field, contributing to the understanding and improvement of station-keeping techniques for these turbines. The additional part of the thesis is designed to offer a general understanding of the research without relying on the articles. It provides the necessary background information and context to comprehend the main findings and conclusions presented.

Thesis
All figures, tables and equations are labelled with two numbers. The first number indicates the present chapter whereas the second number references the specific figure, table or equation in this chapter e.g. **Figure 1.1**.

Abbreviations and symbols used in the thesis are listed at the beginning of the thesis just after the list of contents.

All citations follow the Harvard reference system with the author(s) name followed by the year. Either both are in square brackets e.g. [Mortensen, 2015] where they are separated by a comma or only the year is in square brackets e.g. Mortensen [2015] which is then without a separating comma. A bibliography is added at the end of the thesis, followed by an appendix with chapters denoted in capital letters e.g. *A,B,C* etc.

Articles

All figures, tables and equations are labelled with a single number referencing the specific figure, table or equation in the current article e.g. **Figure. 1**.

Abbreviations and symbols included in a specific article are listed as the final part of the article followed by the reference list. All citations follow the IEEE citation style with either the author(s) name followed by the reference number in square brackets e.g. Mortensen [10] or just the reference number in square brackets e.g. [10].

Contents

Abbreviations

CEL	Coupled Eulerian-Lagrangian
CPT	Cone Penetration Test
FEA	Finite element analysis
FOWT	Floating Offshore Wind Turbine
HSSmall	Hardening Soil model with small-strain stiffness
LCoE	Levelized Cost of Energy
MC	Mohr-Coulomb model
SVR	Support Vector Regression

Symbols

D	Caisson diameter
R^2	Coefficient of determination
$\boldsymbol{X}$	Domain extent in the x-direction
$\boldsymbol{Y}$	Domain extent in the y-direction
$\boldsymbol{Z}$	Domain extent in the z-direction
$\frac{DL}{l_e}$	Normalised target element size
$\frac{u_{tot}}{D}$	Normalised total displacement
μ	Mean value
σ	Standard deviation
ε	Margin of tolerance where no penalty is given to errors in the SVR
w_i	Weight coefficient for the i^{th} support vector
ΔT	Load reduction from mudline to padeye
α_{mud}	Load angle at mudline
α_{pad}	Load angle at padeye
α_{sand}	Ratio of the frictional and normal forces
δ	Interface friction angle
γ'	Effective unit weight of the soil
λ	Caisson aspect ratio
ψ	Dilation angle
τ_f	Force of friction
φ_{cv}	Critical volume friction angle of the soil
φ	Friction angle of the soil
A_{sand}	Empirical factor
D_i	Caisson inner diameter
D_o	Caisson outer diameter
D_r	Relative density of soil
$F_{current}$	Current forces
F_{wave}	Wave forces
F_{wind}	Wind forces
H	Horizontal bearing capacity

$K_0(z)$	*In-situ* lateral earth pressure coefficient varying with depth
K_0	*In-situ* lateral earth pressure coefficient
L	Caisson skirt length
N	Normal force
N_{avg}	Average bearing resistance
P_A	Active earth pressure
P_P	Passive earth pressure
R_c	Bearing capacity of suction caisson
R_{inter}	Interface reduction factor
T_{mud}	Force at mudline
T_{pad}	Force at padeye
V	Vertical bearing capacity
d	Diameter of chain
q_c	Measured cone resistance
$w'_{caisson}$	Submerged weight of the caisson
w'_{chain}	Submerged unit weight of the chain per meter
z	Depth below mudline
z_{pad}	Padeye depth

Part I

Introduction

1 Introduction

In the last decade, there has been an increase of 1.3 % in the world's energy consumption, while the reserves of coal, natural gas, and oil are decreasing every year [BP, 2022]. Figure 1.1 illustrates when the reserves of fossil fuels will be depleted if energy production from these sources is constant from 2021.

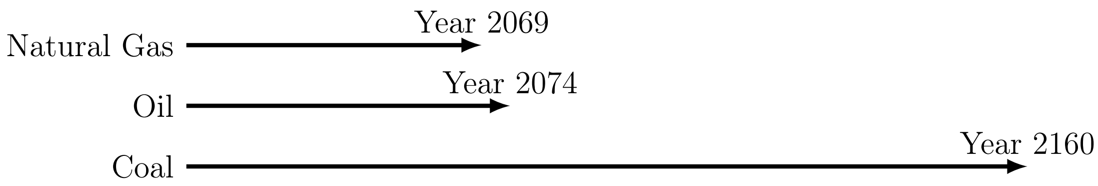

Figure 1.1. The year where the reserves of fossil fuels will be consumed, based on the consumption of 2021 [BP, 2022].

Another problem with fossil fuels is that the reserves are owned by a few countries. Figure 1.2 illustrate the top five countries that each own the largest part of the world's reserves of fossil fuels. The fact that the reserves of fossil fuels are owned by few creates energy inequality and as the reserves get decreased the risk of energy conflicts increases. The distribution of the reserves is furthermore restricted to the developed areas of the world, which means that parts of the world have very limited access.

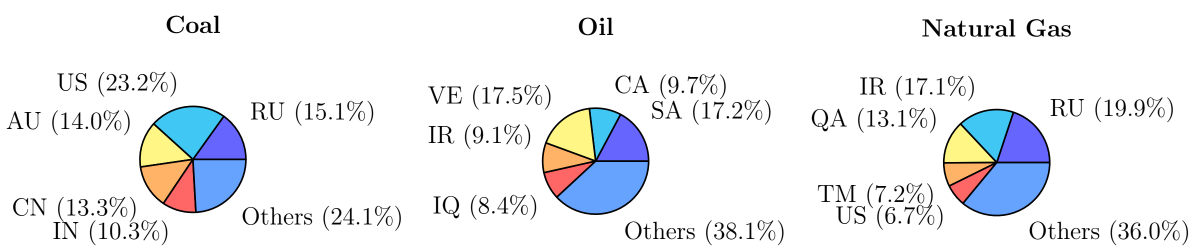

Figure 1.2. Ownership distribution of the world reserves of fossil fuels [BP, 2022]. AU = Australia, CA = Canada, CN = China, IR = Iran, IQ = Iraq, QA = Qatar, RU = Russia, SA = Saudi Arabia, TM = Turkmenistan, US = United States of America, VE = Venezuela

.

Unlike fossil fuels, renewable energy is a way for countries to become self-sufficient in energy, where the country's natural resources and location are decisive for which types of renewable energy to invest in. Renewable energy creates lower emissions, is in most countries cheaper, and generates three times more jobs than fossil fuels [United Nations, 2022]. Thus, renewable energy is a way for countries not only to become self-sufficient but also to reduce their carbon dioxide footprint, supply cheap energy to their population and create new jobs. The typical forms of renewable energy are bioenergy, hydropower, geothermal, solar, and wind. In recent years a significant development in wind energy has been made.

1.1 Wind Energy

Electricity accounted for 17.2 % of the world's energy consumption in 2021 [BP, 2022] and is expected to be between 35-50% in 2050 [BP, 2023]. As stated by BP [2023], the expected increase in energy consumption primarily results from the transition to electric power in the transportation sector and the growing energy requirements for heating, cooling, and ventilation in buildings. Wind energy only produced 6.5 % of the world's electricity consumption in 2021 [BP, 2022], thus the potential of expanding the production of wind energy is significant.

Wind energy technologies use the kinetic energy from the wind to produce electricity and are applicable in most of the world. The technical potential of wind energy exceeds the world's current electricity production [United Nations, 2022]. Onshore wind turbines are the cheapest option [NREL, 2022], but the recent year's developments in size, supply chain, and construction of offshore wind turbines, have made offshore an economical competitor.

Offshore wind turbines are often built as bottom-fixed constructions and are placed in shallow waters, up to 70 meters [Durakovic, 2022]. Some examples of bottom-fixed wind turbines are presented in figure 1.3.

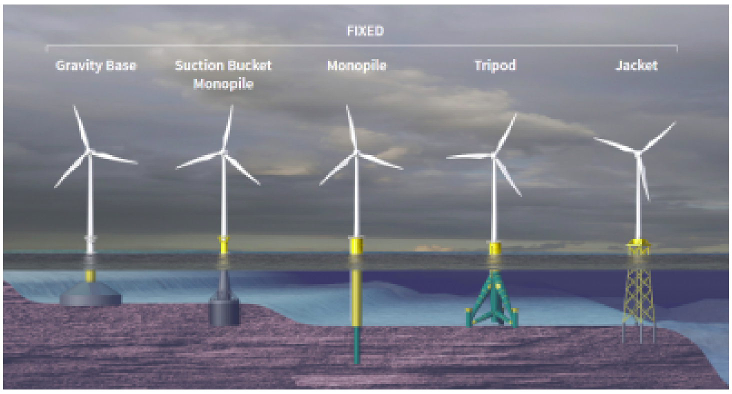

Figure 1.3. Illustration of different bottom-fixed wind turbines Tethys engineering [2022].

Recent developments in floating wind turbine technology have made these structures noteworthy, particularly in water depths exceeding 55 meters [Durakovic, 2022]. An important advantage of floating wind turbines is that the majority, around 80%, of the offshore wind resource is in waters deeper than 60 meters. At these locations, wind conditions are characterised as stronger and more consistent [Equinor, 2022].

Offshore wind turbines must resist forces from wind, waves, and currents. Especially the wind forces acting on the blades will give a large overturning moment. Figure 1.4 shows three types of floating wind substructures, where each type is stabilised by different means. The Spar-Submersible is stabilised by buoyancy, whereas the Spar-Buoy is by means of ballast and the Tension Leg Platform by the moorings lines. Floating wind turbines are a relatively new technology, however, the development within the area is going towards an industrial level.

Figure 1.4. Illustration of different floating wind foundations used for deep waters Tethys engineering [2022].

1.2 Mooring Systems

Floating wind turbines are moored to the seabed with multiple mooring lines and anchors, similar to a floating oil/gas platform. Simple mooring systems consist of two main elements; a mooring line and an anchor. The mooring line is the connection between the wind turbine and the anchor at the seabed. As opposed to the bottom-fixed solutions, where overturning moments from the induced loads are transferred to foundations, the mooring systems for floating structures are limited to only resisting vertical and horizontal forces.

Figure 1.5 illustrates the three main types of mooring systems named after the shape or state of the mooring line; catenary, taut, and tension leg, and a combination of catenary and taut, called semi-taut.

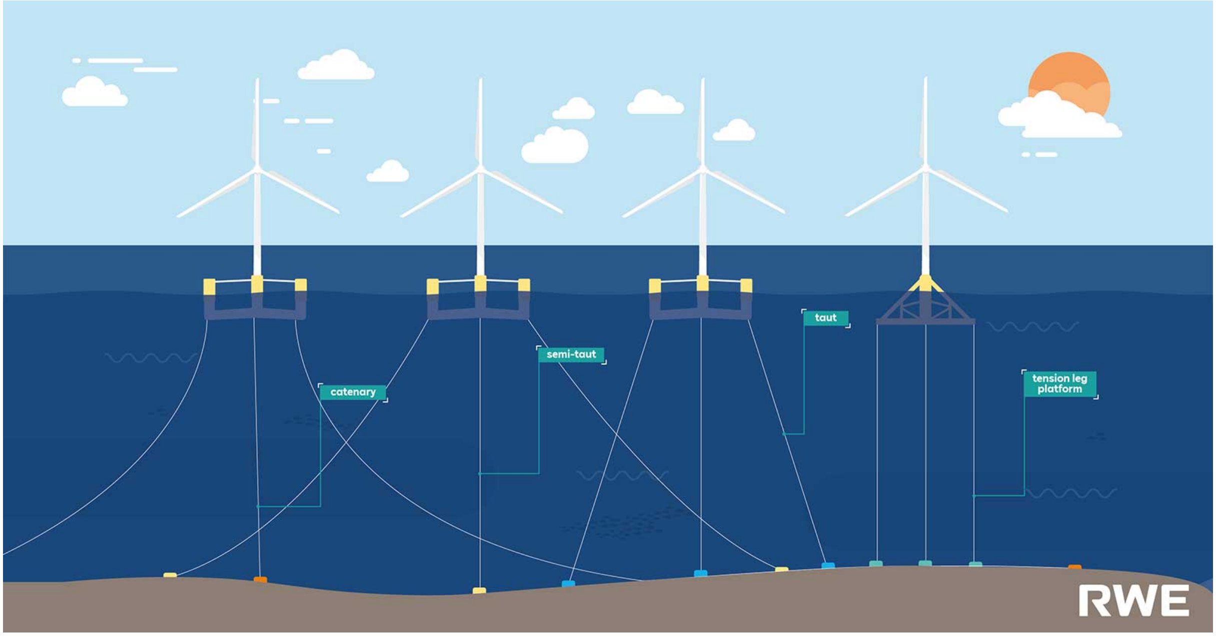

Figure 1.5. Illustration of different mooring systems RWE [2022].

A tension leg mooring system is a system with vertically connected mooring. The tension in the anchoring is provided by the buoyancy from the floating wind turbine. This allows the wind turbine to move horizontally but not vertically which makes it relatively stable in rough seas. The footprint of the mooring system on the seabed is the smallest of the different systems. However, the wind turbine and substructure are not stable without the mooring system and installing a tension-leg mooring system is therefore considered more difficult compared to the other options. Furthermore, the consequence of failure in the mooring system can therefore be quite significant.

A catenary mooring system is commonly used for shallow waters and has a part laying on the seabed and a part suspended in the water which will have the natural shape of a chain suspended between two points. Platforms used in catenary systems are quite stable without the mooring systems and the platform performance with the mooring system is considered acceptable. The mooring system has the largest footprint of the different systems and therefore also becomes less economical as water depth increases, where other mooring systems become more suitable.

A taut system has mooring lines typically made of synthetic rope that is much lighter than conventional mooring chains or cables. The mooring lines are pre-tensioned and typically at an angle to the seabed between 30-45 degrees. This means that a mooring anchor needs to withstand both horizontal and vertical forces. A taut system has a smaller footprint in deep and ultra-deep water conditions compared to a catenary. A combination of the catenary and the taut system is also used in deep waters and is called semi-taut and consists of parts that are taut and parts that are catenary. Semi-taut systems again require less seafloor space and will require shorter mooring lines than catenary, which is why these systems are often used in deep waters. Table 1.1 summarises the mooring systems advantages and disadvantages.

Table 1.1. Comparison of the mooring systems.

	Tension-Leg Mooring System	Catenary Mooring System	Taut Mooring System	Semi-Taut Mooring System
Platform stability (without mooring system)	low	high	medium	medium
Platform performance (with mooring system)	stable	acceptable	acceptable	acceptable
Pre-tension of mooring system	high	low	medium	medium
Footprint size of mooring system	small	large	medium	medium
Installation of mooring system	difficult compared to others	simple compared to tension-leg mooring system	simple compared to tension-leg mooring system	simple compared to tension-leg mooring system

1.2.1 Anchors

A variety of anchors are used for securing the mooring line to the seabed, but they are generally divided into two types - surface and embedded anchors. Surface anchors or gravity anchors get their holding capacity from the weight of the anchor and the friction between the anchor and the seabed. They are often simple box-shaped constructions filled with ballast after placement at the seabed. The bottom of the construction can be rippled to increase the friction between the construction and the seabed. Embedded anchors have a more extended variety of shapes and installation methods than gravity anchors. Figure 1.6 shows the three most commonly used embedded anchors which are drag anchors, piles, and suction caissons [Mark Randolph, 2011].

Drag anchors used for offshore constructions evolved from conventional ship anchors, and have a broad fluke connected to a shank which is visualised in figure 1.6. Typically the penetration depth is between one and five fluke lengths which can be up to six to seven meters [Mark Randolph, 2011] The holding capacity of the drag anchor is developed from the soil in front of the anchor and is normally not designed for larger vertical loads [Mark Randolph, 2011]. This makes them suitable for catenary mooring lines and thereby the anchor is often used in shallow waters. Installation of drag anchors entails significant challenges since the anchor is installed by dragging until the prescribed capacity is reached. The final anchor location at the site after installation is therefore subjected to a rather large amount of uncertainty. Nevertheless, the Kincardine Wind Park located approximately 15 kilometres off the coast of Aberdeen in Scotland used drag anchors in the mooring system [Executive, 2018].

Anchor piles are based on the pile foundations of a bottom fixed turbine and are often hollow steel piles which are driven or drilled into the seabed. The resistance of the pile is obtained by the friction along the pile and lateral soil resistance which makes it capable of resisting both horizontal and vertical forces. The piles often need to be installed at a great depth beneath the seabed to obtain sufficient resistance. For example, a tension leg platform in the Gulf of Mexico is anchored with 16 piles with a diameter of 2.4 meters and is driven to a depth of 130 meters on a water depth of 1,300 meters [Mark Randolph, 2011]. The operations of pile driving at these depths are very complex, thus anchor piles are somewhat unattractive in very deep waters.

(a) Drag anchor (b) Pile anchor (c) Suction caisson anchor

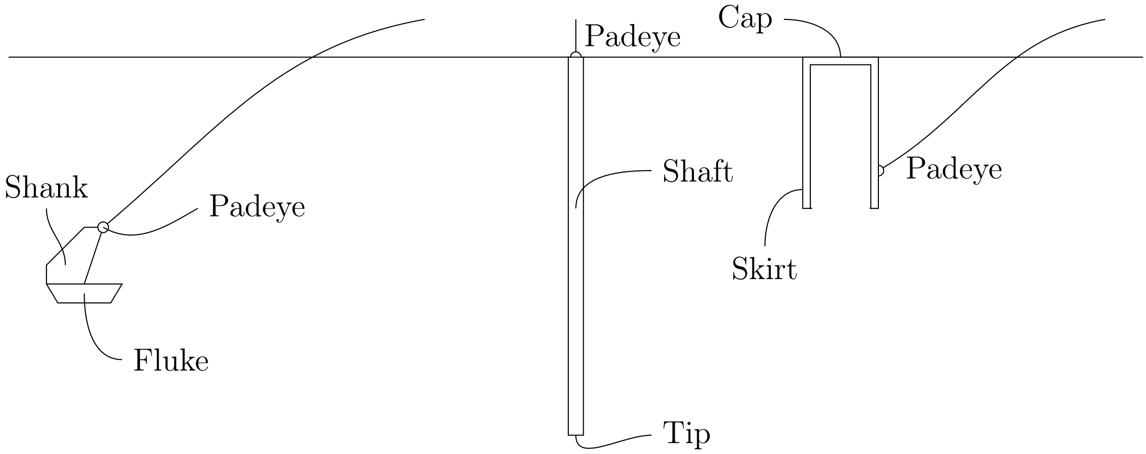

Figure 1.6. Commonly used embedded anchors.

Suction caisson anchors are similar to piles, large diameter cylinders, typically with aspect ratios (λ=L/D) in the range of 3-6, which are smaller than pile anchors that often are much more slender constructions with aspect ratios up to 60 [Mark Randolph, 2011]. The installation process differs, where suction caisson anchors are installed by means of an induced pressure difference. Suction caisson anchors are installed in two steps. After placement on the seabed, it has an initial penetration by the self-weight of the caisson. Afterwards, the required depth is obtained by pumping water out from the top cap, causing the pressure inside the caisson to drop below the outside pressure. This pressure difference must be greater than the resistance at the tip of the caisson as well as the internal and external friction along its skirts. During the installation, the seepage around the caisson skirts will reduce the internal skirt friction and tip resistance. However, there are limitations to the maximum installation depth as the required pressure can reach a critical point that may lead to various failures, such as buckling, piping, liquefaction, or cavitation.

Similar to piles, the horizontal resistance of a suction caisson is obtained by the lateral soil resistance. The vertical resistance is obtained by the friction along the caissons skirts but for a shorter load duration, a reverse end-bearing can be sustained by the suction within the soil plug. Increasing water depths does not significantly increase the complexity of the installation making it suitable for most cases and has been used for floating offshore wind turbines in the Hywind Scotland Project.

Advantages and disadvantages for the three embedded anchors are summarised in table 1.2. Suction caisson anchors are well-known, and it is one of the utilised anchor types for deep mooring applications [Yong Bai and Wei-Liang Jin, 2016]. Considering the advantages of the more reliable installation and a broader application range, suction caisson anchors are chosen as the focal point in this thesis.

Table 1.2. Comparison of commonly used embedded anchors.

	Drag Anchor	Pile Anchor	Suction Caisson Anchor
Vertical capacity	low	high	high
Horizontal capacity	high	high	high
Application depth	shallow	shallow and deep	shallow and deep
Installation	Difficult compared to suction caisson anchor	Difficult compared to suction caisson anchor	Simple compared to others.

1.3 Mooring Systems with Suction Caisson Anchors

Suction caisson anchors can be used for all the different mooring system configurations previously described. Figure 1.7 illustrates a typical mooring system configuration with a suction caisson anchor. The dominating loads are environmental loads from wind, waves, and currents, and these are transferred to the soil as illustrated in the figure. In the case of a catenary mooring system, where the loading from the mooring at the seabed is horizontal, the mooring lines will often be attached to the anchors at a padeye located below the mudline. For this scenario, the load from the floating structure to the anchor will be reduced in the three sections shown in figure 1.7. The reduction from D-C is caused by the weight of the hanging mooring line, and from C-B a reduction is caused by the frictional forces between the seabed and the mooring line.

In section A-B the soil will have resisting, normal- (N) and friction-forces (τ_f), acting on the chain, which results in lower tension loads at the padeye. Load inclination at the padeye will be larger than at the mudline, resulting in an inverse catenary shape below the mudline. The embedded mooring line configuration is substantial when designing the anchoring system since loading at padeye becomes inclined.

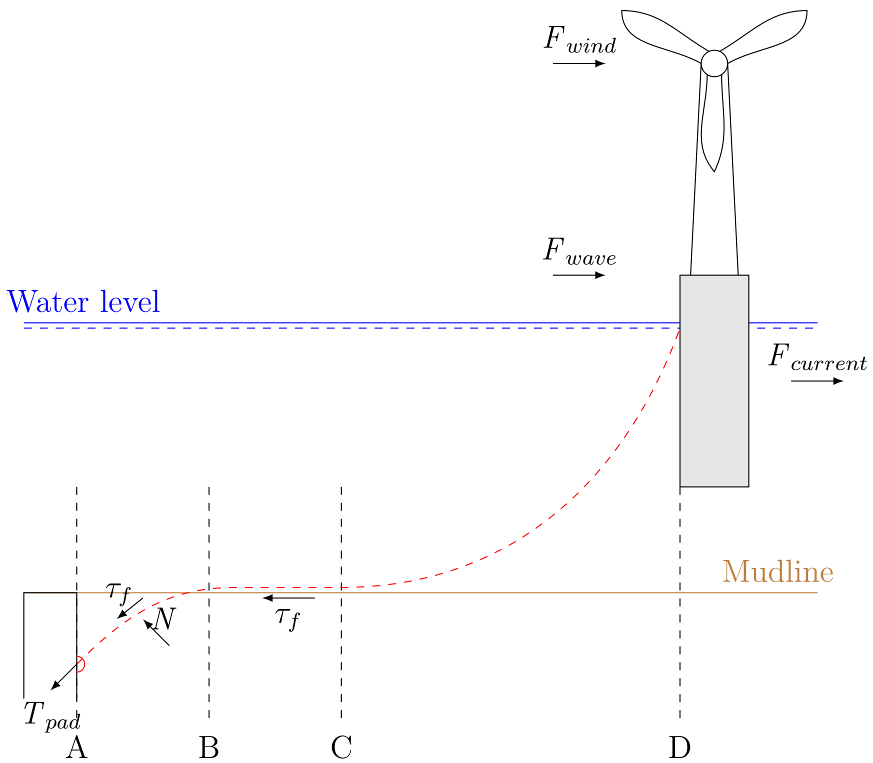

Figure 1.7. Illustration of a mooring system configuration with a suction caisson anchor.

As illustrated in figure 1.8 the load attachment point and inclination will have a significant influence on the failure mechanism and therefore on the bearing capacity of the anchor. Three main displacement types governing the response can be imagined; clockwise and counterclockwise rotation, and horizontal translation where a true mechanism will be a combination with a vertical displacement. The failure mechanism of the pure horizontal translation will provide the largest bearing capacity and the padeye placement is therefore often placed to obtain this.

(a) Clockwise rotation (b) Horizontal translation (c) Counter clockwise rotation

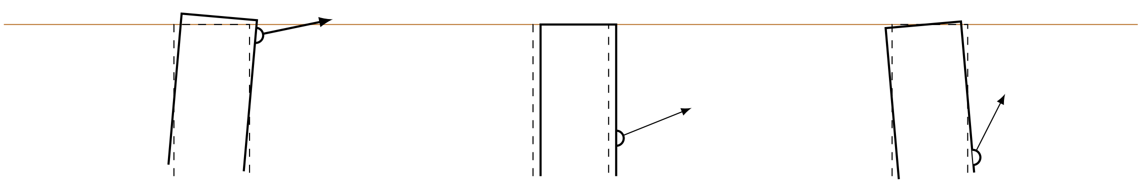

Figure 1.8. Different failure mechanisms for different load applications.

1.4 Opportunities for Cost Reduction in Floating Wind

The Levelized Cost of Energy (LCoE) of floating wind turbines is 70 % higher than for the bottom fixed turbines [NREL, 2022], so efforts are needed to reduce the cost of floating wind significantly. Floating offshore structures have been used in the oil and gas industry for several years. For these projects, station-keeping has traditionally been a minor component of the total costs. As a result, conservatism has often been applied to station-keeping due to its relative cost. As a means of cost reduction in floating wind projects, the further development of anchor design is vital.

Further developing the current knowledge of the bearing capacity of both the anchor and the embedded chain would improve reliability. Investigating the effects of parameters affecting the capacity could further improve anchor designs, as parameter uncertainties could be better assessed. By improving the current knowledge and reliability of methods and results, the added safety could be reduced. In addition, developing reliable and efficient methods for predicting capacities is vital, as it will facilitate better methods for optimisation as design changes can be assessed more quickly. The guidelines by DNVGL-RP-E303 [2017] focus on the geotechnical design of suction anchors in clay; however, no specific guidelines are presented by them for the installation of suction anchors in sand. Empirical formulas for inclined capacity in cohesionless soil have been developed based on the ultimate bearing capacity of vertically and horizontally loaded suction anchors. These formulas assume an elliptical failure envelope in (H, V)-space Zhao et al. [2019] Cheng et al. [2021]. However, these formulations are calibrated on relatively few finite element analyses, only considering very few soil conditions. As a result, the study of suction anchor design in cohesionless soil is of significant interest.

In summary, suction caisson anchors are versatile as they can be used in different mooring system configurations for floating offshore wind turbines, efficiently transferring environmental loads to the seabed. To reduce costs and improve design, evaluating current methodologies and optimising interactions between mooring lines and anchors in cohesionless soil is essential.

Objective and Outline of Thesis 2

There is a need to significantly reduce the Levelized Cost of Energy (LCoE) of Floating Offshore Wind Turbines (FOWTs), for which reason it is important to address if the anchoring systems are optimally designed. Given that FOWTs are a relatively young industry no consensus on the matter of optimal substructure or mooring system is present. Hence studies on the possibilities and limitations of different anchoring solutions are needed as these could influence the optimal design of FOWTs in a more holistic sense.

Addressing the compatibility and effectiveness of current design methodologies and industry know-how is crucial in the context of employing suction caisson anchors for FOWT station-keeping. The design must achieve both safety and efficiency, consequently, the sensitivity of design parameters must be clarified. Furthermore, design choices concerning the mooring lines will influence the anchor, as a result, methods to efficiently evaluate the effects of these interactions are of interest.

The aim of the thesis is to provide insight into the field of high-capacity marine anchoring. The thesis concerns several geotechnical aspects considering both the embedded chain, suction caisson anchor and the interaction between these structures. The thesis seeks to address various aspects of the anchoring design and optimisation, with the following three questions providing a guideline for the topics analysed and discussed.

1. Which methods can be recommended for determining the embedded chain interactions and what parameters affect the load reduction and angle at padeye?
2. How can the pull-out capacity of a suction anchor be modelled using finite element analysis and what parameters affect the pull-out capacity dependent on the load configuration?
3. How can the combined bearing capacity of a suction anchor and the embedded chain be optimised efficiently and what are general tendencies in terms of an optimised design of a suction anchor?

2.1 Thesis Structure

The following thesis is structured into four parts, each serving a specific purpose in the exploration of the thesis objective. In Figure 2.1, the visual representation of the thesis structure provides an overview of these four parts.

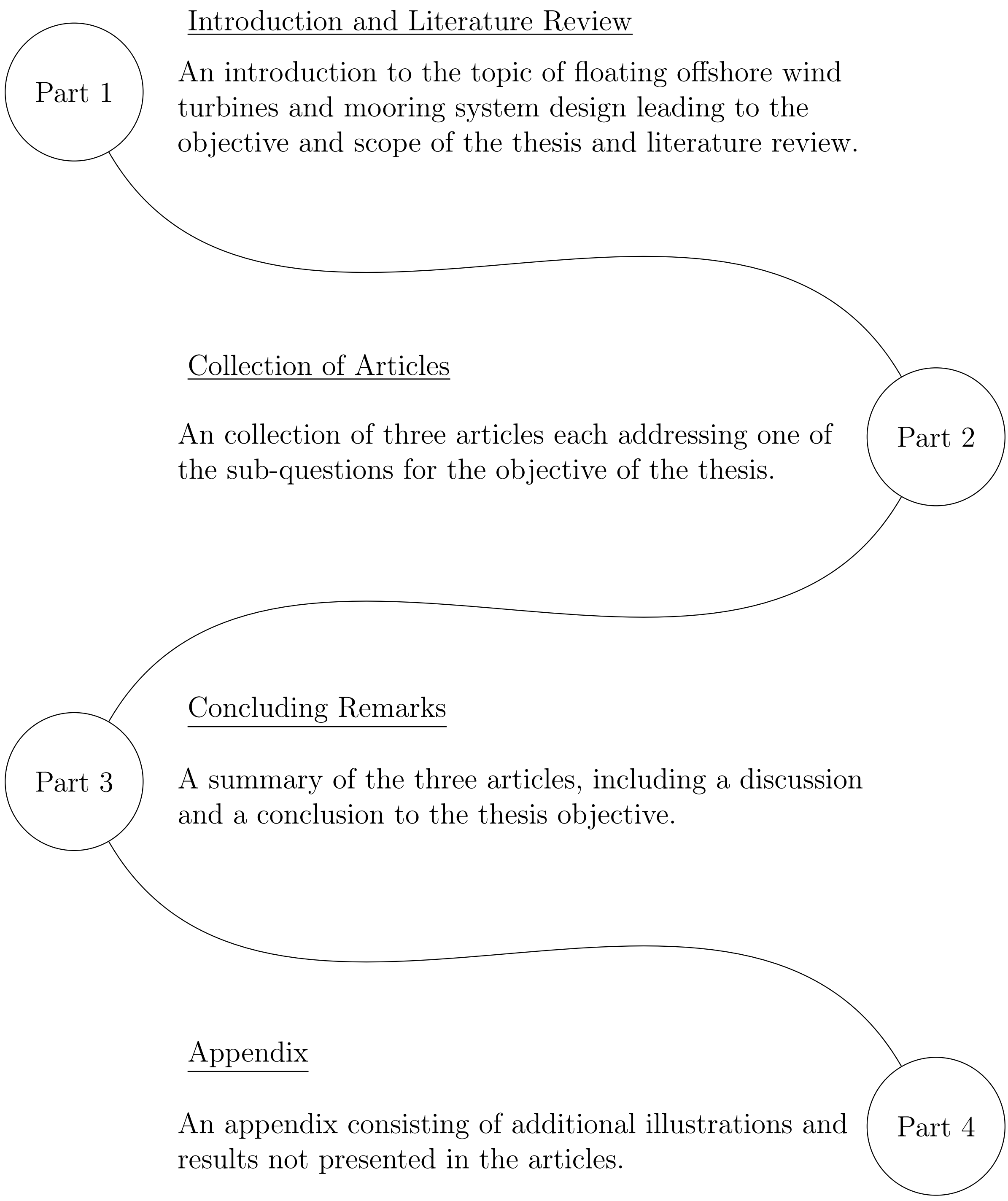

Figure 2.1. Illustration of the thesis structure.

2.1.1 Overview of Articles

The three sub-questions defining the objective of the thesis presented in this chapter are divided such that the components of the mooring system, chain and anchor, are investigated individually and are then combined. The following section briefly describes the three articles, providing readers with a general understanding of the research topics addressed in each one.

Article 1: Chain-Soil Interactions in Cohesionless Soil under Static Loads with CPT Interpretation

This article addresses the first sub-question - *Which methods can be recommended for determining the embedded chain interactions and what parameters affect the load reduction and angle at padeye?* and compares different methods to estimate the embedded chain interaction in cohesionless soils. Methods proposed by Neubecker and Randolph [1995], Lee et al. [2014] and Mortensen [2015] are compared on large-scale test results conducted by Mortensen [2015]. CPT correlations are used to determine geotechnical parameters and as a result, the analyses are extended to address the effect of different CPT interpretation methods in combination with the methods for estimating the chain-soil interaction. The sensitivity of design parameters is examined, as to identify where uncertainties will have the most significant effect on the responses. The article seeks to present valid combinations of CPT interpretation methods and chain-soil interaction methods providing recommendations for geotechnical engineers within the field of offshore engineering.

Article 2: Modelling the Drained Capacity of Inclined Loaded Suction Anchors in Cohesionless Soil: A Finite Element Study

The second article concerns the second sub-question - *How can the pull-out capacity of a suction anchor be modelled using finite element analysis and what parameters affect the pull-out capacity dependent on the load configuration?* and presents a series of finite element analyses addressing the various aspect of modelling the drained static pull-out capacity. Finite element models are widely used in engineering practice but are highly sensitive to input parameters. The development of finite element models is a relatively cumbersome task, hence the article attempts to provide general recommendations for the construction of the models, as it can provide a basis for future work. Sensitivity studies of geotechnical parameters are conducted for various load inclinations and padeye depths to provide insight into the bearing capacity dependency in relation to the load configuration and the examined parameters.

Article 3: Surrogate-Based Optimisation of Suction Anchors with Embedded Mooring Chain

The final article investigates the third sub-question - *How can the combined bearing capacity of a suction anchor and the embedded chain be optimised efficiently and what are general tendencies in terms of an optimised design of a suction anchor?*. The study combines key findings of the previous articles developing a method for estimating the combined bearing capacity and presents a vast series of optimised anchor designs for different site and loading conditions. To achieve a significant increase in computational efficiency, the study trades accuracy in predictions by employing methods within the field of supervised machine learning, i.e., surrogate models. These surrogate models are trained on data obtained from higher fidelity models, such as finite element analysis, and the proposed method by Mortensen [2015] for the response of the chain-soil interactions. The article describes the development of the surrogate model and the optimisation procedure. Thus providing a basis for further development of the models and optimisation procedure.

2.2 Scope and Delimitation of Thesis

This thesis focuses on the analysis and optimisation of suction anchors for the case of the drained static capacity in cohesionless soils. The present study limits the analysis of mooring lines to include only studless mooring chains. Furthermore, load configurations considered are those anticipated for the case of both catenary and taut mooring. In addition, the study concerns the anchor capacity for a single mooring line connection.

Anchor and mooring design is a complex and multi-disciplinary endeavour. As a result, some considerations are excluded from the present study. Noticeably, the effects of cyclic and dynamic loading are not included. Unless otherwise stated, soil conditions in the following analyses are assumed homogeneous. Practical limitations and effects of the installation procedure are not included in the present study, thus not addressing its implications on optimised designs. Furthermore, the structural analysis of the anchor and chain is not considered, and as such, its effect is not assessed.

Literature Review 3

The following chapter presents a description of current methods for designing suction caisson anchors in cohesionless soils. The literature review provides findings on the topic of both the embedded chain-soil interaction and the inclined pull-out capacity of suction caisson anchors.

3.1 Embedded Chain-Soil Interactions

The early application of high-capacity anchoring systems was initiated by the oil and gas industry for the station-keeping of floating production, storage and offloading facilities. An anchor pile-chain mooring system of floating platforms was widely used within the industry. The connection between the anchor and piles was in many cases placed at the top of the pile, as it provided the ability to inspect the connection. However, lowering the connection or padeye could be optimal as bending moments in the pile would be reduced. In addition, the friction between the soil and chain would reduce the load at the pile connection. Furthermore, by increasing the embedment, the horizontal load component on the pile is significantly decreased, leading to an even greater reduction in bending moments. As a result, interest in the development of methods to estimate chain-soil interactions, i.e., the load reduction and change in load inclination, increased.

Vivatrat et al. [1982] presented a simple procedure for estimating the influence of chain friction on the pile load. The chain-soil interactions were modelled in terms of the chain embedment depth (z_{pad}), chain diameter (d) and soil strength profile. The method assumes a two-dimensional chain configuration, where two ordinary differential equations describing the changes in the tension and chain orientation were rewritten from equilibrium equations for the force components tangential and normal to an infinitesimal chain segment. Hence, from known starting conditions, the tension and chain inclination further down the chain can be obtained by integrating these two equations in small increments. The primary focus of the study was on cohesive soils, however, the approach and assumptions used were considered to be extendable to cohesionless soils. Dutta and Degenkamp [1989] continued this work experimentally conducting tests on different cohesive soils, chain sizes and attachment depths.

Neubecker and Randolph [1995] derived closed-form solutions for the ordinary differential equations proposed by Vivatrat et al. [1982] by averaging the resistance offered by the soil normal to the chain (N_{avg}) over the depth range. Neubecker and Randolph [1995] validated their solution on experimental data considering both cohesive and cohesionless soils. In the case of cohesionless soil, the tests were conducted under enhanced gravity at 40g. Comparisons between the derived closed-form expressions, laboratory tests, and incremental approach used by Vivatrat et al. [1982] showed good agreement.

Lee et al. [2014] adopted the governing equations from previous studies on clay and reanalysed the frictional and bearing resistances for the case of cohesionless soils. Lee et al. [2014] calculated the frictional force acting on the mooring line by multiplying the normal stress and a coefficient of friction ($\tan(\delta)$). The normal stress was expressed by the soil weight (($\gamma' z \cos(\alpha)$), and the passive earth pressure (P_P) and active earth pressure (P_A) generated in front and the back of the mooring line. The study validated the proposed analytical method on a number of centrifuge tests at 50g, however, the tests were conducted using steel wires. Parametric studies found that the pulling force at the attachment point (T_{pad}) is influenced by padeye depth (z_{pad}), friction angle of the soil (φ), load inclination at the mudline (α_{mud}), effective mooring line self-weight in soil (w'_{chain}), and chain diameter (d), but soil unit weight (γ') has minimal effect on the load reduction. The angle at the attachment point (α_{pad}) is influenced by padeye depth (z_{pad}), friction angle of the soil (φ), and chain diameter (d). In contrast, unit weight (γ'), load at the mudline (T_{mud}), and effective mooring line self-weight in soil (w'_{chain}) had minimal effect on the mooring line's angle at the attachment point.

Mortensen [2015] conducted large-scale field testing using mooring lines made of chains and wires embedded in sand. The primary objectives of the project were to measure the embedment depth along the mooring line, determine the forces at both ends and establish a theoretical framework based on the obtained measurements. The theoretical framework developed by Mortensen [2015] used aspects from the work of Vivatrat et al. [1982]. However, unlike Lee et al. [2014], Mortensen [2015] determined that the frictional force acting tangentially to the chain was proportional to the normal force on the chain link, with an empirical factor (α_{sand}). The large-scale tests demonstrated that the theoretical framework developed could be utilised, however, a detailed description of the variation in the friction angle was necessary for its application. Thus indicating that accurately accounting for the friction angle variation is crucial for obtaining reliable results for situations outside of laboratory testing.

3.2 Inclined Pull-Out Capacity of Suction Anchors

Limited research exists on the inclined capacity of suction caisson anchors in cohesionless soils, likely due to their sparse application in such soil conditions. Nonetheless, studies have been conducted using both experimental and numerical methods to examine the pull-out capacity in sand.

Bang et al. [2009] conducted a series of centrifuge model tests on suction piles in sand to determine the inclined loading capacities. The centrifuge model tests included as main variables load inclination (α_{pad}) and padeye depth (z_{pad}). The model of the suction pile used for the tests were made of a stainless steel tube with ($D_o = 30\,\text{mm}$), ($D_i = 28\,\text{mm}$) and skirt length ($L = 60\,\text{mm}$). The tests were conducted under 100 g thus corresponding to a suction pile with an outer diameter ($D_o = 3\,\text{m}$). The smallest thickness of the mooring line able to resist the maximum load during testing was used to exclude its effects on the results. 80 tests were conducted at five different load inclinations and padeye positions.

The tests were conducted on poorly graded sand with diameters of all particles less than 1.0 mm and greater than 0.1 mm. Bang et al. [2009] reported that the sand had a specific gravity of 2.62, an average internal friction angle ($\varphi = 33°$), and a relative density ($D_r = 60\,\%$). The sand was sprayed into the water-filled model container prior to testing, thus ensuring a uniform density of the sand throughout the container. Before installation of the model pile the centrifuge was initially operated to stabilise the sand. The model suction pile was then later installed by pushing it into the sand under 1 g.

An electric actuator was used to generate the pull-out force, where the loading rate was slow to ensure that an excess pore water pressure wasn't generated. The actuator movement was stopped as soon as the pulling force passed its peak.

Figure 3.1a presents the prototype pull-out capacity at different padeye positions and for different load inclinations obtained from the centrifuge tests. The centrifuge test results indicate that for small load inclinations, the pull-out capacity increases, peaks, and decreases as the padeye depth is increased. For larger load inclinations ($\alpha_{pad} > 45°$) the dependence on load application depth is reduced significantly. A relatively large scatter in the results is seen for load inclination ($\alpha_{pad} = 0°$) and ($\alpha_{pad} = 22.5°$), especially at ($z_{pad} = 0.75$) which coincides with the largest capacities.

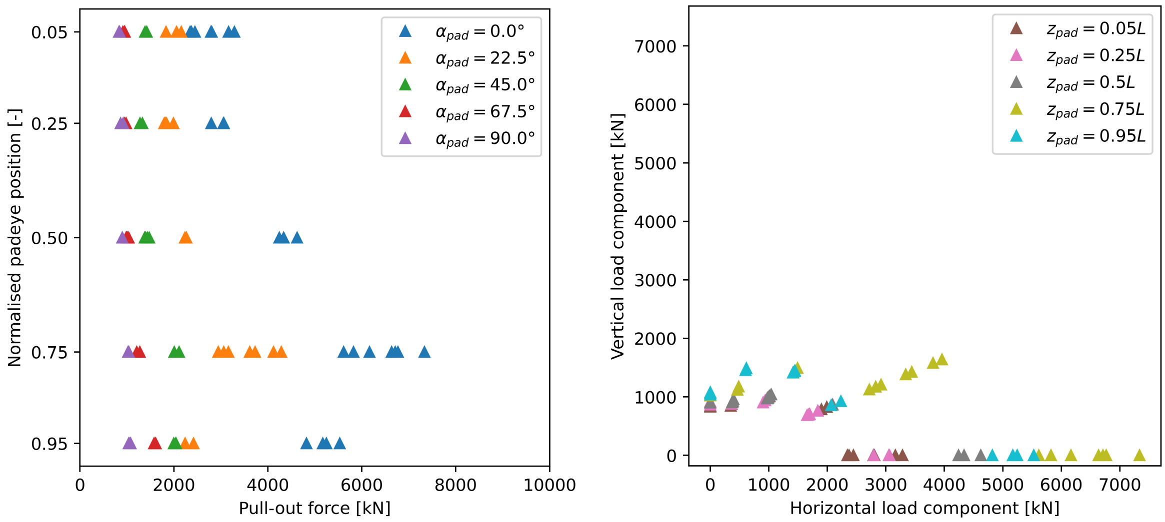

(a) Pull-out capacity at different padeye positions and load inclinations from centrifuge tests conducted by [Bang et al., 2009].

(b) Horizontal and vertical load component at different padeye depths from centrifuge tests conducted by [Bang et al., 2009].

Figure 3.1b presents the horizontal and vertical components of the pull-out force at different padeye depths. Connecting these results for each padeye depth the resulting curve could describe the failure envelope of the suction caisson anchor. For increasing padeye depth the size of the failure envelope increases peaking at padeye depth of ($z_{pad} = 0.75L$) and then decreasing, where the shape of the failure envelope changes most significantly in terms of the horizontal capacity.

Ahmed and Hawlader [2014] aimed to determine the pull-out capacity of a suction caisson when subjected to inclined loading in sand. The study conducted three-dimensional finite element analyses examining the effects of key variables such as loading angle (α_{pad}), padeye position (z_{pad}), and aspect ratio (λ) on the pull-out capacity and rotation. The findings aligned with the centrifuge tests by Bang et al. [2009] producing similar results in terms of the effect of loading angle and padeye position. In addition, it was found that the normalised capacity of the caisson increased with a higher aspect ratio. The study used an Arbitrary Lagrangian-Eulerian method available in finite element software Abaqus/Explicit to address numerical issues caused by mesh distortion at large displacements, assuming that the caisson would experience significant displacement and rotation before reaching its maximum pull-out force.

The anchor was displaced 50% of its diameter in the analyses, however, the pull-out force was determined as the force at 10% of the caisson's diameter. At large displacements, the pull-out force generally decreased due to the upward movement and rotation of the anchor. The study opted to model the sand using the Mohr-Coulomb model, where soil parameters were chosen to represent the soil conditions during the centrifuge tests.

Through a series of three-dimensional finite element analyses Zhao et al. [2019] developed a calculation framework for the pull-out capacity based on caisson diameter (D), caisson skirt length (L), load inclination angle at padeye (α_{pad}), submerged caisson self-weight ($w'_{caisson}$), effective unit weight of the soil (γ'), and critical-state friction angle (φ_{cv}). The study ignored the effects of soil dilatancy stating that the approach yields a lower-bound estimate of the capacity since the analyses considered critical-state conditions, where there is no longer an effect from dilation. The study likewise used a Mohr-Coulomb model for the modelling of the sand. The framework assumed an elliptical failure envelope in (H, V)-space. The failure envelopes were normalised with respect to ultimate bearing capacities for one-dimensional loading and for horizontal and vertical loading. Parametric studies showed a significant influence of padeye depth (z_{pad}) on yield envelopes and optimal padeye depth (resulting in the largest pull-out capacities) was found to vary with load inclination. The analyses suggest that the optimal depth of the padeye is 0.15–0.4 times the caisson length for load inclinations between 40° and 60°, which the study considered relevant for practical applications.

Cheng et al. [2021] presented similar ideas as Zhao et al. [2019] developing a calculation framework for failure envelopes of suction caisson anchors subjected to inclined loading. Noticeable differences between the studies being that Cheng et al. [2021] included the relative density of the sand (D_r) into the framework. Furthermore, the study used an a Modified Mohr-Coulomb model to capture the stress-dependent hardening – softening behaviour of the sand. The study found the optimum padeye depth with maximum pull-out capacity was largely independent of sand density and ranges from $0.6L$ to $0.7L$ from the caisson top for load inclination ($\alpha_{pad} = 30°$).

As illustrated by this literature review, the proposed methods for determining the embedded chain-soil interactions in cohesionless soil are principally attempts to extend the work conducted by Vivatrat et al. [1982] on cohesive soil. Consequently, Neubecker and Randolph [1995], Lee et al. [2014], and Mortensen [2015] all present methods that share very similar ideas and assumptions. However, as only Mortensen [2015] validated the method on large-scale test results, it is of interest to investigate how the three different methods compare to large-scale test results with real soil conditions.

The present work conducted on the inclined pull-out capacity in cohesionless soil indicates that finite element analysis is a valid approach, as the results obtained generally compare well with centrifuge test results. The current research investigated the effects of padeye position (z_{pad}), load inclination (α_{pad}) and aspect ratio (λ). As a result, the effect of geotechnical parameters and more general assumptions made in terms of the finite element models are not investigated in detail. Consequently, how these parameters and assumptions influence the capacity for different padeye positions and load inclinations is of interest, as it can inform about the reliability of the finite element results, as the result of uncertainties in parameters can be assessed.

Part II

Articles

Article 1

Chain-Soil Interactions in Cohesionless Soil Under Static Loads with CPT Interpretation

Chain-Soil Interactions in Cohesionless Soil Under Static Loads with CPT Interpretation

CHRISTIAN LYKKE JENSEN[1], STEFAN RYSGAARD HOUMANN[1], TROELS JUUL PEDERSEN[1], AND LARS BO IBSEN[2]

[1] M.Sc. student, Dept. of Civil Engineering, Aalborg University, Denmark
[2] Prof., Dept. of Civil Engineering, Aalborg University, Denmark

ABSTRACT: Floating offshore structures are often moored to embedded geotechnical structures, where the padeye for the mooring line can be placed below the mudline. Designing these structures optimally heavily relies on the estimation of the load reduction from the chain-soil interaction and the change in angle from mudline to padeye. Existing methods for estimating load reduction and change in angle are validated against laboratory-derived parameters. By considering the available data when designing an offshore wind turbine farm, this study assessed the combined outcome of Cone Penetration Test (CPT) interpretation and the determination of the chain-soil interactions. This assessment is compared to measurements obtained from a large-scale field test conducted with a four-meter-diameter suction caisson and a studless chain with a diameter of 32 millimetres. The conclusion of the assessment is that a combination of Jamiolkowski et al. [7] with constant K_0, Bolton [2] and Mortensen [15] for determining the relative density, friction angle and chain-soil interactions respectively, will provide reasonable results.

1. INTRODUCTION

Offshore wind turbines are a well-established and scalable concept for the transition to renewable energy, thus the capacity of offshore wind is expected to increase significantly within the next decade. This growing capacity will require a more adaptable approach to addressing varying water depths. Floating wind turbines can be installed at greater depths than bottom-fixed turbines, where the wind is stronger and more consistent. The United States, Norway, Portugal, South Korea, and Japan are among the countries that have proposed the installation of floating wind turbines along their deep-water coastlines [19], where conventional bottom-fixed turbines are not feasible or cost-effective. While floating offshore structures have been used in the oil and gas industries for several years, more research is necessary to make floating wind turbines commercially feasible. Efforts are needed to reduce the Levelized Cost of Energy (LCoE) significantly.

Multiple mooring lines anchor the floating wind turbine, which makes reducing the cost of these mooring systems of high importance. A versatile solution to anchoring the floating wind turbine is the suction caisson, which has a low environmental impact regarding the installation and can be used for most mooring types. With the exception of tension-leg mooring systems, it is common for the mooring lines to be connected to the caisson below the mudline. This paper focuses on the use of a chain in the embedded part of a mooring system.

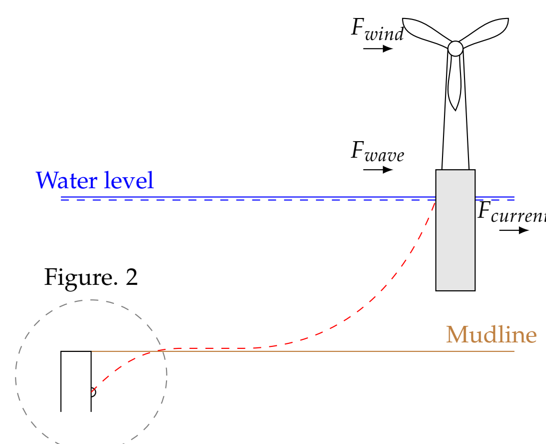

Figure. 1. Illustration of a catenary mooring system for a spar-bouy floating wind turbine.

Figure 1 illustrates a catenary mooring system, with a spar-buoy substructure for the wind turbine. The moment, primarily caused by environmental forces such as wind, waves, and currents (F_{wind}, F_{wave}, $F_{current}$), is resisted by the substructure, resulting in pure tension being transferred to the mooring system.

Figure 2 illustrates a suction caisson anchor with an embedded mooring chain. The chain is attached to the anchor at the padeye, which is placed at a depth below the mudline (z_{pad}). The chain for a suction anchor will run vertically along the skirt after installation and gradually cut through the sand as it is loaded. As a result of the normal and frictional forces (N and τ_f), the chain will form an inverse catenary. The bearing capacity of the anchor is significantly influenced by the angle at the padeye (α_{pad}) which was concluded by Jensen et al. [8]. Furthermore, the frictional force (τ_f) from the soil acting on the chain will reduce the load from mudline (T_{mud}) to padeye (T_{pad}) by 20–50% [4], thus methods to determine the chain-soil interactions with acceptable precision are vital. The chain-soil interactions of the system include the behaviour of the embedded chain, covering its configuration, the angle at the padeye, and the reduction of load from the mudline to the padeye.

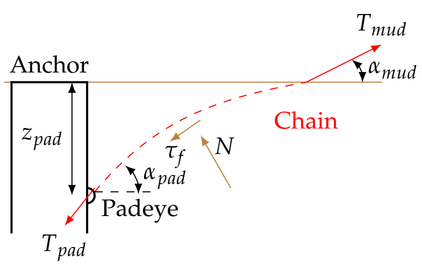

Figure. 2. Illustration of the embedded part of the mooring system illustrated in figure 1.

Approximately four decades ago, Vivatrat et al. [21] and Dutta and Degenkamp [4] developed techniques for evaluating chains in clay. Neubecker and Randolph [16] and Lee et al. [10] utilised the studies of Vivatrat et al. [21] and Dutta and Degenkamp [4] to derive methodologies for chains in sand. Neubecker and Randolph [16] and Lee et al. [10] validated their method against centrifuge tests in which friction between the mooring line and the soil is challenging to reproduce. These centrifuge tests were conducted with one soil layer, and the soil parameters were determined using laboratory tests.

Mortensen [15] validated his method for estimating the chain-soil interactions in sand with results obtained from a large-scale field test but derived the friction angles based on an extensive amount of triaxial tests. To implement this methodology for an offshore wind farm, a substantial number of triaxial tests would be required. Given the difficulty and expense of collecting offshore samples for laboratory tests, it would be more practical to evaluate soil conditions using a large number of Cone Penetration Tests (CPTs) which often are available.

It has generally been the approach to omit the first part of a CPT where the measurements are less reliable because the correlations for the soil parameters are derived based on stress levels above 50 kPa [9]. CPT measures in a state of failure where the failure mechanism is changing as the measuring depth is increasing. Figure 3 show different failures investigated by Emerson et al. [5], who concluded that the failure of a CPT can be divided into the three phases, listed below.

1. Soil dilation results in upward failure
2. Soil transitions from dilative to compressive behaviour
3. A quasi-stationary phase that occurs at a critical depth

The critical depth varies depending on soil type, with higher cone resistance resulting in a deeper critical depth. Figure 3 displays the three phases for two frictional soils with different relative densities.

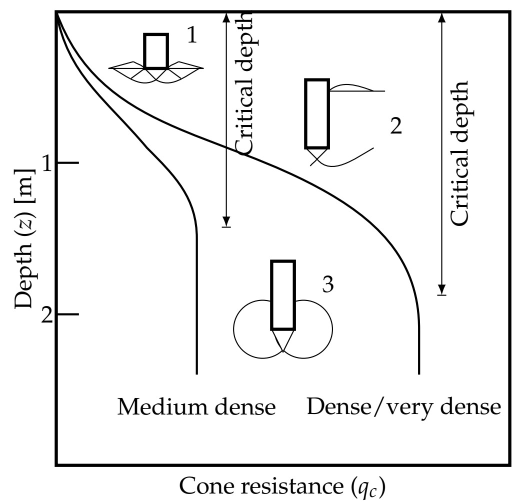

Figure. 3. Illustration of the different failure mechanisms of the soil. (Modified from Puech and Foray [18]).

The inverse catenary shape of the chain will cause a relatively large part of the chain to be at shallow depths. Consequently, the CPT correlations competence for stress levels below 50 kPa needs to be assessed.

Krogh et al. [9] investigated the performance of the different correlations for stress levels below 50 kPa. Krogh et al. [9] concluded that even though the approach explained in section 3.1 doesn't consider the different failures, it is able to capture the response measured by the CPT.

The objective of this article is to investigate and assess methods to estimate chain-soil interactions. Four methods for the interpretation of the CPTs will be combined with three methods for determining the chain-soil interaction to be evaluated against the large-scale test results.

This paper will present:

- A description of the setup and the results obtained by the large-scale tests.
- Methods to interpret CPT data to obtain soil parameters.
- Methods to estimate the chain-soil interactions.
- A combined analysis of the CPT interpretation and the chain-soil interactions
- A sensitivity analysis of parameters in the chain-soil interaction model recommended by Mortensen [15].

2. DATA FOR THE ARTICLE

In 2005, a corporation was formed between The Norwegian Geotechnical Institute (NGI) and Aalborg University, Denmark (AAU), to conduct large-scale tests of the chain-soil interactions. Mortensen [15] also used these large-scale tests for the validation of his method. Figure 4 shows the location of the test site in Frederikshavn, Denmark. The tests were performed in a basin at the harbour. The purpose of the test was to measure the angle

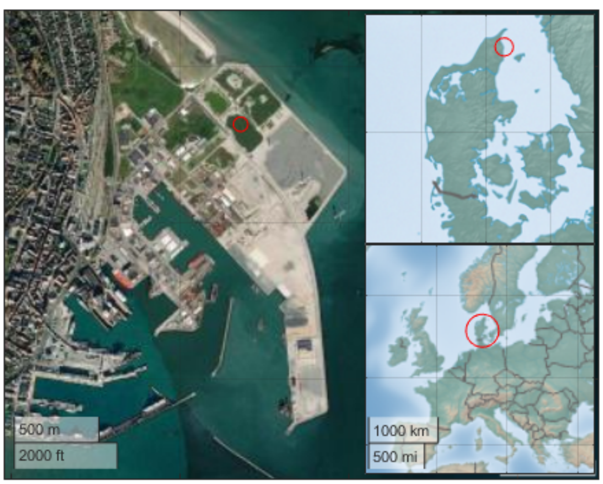

Figure. 4. A map showing the test site in Frederikshavn, Denmark.

at padeye, the load reduction from mudline to padeye, and the position of the chain under an applied static load. Two tests were conducted one for each padeye depth of 2.25 m and 3.32 m.

2.1. Test Setup

Figure 5 show a principle sketch of the test setup, where the test conditions (T_{mud}, α_{mud} and z_{pad}) is listed in table 1. Two tests were performed with a suction anchor measuring 4.0 meters in diameter and length. The suction anchor was installed in sand with the mean water surface at ground level. The chain was attached to the padeye before the installation of the suction anchor in each test. The force to the chain was applied by a hydraulic jack positioned 40–50 meters from the caisson. The force applied to the chain didn't introduce settlements of the suction anchor.

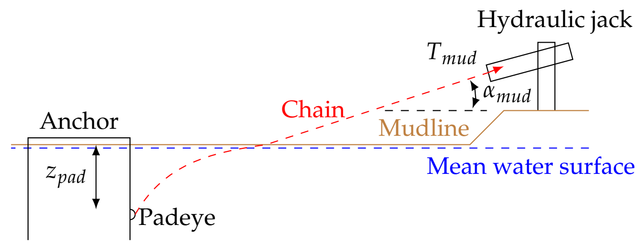

Figure. 5. Principle sketch of the test setup for the large-scale test.

Figure 6 shows the dimensions of the studless chain used for the test, the unit weight of the chain was 19 kg/m.

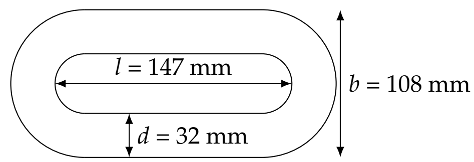

Figure. 6. The characteristic of the chain link used for the large-scale test.

2.2. Soil Conditions

Geotechnical boreholes and CPTs conducted at the site were used to identify the soil conditions. A fine-grained, post-glacial, and dense sand was detected in the first 3.5 m. Figure 7 shows the derived corrected cone resistance (q_t), the friction ratio (R_f), the pore pressure ratio (B_q) and the material index (I_c) from the CPTs. From these parameters, it is concluded that the soil at the test site has a similar behaviour. Laboratory tests on the soil samples showed that the sand has a mean diameter (d_{50}) of 0.15 mm and relative densities (D_r) around 90 %. The sand was clean with a silt content lower than 2 %, and the loss of ignition was less than 1 %. The test site is exposed to repeating waves at a shallow depth, thereby the top layers are assumed to be compacted and behave as OC [12].

2.3. Measured Values

Figure 8 shows the setup used in the tests to determine the angle at padeye. Thin wires with a diameter of 2 mm were attached to the chain, passing through an eyelet on the caisson's skirt. The attachment point of each wire on the chain and the eyelet were initially at the same horizontal level. As the load was applied to the chain, the wires were extended by following the displacement of the chain. The extension of each wire was digitally measured with a precision of ±5 mm.

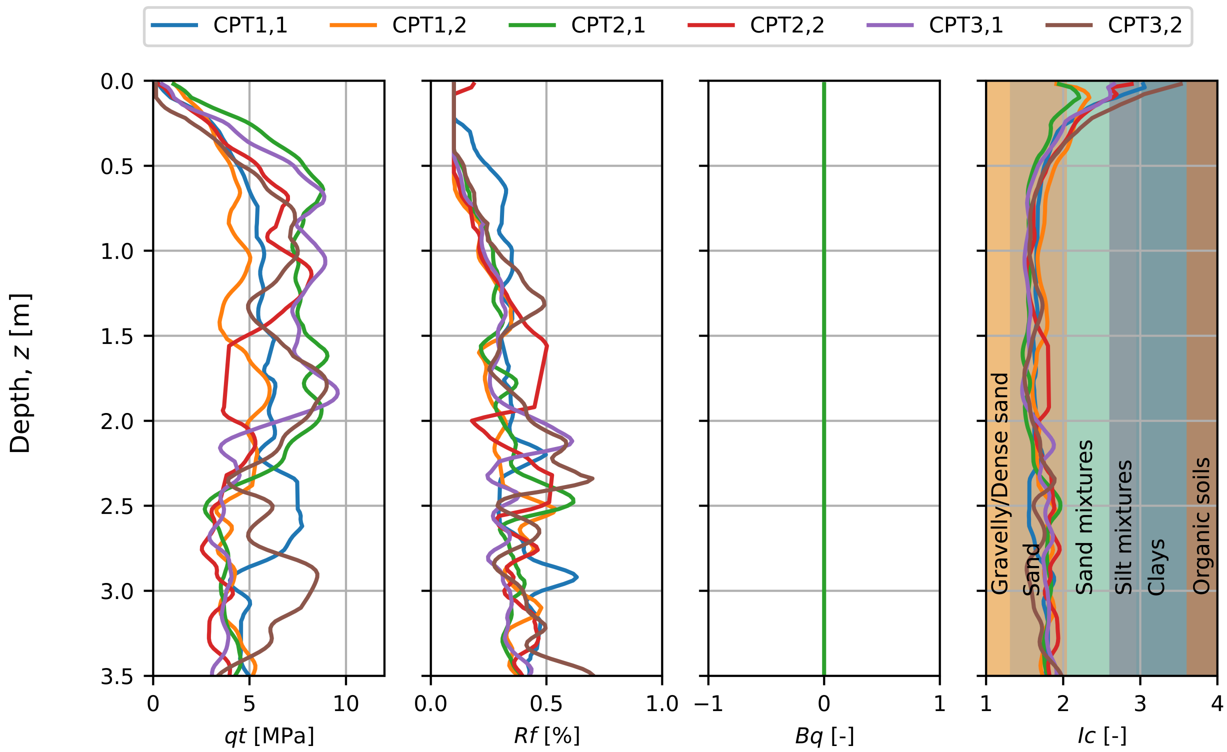

Figure. 7. CPT parameters measured/derived for both test 1 and test 2

The embedment depth of the chain was measured after the maximum load was applied by penetrating a thin rod until contact with the chain was obtained. The horizontal distance between the anchor and the penetrating rod was measured. These measurements were done manually with an accuracy of ±10 mm.

To determine the load reduction, two load transducers measured the load at the hydraulic jack and the padeye. The loads were measured with an accuracy of ±1.5 kN.

Before the suction anchor was installed, three CPTs were conducted in the direction of the chain to estimate the soil conditions for the test. The applied load, angle at mudline, and padeye depth are listed in table 1, where the positions of the CPTs are in figure 9. General CPT parameters measured at test 1 are presented in figure 7.

The load reduction from mudline to padeye for test 1 was around 27 %, whereas the load reduction for test 2 was only 14 %. As test 2 had a padeye position deeper than that of test 1, a higher load reduction was expected. This expectation wasn't confirmed from these tests, and an explanation for this relatively low load reduction wasn't found [15]. Therefore, the load reduction for test 2 will not be used for comparison in section 5.

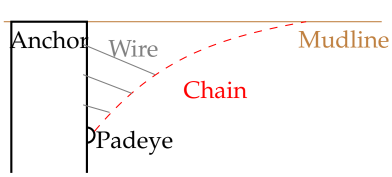

Figure. 8. A visualization of the extended wire after applying load.

Table 1. The applied load (T_{mud}), load angle at mudline (α_{mud}), and padeye depth (z_{pad}) for the two large-scale tests.

	T_{mud} [kN]	α_{mud} [^{o}]	z_{pad} [m]
Test 1	691	3	2.25
Test 2	710	4.4	3.32

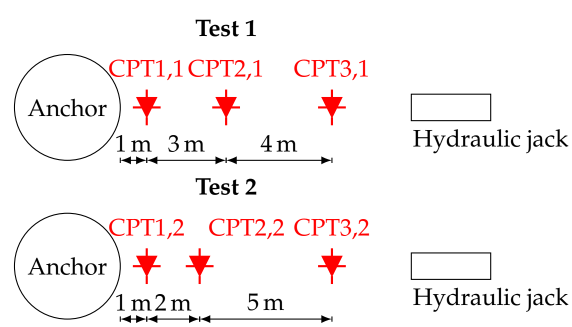

Figure. 9. A principle drawing of the two test setups seen from above, to show the distance of the CPTs from the caissons.

3. METHODS FOR CPT INTERPRETATION

For stress levels below 50 kPa, Krogh et al. [9] recommended the use of a varying lateral earth pressure coefficient ($K_0(z)$) to determine the soil's relative density (D_r) more accurately. To assess its impact on chain-soil interactions, this approach will be compared to a simple approach that assumes a constant value of (K_0). A value of 1 for (K_0) has been selected as it represents an Over-Consolidated soil.

3.1. Shallow CPT by Krogh et al. [9]

The suggested CPT method by Krogh et al. [9] is explained in the following.

The over consolidation ratio (OCR) is determined with Eq. (1)

$$OCR = \frac{\sigma_p'}{\sigma_v'} \quad \textbf{(1a)}$$

$$\sigma_p' = 0.33(q_t - \sigma_v)^{m'} \quad \textbf{(1b)}$$

The fitting exponent m' is applied as a value of 0.72 as provided by Krogh et al. [9]. This value is valid for clean quartz and silica sand, which corresponds to the soil conditions in this study.
The lateral earth pressure coefficient is estimated by applying Eq. (2).

$$K_0(z) = \left(1 - sin(\varphi_{cv})\right) OCR^{sin(\varphi_{cv})} \quad \textbf{(2)}$$

For clean quartz sand, the constant volume friction angle (φ_{cv}) is often of the order 32° as stated by Mayne [13], which is therefore applied in this paper. As ($K_0(z)$) is determined, this value is used to obtain the mean effective stress given by Eq. (3)

$$\sigma_m' = \frac{\sigma_v'}{3}(1 + 2K_0(z)) \quad \textbf{(3)}$$

Krogh et al. [9] suggests an upper limit of ($K_0(z)$ = 3.5).

The mean stress is utilised as a final step to determine the relative density (D_r) based on the measured cone resistance. See Eq. (4).

$$D_r = \frac{1}{C2} \ln\left(\frac{q_c/P_a}{C0(\sigma_m'/P_a)^{C1}}\right) \quad \textbf{(4a)}$$

The fitting constants $C0$, $C1$, $C2$ are determined by Jamiolkowski et al. [7] based on three different sands. The best fit was found to be ($C0 = 24.94$), ($C1 = 0.46$) and ($C2 = 2.96$).

3.2. CPT Correlations

Several correlations of the unit weight (γ) have been evaluated. It was found that Mayne et al. [14] provides the best results with values around 18 kN/m^3 (See Eq. (5)). This corresponds well with typical values of saturated unit weight of sand which are expected between 18 - 20 kN/m^3 [3]. Other assessed correlations are considered too conservative as they provide lower values.

$$\gamma = 11.46 + 0.33 \cdot \log(z) + 3.10 \cdot \log(f_s) + 0.70 \cdot \log(q_t) \quad \textbf{(5)}$$

Several correlations for the relative density (D_r) are evaluated, and Baldi et al. [1] is found to give reasonable results and is applied for the assessment. This relation is shown in Eq. (6) and is in the same form as the equation by Jamiolkowski et al. [7]. The corresponding experimental coefficients determined by Baldi et al. [1] are ($C0 = 181$), ($C1 = 0.55$) and ($C2 = 2.61$).

$$D_r = \frac{1}{C2} \cdot \ln\left(\frac{q_c}{C0 \cdot \sigma_m'^{C1}}\right) \quad \textbf{(6)}$$

Both correlations of relative density depend on the stress conditions and thereby (K_0) which Krogh et al. [9] concluded to have a major impact. The correlation of Bolton [2], stated in Eq. (7), is utilised to predict the friction angle through the use of relative density.

$$\varphi = \varphi_{cv} + 3IR \quad \textbf{(7a)}$$

$$IR = D_r(Q_{min} - \ln(\sigma_m')) - 1 \quad \textbf{(7b)}$$

The value of (Q_{min}) is 10 for quartz and feldspar-type soils. A maximum value of (IR = 4) is applied as suggested by Bolton [2].

4. METHODS FOR CHAIN-SOIL INTERACTIONS

Three methods for determining the chain-soil interactions explained by Neubecker and Randolph [16], Lee et al. [10], and Mortensen [15] will be compared. For all three methods, the horizontal chain part is assumed not to embed the mudline. The mooring system is assumed not to have experienced higher loads in the past and is thereby available for Ultimate Limit State (ULS) calculations. The bearing capacity of a strip footing is used to calculate the normal force (N) on the chain, and consequently, the corresponding bearing capacity factors (N_q, N_γ) for a strip footing in cohesionless soils are employed. The three methods are explained in the following subsections, and the results of the methods are presented in section 5.

4.1. Neubecker and Randolph

Neubecker and Randolph [16] derived closed-form expressions to estimate the load and angle at padeye and validated their model against a centrifuge model test setup with a chain of 3 mm in diameter and at an acceleration level of 40g. Figure 10 shows the principle of the method described by Neubecker and Randolph [16], here is it shown that the normal force is an average bearing resistance (N_{avg}) over the chain.

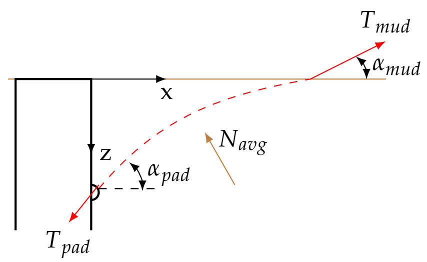

Figure. 10. The loads acting on the chain considered by Neubecker and Randolph [16].

The equations for the method derived by Neubecker and Randolph [16] are set up by Eq. (8) and Eq. (9), where these are based on the shape of an inverse catenary. Neubecker and Randolph [16] used a friction coefficient (μ_f) in Eq. (8) for the friction along the chain.

$$T_{mud} = T_{pad} e^{\mu_f(\alpha_{pad} - \alpha_{mud})} \tag{8}$$

$$\frac{T_{pad}}{2}(\alpha_{pad}{}^2 - \alpha_{mud}{}^2) = \int_0^{z_{pad}} N_{avg} dz \tag{9}$$

Eq. (10) is the average bearing resistance (N_{avg}), where a effective width factor (B_b) is multiplied to the diameter (d) of the chain. In this method, the integration over the average bearing resistance (Eq. (9)) considers values from CPT 1 exclusively, neglecting any horizontal variation. Neubecker and Randolph [16] only used the surcharge term ($N_q\gamma' z$) to determine the normal force.

$$N_{avg} = B_b d N_q \gamma' z \tag{10}$$

$$N_q = \frac{1+\sin(\varphi)}{1-\sin(\varphi)} e^{\pi} \tan(\varphi) \tag{11}$$

The friction coefficient (μ_f) between the chain and the soil is in the range of 0.4 to 0.6 for clay, but Neubecker and Randolph [16] expected it to be within the same range for sand. The range of the friction coefficient (μ_f) was investigated for this study, and a value of 0.5 was found to give the best fit for this method. No recommendations for the bearing capacity factor (N_q) are given; thus, in this study, the normally used factor derived by Prandtl [17] (Eq. (11)) is used. According to Neubecker and Randolph [16], the weight of the chain only affects the chain-soil interactions in soft soil. By considering the soil conditions for the large-scale test, the weight of the chain is neglected for this method.

The chain configuration is estimated by Eq. (12).

$$x^* = \left(\sqrt{\frac{T^* \alpha_{pad}{}^2}{2} + 1} - \sqrt{\frac{T^* \alpha_{pad}{}^2}{2} + z^*} \right) \sqrt{2T^*} \tag{12}$$

$$T^* = \frac{T_{pad}}{z_{pad} N_{avg}} \tag{13}$$

Where (x^* and z^*) is x- and z-coordinates normalized with the padeye depth (z_{pad}).

As Eq. (8) and Eq. (9) show, this method is two nonlinear equations with two unknowns. In this paper, the Newton-Raphson method is employed to resolve the issue of solving a system of nonlinear equations. The angles in Eq. (8) and Eq. (9) are in radians.

4.2. Lee et al.

Both Lee et al. [10] and Mortensen [15] created an incremental solution, where the forces are determined for a single chain link. Lee et al. [10] validated their model against a centrifuge model test setup with a wire of 2.4 mm and an acceleration level of 50g. Figure 11 shows the forces considered by Lee et al. [10] for the chain links.

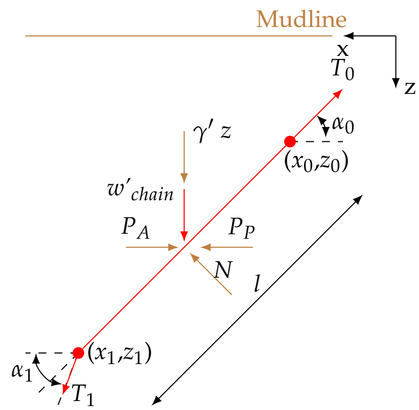

Figure. 11. The forces on a chain link considered by Lee et al. [10].

Based on the known conditions at the mudline (T_{mud}, α_{mud}), the force (T_1) and angle (α_1) at local node 1 can be determined. Node 1 for the first chain link will then be the condition for node 0 at the following chain link and etc. This calculation from mudline to padeye is solved with several iterative loops:

1. The x-position of the local node 0 of the first chain link at the mudline is assumed
2. Chain links are added until the z-coordinate of the padeye is passed
3. Check if the x-position of node 1 of the last chain link has passed the padeye position
4. Repeat 1-3 until both x- and z-positions of node 1 of the last chain link have passed the padeye position
5. Shorten the first chain link and repeat 2–5 until the distance from the padeye position in both x- and z-directions to node 1 of the last chain link is below 1 cm

Eq. (14) and Eq. (15) shows how Lee et al. [10] determines the force (T_1) and the angle (α_0) respectively.

$$T_1 = T_0 - l(\tau_f + w'_{chain}\sin(\alpha_0)) \quad \textbf{(14)}$$

$$\alpha_1 = \alpha_0 + l(N - w'_{chain}\sin(\alpha_0)) \quad \textbf{(15)}$$

Lee et al. [10] determined the forces per unit length on a chain link by Eq. (16) and Eq. (17). Lee et al. [10] used different effective width (B_b, B_s) for determining the normal force (N) and the friction (τ_f). Lee et al. [10] also considered the above laying soil effect to the normal force (N). To determine the friction along the chain link (τ_f), Lee et al. [10] considered the active and passive earth pressure.

$$N = B_b(\gamma' z N_q + 0.5 d\gamma' N_\gamma - \gamma' z) \quad \textbf{(16)}$$

$$\tau_f = [B_s(\gamma' z\cos(\alpha_0) + (P_A + P_P)\sin(\alpha_0))]\tan(\delta) \quad \textbf{(17)}$$

$$N_\gamma = \left(\frac{\tan^2(45° + \varphi/2)}{\cos^2(\varphi)} - 1\right)\tan(\varphi) \quad \textbf{(18)}$$

$$P_A = 0.5\gamma' z\frac{1-\sin(\varphi)}{1+\sin(\varphi)} \quad \textbf{(19)}$$

$$P_P = 0.5\gamma' z\frac{1+\sin(\varphi)}{1-\sin(\varphi)} \quad \textbf{(20)}$$

The frictional force (τ_f) acting on the chain was determined by Lee et al. [10] through consideration of the soil above, active and passive earth pressures, and a friction coefficient of $\tan(\delta)$. Lee et al. [10], obtained the steel-sand contact friction angle (δ) with a direct shear test where half of the sand was replaced by a steel specimen and estimated that (δ = 2/3 φ). According to Lee et al. [10], the effective widths (B_b and B_s), of a chain should be 2.5 and 8 times its diameter, respectively, which is used for this method. These values were derived by Dutta and Degenkamp [4] for clay; one could imagine they would be different for sand. Lee et al. [10] recommended the use of the bearing capacity factors (N_γ and N_q) as determined by Terzaghi [20] (Eq. (18)) and Prandtl [17] (Eq. (11)) respectively, which are used for this method.

Lee et al. [10] determined the position of the next chain link by Eq. (21) and Eq. (22) and used an average value of the angle at node 0 and 1 (α_0, α_1).

$$x_1 = x_0 + l(\cos(\alpha_0) + \cos(\alpha_1))/2 \quad \textbf{(21)}$$

$$z_1 = z_0 + l(\sin(\alpha_0) + \sin(\alpha_1))/2 \quad \textbf{(22)}$$

4.3. Mortensen

Mortensen [15] also created an incremental solution as Lee et al. [10], and is solved with the same approach as explained in the previous subsection. Mortensen [15] validated the model to the large-scale tests at Frederikshavn as explained in section 2. Figure 12 shows the forces on a chain link considered by Mortensen [15], here it can be noted that Mortensen [15] doesn't consider the above laying soil.

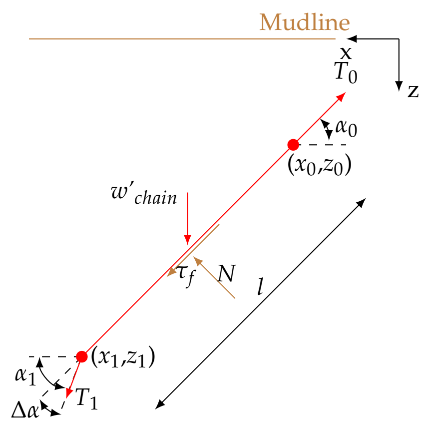

Figure. 12. The forces on a chain link considered by Mortensen [15].

The change in angle and force derived by Mortensen [15] is set up by Eq. (23) and Eq. (24).

$$T_1 = \frac{T_0 - w'_{chain} l\sin(\alpha_0) - \tau_f}{\cos(\Delta\alpha)} \quad \textbf{(23)}$$

$$\tan(\Delta\alpha) = \frac{N - w'_{chain} l\cos(\alpha_0)}{T_0 - w'_{chain} l\sin(\alpha_0) - \tau_f} \quad \textbf{(24)}$$

Mortensen [15] determined the forces on a chain link by Eq. (25) and Eq. (26). The main difference compared to Lee et al. [10] is that Mortensen [15] determine the frictional force (τ_f) on the chain as a factor (α_{sand}) multiplied by the normal force (N) where a value of 0.5 was recommended by Mortensen [15] and used in this study.

$$N = dA_{sand}(0.5\gamma' dA_{sand}N_\gamma + N_q\gamma' z) \quad \textbf{(25)}$$

$$\tau_f = N\alpha_{sand} \quad \textbf{(26)}$$

$$N_\gamma = 0.25\left((N_q - 1)\cos(\varphi)\right)^{1.5} \quad \textbf{(27)}$$

As it can be seen from Eq. (25) Mortensen [15] also used an empirical factor (A_{sand}) multiplied by the diameter of the chain (d). He discovered that the width of the chain (b) approximately corresponds to (dA_{sand}) which is then employed in this study. Mortensen [15] recommended determining the bearing capacity factor (N_γ) for a smooth strip-footing according to Lundgren and Mortensen [11] (Eq. (27)), and the bearing capacity factor (N_q) according to Prandtl [17] (Eq. (11)).

Mortensen [15] determined the position of the next chain link by Eq. (28) and Eq. (29)

$$x_1 = x_0 + l\cos(\alpha_0) \quad \textbf{(28)}$$

$$z_1 = z_0 + l\sin(\alpha_0) \quad \textbf{(29)}$$

4.4. Employed Soil Parameters

The soil parameters are derived for each measurement of the CPTs, hence for each 2 cm. To apply this in a more practical matter when calculating the chain-soil interactions, the method employed is as follows:

1. A mean value of the soil parameters derived for each CPT along the chains is computed for every 25 cm
2. If a chain link is estimated to lie between two CPTs, then the soil parameters applied in further calculations are determined based on an interpolated value
3. If a chain link is estimated not to be located between two CPTs, e.g. between the caisson and CPT 1, then the soil parameters are determined as the value in the present 25 cm section of the nearest CPT, in this example, CPT 1.

The unit weight (γ') of the soil is determined based on a correlation that is not derived for shallow depth. Therefore, to avoid underestimating the unit weight of the soil when applied in the chain-soil interaction methods, the value of the uppermost soil layer is determined based on the depth at which the CPTs has reached the quasi-stationary phase. For all CPTs, this is around 0.75 m.

5. RESULTS

The results presented in the following include the CPT interpretation, chain-soil interaction and conclusively a sensitivity analysis based on selected influencing parameters.

5.1. CPT

Figure 13 illustrates the soil parameters obtained from the various CPT correlations utilised in this study. The figure is based on CPT 1 at test 1 but the same tendencies are observed for all the CPTs. The figure includes subplots of the cone resistance (q_c), relative density (D_r), friction angle (φ) and the lateral earth pressure coefficient (K_0).

The measured cone resistance (q_c) is shown together with the estimated (q_c) profiles determined with the four methods described in section 3. Here, an average value of the relative density with a depth-dependent ($K_0(z)$) is applied. These average values of (D_r) are likewise shown in figure 13, where it is noteworthy, that the soil has been divided into two layers as a decrease in the measured cone resistance is observed.

In figure 13, the relative densities estimated by the four methods are illustrated together with laboratory data of the sand at Frederikshavn and the former average values applied in the calculation of (q_c). The friction angles estimated based on the four methods are plotted together with the interval of friction angles determined from triaxial tests of the sand at Frederikshavn. The triaxial results are shown as an interval since the depth they represent is deeper than the CPTs. Lastly presented are the (K_0) values used in the calculations. This includes the constant value of 1 and a depth-dependent value.

The method suggested by Krogh et al. [9] with ($K_0(z)$) provides more satisfactory results compared to using a constant value of (K_0) when solely assessing how to interpret CPT as this captures the development of (q_c) more accurately. This applies regardless of the correlation used to estimate the relative density (D_r). However, different correlations of relative density result in significantly different friction angles.

It is apparent that by using a depth-dependent ($K_0(z)$), lower values of the friction angle (φ) are obtained when derived from Bolton [2]. The estimates obtained from all four methods are similar to the laboratory data since they mostly fall within the range of values obtained from triaxial tests. However, Baldi et al. [1] seems to provide values in the high end. This is observed for both constant (K_0) and depth-dependent ($K_0(z)$). The limit of 44° on the friction angle is due to the limit of 4 on the relative density index (IR) in Eq. (7) and the value of 32° for the dilation angle (ψ).

By applying a depth varying ($K_0(z)$), lower values of relative density (D_r) will be obtained. This is true for both Jamiolkowski et al. [7] and Baldi et al. [1]. In laboratory data comparison, Baldi et al. [1] with a constant lateral earth pressure coefficient of 1 captures the estimated values better than the three other methods. According to Krogh et al. [9] a CPT derived relative density (D_r) is overestimated in the surficial part of OC sand. Therefore, even though Baldi et al. [1] captures the lab data most accurately, it does not necessarily imply that it is a correct interpretation.

5.2. Chain-Soil Interactions

The results of the chain-soil interactions obtained by the different methods are divided into three separate parts. The load reduction of the chain will be introduced initially followed by the angle at padeye and the chain configuration. General trends and observations of the different methods will be addressed. This includes their ability to estimate the individual responses accurately with respect to the results of the large-scale test.

5.2.1. Load Reduction

Figure 14 shows the estimated load reduction for each method and is compared to the results of test 1. The same tendency across the different combinations is discovered for test 2, thus, this is not shown. The load reduction estimated by Neubecker and Randolph [16] is relatively close to the measured load reduction, where Mortensen [15] estimates a relatively low load

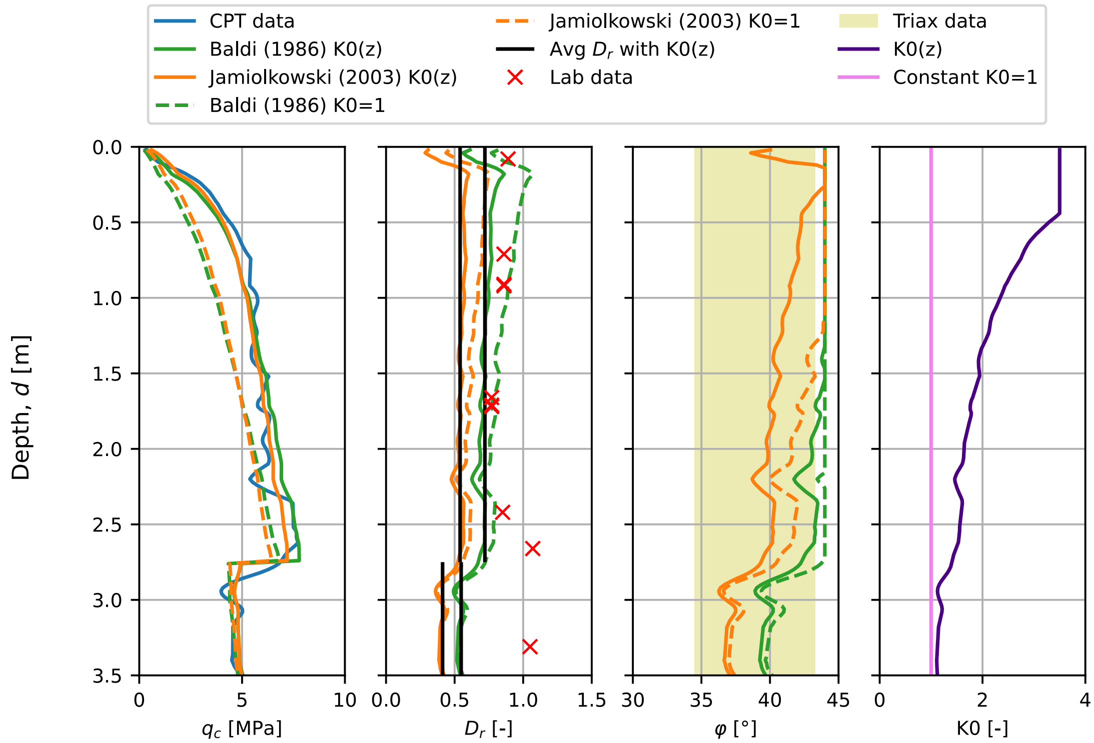

Figure. 13. Soil parameters derived for CPT 1 at test 1. The triaxial results are shown as an interval in the friction plot.

reduction. The CPT methods show the same tendency for both Neubecker and Randolph [16] and Mortensen [15], where the lowest load reduction is estimated with Jamiolkowski et al. [7] with varying ($K_0(z)$) and the highest with Baldi et al. [1] with constant (K_0).

As can be seen from figure 14 Lee et al. [10] is far from the load reduction measured in the large-scale test and thereby this method will not be considered in the following comparisons.

5.2.2. Angle at Padeye

Figure 15 shows the estimated angle at padeye for each method and is compared to the results of the two large-scale tests. Both methods, Neubecker and Randolph [16] and Mortensen [15], estimate a higher angle for test 2, even though the measurement

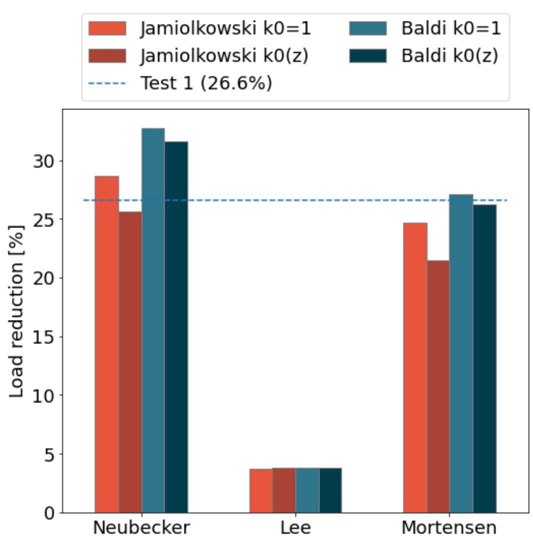

Figure. 14. The load reduction - for test 1 - estimated for the 12 different combinations of chain-soil interaction and CPT-interpretation, compared to the results of the large-scale test.

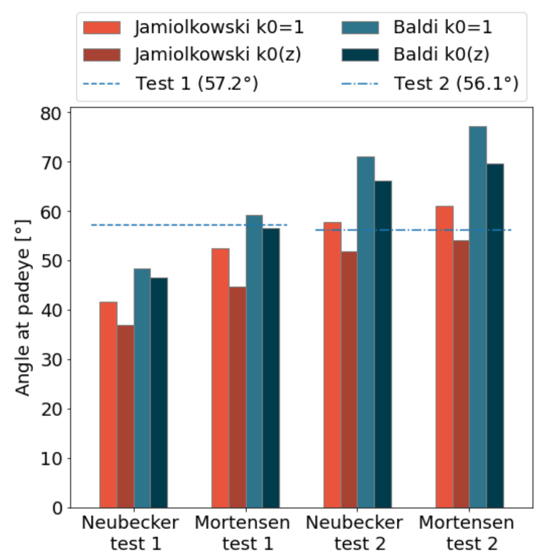

Figure. 15. The estimated angle at padeye for the different combinations of methods compared to the large-scale results for both chains.

from the test is almost identical. Neubecker and Randolph [16] generally estimates the angle lower than Mortensen [15], where Mortensen [15] have a closer fit to the measured value. Considering the low angle at padeye estimated by Neubecker and Randolph [16], only Mortensen [15] will be used in the following comparison.

5.2.3. Chain Configuration

Figure 16 shows the estimated chain configuration and is compared to the results of the two large-scale tests. No clear trend

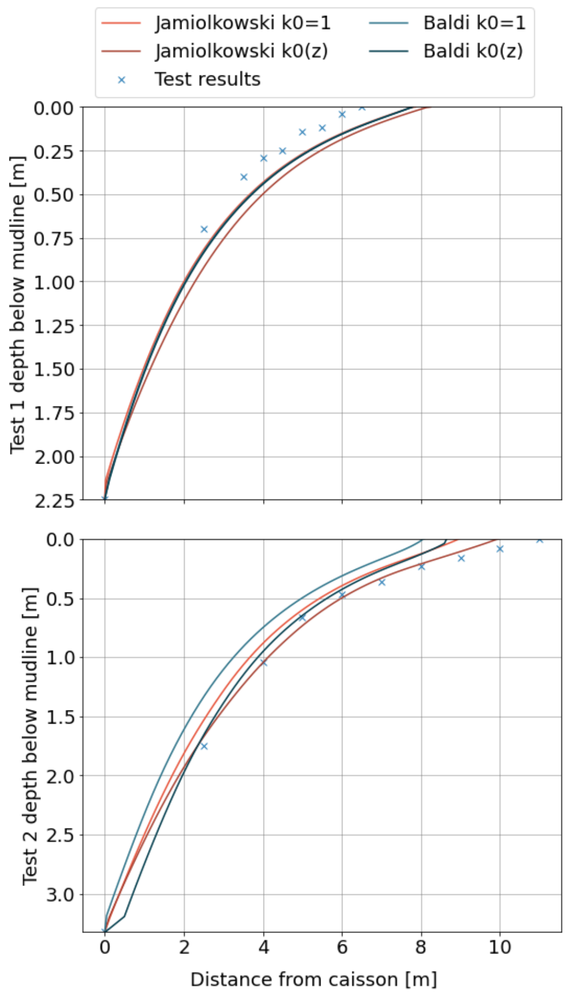

Figure. 16. The chain configuration estimated by Mortensen [15] for the different CPT methods both tests.

has been detected between the two chains but a relatively close fit to the measured chain configurations is obtained.

5.3. Sensitivity Analysis

Based on the observations made in this study, along with figure 14, 15, and 16, it appears that Mortensen [15] provides a reliable estimation of chain-soil interactions. Therefore, a sensitivity analysis of the parameters on the estimation of load reduction and the angle at padeye will be presented.

The parameters are chosen based on the accuracy of determining the values. The parameters examined in the sensitivity analysis are; Force at mudline (T_{mud}), Angle at mudline (α_{mud}), Unit weight of soil (γ'), Friction angle of soil (φ), the two empirical factors (A_{sand}) and (α_{sand}).

The results of test 1 with the CPT correlation Jamiolkowski et al. [7] and a constant (K_0) are used as the base values for the sensitivity analysis. The parameters examined are varied in intervals of 2.5 % from -5.0 % to +5.0 % of the base values. The y-axis of the plot in figure 17 shows the change from the estimated response based on the base values. From the sensitivity analysis

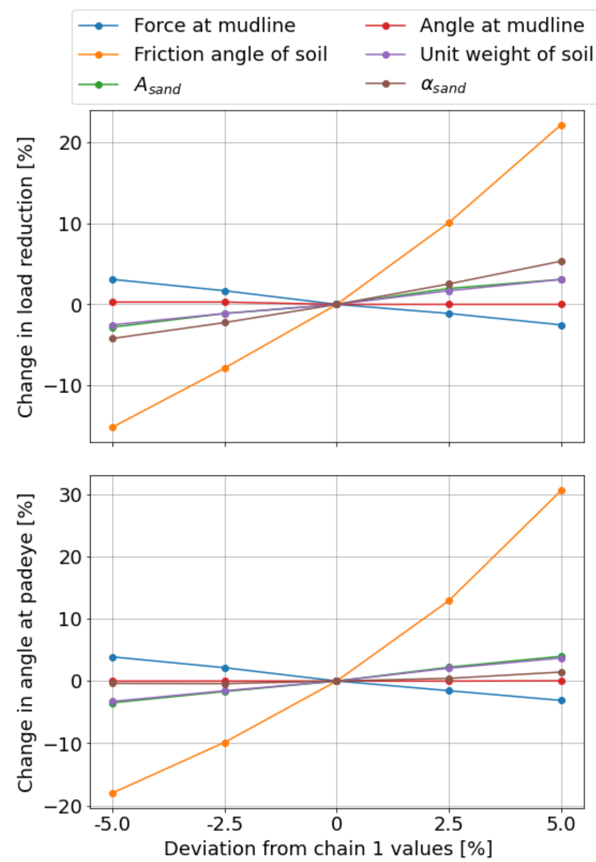

Figure. 17. The results of the sensitivity analysis of the input parameters of the method derived by Mortensen [15] for the load reduction and the angle at padeye.

in figure 17 it can be seen that the precision of determining the angle at the mudline is not vital for the responses. The empirical friction factor (α_{sand}) does not affect the angle at padeye. The most significant influence comes from the friction angle, where higher-order effects are observed. It is furthermore notable that the force at the mudline is inversely proportional to both the load reduction and the change in angle at the padeye. The rest of the parameters have an almost identical positive linear influence on the responses.

6. DISCUSSION

Generally, this analysis doesn't provide a clear answer to the best combination for estimating the chain soil interactions, but a combination of Mortensen [15] and Jamiolkowski et al. [7] yields satisfactory outcomes.

The sensitivity analysis (Fig. 17) has revealed that a too-conservative estimate of the design load will have a negative linear effect on the load reduction and angle at padeye. It is crucial to take this into account since a smaller angle at the padeye can lead to an overestimation of the anchor's bearing capacity.

The estimation of the normal force on the chain will have a significant impact on the angle at the padeye and the chain configuration. The bearing capacity factors used to determine the normal force are nonlinear functions of the friction angle, which is why the higher-order effects in the sensitivity analysis are seen (figure 17). The importance of accurately determining the friction angle is highlighted by the sensitivity analysis. The four CPTs all estimated the friction angle as relatively high compared to the triaxial tests, but since a relatively close fit of the angle was obtained to the measured it can be assumed that Mortensen [15] has a tendency to underestimate the normal force. The higher friction angle is then compensating for the low normal force determined, which also could explain why the error of the angle between the chains isn't consistent.

The relatively high estimate of the load reduction by Mortensen [15] indicates that the empirical factor (α_{sand}) may need to be lower than 0.5. By conducting a centrifuge test in sand on an inverse catenary chain under static loading, Frankenmolen et al. [6] found that the factor (α_{sand}) should be lowered. Frankenmolen et al. [6] obtained results of (α_{sand}) between 0.22 and 0.37, leading to the conclusion that the friction along the chain link isn't fully mobilized because the link moves through the soil instead of along its axis.

In general, Neubecker and Randolph [16] calculates a lower angle at the padeye compared to Mortensen [15] (figure 15). Compared to the large-scale tests, it is unclear which method generates the best results, but it is apparent that Neubecker and Randolph [16] significantly underestimates the angle for test 1 compared to Mortensen [15].

The load reduction (figure 14) clearly indicates that the approach by Lee et al. [10] is determining the load reduction overly cautious. In contrast to Mortensen [15], who used a fraction of the normal force, Lee et al. [10] relied on active and passive earth pressure coefficients to determine friction along the chain, resulting in frictional forces that were one-tenth of the friction determined by Mortensen [15].

7. CONCLUSION

The assessment of different methods for determining chain-soil interactions is based on their ability to estimate the chain-soil interactions observed in the two large-scale tests. The analysis highlights that the method proposed by Lee et al. [10] is not proficient in determining friction along the chain. There is no definitive answer as to which method - Neubecker and Randolph [16] or Mortensen [15] - is better. However, it has been assessed that an underestimation of an angle is a bigger error than an overestimation., thus the method proposed by Mortensen [15] was chosen for the sensitivity analysis.

To assess the impact of various parameters used by Mortensen [15], a sensitivity analysis was performed. Results showed that the friction angle has a significant influence on the load reduction and the angle at the padeye, while the unit weight has a small effect. Empirical parameters, (A_{sand}) and (α_{sand}) had a small positive linear impact on the load reduction, with only (A_{sand}) affecting the angle at padeye. The accuracy of the angle at the mudline had little to no effect on the responses. The force at the mudline had a negative linear effect on both responses.

Although the CPT analysis indicated that Jamiolkowski et al. [7] with varying ($K_0(z)$) is in better agreement with the laboratory results, and the sensitivity analysis revealed that determining the friction angle relative precision is of high importance, the optimal outcome was obtained by utilising Jamiolkowski et al. [7] with constant K_0.

In conclusion, it is not clear which CPT correlation or chain-soil interaction method to use. According to this study, using Jamiolkowski et al. [7] with constant (K_0) in combination with the approach suggested by Mortensen [15] can produce reasonable results and is thereby the recommended approach.

ACKNOWLEDGEMENTS

The permission to publish the large-scale test by Aalborg University, performed in corporation with The Norwegian Geotechnical Institute, is greatly appreciated.

The authors are grateful for the guidance and constructive feedback from senior specialist Søren Dam Nielsen and leading specialist Søren Peder Hyldal Sørensen both from COWI.

The authors are grateful for not only the office space provided by COWI Aalborg but also that we could be a part of the offshore wind section during the last year of the education.

ABBREVIATIONS

AAU	Aalborg University, Denmark
CPT	Cone Penetration Test
LCoE	Levelized Cost of Energy
NGI	The Norwegian Geotechnical Institute
OC	Over-Consolidated
ULS	Ultimate Limit State

SYMBOLS

IR	Relative dilatancy index
Q_{min}	Soil type dependent parameter
$\Delta\alpha$	Change in angle between the local nodes 0 and 1
α_0	Load angle at local node 0
α_1	Load angle at local node 1
α_{mud}	Load angle at mudline
α_{pad}	Load angle at padeye
α_{sand}	Empirical friction factor
δ	Interface friction angle
γ'	Effective unit weight of the soil
γ	Unit weight of the soil
μ_f	Friction coefficient
ψ	Dilation angle
σ'_m	Mean effective stress
σ'_p	Past effective consolidation pressure or pre-consolidation pressure
σ_v	Vertical total stress
σ'_v	Vertical effective stress
τ_f	Force of friction
φ_{cv}	Critical volume friction angle of the soil
φ	Friction angle of the soil
A_{sand}	Empirical factor to consider the 90° rotation for each chain link
B_q	Pore pressure ratio
B_b	Effective width of bearing
B_s	Effective width of shearing
D_r	Relative density of soil
$F_{current}$	Current forces
F_{wave}	Wave forces
F_{wind}	Wind forces
I_c	Material parameter
$K_0(z)$	*In-situ* lateral earth pressure coefficient varying with depth
K_0	*In-situ* lateral earth pressure coefficient
N	Normal force
N_γ	Bearing capacity factor of soil unit weight
N_{avg}	Average bearing resistance
N_q	Bearing capacity factor of surcharge
OCR	Over consolidation ratio
P_a	Atmospheric pressure
P_A	Active earth pressure
P_P	Passive earth pressure
R_f	Friction ratio
T^*	Normalised force at padeye
T_0	Force at local node 0
T_1	Force at local node 1

T_{mud}	Force at mudline
T_{pad}	Force at padeye
b	Width of chain-link
d	Diameter of chain
d_{50}	Mean grain size
f_s	Measured sleeve friction
l	Length of chain-link
m'	Fitting exponent
q_c	Measured cone resistance
q_t	Corrected cone resistance
w'_{chain}	Submerged unit weight of the chain per meter
x^*	Normalised x-coordinate
x_0	x-coordinate for local node 0
x_1	x-coordinate for local node 1
z	Depth below mudline
z^*	Normalised z-coordinate
z_0	z-coordinate for local node 0
z_1	z-coordinate for local node 1
z_{pad}	Padeye depth

REFERENCES

1. **Baldi et al., 1986**. G. Baldi, D. Bruzzi, S. Superbo, M. Battaglio and M. Jamiolkowski. *Refined Model for Interpreting Shallow Penetration CPTs in Sands.* Proceedings of the Fourth International Geotechnical Seminar, pages 143–156, 1986.
2. **Bolton, 1986**. M.D. Bolton. *Strength and dilatancy of sands.* Géotechnique, 36(1), 65–78, 1986.
3. **Budhu, Jan 2011**. Muniram Budhu. *Soil Mechanics and Foundations*, volume 3. 2011. ISBN 978-0-470-55684-9.
4. **Dutta and Degenkamp, 1989**. A. Dutta and G. Degenkamp. *Behaviour of Embedded Mooring Chains in Clay During Chain Tensioning.* proc., 21st Annu. Offshore Technology Conference, All Days, 551–562, 1989.
5. **Emerson et al., 2008**. M. Emerson, P. Foray, A. Puech and E. Palix. *A global model for accurately interpreting CPT data in sands from shallow to greater depth.* page 687–694, 2008.
6. **Frankenmolen et al., 2016**. S. F. Frankenmolen, D. J. White and C. D. O'Loughlin. *Chain-Soil Interaction in Carbonate Sand.* OTC Offshore Technology Conference, Day 4, OTC–27102–MS, 2016.
7. **Jamiolkowski et al., 2003**. M. Jamiolkowski, D. C. F. Lo Presti and M. Manassero. *Evaluation of Relative Density and Shear Strength of Sands from CPT and DMT.* pages 201–238, 2003.
8. **Jensen et al., 2023**. Christian Lykke Jensen, Stefan Rysgaard Houmann, Troels Juul Pedersen and Lars Bo Ibsen. *Modelling the Drained Capacity of Inclined Loaded Suction Anchors in Cohesionless Soil: A Finite Element Study.* Not decided for now, 2023.
9. **Krogh et al., 2022**. Lone Krogh, Santiago Quinteros, Harun Kursat Engin and Tom Lunne. *Revisiting interpretation of relative density from shallow depth CPTs in sand.* Canadian Science Publishing, 59(6), 808–826, 2022.
10. **Lee et al., 2014**. Hoonyoung Lee, Dong-Soo kim and Yun Wook Choo. *Profile and Frictional Capacity of a Mooring Line Embedded in Sand via Centrifuge Model Testing.* Journal of Geotechnical and Geoenvironmental Engineering, 140(11), 04014059, 2014.
11. **Lundgren and Mortensen, 1953**. H Lundgren and K Mortensen. *Determination by the theory of Plasticity of the bearing capacity of Continuous Footings on Sand.* Proc. 3rd Int. Conf. Soil Mech, 1, 409, 1953.
12. **Massarsch et al., 2020**. K. Rainer Massarsch, Carl Wersäll and Bengt H. Fellenius. *Horizontal stress increase induced by deep vibratory compaction.* Proceedings of the Institution of Civil Engineers - Geotechnical Engineering, 173(3), 228–253, 2020. . URL http://dx.doi.org/10.1680/jgeen.19.00040.
13. **Mayne, 2014**. Paul Mayne. *Interpretation of geotechnical parameters from seismic piezocone tests*, 2014.
14. **Mayne et al., 2010**. P.W. Mayne, J. Peuchen and D. Bouwmeester. *Soil unit weight estimation from CPTs*, 2010.
15. **Mortensen, 2015**. N. Mortensen. *Chain configuration in sand, theory and large scale field testing.* Frontiers in Offshore Geotechnics III : Proceedings of the 3rd International Symposium on Frontiers in Offshore Geotechnics (ISFOG 2015), 1, 905–912, 2015.
16. **Neubecker and Randolph, 1995**. S. R. Neubecker and M. F. Randolph. *Profile and Frictional Capacity of Embedded Anchor Chains.* Journal of Geotechnical Engineering, 121(11), 797–803, 1995.
17. **Prandtl, 1920**. L. Prandtl. *Über die Härte plastischer Körper.* Nachrichten von der Gesellschaft der Wissenschaften zu Göttingen, Mathematisch-Physikalische Klasse, 1920, 74–85, 1920.
18. **Puech and Foray, 05 2002**. Alain Puech and Pierre Foray. *Refined Model for Interpreting Shallow Penetration CPTs in Sands.* All Days (OTC-14275-MS), 2002.
19. **Rosa-Aquino, Aug 2021**. *Paola Rosa-Aquino*, 2021. URL https://www.theguardian.com/environment/2021/aug/29/floating-wind-turbines-ocean-renewable-power.
20. **Terzaghi, 1943**. Karl Terzaghi. *Bearing Capacity.* Theoretical Soil Mechanics, pages 118–143, 1943.
21. **Vivatrat et al., 1982**. Vitoon Vivatrat, Philip J. Valent and Albert A. Ponterio. *The Influence of Chain Friction on Anchor Pile Design.* OTC Offshore Technology Conference, All Days, 1982.

Article 2

Modelling the Drained Capacity of Inclined Loaded Suction Anchors in Cohesionless Soil: A Finite Element Study

Modelling the Drained Capacity of Inclined Loaded Suction Anchors in Cohesionless Soil: A Finite Element Study

CHRISTIAN LYKKE JENSEN[1], STEFAN RYSGAARD HOUMANN[1], TROELS JUUL PEDERSEN[1], AND LARS BO IBSEN[2]

[1] *M.Sc. student, Dept. of Civil Engineering, Aalborg University, Denmark*
[2] *Prof., Dept. of Civil Engineering, Aalborg University, Denmark*

Abstract: As the Levelized Cost of Energy (LCoE) is progressively being reduced, the viability of floating offshore wind turbines is increased. The anchors ensuring the station-keeping of these offshore structures are characterised as an important factor in the design and the total cost. Numerical models are widely used in engineering practice when designing such structures. While these numerical representations should portray reality, it is often difficult to model all aspects accurately. This study conducted a variety of investigations with respect to different modelling techniques and the influence of multiple soil parameters. The investigations have led to assessments and recommendations for modelling suction caisson anchors undergoing static inclined loading in cohesionless soils. The analyses concluded that the self-weight of the anchor should be modelled as this significantly influences the displacement field. Furthermore, applying a force-controlled loading type provided the most reasonable results in contrast to a displacement-controlled loading type which led to unexpectedly large bearing capacities.

1. INTRODUCTION

As the world continues to combat climate change and accelerate the green transition, advancements in floating wind technology are moving its application toward commercial use. Efforts are continuously being made to reduce the Levelized Cost of Energy (LCoE) to make the technology more financially viable.

Floating offshore structures have been used in the oil and gas industry for several years. For these projects, station-keeping has traditionally been a minor component of the total costs. As a result, conservatism has often been applied to station-keeping due to the relative cost. For floating wind structures, significant reductions in the LCoE could therefore be found by further optimising the mooring system.

An essential component of the mooring system is the anchor. Various types of anchors are available, including gravity-based, drag-embedded, and driven anchors. An alternative anchor solution is suction caissons. These are large-diameter cylinders with an open end at the base and a closed top. As the anchors are installed by suction, installation is easier in deep waters compared to other anchor types. Additionally, the simple geometry is advantageous in terms of the manufacturing process. Major field applications of suction caissons have mostly been in clay at great water depths. As a result, a lot of research and design methodology concerns the capacity of cohesive soils. The capacity of anchors installed in cohesionless soils is therefore of interest and chosen as a focal point of this study.

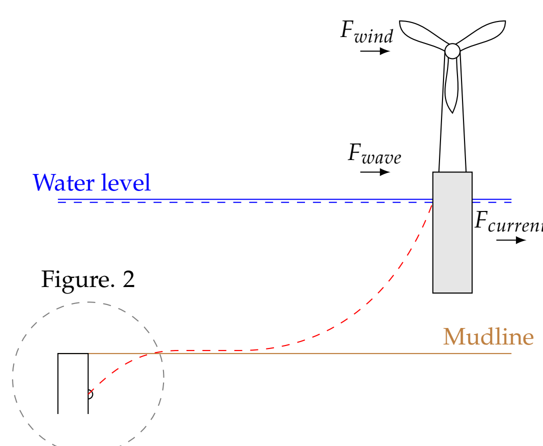

Figure. 1. Illustration of a mooring system configuration with a suction caisson anchor.

Suction anchors are versatile, as they can be used for the station-keeping of all floating wind concepts. However, in this study, their application is considered for spar and semi-submersible concepts. These concepts typically use a catenary or a taut mooring system. Figure 1 depicts an example of a catenary mooring system used for spar buoy station-keeping, including the working loads. As the loading originates from wind, waves, and currents, the anchor will experience cyclic loading. If these cyclic loads lead to mean tensile forces for a sufficiently long duration, this could be modelled as a static load. As a result, the drained response will govern the anchor's capacity. The short duration and high loading rate of the peak loads will typically lead to the generation of negative excess pore pressure and enhance the tensile capacity of the anchor. The drained static capacity of suction caisson anchors in cohesionless soil is therefore of importance.

When suction anchors are used for catenary and taut mooring systems, the padeye is usually placed below the mudline. In this case, the soil imposes shear forces and normal forces on the chain. These forces result in an inverse catenary shape and an inclined loading of the anchor. As illustrated in figure 2 depending on the load configuration, i.e., inclination (α_{pad}) and padeye depth (z_{pad}), the failure mechanism will be a unique combination of both translation and rotation. The different failure mechanisms will mobilise to different extents vertical and horizontal capacities. As a result, the pull-out force or bearing capacity of the anchor is dependent on the load configuration.

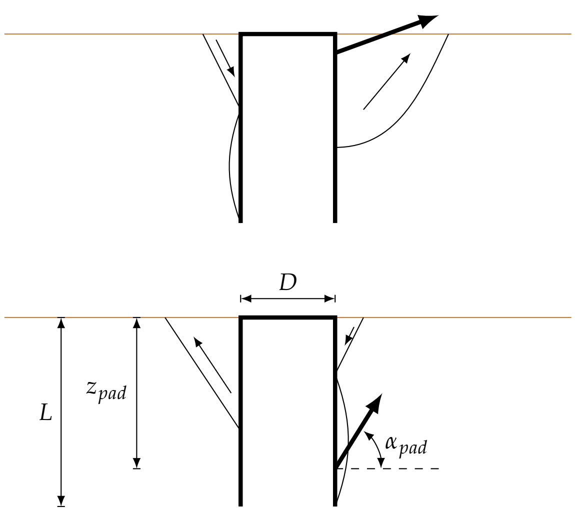

Figure. 2. Illustration of different failure mechanisms for different load applications.

The drained bearing capacity of suction-installed foundations or anchors in cohesionless soils has been studied by a number of authors. Studies have been carried out experimentally, numerically, or by using analytical techniques. Studies on the inclined loading capacity of suction anchors installed in cohesionless soil are scarcer than those on horizontal or vertical one-dimensional loading, which has received the majority of attention in the literature.

Most research on inclined loading arises from a series of centrifuge model tests conducted by Bang et al. [3] on suction piles in sand to determine the inclined loading capacities. According to the study, the load inclination (α_{pad}) and padeye depth (z_{pad}) have a significant impact on the pull-out capacity.

Ahmed and Hawlader [1] conducted a series of finite element analyses comparing results with the centrifuge tests. Zhao et al. [10] and Cheng et al. [6] used finite element analysis to establish failure envelopes in (H, V)-space of the drained capacity. These finite element analyses were performed using Abaqus/Explicit FE software in order to model large displacements. Ahmed and Hawlader [1] and Zhao et al. [10] both used a Mohr-Coulomb model (MC) for the constitutive modelling of the sand, whereas Cheng et al. [6] used a Modified Mohr-Coulomb model to capture the stress-dependent hardening – softening behaviour of the sand.

These previous studies considered the effects of load inclination (α_{pad}), padeye depth (z_{pad}) and caisson aspect ratio ($\lambda = \frac{L}{D}$). In contrast, the primary objective of this study is to identify and quantify significant soil parameters that govern the drained pull-out force for different load configurations. Secondly, the study provides a general description and a recommended approach to finite element modelling of the drained pull-out capacity of suction caisson anchors using PLAXIS 3D.

This paper presents a series of Finite element analysis (FEA) calculating the drained pull-out force of a suction caisson in sand. The calculations are performed at various padeye depths (z_{pad}) and load inclinations (α_{pad}).

Different modelling techniques are considered for the representation of the anchor, and two constitutive models, a Mohr-Coulomb model (MC) and a Hardening Soil model with small-strain stiffness (HSSmall), are compared. Force and displacement-controlled calculation methods are performed and compared.

Sensitivity analyses are conducted to examine the effects of friction angle (φ), unit weight (γ'), dilatancy angle (ψ) and interface strength reduction (R_{inter}). The effect of the parameters on the pull-out force was found to differ for the different load configurations investigated in the study. The stiffness parameter Young's modulus and Poisson's ratio had little effect on the results and are therefore not included in the sensitivity analyses presented. Table 1 provides a summary of all the analyses conducted.

2. FINITE ELEMENT MODEL

The finite element software used to model the suction caisson anchor is PLAXIS 3D Ultimate. 10-node tetrahedral elements with a second-order interpolation of displacements are used in the analyses. As a result, linear strain variation is modelled across elements.

Figure 3 illustrates the model used in the analyses. An anchor with a diameter (D) and skirt length (L) is modelled with a load with an inclination (α_{pad}) at padeye depth (z_{pad}).

Only half of the soil domain is modelled due to the symmetry of the problem, which significantly reduces the computational effort needed to do the calculations. The size of the model is given by the length ($\boldsymbol{X}$), width ($\boldsymbol{Y}$), and depth ($\boldsymbol{Z}$). The bottom of the soil domain is fully fixed, whereas all vertical boundaries are simply supported. The water level is set 1 meter above the soil as it is not important in effective stress analyses.

A conventional small deformation finite element analysis is used. However, some level of displacement is necessary to mobilise the earth pressure, i.e., the capacity of the anchor. DNVGL-RP-E303 [7] states that for suction caisson anchors installed in clay a displacement of 10%-30% of the diameter (D) should be expected for the anchor to mobilise its capacity. Ahmed and Hawlader [1] found that for most load configurations peak pull-out force was found at a displacement of around 10% of the caisson diameter (D). As a result, the pull-out force is defined in this study defined at a normalised total displacement ($\frac{u_{tot}}{D}$=0.1) of the node representing the padeye.

An initial investigation of the updated mesh option in PLAXIS 3D indicated only a small difference in displacements until the failure criteria of 0.1 times the caisson diameter (D) was reached. The updated mesh option is therefore not used as this affects the simulation rate.

2.1. Suction Caisson Anchor Properties

A suction caisson anchor with diameter ($D = 3\,\text{m}$), length ($L = 6\,\text{m}$) and wall thickness ($t = 0.1\,\text{m}$) is modelled. The geometry is based on prototype dimensions used in Bang et al. [3].

Suction caissons are rigid structures that usually experience small structural deformations. In geotechnical finite element analysis, these are therefore often modelled as rigid bodies. This idealisation ensures that the distance of any two points on the structure remains unchanged regardless of the displacements and loads applied to it. PLAXIS 3D does not include the anchor's self-weight when modelled as a rigid body. However, including the self-weight may affect the numerical results. Three different modelling techniques are therefore considered in the study.

1. Modelling the anchor as a Rigid body without self-weight (RB).
2. Modelling the anchor as a Rigid body with self-weight (RBSW).
3. Modelling the anchor with Plate elements (PE).

Rigid body with self-weight (RBSW) is modelled with an evenly distributed surface load on top of the rigid body, where an assumed unit weight ($\gamma_c = 78.5\,\text{kN/m}^3$) has been used for the anchor. Applying Plate elements (PE) PE allows for specifying the unit weight and wall thickness of the anchor. The self-weight is therefore computed and included automatically. However, the stiffness of the elements must also be specified. The typical elastic stiffness of steel is $210 \cdot 10^6$ kPa, which has been applied.

Regardless of the methods used to model the anchor, PLAXIS 3D uses non-continuum elements. As illustrated in figure 4, the true structure volume is therefore replaced by the soil. When non-continuum elements are used to model structures, the net structure weight has to be applied to obtain the correct soil stresses [8]. For the two cases considering the self-weight, the unit weight of the soil occupying the true structure volume has to be subtracted from the unit weight of the anchor. This results in some conservatism in the self-weight of the anchor; however, as stated, the soil stresses are modelled more accurately.

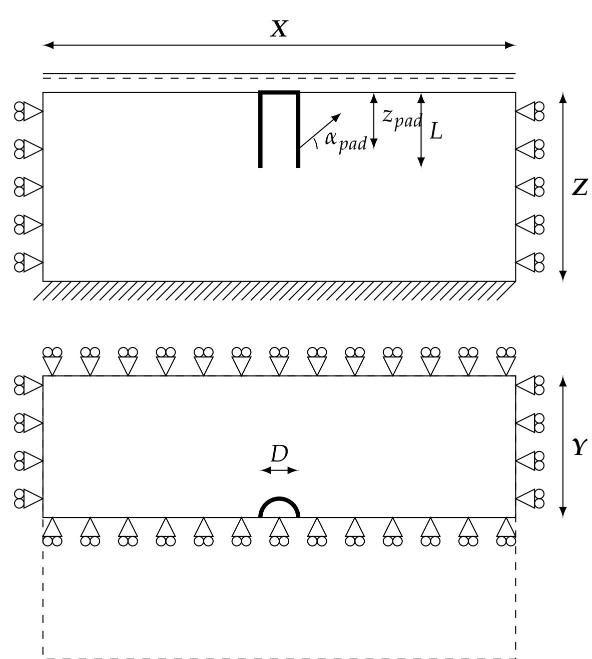

Figure. 3. Illustration of the finite element model.

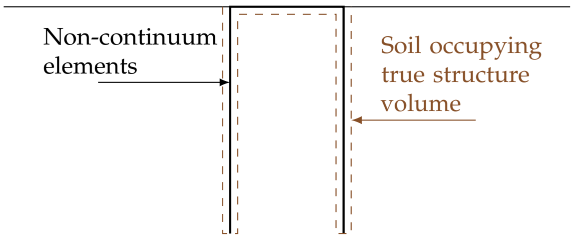

Figure. 4. Illustration of soil occupying true structure volume.

2.2. Soil and Interface Properties

An important aspect of finite element modelling of geotechnical problems is choosing appropriate constitutive models. A Mohr-Coulomb model is in many cases adequate for drained conditions when only failure is of interest. However, this linear elastic perfectly plastic material model does not account for the non-linear stress-strain behaviour of actual soils. Results are therefore evaluated using the Hardening Soil model with small-strain stiffness, which employs stress-dependent stiffness and isotropic hardening due to plastic strain.

Parameters for the constitutive soil models are determined using formulas presented by Brinkgreve et al. [4]. The mechanical properties are thus all related to the relative density of the soil (D_r). A relative density of ($D_r = 0.6$) is used since it corresponds to the relative density of the soil described in Bang et al. [3].

Only one stiffness parameter is used when using a Mohr-Coulomb model. In this study, a secant modulus at 50% strength (E_{50}) is chosen as the basic stiffness modulus (E_{ref}) in the model. A Poisson's ratio ($\nu = 0.3$) is used in the Mohr-Coulomb model.

For analyses using the HSSmall, the dilatancy cut-off option is used to limit dilation when the soil has reached a state of critical density. For these cases, a minimum void ratio ($e_{min} = 0.35$) and maximum void ratio ($e_{max} = 0.8$) are assumed.

For drained analyses, sand is assumed to be cohesionless, i.e., ($c = 0$). However, in numerical calculations, this generally does not perform well. At the ground surface, where the effective stresses are zero, the soil will fail instantaneously, creating numerical instabilities. In this study, a small surface load ($\sigma_z = 1\,\text{kPa}$) is added to the ground surface, increasing the effective stresses. This does not correspond to any physical phenomena but is a solution to a numerical obstacle and is assumed to have a minimal effect on the capacity.

Interfaces are added between the anchor and soil, as illustrated in figure 8. The interface strength is modelled using the properties of the adjacent soil, where the strength parameters are reduced by a factor (R_{inter}) defined by Eq. (1). An interface friction angle (δ=30°) is used in this study based on a database of ring shear stress presented by Liu et al. [9].

$$R_{inter} = \frac{\tan\delta}{\tan\varphi} \tag{1}$$

The vertical interfaces are extended a distance of ($0.2D$) in the z-direction. Additionally, a horizontal interface with a ($1.4D$) diameter is added at the bottom of the anchor. No strength reduction is applied to these interfaces; they are only added to improve the mesh flexibility at the corner points and help avoid high-stress concentrations.

2.3. Domain Size

In reality, the subsoil is effectively unlimited; however, boundaries are needed to solve the finite element models. These boundaries and their boundary conditions need to be chosen so as not to introduce significant boundary effects to the results. Model boundaries can generally be placed closer to the areas of interest for bearing capacity calculations compared to deformation calculations [5].

Ahmed and Hawlader [1], Zhao et al. [10] and Cheng et al. [6] used half-circular soil domains with diameters of ($14D$), ($9D$), and ($12D$), and depth of ($3.33L$), ($4L$), and ($3L$), respectively.

To assess the boundary effects in this study, the pull-out force with a padeye depth at ($z_{pad} = 0.75L$) for load inclination ($\alpha_{pad} = 0°$) and ($\alpha_{pad} = 90°$) is calculated for five different domain sizes. Figure 5 presents the pull-out forces as a function of the normalised total displacement ($\frac{u_{tot}}{D}$) for different domain sizes ($\boldsymbol{X}$, $\boldsymbol{Y}$, $\boldsymbol{Z}$). For load inclination ($\alpha_{pad} = 90°$) the force-displacement curves are similar. For load inclination ($\alpha_{pad} = 0°$) a slightly more noticeable difference is seen.

Figure 6 presents the pull-out force at normalised total displacement ($\frac{u_{tot}}{D} = 0.1$). For load inclination ($\alpha_{pad} = 90°$) a 3.5% difference is found between the minimum and maximum pull-out forces, whereas for load inclination ($\alpha_{pad} = 0°$) the difference is 5.4%.

As the domain size increases, no definitive trend is seen in the results. The fluctuations in pull-out capacity could most likely be indirect effects of changes in domain size, e.g., a change in the mesh configuration. For the investigated domain sizes, none appears to have a direct effect on the failure mechanisms of the two load configurations considered. A small domain size is preferred in terms of computational demands; however, due to the meshing used in this study, the calculation time did not increase dramatically when increasing the domain size. As a result, a domain size of ($\boldsymbol{X} = 12D$, $\boldsymbol{Y} = 6D$, $\boldsymbol{Z} = 4L$) is used in this study.

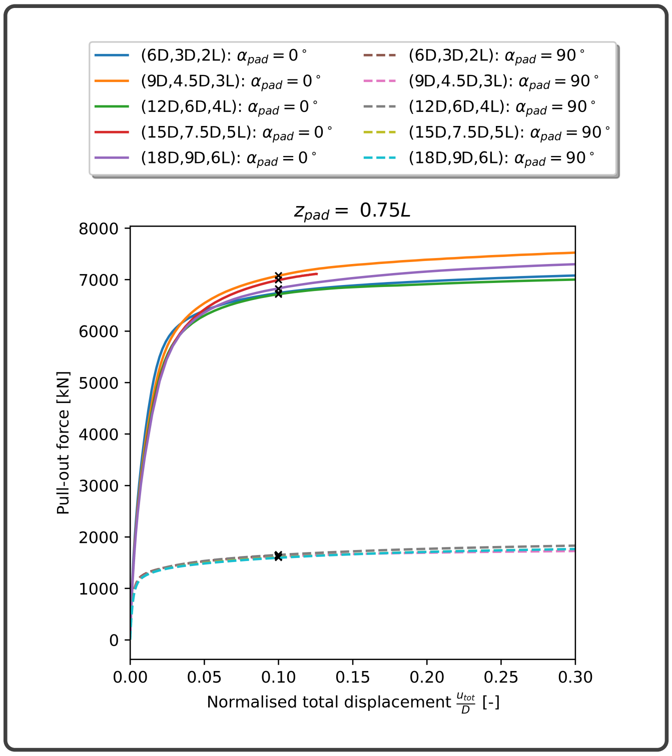

Figure. 5. Pull-out force as a function of normalised total displacement ($\frac{u_{tot}}{D}$) for load inclination (α_{pad}=0°) and (α_{pad}=90°) using different domain sizes (X, Y, Z).

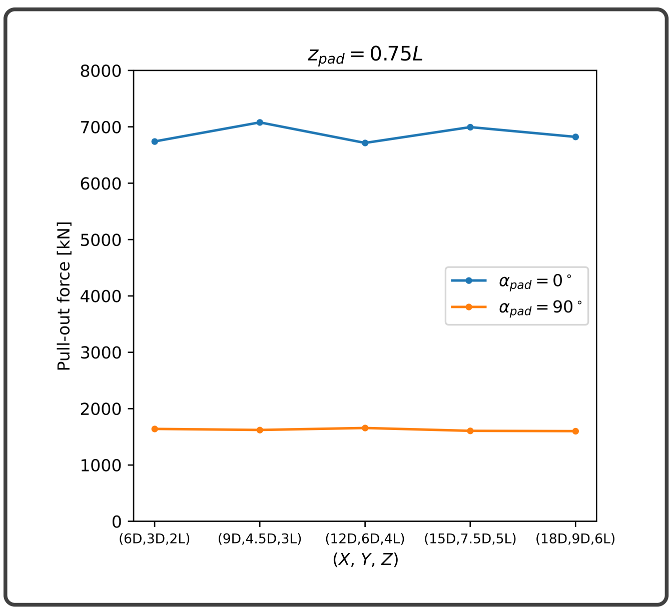

Figure. 6. Pull-out force as a function of domain size (X, Y, Z) for load inclination (α_{pad}=0°) and (α_{pad}=90°).

2.4. Meshing

Finite element results depend on both the type and size of elements used in the calculations. The accuracy of finite element solutions tends to improve with global and local mesh refinement. The mesh is therefore refined with a factor ($CF = 0.25$) in a semicircle with a diameter ($1.5D$) and height ($2L$). In addition, the surface representing the anchor is refined by a coarseness factor ($CF = 0.1$). The meshing procedure is automated in PLAXIS 3D. The procedure requires a global meshing parameter (l_e), which represents the target element dimension. As a coarse mesh will generally predict higher capacity compared to a finer mesh, obtaining a reasonable mesh convergence is needed to acquire reliable results Brinkgreve et al. [4]. To assess this issue, a mesh sensitivity analysis has been conducted with respect to a normalised target element size ($\frac{DL}{l_e}$). Numerical instabilities were encountered for higher values of ($\frac{DL}{l_e}$) with small load inclinations. This was observed as the model terminated the calculation processes progressively earlier hence the failure criteria of ($\frac{u_{tot}}{D} = 0.1$) could not be reached. Figure 7 presents the pull-out force as a function of the normalised total displacement ($\frac{u_{tot}}{D}$) for load inclination ($\alpha_{pad} = 0°$) at a padeye position ($z_{pad} = 0.75L$) for different normalised target element sizes ($\frac{DL}{l_e}$). The range of the centrifuge results by Bang et al. [3] is illustrated in the figure as well for comparison. For load inclination ($\alpha_{pad} = 0°$) results appear to converge at a normalised target element size ($\frac{DL}{l_e} = 3.0$) and the results are within the range of capacities determined by Bang et al. [3]. A normalised target element size ($\frac{DL}{l_e} = 3.0$) is therefore used in this study, as it is assessed to be an acceptable balance between accuracy and calculation performance. A mesh is illustrated in figure 8 where normalised target element size ($\frac{DL}{l_e} = 3$) is applied.

2.5. Phases in the Calculation

The calculation process involves four phases:

1. An initial phase
2. An installation phase
3. A plastic nil-phase
4. A loading phase

In the first phase, soil stresses are initiated in the soil domain. As the numerical model results are compared to the centrifuge tests conducted by Bang et al. [3] the initial soil stresses should resemble these soil conditions. Prior to the installation of the model anchor, the sand was sprayed into a water-filled model container, and the centrifuge was initially operated to stabilize the sand. Consequently, the "K_0-procedure" is chosen as the best to initiate similar soil stresses within the numerical model. The model anchor used in the centrifuge tests was installed by pushing it into the sand at 1g. However, in the numerical model, the anchor is modelled as *wished in place*, as the components of the corresponding suction anchor model are activated after the initiation of soil stresses.

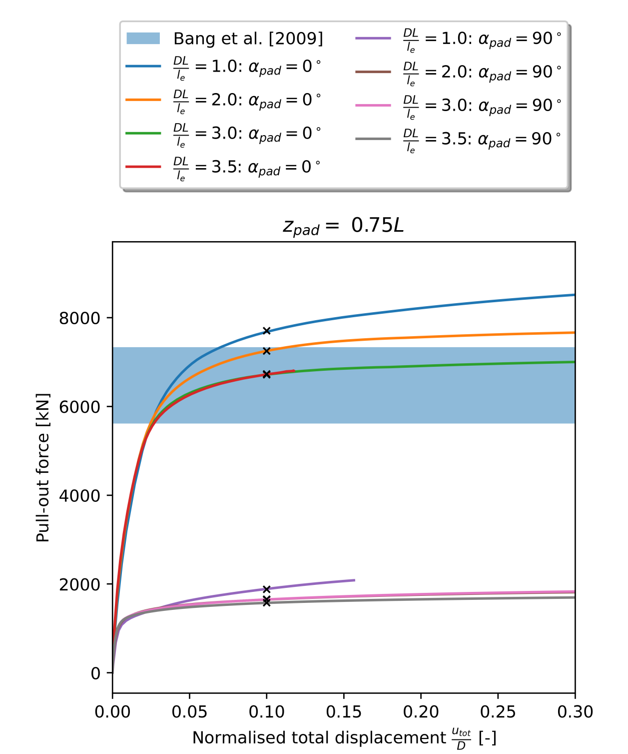

Figure. 7. Pull-out force as a function of the normalised total displacement ($\frac{u_{tot}}{D}$) for various meshes using different normalised target element sizes ($\frac{DL}{l_e}$) plotted along centrifuge results by Bang et al. [3].

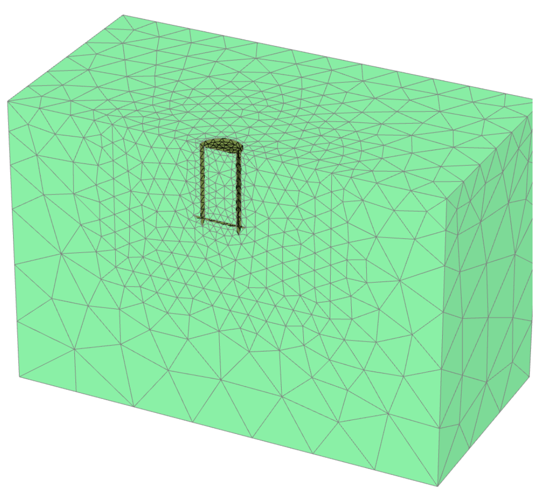

Figure. 8. Illustration of a mesh with an normalised target element size ($\frac{DL}{l_e} = 3$) and local mesh refinement.

A plastic nil-phase is added after the installation phase. The additional step ensures the stress field is in equilibrium and that all stresses obey the failure condition.

In the final calculation phase, the loading is applied. The loading of the anchor can be modelled as applying a prescribed force or a prescribed displacement. In reality, as the anchor translates and rotates to mobilise the bearing capacities, the load inclination (α_{pad}) will change. For this study, loading is applied by a prescribed force, which is assumed to represent the most realistic displacements since the anchor is able to translate both horizontally and vertically freely. However, an analysis is performed to investigate the difference between the two approaches.

All the investigations conducted for this study are documented in table 1. Every combination of parameters for each analysis listed in the table has been simulated using PLAXIS 3D. Analysis of domain size and mesh has been assessed previously. The remaining analyses are presented in section 3.

Table 1. Summary of finite element analyses conducted in the study.

Analysis	Domain size	$\frac{DL}{l_e}$	Anchor model	Material model	φ	γ'	ψ	R_{inter}	K_0	z_{pad}	α_{pad}
Effect of domain size	$(6D, 3D, 2L)$, $(9D, 4.5D, 3L)$, $(12D, 6D, 4L)$, $(15D, 7.5D\ 5L)$, $(18D, 9D, 6L)$	3	RBSW	MC	35.5°	$10\,kN/m^3$	5.5°	0.81	0.42	$0.75L$	0°, 90°
Effect of meshing	$(12D, 6D, 4L)$	1, 2, 3, 3.5	RBSW	MC	35.5°	$10\,kN/m^3$	5.5°	0.81	0.42	$0.75L$	0°, 90°
Effect of suction caisson model	$(12D, 6D, 4L)$	3	RB, RBSW, PE	MC	35.5°	$10\,kN/m^3$	5.5°	0.81	0.42	$0.05L$, $0.25L$, $0.5L$, $0.75L$, $0.95L$	0°, 22.5°, 45°, 67.5°, 90°
Effect of material model	$(12D, 6D, 4L)$	3	RBSW	MC, HSSmall	35.5°	$10\,kN/m^3$	5.5°	0.81	0.42	$0.05L$, $0.25L$, $0.5L$, $0.75L$, $0.95L$	0°, 22.5°, 45°, 67.5°, 90°
Effect of loading type	$(12D, 6D, 4L)$	3	RBSW	MC	35.5°	$10\,kN/m^3$	5.5°	0.81	0.42	$0.05L$, $0.25L$, $0.5L$, $0.75L$, $0.95L$	0°, 22.5°, 45°, 67.5°, 90°
Comparison with centrifuge tests	$(12D, 6D, 4L)$	3	RBSW	MC	35.5°	$10\,kN/m^3$	5.5°	0.81	0.42	$0.05L$, $0.25L$, $0.5L$, $0.75L$, $0.95L$	0°, 22.5°, 45°, 67.5°, 90°
Effect of R_{inter}	$(12D, 6D, 4L)$	3	RBSW	MC	35.5°	$10\,kN/m^3$	5.5°	0.5, 0.81, 1.0	0.42	$0.05L$, $0.25L$, $0.5L$, $0.75L$, $0.95L$	0°, 22.5°, 45°, 67.5°, 90°
Effect of ψ	$(12D, 6D, 4L)$	3	RBSW	MC	35.5°	$10\,kN/m^3$	0°, 5.5°, 35.5°	0.81	0.42	$0.05L$, $0.25L$, $0.5L$, $0.75L$, $0.95L$	0°, 22.5°, 45°, 67.5°, 90°
Effect of φ	$(12D, 6D, 4L)$	3	RBSW	MC	33.7°, 35.5°, 37.3°	$10\,kN/m^3$	5.5°	0.81	0.42	$0.05L$, $0.25L$, $0.5L$, $0.75L$, $0.95L$	0°, 22.5°, 45°, 67.5°, 90°
Effect of γ'	$(12D, 6D, 4L)$	3	RBSW	MC	35.5°	$9\,kN/m^3$, $10\,kN/m^3$, $11\,kN/m^3$	5.5°	0.81	0.42	$0.05L$, $0.25L$, $0.5L$, $0.75L$, $0.95L$	0°, 22.5°, 45°, 67.5°, 90°
Effect of K_0	$(12D, 6D, 4L)$	3	RBSW	MC	35.5°	$10\,kN/m^3$	5.5°	0.81	0.42, 1.0	$0.05L$, $0.25L$, $0.5L$, $0.75L$, $0.95L$	0°, 22.5°, 45°, 67.5°, 90°

3. RESULTS

The result section presents the results of the numerical analyses addressing the finite element modelling of suction caisson anchors.

3.1. Comparison with Centrifuge Tests

Figure 9 presents a comparison between the pull-out force for various load inclinations (α_{pad}) and normalised padeye positions ($\frac{z_{pad}}{L}$) obtained from the PLAXIS 3D models and the centrifuge tests conducted by Bang et al. [3]. The difference between the results obtained from the finite element analysis and the centrifuge tests tends to increase as the load inclination (α_{pad}) increases. The largest discrepancy is observed with a load inclination of ($\alpha_{pad} = 90°$), where the finite element results predict twice the load capacity compared to the model tests; overall, the finite element analysis method generally yields higher load capacities than the centrifuge tests, when the load has a vertical component.

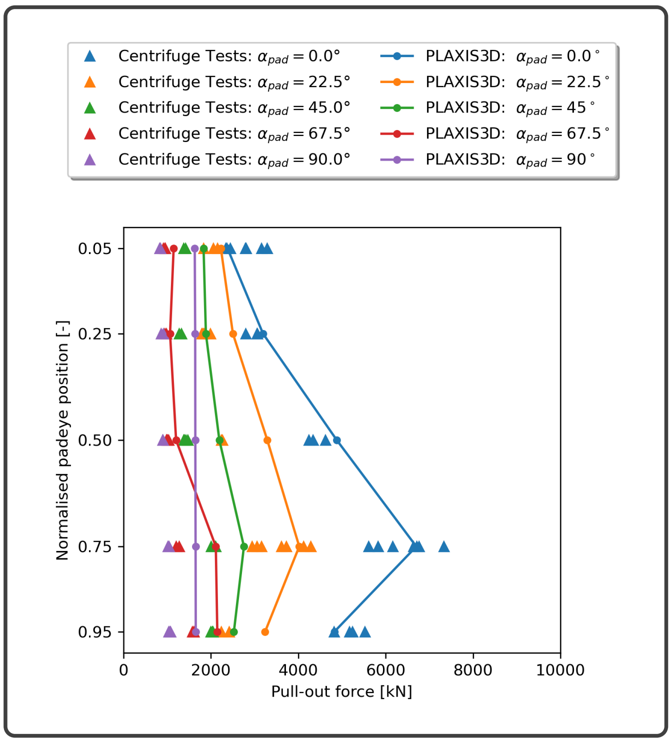

Figure. 9. Finite element results compared with centrifuge tests conducted by Bang et al. [3] for various load inclinations (α_{pad}) and padeye depths (z_{pad}).

3.2. Failure Mechanisms

The figures 10a - 10h illustrate various failure mechanisms of the suction anchor dependent on different padeye positions and load inclinations. When the padeye is positioned near the top of the anchor, and the load inclination is horizontal, the anchor will be dragged in the direction of the force with a slight clockwise rotation. The soil will move upward on the passive side and downward on the active side. As the loading angle increases, the failure mechanism changes. The displacement of the anchor becomes more vertical and essentially it will start rotating counterclockwise, hence the passive and active sides are reversed and the largest soil body is then mobilised on the opposite side of the anchor. A large counterclockwise rotation is observed when the padeye is located near the bottom of the anchor and the load inclination is horizontal. The failure zones of the soil are displaced with the anchor in the same rotating manner. When the loading angle increases, the anchor will rotate slightly less and the soil will start failing in an upward direction. Eventually, when the load angle is 90 degrees the failure mechanism is very similar to the failure mechanism when the padeye is located near the top of the anchor with the same load inclination. This similarity is likewise observed when examining the bearing capacity in figure 9. There is no visible change with padeye depth for a loading angle of 90 degrees. This is observed for both the numerical results and the centrifuge test results.

3.3. Effect of Suction Caisson Model

Figure 11 presents the pull-out force at different normalised padeye positions ($\frac{z_{pad}}{L}$) and different load inclinations (α_{pad}) for the three different anchor models.

Modelling the anchor as a Plate elements (PE) or a Rigid body with self-weight (RBSW) predicts similar pull-out forces for all the different load configurations. However, using a Rigid body with self-weight generally estimates slightly lower capacities compared to the Plate elements.

Modelling the anchor as a Rigid body without self-weight (RB) predicts lower pull-out forces for all load configurations. The percentage difference between the RB and RBSW varies across the padeye depths (z_{pad}) and load inclinations (α_{pad}). The percentage difference tends to be higher at larger load inclinations, however, the largest differences are at load inclinations ($\alpha_{pad} = 45°$) and ($\alpha_{pad} = 67.5°$). For load inclination ($\alpha_{pad} = 90°$) the difference is relatively consistent for all padeye depths at around 34%. The largest difference of 78% is at a padeye depth ($z_{pad} = 0.75L$) with a load inclination ($\alpha_{pad} = 67.5°$).

Figure 12 presents a normalised displacement field for various load inclinations (α_{pad}) at a padeye depth ($z_{pad} = 0.5L$). When modelling the anchor as a Rigid body without self-weight the displacement field is more dominated by vertical displacement than horizontal compared to the other methods.

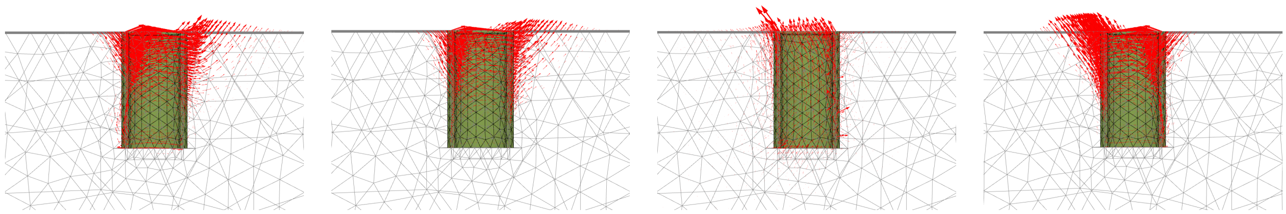

(a) $\alpha_{pad} = 0°, z_{pad} = 0.05L$. **(b)** $\alpha_{pad} = 45°, z_{pad} = 0.05L$. **(c)** $\alpha_{pad} = 67.5°, z_{pad} = 0.05L$. **(d)** $\alpha_{pad} = 90°, z_{pad} = 0.05L$.

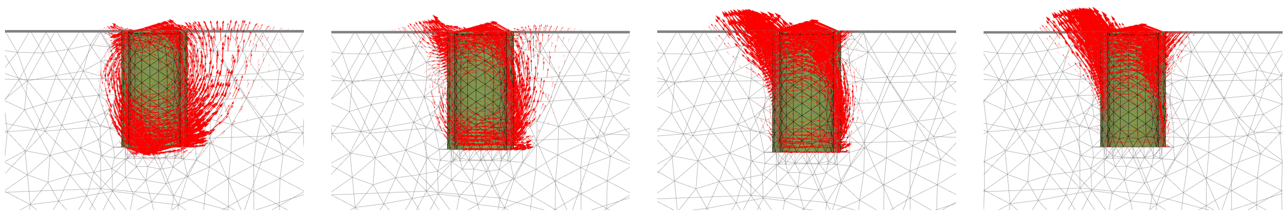

(e) $\alpha_{pad} = 0°, z_{pad} = 0.95L$. **(f)** $\alpha_{pad} = 45°, z_{pad} = 0.95L$. **(g)** $\alpha_{pad} = 67.5°, z_{pad} = 0.95L$. **(h)** $\alpha_{pad} = 90°, z_{pad} = 0.95L$.

Figure. 10. Incremental displacement (Δu_{tot}) at normalised displacement ($\frac{u_{tot}}{D} = 0.1$) for different load configuration.

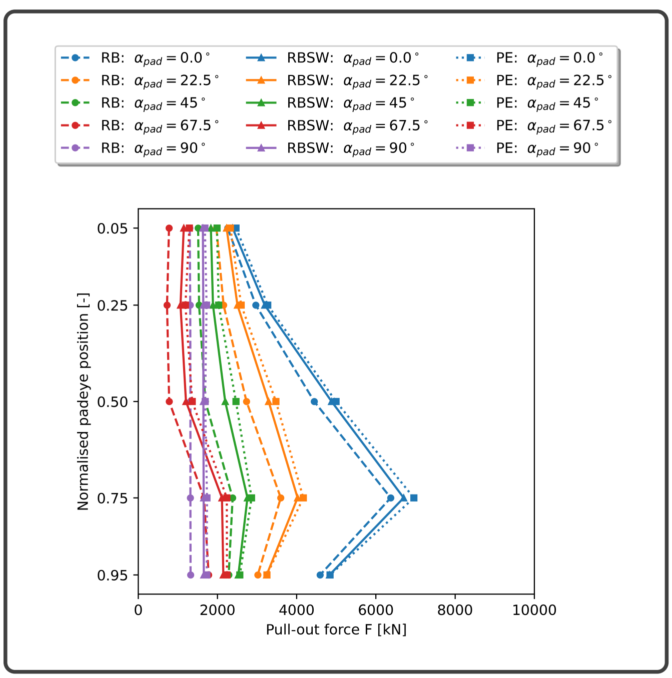

Figure. 11. Pull-out force at various normalised padeye positions ($\frac{z_{pad}}{L}$) for various load inclinations (α_{pad}) using three different anchor models (RB, RBSW, PE).

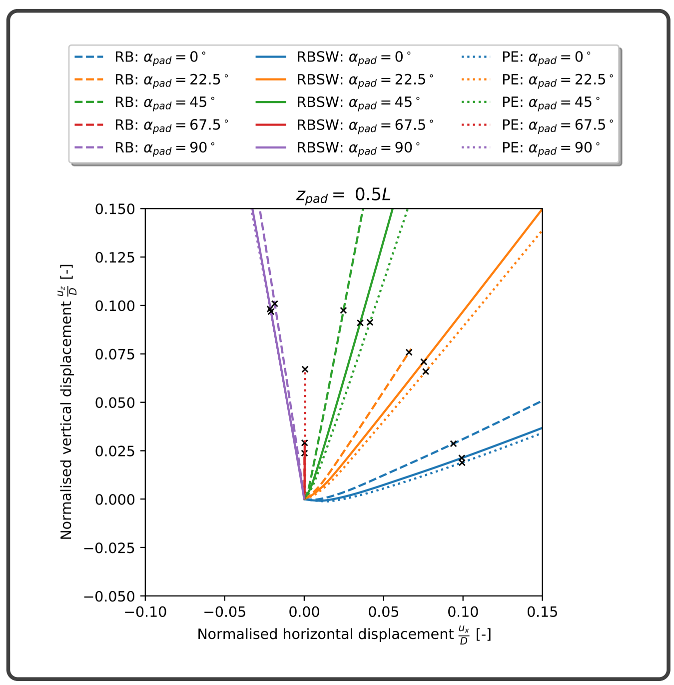

Figure. 12. Displacement field for various load inclinations (α_{pad}) and padeye depth ($z_{pad} = 0.5L$) for the three different anchor models (RB, RBSW, PE).

3.4. Effect of Loading Type

Figure 13 presents the pull-out forces at different normalised padeye positions ($\frac{z_{pad}}{L}$) where loading is either force or displacement controlled. The two methods compared show a significant difference in the results. For load inclination ($\alpha_{pad} = 0°$) and padeye depth ($z_{pad} = 0.95L$), the displacement-controlled method gives twice the capacity compared to the force-controlled method. However, for load inclination ($\alpha_{pad} = 90°$), the displacement-controlled method gives lower capacities, with a maximum difference in the pull-out force of 70% lower than the force-controlled method at padeye depth ($z_{pad} = 0.05L$). For intermediate load inclinations, the difference tends to be less extreme, but is still significant, with the largest difference occurring at padeye depths ($z_{pad} = 0.5L$) and ($z_{pad} = 0.75L$). Figure 14 presents the displacement field for various load inclinations (α_{pad}) and padeye depth ($z_{pad} = 0.95L$). When loading is force controlled substantial vertical displacement is obtained even for load inclination ($\alpha_{pad} = 0°$).

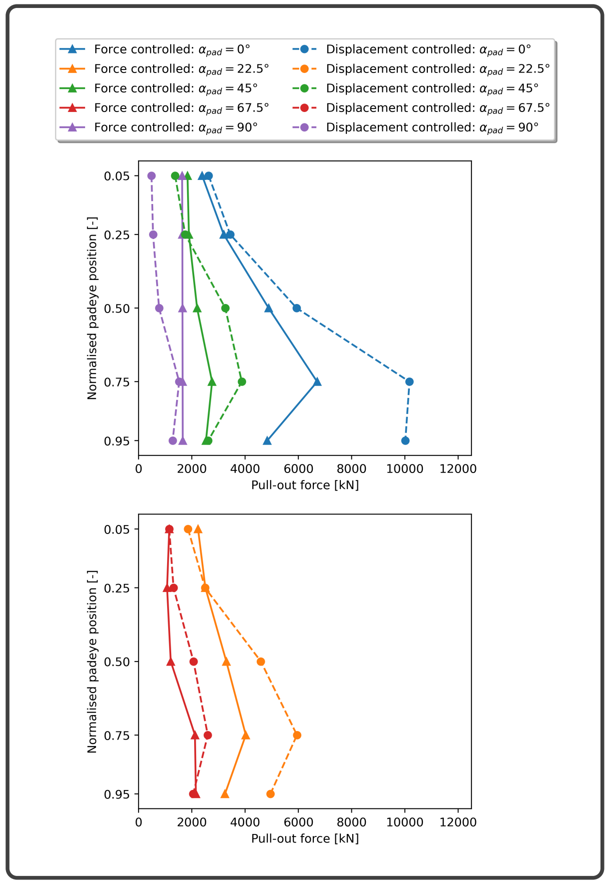

Figure. 13. Pull-out force at various normalised padeye positions ($\frac{z_{pad}}{L}$) for various load inclinations (α_{pad}) using both force and displacement controlled loading.

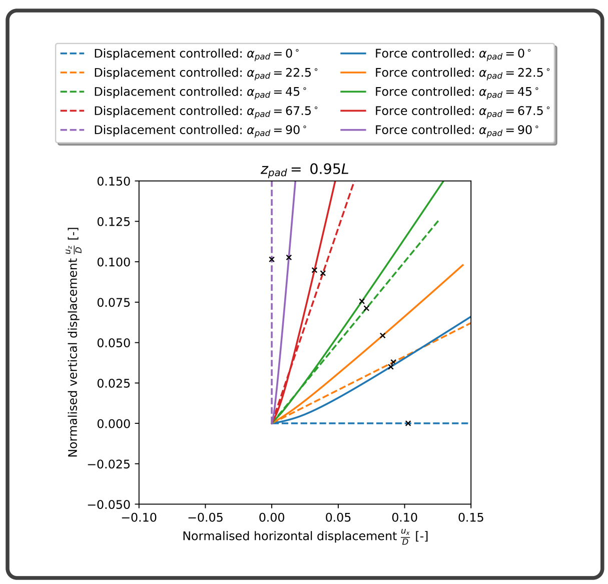

Figure. 14. Displacement field for various load inclinations (α_{pad}) and padeye depth ($z_{pad} = 0.95L$) using both force and displacement controlled loading.

3.5. Effect of Material Model

Figure 15 presents the pull-out forces at different normalised padeye positions ($\frac{z_{pad}}{L}$) using both a Mohr-Coulomb model (MC) or Hardening Soil model with small-strain stiffness (HSSmall) material model. The results are very similar using the two material models. The largest difference in the capacities is seen at load inclination ($\alpha_{pad} = 0°$).

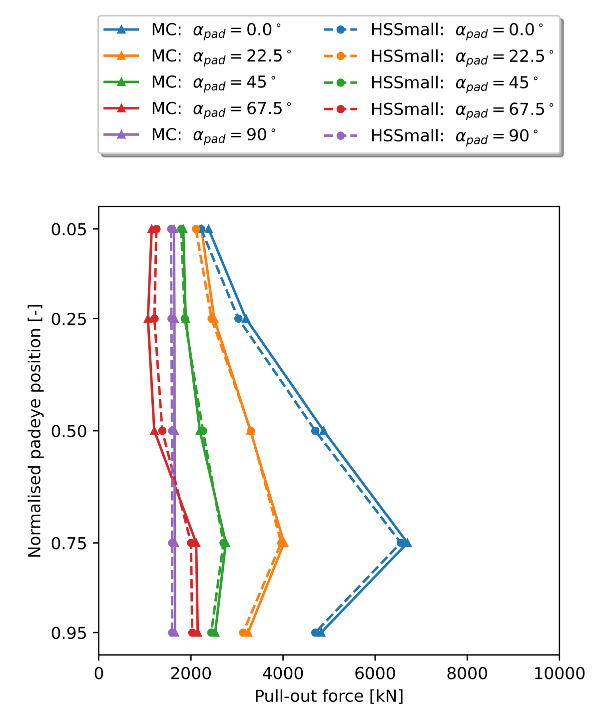

Figure. 15. Pull-out force at various normalised padeye positions ($\frac{z_{pad}}{L}$) for various load inclinations (α_{pad}) using both a Mohr-Coulomb model (MC) and Hardening Soil model with small-strain stiffness (HSSmall) material model.

3.6. Effect of Interface Strength Reduction

Figure 16 presents the pull-out force at various normalised padeye positions ($\frac{z_{pad}}{L}$) and load inclinations (α_{pad}) using an interface strength reduction factor ($R_{inter} = 0.5, 0.81$, or 1.0). The solid line plots the results using ($R_{inter} = 0.81$) corresponding to an interface friction angle of ($\delta = 30°$). The shaded area corresponds to the range in pull-out force obtained using this analysis's upper and lower limits.

As load inclination (α_{pad}) increases, the significance of the interface strength reduction factor (R_{inter}) also increases, resulting in a greater impact on the pull-out force. Significant effect of the interface strength reduction factor (R_{inter}) on the pull-out force for load inclinations ($\alpha_{pad} = 45°, 67.5°$ and $90°$). These results emphasize the need for careful consideration of the interface strength reduction factor (α_{pad}) in the design of anchors when exposed to inclined loads.

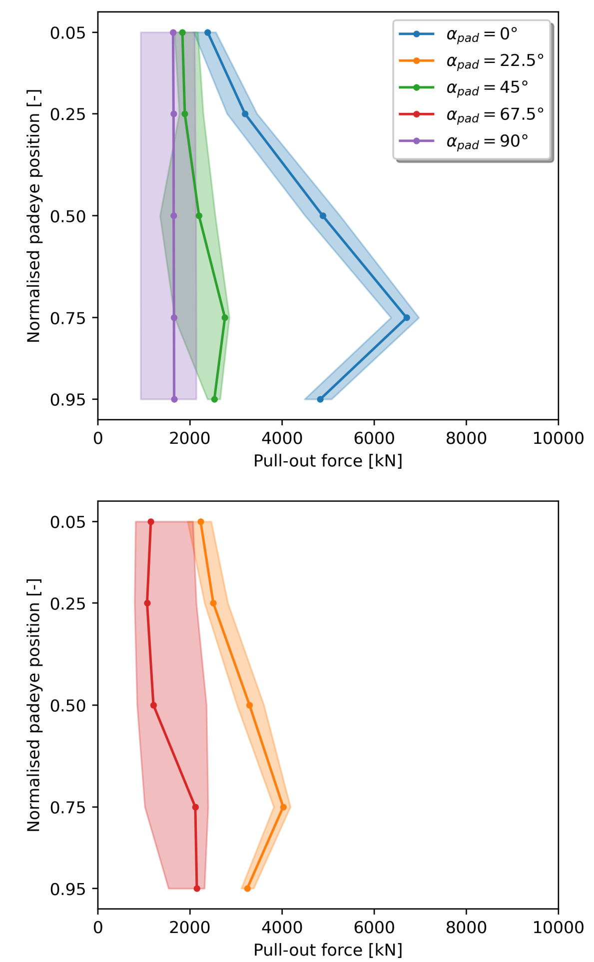

Figure. 16. Pull-out force at various normalised padeye positions ($\frac{z_{pad}}{L}$) for various load inclinations (α_{pad}) using a interface strength reduction factor ($R_{inter} = 0.5, 0.81$, or 1.0)

.

3.7. Effect of Dilatancy Angle

The results presented in figure 17 are the pull-out force at varying padeye depths (z_{pad}) and load inclinations (α_{pad}) using different dilatancy angles (ψ). The use of an associated flow rule significantly increases the pull-out force. Notably, at padeye depths (z_{pad}) ranging from $0.05L$ to $0.5L$ and for a load inclination of ($\alpha_{pad} = 67.5°$), the dilatancy angle (ψ) does not affect the results. However, in general, using a non-associated or associated flow rule predicts a relatively large range in the pull-out force.

3.8. Effect of Friction Angle

Figure 18 plots the results for different padeye depths (z_{pad}) and load inclinations (α_{pad}) using a friction angle of ($\varphi = 35.5°$),

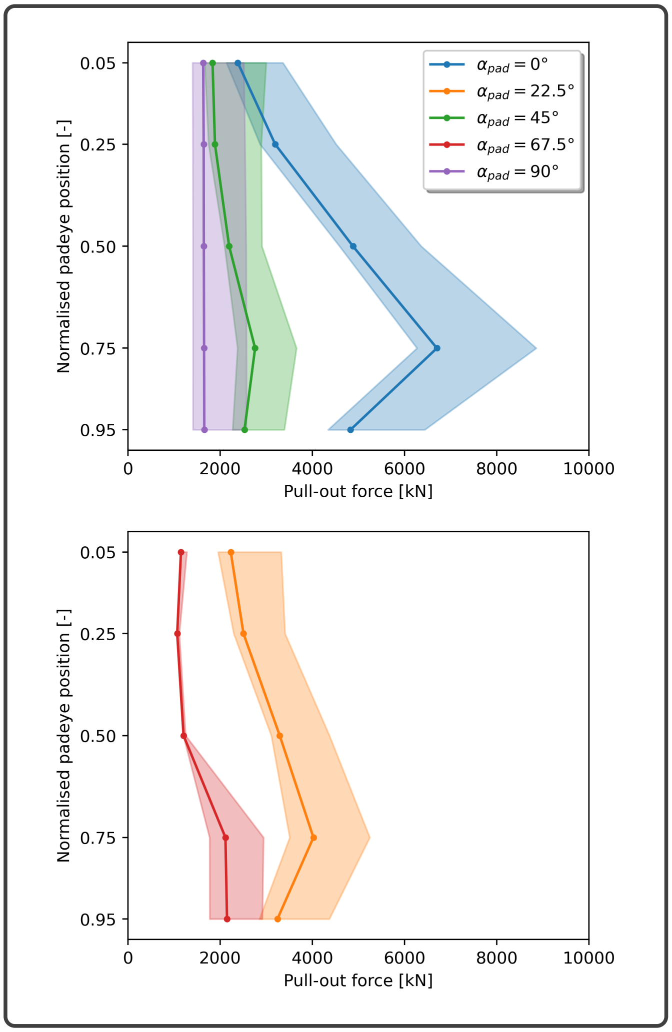

Figure. 17. Pull-out force at various normalised padeye positions ($\frac{z_{pad}}{L}$) for various load inclinations (α_{pad}) using a dilatation angle ($\psi = 0$, $\varphi - 30°$, or φ).

with the shaded area indicating the effect of varying the friction angle by 5%. The results suggest that the sensitivity of friction angle (φ) is more pronounced at lower load inclinations. For load inclinations greater than 45 degrees, the pull-out force is relatively insensitive to small changes in friction angle.

3.9. Effect of Unit Weight

The effect of unit weight (γ') on the pull-out force at various padeye depths (z_{pad}) and load inclination (α_{pad}) are presented in figure 19. The solid line represents the results obtained using a ($\gamma' = 10\,\text{kN/m}^3$), while the shaded area shows the effect of varying the unit weight by 5%. It was found that the effect of unit weight becomes more pronounced as the load inclination decreases.

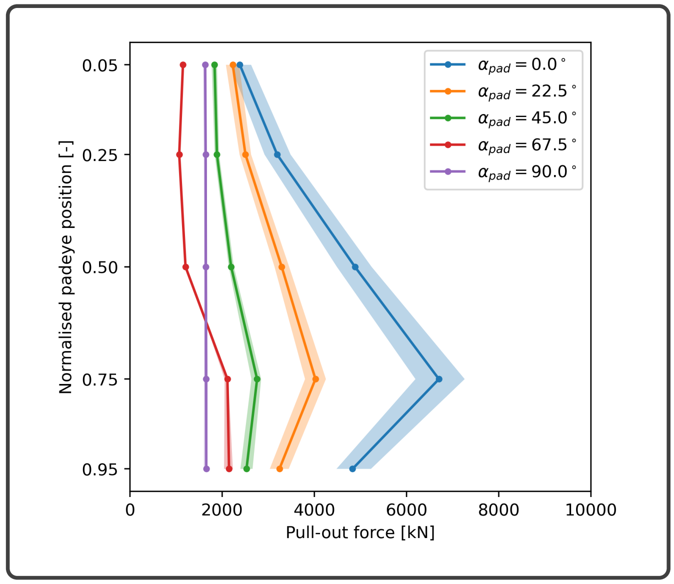

Figure. 18. Friction angle (φ) sensitivity on the pull-out force at various normalised padeye positions ($\frac{z_{pad}}{L}$) for various load inclinations (α_{pad}).

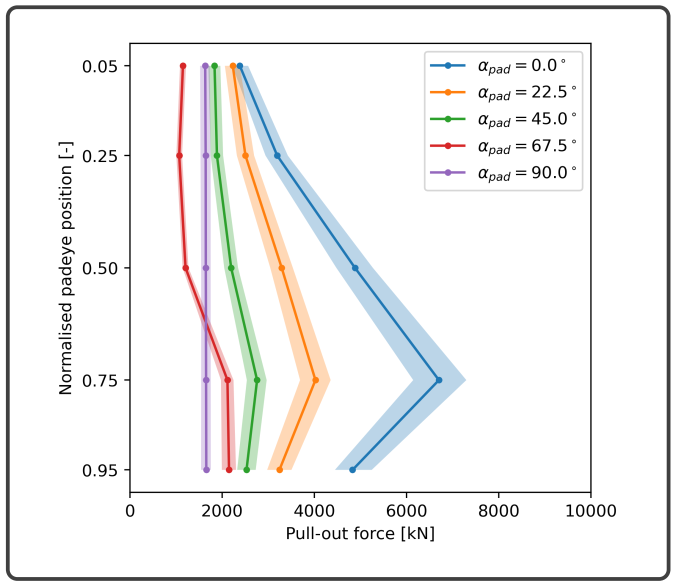

Figure. 19. Unit weight (γ') sensitivity on the pull-out force at various normalised padeye positions ($\frac{z_{pad}}{L}$) for various load inclinations (α_{pad}).

3.10. Effect of in-situ Earth Pressure Coefficient

Figure 20 shows the pull-out force at different padeye depths (z_{pad}) and load inclinations (α_{pad}) for two values of (K_0): $1 - \sin(\varphi)$ and 1.

The results indicate that the variation of (K_0) has a limited effect on the pull-out force. Except for load inclination of ($\alpha_{pad} = 67.5°$) and padeye depth (z_{pad}) ranging from $0.05L$ to $0.5L$, the value of (K_0) affect the pull-out force.

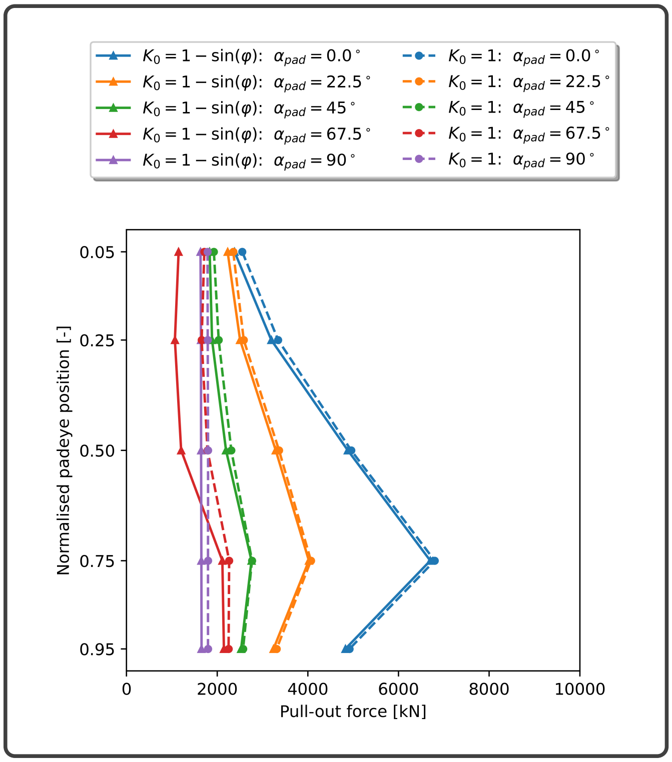

Figure. 20. Effect of (K_0) on the pull-out force at various normalised padeye positions ($\frac{z_{pad}}{L}$) for various load inclinations (α_{pad}).

4. DISCUSSION

The results of this study include implications for design processes and the reliability of numerical models as they are deeply affected by the choice of parameters and modelling methods. The sensitivity study conducted in this paper focused on examining the practical implications of various parameters on the pull-out force of suction bucket anchors subjected to inclined loading in homogeneous sand conditions.

One of the key findings was the influence of padeye locations and load angles on the pull-out force. It was observed that the displacement field and bearing capacity could vary significantly depending on these factors. In general, the effect of the parameters examined depend on the failure mechanism of the anchor. Parameters affecting the friction along the skirt of the caisson such as the interface reduction factor (R_{inter}) have a significant impact when the anchor experiences more vertical translation. The opposite trend was noticed for factors whose influence is dependent on the mobilised soil volume. This includes the friction angle (φ) where a small loading angle indicated a larger effect. However, the various results also show that a parameter may have a considerable influence on one combination of padeye location and load inclination, while the effect is negligible for the same load inclination but with another position for the padeye.

The inclusion of the anchor's self-weight in the numerical model was found to be crucial, as neglecting it resulted in lower bearing capacities and altered displacement fields. An approach employed by Ahn et al. [2] was to conduct the numerical analysis without consideration of the self-weight and then simply add the weight of the anchor to the vertical bearing capacity afterwards. This study suggests that the method by Ahn et al. [2] provides an incorrect result as the effect of adding the self-weight was found to be not only depending on the loading angle but also on the padeye position.

The choice of constitutive model HSSmall and MC, had a negligible impact on the pull-out force as the MC failure criteria are used in both models. The HSSmall model would provide more accurate results for soil deformation problems whereas the MC model was deemed adequate for this study as the ultimate capacity was the focal point. Additionally, the MC model is simpler and computationally more efficient.

One approach in numerical modelling is to use displacement-controlled loading, as this is more stable and efficient than force-controlled loading. As illustrated in figure 21, a displacement-controlled numerical model initially creates a displacement and then finds a stress state, which can induce the displacement. In contrast, a force-controlled model applies a load and then seeks a corresponding displacement. However, when the soil reaches the failure criteria, the stress curve will flatten out, and a further increase in the load will therefore not have a corresponding displacement. As a result, a displacement-controlled loading type provides a more stable calculation. In PLAXIS 3D, this issue of force-controlled calculations is solved by using an arc-length control algorithm, where the final load step size is reduced until convergence. The study found that the loading type has a significant effect on the pull-out force and the displacement field. Force-controlled loading allows the anchor to move freely as the displacement field is not defined by a prescribed displacement. In general, displacement-controlled loading yielded larger bearing capacities as the anchor mobilised larger soil volumes. An exception where the effect is opposite is when the loading angle is 90°. From the displacement field in figure 14, it is seen that in this case, the anchor moves entirely vertically using displacement-controlled loading. Thus suggesting that a smaller soil volume is mobilised, and the bearing capacity would originate mostly from the friction along the caisson skirt.

Comparisons between the numerical model and centrifuge tests revealed some agreement in terms of general trends. However, the numerical model predicted higher pull-out forces than the centrifuge tests as the load inclination increased. This deviation may originate from the difficulties of acquiring true friction in scaled experiments, as scaling effects are expected. This sug-

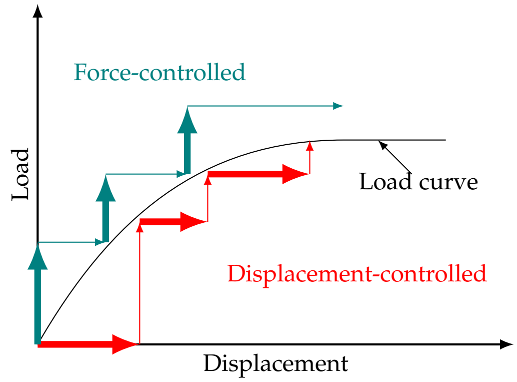

Figure. 21. Illustration of force-controlled and displacement-controlled loading

gests that an error is introduced in the centrifuge tests where a lower frictional force has been present. Furthermore, an interface reduction factor $R_{inter} = 0.81$ has been applied in this study to ensure an interface friction angle of 30° based on the work done by Liu et al. [9], which may be a value in the high end. Therefore, a deviation between the experiment and the numerical model increases as the pull-out force's dependency on the friction along the skirt increases.

5. CONCLUSION

This study assessed different modelling techniques in PLAXIS 3D for predicting the pull-out force of a suction caisson anchor in cohesionless soils. The effects have been studied for various padeye locations and load inclinations.

The investigations found that a simple Mohr-Coulomb model (MC) model is adequate to predict the pull-out force.

The self-weight of the anchor should be taken into account during the calculations, as this affects the displacement field and thereby the failure mechanisms. However, the study found that modelling the anchor as a rigid body is sufficient when only the bearing capacity is of interest.

For the most accurate representation of the failure mechanisms, it is recommended to simulate force-controlled loading conditions. Displacement-controlled loading generally predicts higher capacities resulting in excessively large pull-out forces in most scenarios, making it less safe.

Soil parameters such as the interface reduction factor (R_{inter}) and the dilation angle (ψ) impact the results significantly and should be selected carefully with consideration to loading conditions as it affects their influence significantly.

The study found that the pull-out force is more sensitive to variation in friction angle (φ), unit weight (γ'), and dilation angle (ψ) as the loading angle decreases. Whereas, for the interface reduction factor (R_{inter}) the sensitivity increase as the loading angle increase.

ACKNOWLEDGEMENTS

The authors are grateful for the guidance and constructive feedback from senior specialist Søren Dam Nielsen and leading specialist Søren Peder Hyldal Sørensen both from COWI.

The authors are grateful for not only the office space provided by COWI Aalborg but also that we could be a part of the offshore wind section during the last year of the education.

ABBREVIATIONS

FEA	Finite element analysis
HSSmall	Hardening Soil model with small-strain stiffness
LCoE	Levelized Cost of Energy
MC	Mohr-Coulomb model
PE	Plate elements
RB	Rigid body without self-weight
RBSW	Rigid body with self-weight

SYMBOLS

CF	Coarseness factor in PLAXIS
D	Caisson diameter
E_{50}	Young's modulus in the Mohr-Coulomb material model
E_{ref}	Secant modulus at 50% strength
K_0	Earth pressure coefficient at rest
R_{inter}	Interface strength reduction
α_{pad}	Load inclination at padeye
X	Domain extent in the x-direction

$\boldsymbol{Y}$	Domain extent in the y-direction
$\boldsymbol{Z}$	Domain extent in the z-direction
δ	Interface friction angle
$\frac{DL}{l_e}$	Normalised target element size
$\frac{u_{tot}}{D}$	Normalised total displacement
γ'	Effective unit weight of the soil
γ_c	Caisson unit weight
λ	Caisson aspect ratio
ν	Poisson's ratio in the Mohr-Coulomb material model
ψ	Dilation angle
φ	Friction angle of the soil
l_e	Global meshing parameter used in PLAXIS 3D
z_{pad}	Padeye depth
D_r	Relative density of soil
$F_{current}$	Current forces
F_{wave}	Wave forces
F_{wind}	Wind forces
H	Horizontal bearing capacity
L	Caisson skirt length
V	Vertical bearing capacity

REFERENCES

1. **Ahmed and Hawlader**, **2014**. Sheikh Sharif Ahmed and Bipul Chandra Hawlader. *Finite Element Modeling of Inclined Load Capacity of Suction Caisson in Sand with Abaqus/Explicit.* All Days, 2014. ISOPE-I-14-191.
2. **Ahn et al.**, **Mar 2014**. Jaehun Ahn, Hanmin Lee and Yun-Tae Kim. *Holding capacity of suction caisson anchors embedded in cohesive soils based on finite element analysis.* International Journal for Numerical and Analytical Methods in Geomechanics, 38(15), 1541–1555, 2014. . URL http://dx.doi.org/10.1002/nag.2268.
3. **Bang et al.**, **07 2009**. S. Bang, K.O. Kim, Y.S. Kim, Y. Cho, and K. Jones. *Centrifuge Model Tests On Suction Piles In Sand Under Inclined Loading.* International Ocean and Polar Engineering Conference, All Days, 148, 2009.
4. **Brinkgreve et al.**, **2010**. R. Brinkgreve, Erjona Engin and Harun Kürşat Engin. *Validation of empirical formulas to derive model parameters for sands.* 2010. ISBN 978-0-415-59239-0. .
5. **Brinkgreve and Swolfs**, **2008**. RBJ Brinkgreve and WM(extern) Swolfs. *Possibilities and limitations of the finite element method for geotechnical applications.* pages 11–15, 2008.
6. **Cheng et al.**, **2021**. L. Cheng, M.S. Hossain, Y. Hu, Y.H. Kim and S.N. Ullah. *Failure envelope of suction caisson anchors subjected to combined loadings in sand.* Applied Ocean Research, 114, 102801, 2021. ISSN 0141-1187.
7. **DNVGL-RP-E303**, **2017**. DNVGL-RP-E303. *Recommended practice - DNVGL-RP-E303*, 2017.
8. **Lees**, **2016**. Andrew Lees. *Geotechnical Finite Element Analysis.* ICE Publishing, 2016. ISBN 978-0-7277-6087-6. .
9. **Liu et al.**, **2019**. Tingfa Liu, Santiago Quinteros, Richard Jardine, J. H. Carraro and Robinson. *A Unified Database of Ring Shear Steel-Interface Tests on Sandy-Silty Soils (Bishop Ring Shear Tests).* Proc. 17th. European Conf. Soil Mech. and Geotechnical Engg., page 0268, 2019.
10. **Zhao et al.**, **2019**. L. Zhao, C. Gaudin, C. D. O'Loughlin, J. P. Hambleton, M. J. Cassidy and M. Herduin. *Drained Capacity of a Suction Caisson in Sand under Inclined Loading.* Journal of Geotechnical and Geoenvironmental Engineering, 145(2), 04018107, 2019.

Article 3

Surrogate-Based Optimisation of Suction Anchors with Embedded Mooring Chain

Surrogate-Based Optimisation of Suction Anchors with Embedded Mooring Chain

CHRISTIAN LYKKE JENSEN[1], STEFAN RYSGAARD HOUMANN[1], TROELS JUUL PEDERSEN[1], AND LARS BO IBSEN[2]

[1] *M.Sc. student, Dept. of Civil Engineering, Aalborg University, Denmark*
[2] *Prof., Dept. of Civil Engineering, Aalborg University, Denmark*

ABSTRACT: This study investigates the optimal design of suction anchors in cohesionless soil, incorporating the influence of embedded chains in the optimisation process. To address the computational demands associated with high-fidelity models, a surrogate-based optimisation approach is employed. The chain-soil interactions of the embedded chain are modelled using the method proposed by Mortensen [14], while the pull-out capacity of the suction caisson anchor is assessed through finite element analysis using PLAXIS 3D. The analysis focuses on static loading conditions, modelling the drained behaviour of the soil with a Mohr-Coulomb material model. Surrogate models are trained using a Latin Hypercube Sampling dataset, and the regression and optimisation of these models are performed using open-source Python code. By conducting a Monte Carlo simulation encompassing various site conditions, the study examines the optimal anchor design across a wide range of scenarios. The findings indicate that when anchors are optimised to reduce material consumption, a larger aspect ratio is optimal. Contrary to prior research, this study reveals that the optimal padeye positions predominantly fall within the range of 0-0.25L for most site conditions. These insights can contribute to the further development of suction caisson anchors as effective solutions for floating offshore wind turbines.

1. INTRODUCTION

Fossil fuel deposits are rapidly depleting, while energy consumption worldwide is increasing. While wind energy still only constitutes a small part of energy production worldwide, the wind sector receives more and more attention and is becoming a higher priority. Offshore wind turbines are a well-established renewable energy source, but efforts are being made to develop the area further. However, deep water makes up 80% of the world's maritime waters, where bottom-fixed offshore wind turbines are no longer a cost-effective solution. Therefore, Floating Offshore Wind Turbines (FOWTs) are a technology moving towards commercial use, as efforts are made to reduce the Levelized Cost of Energy (LCoE).

When considering a wind farm of FOWTs, mooring systems will significantly affect the total project cost. Still, no clear solution exists regarding the best choice of mooring system for Floating Offshore Wind Turbine. Different solutions must consequently be considered for each project. This may result in comprehensive analyses to decide on a potential design, and methods to ease this process are vital. To achieve a significant reduction in costs, mooring systems need to be optimised. This study focuses on the optimisation of a catenary or taut mooring system consisting of suction caisson anchors.

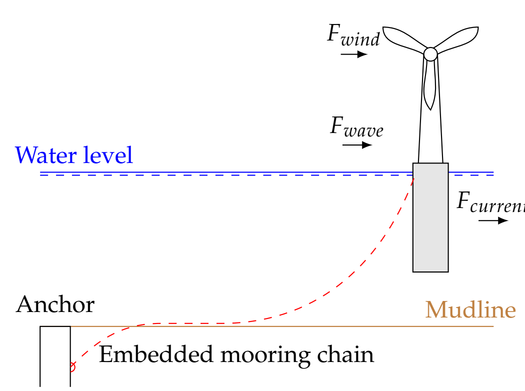

Figure. 1. Illustration of a mooring system for a FOWT.

Suction caissons are large diameter cylinders, typically in the range of 3–8 m, open at the bottom and closed at the top, and generally with a length to diameter ratio ($\lambda = \frac{L}{D}$) in the range 3 to 6 Mark Randolph [12]. Figure 1 illustrates a catenary mooring system for a Floating Offshore Wind Turbine.

Previous studies have considered either the embedded chain or anchor separately. Cheng et al. [6] and Zhao et al. [20] developed failure envelopes in (H, V)-space for the design of suction caisson anchors in cohesionless soil using finite element analyses. However, their studies were based on a limited number of finite element models and only considered a small range of soil conditions and anchor geometries. Therefore, this study aims to expand on the range of studied instances by conducting a significant number of finite element analyses determining the pull-out capacity in cohesionless soil.

Significant load reduction is obtained from the shear forces acting on the embedded chain. However, normal forces acting on the chain will increase the load inclination at the padeye of the anchor. These interactions between the chain and soil have been previously investigated by Neubecker and Randolph [15], Lee et al. [11] and Mortensen [14]. Jensen et al. [8] discovered that the method proposed by Mortensen [14] provided the most accurate estimation compared to other available methods.

As higher load inclinations result in lower pull-out capacities it is important to assess whether the load reduction from shear forces is greater than the loss of capacity in the anchor. Consequently, this interaction is vital to the optimisation process.

An optimisation based on the utilisation of these high-fidelity models, i.e., the incremental solution method proposed by Mortensen [14] for the chain and finite element models to determine the bearing capacity of the anchor, will be computationally very demanding and unfeasible. Hence, this study employs a surrogate-based approach to solve the optimisation problem while maintaining sufficient accuracy.

This paper presents a series of Monte Carlo simulations of geotechnical parameters and loading conditions for the station-keeping of FOWTs. For each given simulation, the padeye position and geometry of the anchor are optimised to reduce material consumption. As a result, distributions of the optimal design are presented for a vast range of geotechnical parameters and loading conditions. The purpose of the analyses is to further develop knowledge on the optimal mooring design using suction caisson anchors for the station-keeping of FOWT. Furthermore, the study investigates the usability of surrogate models for the prediction of the combined bearing capacity of the embedded chain and anchor.

2. METHODS

The study utilises multiple surrogate models derived from high-fidelity models. As mentioned earlier, the computational requirements of high-fidelity models often restrict the implementation of optimisation algorithms. As illustrated by Queipo et al. [17], to overcome this challenge, a surrogate-based analysis can be employed as a viable solution.

Figure 2 illustrates the process of developing and using a surrogate model. Initially, a Design of Experiments (DoE) is conducted using standardised methods to select data points within the design space ($\boldsymbol{x}$).

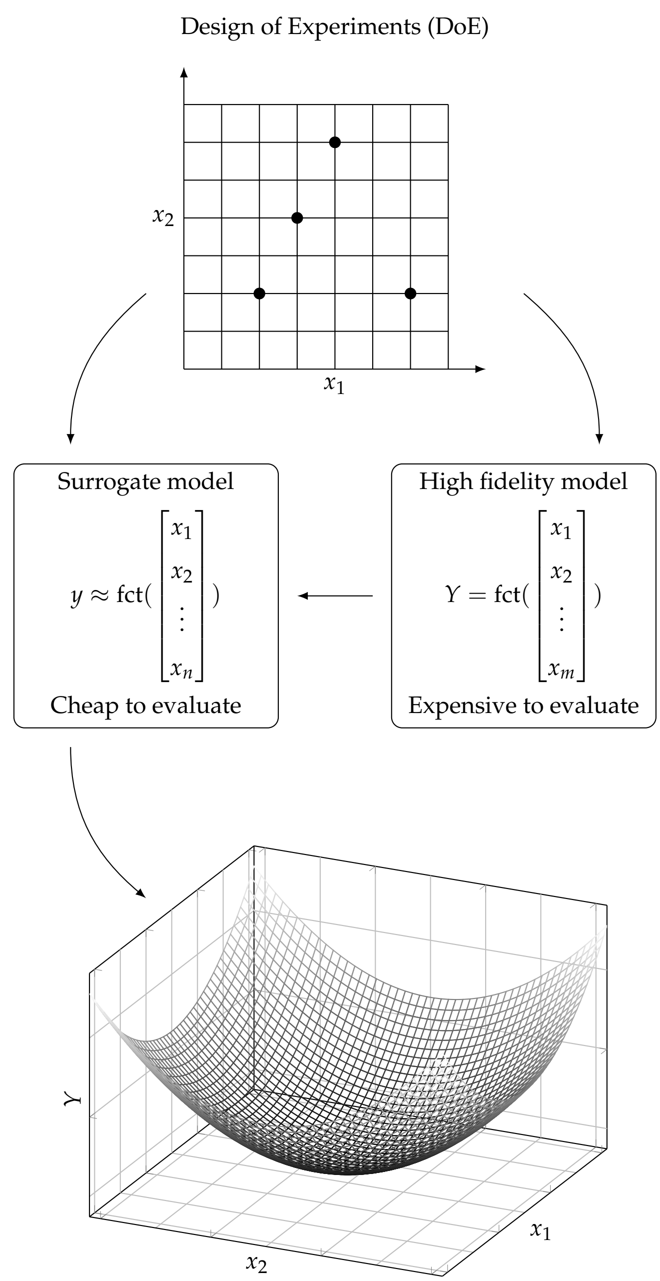

Figure. 2. Illustration of the development and usage of a surrogate model.

The response of the high-fidelity model (Y) is then evaluated for each of these data points. The obtained responses are then utilised to train a more cost-effective model (y) to approximate the response. Additionally, feature engineering is applied as the surrogate model approximates using a reduced number of features or parameters n compared to the number of parameters m used in the high-fidelity model. To assess the reliability of the surrogate model, its performance is evaluated on independent data not used during the training of the models.

In the following section, a description of each high-fidelity model is provided. Furthermore, is the development and validation of the surrogate models presented.

2.1. High Fidelity Models

The following describes the high-fidelity models used in the study.

2.1.1. Embedded Chain-Soil Interaction

This study utilises the method proposed by Mortensen [14] for the calculation of load reduction (ΔT) and the resulting angle at the padeye (α_{pad}). The method is an iterative incremental calculation method. It assumes a fully developed failure mechanism, with normal and shear forces acting on the chain. The force equilibrium of one chain link is used to solve the change in load and angle for the subsequent chain link. Chain links are added until the padeye depth is exceeded, and the calculation is then repeated with the first chain link shortened until the final link reaches the padeye.

The normal force is determined using the geotechnical parameters friction angle (φ) and unit weight (γ'). The force equilibrium is initiated with a load magnitude (T_{mud}) and inclination (α_{mud}) at the mudline. The effective width of the chain is determined empirically by multiplying an empirical factor (A_{sand}) with the chain diameter. The shear forces are determined using an empirical factor (α_{sand}) multiplied by the normal forces.

Mortensen [14] validated the method through large-scale tests. However, the loading and padeye depths used were small compared to the load magnitude expected from the mooring of FOWT. Consequently, this study imposes limitations on the calculation framework, restricting the angle to a maximum of 90 degrees and stopping the load reduction when a 90-degree angle is reached. Initial trials not included in this article showed unreasonable load reductions without this restriction imposed.

In the present study, the chains considered are limited to R3 studless link mooring chains. This study does not consider the structural design of the mooring chains. However, to use reasonable chain dimensions in the analyses, chains are selected using the design chart provided by Jinbo Marine [10].

Mortensen [14] provided recommendations for the empirical factors used in the study. As a result, the surrogate model used to determine load reduction and the angle at the padeye is constructed using only five parameters: friction angle (φ), unit weight (γ'), load angle at the mudline (α_{mud}), load at the mudline (T_{mud}), and padeye depth (z_{pad}).

2.1.2. Suction Anchor

Finite element analysis is commonly used in geotechnical engineering due to its ability to provide accurate predictions for various geotechnical problems. Providing a full description of finite element modelling of suction caisson anchors installed in sand is considered beyond the scope of this paper. This aspect has already been covered in a study conducted by the same authors in Jensen et al. [9].

In short, Jensen et al. [9] found that a Mohr-Coulomb material model was suitable for modelling the drained pull-out capacity. Consequently, geotechnical parameters friction angle (φ), unit weight (γ'), dilatation angle (ψ), Young's modulus (E_{50}^{ref}), and Poisson's ratio (ν) need to be defined for the constitutive modelling.

Jensen et al. [9] found that the stiffness parameters had minimal sensitivity to the accuracy of the capacity. As a result, they are excluded as input parameters for the surrogate model. Poisson's ratio is assumed to be ($\nu = 0.3$), whereas Young's modulus (E_{50}^{ref}) is determined based on the formulas for the calibration parameters proposed by Brinkgreve et al. [5]. For a given friction angle (φ), a relative density (D_r) is determined using Eq. (1b) which is then subsequently used to determine Young's modulus using Eq. (1a).

$$E_{50}^{ref}\,[kPa] = \frac{60 \cdot 10^3 \cdot D_r[\%]}{100} \tag{1a}$$

$$\varphi[^\circ] = 28 + \frac{12.5 \cdot D_r[\%]}{100} \tag{1b}$$

Jensen et al. [9] found that as the load inclination at padeye (α_{pad}) increased, the interface strength reduction factor (R_{inter}) had a significant influence on the pull-out capacity. As a result, the factor is included as a feature of the surrogate model.

Furthermore, Jensen et al. [9] found that for load inclinations resulting in vertical translation, increasing the in-situ earth pressure coefficient (K_0) increased the pull-out capacity. However, for all calculations in this study, a value of ($K_0 = 1 - \sin\varphi$) is used, as it is often conservatively assumed in design.

For most inclinations and padeye positions, Jensen et al. [9] found that the pull-out capacity was highly influenced by the dilatation angle (ψ). However, to reduce the number of features in the surrogate model, the dilatation angle used in the finite element models is determined using Eq. (2), which is commonly assumed in geotechnical design.

$$\psi[°] = \varphi[°] - 30 \quad \textbf{(2)}$$

The analysis does not consider the structural integrity of the anchor, however, the wall thickness (t) of the anchor is determined using Eq. (3) to provide a reasonable estimate of the anchor's self-weight and material consumption [4].

$$t[\text{mm}] = 6.35 + \frac{D[\text{mm}]}{100} \quad \textbf{(3)}$$

The surrogate model used to determine the pull-out capacity is constructed using seven features: friction angle (φ), unit weight (γ'), interface strength reduction factor (R_{inter}), load angle at the padeye (α_{pad}), normalised padeye position ($\frac{z_{pad}}{L}$), caisson diameter (D), and the caisson aspect ratio ($\lambda = \frac{L}{D}$), where (L) is the caisson skirt length.

2.2. Design of Experiments

As mentioned earlier, high-fidelity models require significant computational resources. Consequently, the Design of Experiments (DoE) methodology is employed. DoE is a systematic and efficient approach for studying the relationship between multiple input variables and output variables, providing a structured method for data collection and result analysis.

2.2.1. Design Space

Before constructing the DoE, it is necessary to define the range of parameters, known as the design space. These intervals also determine the validity range of the surrogate models, as extrapolation is not advised. Generally, larger intervals require more evaluations, resulting in higher computational costs. As a result, the design space should only include plausible values.

Pillai et al. [16] conducted a study on various load cases of a catenary mooring system with a 15 MW Floating Offshore Wind Turbine located at a water depth of 70 meters. Based on their findings, this study considers load at the mudline (T_{mud}) ranging from 2.5 MN to 14 MN.

This study considers load inclinations at the mudline (α_{mud}) ranging from 0 to 35 degrees, which are assumed feasible for catenary and taut mooring systems under design load cases.

Soil conditions are site-dependent and possess significant uncertainty. In this study, soil conditions are analysed within the range of 30-40 degrees for the friction angle (φ) and 8-11 kN/m^3 for the unit weight (γ'). Determining the interface reduction factor (R_{inter}) is challenging without laboratory testing. The PLAXIS manual suggests applying a factor of 2/3 in such cases. Consequently, the interface strength reduction factor is studied for values from 0.5 to 0.8.

The study considers caisson diameters (D) ranging from 3 to 5 and aspect ratios (λ) ranging from 1 to 5. In design situations involving installation, the aspect ratio is limited by the pressure difference due to water depth and the avoidance of buckling. However, these considerations are not included in the present study.

Since this study aims to investigate interactions between the embedded chain and anchor, the padeye position is examined at all positions from the top to the bottom of the anchor. The design space considered in the present study is summarised in table 1.

Table 1. Design space or range of parameters used in the DoE.

Parameters	Interval	Unit
Load angle at mudline (α_{mud})	0 - 35	°
Tension at mudline (T_{mud})	2.5 - 14	MN
Friction angle (φ)	30 - 40	°
Unit weight (γ')	8 - 11	kN/m^3
Interface reduction factor (R_{inter})	0.5 - 0.8	-
Diameter of anchor (D)	3 - 5	m
Aspect ratio (λ)	1 - 5	-
Normalised padeye position (z_{pad})	0 - 1	-

2.2.2. Training Data

Several methods exist for selecting which design points to evaluate, such as Full Factorial Design, Central Composite Design, or Latin Hypercube Sampling. Full Factorial and Central Composite designs include repeated parameter values in the DoE, which can be relevant for any modelling procedure with aleatoric uncertainty. In contrast, the Latin Hypercube Sampling (LHS) does not include repeated parameter values and is often used for computational experiments where the responses are not expected to possess random uncertainties [13].

In this study, the LHS is utilised. Latin Hypercube Sampling subdivides the design space into a grid with an equal number of desired elements for each parameter, and sample points are randomly selected within sub-volumes. The Latin Hypercube Sampling in this study is performed using the Python module scipy.stats.qmc.LatinHypercube [1].

In the present study, a sample size of 330 evaluations is used for the regression of each surrogate model. The number of evaluations in the DoE must be sufficiently large as model performance generally improves along with an increase in the sample size. However, increasing the sample size increase the computational demand of evaluating the high-fidelity models as such a balance as to be struck.

For the specific case of sampling the training data for the bearing capacity of the anchor, a novel approach is employed in this study. A random sampling of angles at the padeye from 0 to 90 degrees would in many cases result in combinations of padeye depths and load inclinations that are highly unlikely. Consequently, these design points would introduce unnecessary noise in the regression of the surrogate models. As a solution, the angle at the padeye for each data point is determined using the high-fidelity chain model, where a load and angle at the mudline are sampled instead. This method provides more reasonable angles at the padeye for the training data and is considered to facilitate a better dataset for the regression of the surrogate model.

Figure 3-5 presents a grid plot displaying the LHS and the resulting responses (Y) used for the regression of the surrogate models. In general, the input parameters are well distributed throughout the design space. However, when examining the responses, noticeable trends in the hyper-planes of the responses are observed.

In figure 3 and 4 a consequence of the limitations imposed on the high-fidelity chain model is seen. Initially, the angle at the padeye (α_{pad}) increases linearly until it reaches its ultimate value of 90 degrees around padeye depths of 6–8 meters. As a result, the load reduction (ΔT) reaches maximum values at similar padeye depths. Similar to the angle at padeye the load reduction varies linearly for smaller padeye depths. Furthermore, the maximum load reduction is limited by the angle at the mudline (α_{mud}), where an increase in the angle decreases the maximum load reduction.

As shown in both figures, even though the design space is evenly distributed, the responses are not well distributed. For load reduction, most evaluations result in reductions around 40-50%, and for the angle at the padeye, the angle is mostly 90 degrees. The uneven distribution in response is not necessarily an issue, however, it is important to assess whether the surrogate models over-fit to the maximum values losing the ability to predict for lower padeye depths.

Regarding the bearing capacity of the anchor presented in figure 5, most of the load and soil conditions exhibit a load inclination of 90 degrees. For the remaining angles, an inclination of around 30 degrees predominates in the sampled conditions. A positive correlation is observed between the caisson diameter, aspect ratio, and the bearing capacity. The maximum bearing capacity for the angle at the padeye is found within the range of 30-50 degrees.

Overall, the training data is considered sufficiently large, and the design space is adequately populated to provide a basis for constructing the surrogate models.

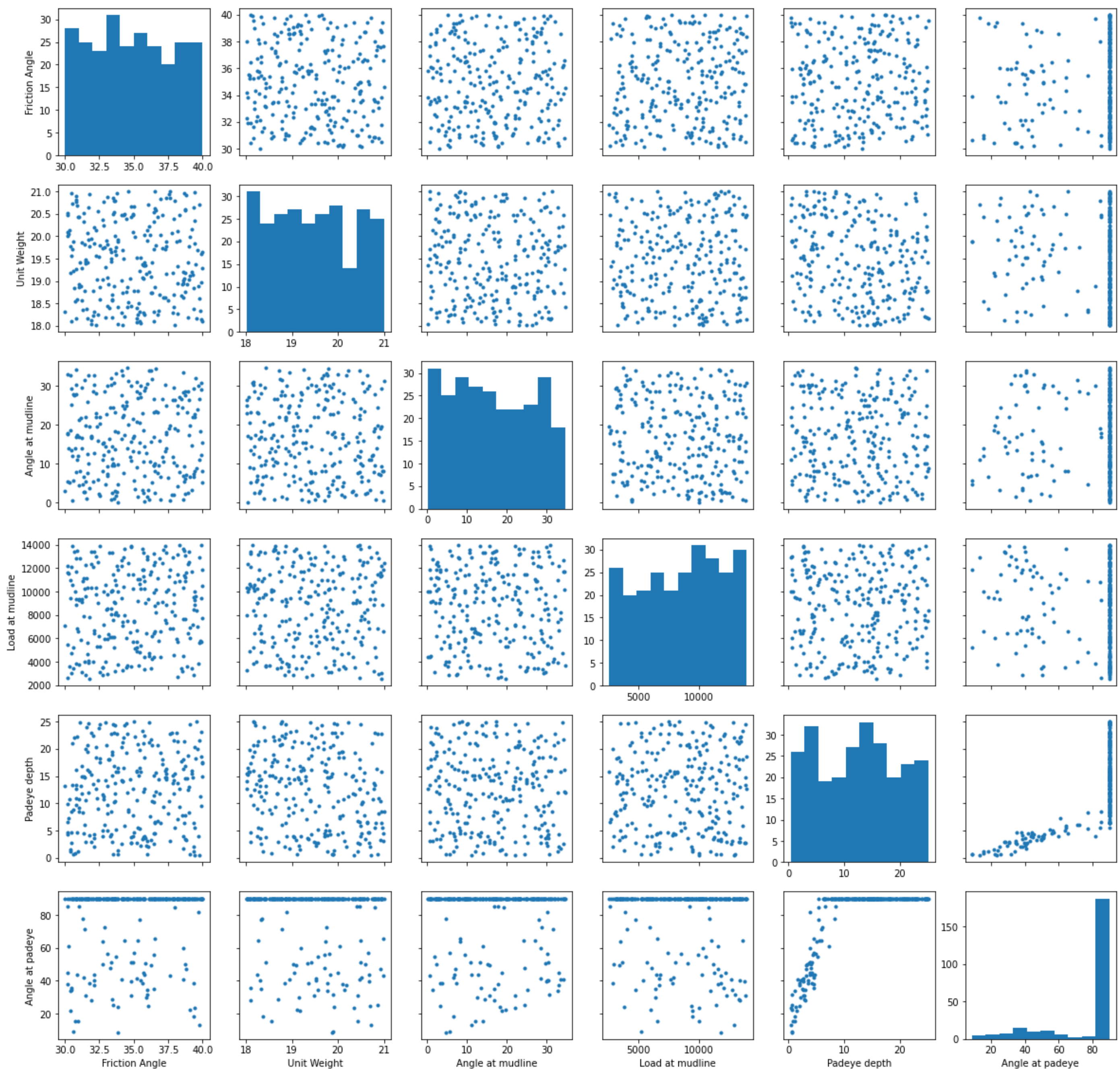

Figure. 3. Sampling space and resulting angle at padeye (α_{pad}) using high-fidelity chain model.

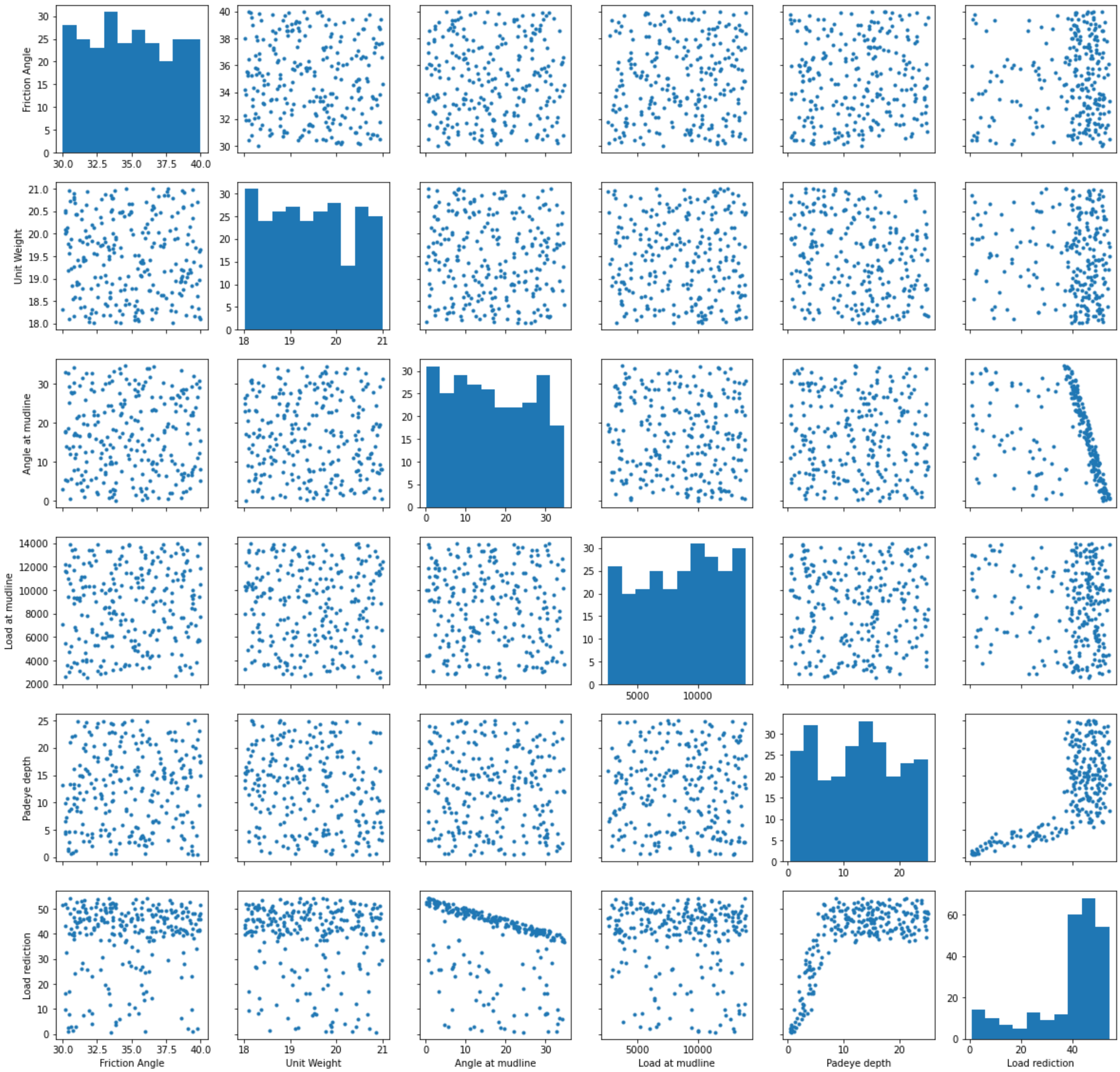

Figure. 4. Sampling space and resulting load reductions (ΔT) using high-fidelity chain model.

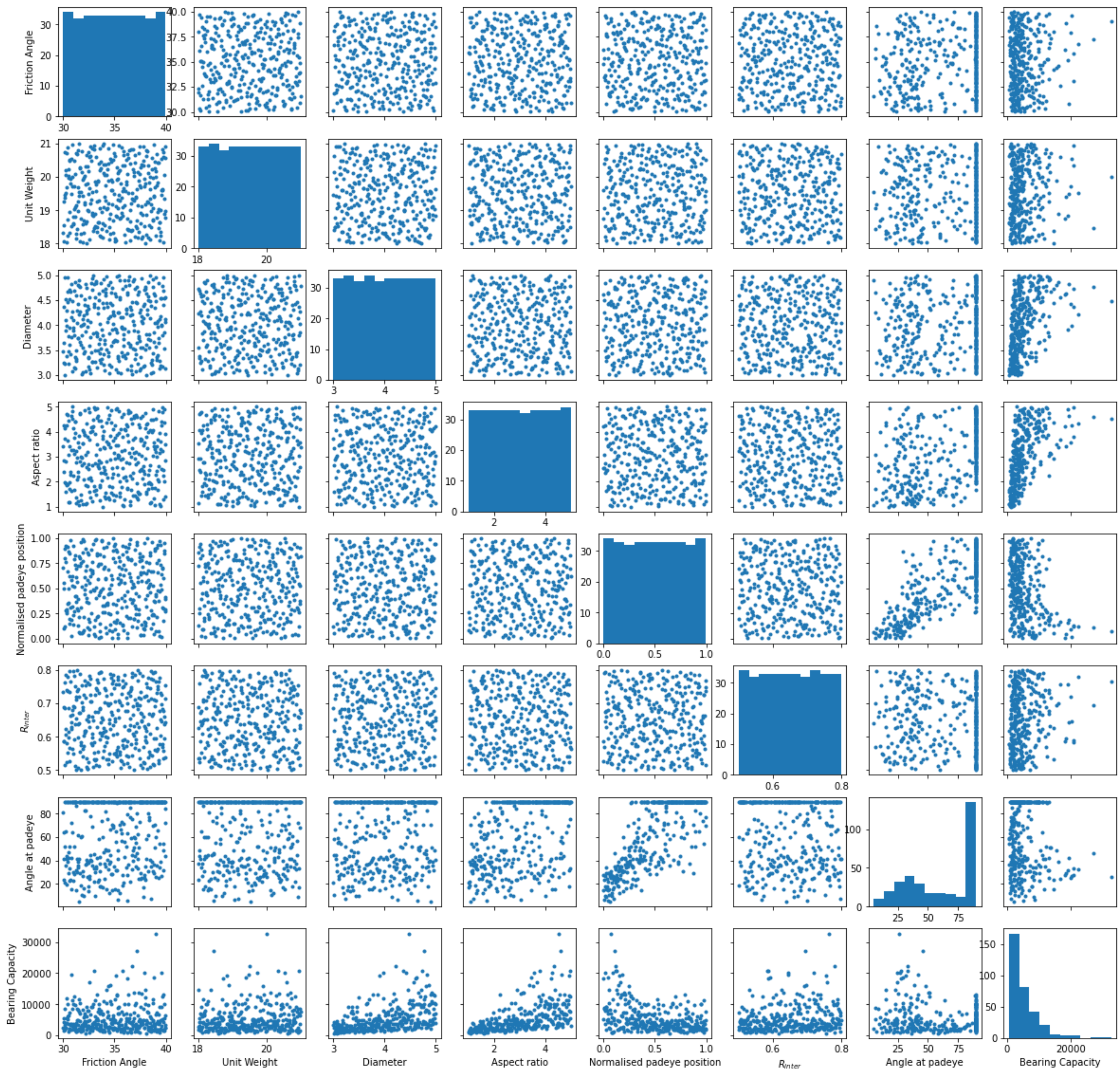

Figure. 5. Sampling space and finite element results of bearing capacity (R_c) using high-fidelity suction anchor model.

2.3. Surrogate Models

Using surrogate models or analytical function approximations of high-fidelity models is a well-known approach and has been applied in various engineering fields. However, determining the most suitable function formulation for approximating responses is generally unknown prior to analysis.

In this study, a 3-degree polynomial function fitted using Ordinary Least Squares (OLS) was deemed adequate for the chain models. Conversely, for the suction caisson model, a Support Vector Regression (SVR) model was found to be an appropriate choice. SVR models have been utilised by other researchers in the field of geotechnics, such as Samui et al. [19], for predicting the over consolidation ratio (OCR) and Samui [18] pile-bearing capacity prediction.

In the present study, the regression for surrogate models is performed using the Python module sklearn [2].

2.3.1. Polynomial Regression Model

For the chain models, the responses ($y(\boldsymbol{x})$) are computed by Eq. (4), where the mapping function ($\phi(\boldsymbol{x})$) utilised is the PolynomialFeatures function from the sklearn module, which generates all possible polynomial combinations of parameters up to a specified degree [3]. In this study, all polynomial combinations of parameters up to the third degree are used.

The vectors of beta coefficients ($\boldsymbol{\beta}$) for the chain models is determined through Ordinary Least Squares (OLS) regression. This algorithm aims to find the best-fitting line or hyperplane that minimises the sum of squared differences between the high-fidelity and surrogate model as shown in Eq. (5).

$$y(\boldsymbol{x}) = \boldsymbol{\beta}^T \phi(\boldsymbol{x}) \tag{4}$$

$$\min \sum_i (e_i)^2 \tag{5}$$

Figure 6 illustrates the non-linear mapping of the mapping function and the subsequent OLS regression in a higher-dimensional space. Despite the responses being non-linear in the original design space, the assumption is made that they are linear in a higher-dimensional space.

2.3.2. Support Vector Regression Model

For the surrogate model of the bearing capacity of the anchor Support Vector Regression (SVR) is employed. The bearing capacity ($y(\boldsymbol{x})$) is approximated by Eq. (6), where (N_{sv}) is the number of support vectors, (w_i) is the weight coefficient of the corresponding support vector, ($K(\boldsymbol{x}, \boldsymbol{x}_i)$) the kernel function and (b) the bias. In the present study, a radial basis function presented in Eq. (7) is used as the kernel function.

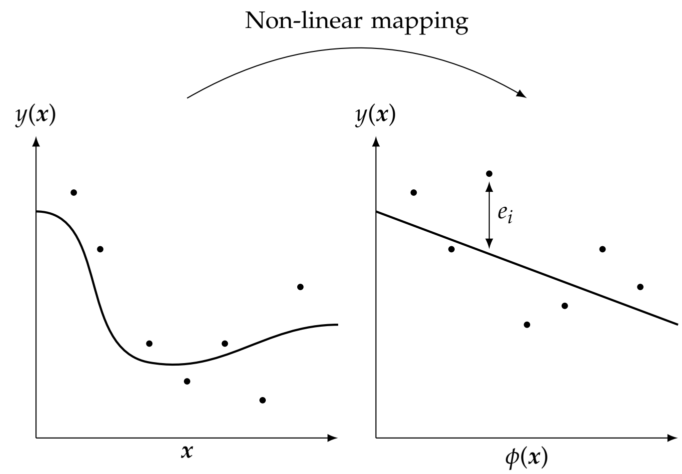

Figure. 6. Illustration of non-linear mapping and Ordinary Least Squares (OLS) regression in higher dimensional space.

$$y(\boldsymbol{x}) = \sum_{i=1}^{N_{sv}} w_i K(\boldsymbol{x}, \boldsymbol{x}_i) + b \tag{6}$$

$$K(\boldsymbol{x}, \boldsymbol{x}_i) = \exp(\frac{1}{2} ||\boldsymbol{x} - \boldsymbol{x}_i||^2) \tag{7}$$

The general principle of SVR is illustrated in figure 7. SVR is a machine learning algorithm that predicts by finding a line or hyperplane that best fits the data points in a high-dimensional space. It aims to minimise the errors between predicted and actual values while allowing a certain margin of error (ε).

The radial basis function offers the advantage of implicitly transforming the data into a higher polynomial space. The SVR obtains the number of support vectors (N_{sv}) and vector of weight coefficients ($\boldsymbol{w}$) by minimising the optimisation objective defined in Eq. (8) under the constraint in Eq. (9), where (ξ_i) is the deviation from the margin and (C) a regularisation parameter.

$$\min \frac{1}{2} ||\boldsymbol{w}||^2 + C \sum_{i=1}^{N_{sv}} |\xi_i| \tag{8}$$

$$|Y_i - w_i \boldsymbol{x}_i| \leq \varepsilon + |\xi_i| \tag{9}$$

The Support Vector Regression requires the selection of the hyper-parameters (ε) and (C) prior to the regression. In the present study, a margin of error $\varepsilon = 250\,\text{kN}$ was chosen and a study investigated the selection of the regularisation parameter (C) is conducted. Figure 8 shows the results of the study, where the percentage of vectors within the ε-tube and Mean Absolute Error (MAE) are plotted against the regularisation parameter. The MAE is determined using Eq. (10), where (N) is the number of vectors in the entire training data.

$$\text{MAE} = \frac{\sum_i^N |Y_i - y_i|}{N} \tag{10}$$

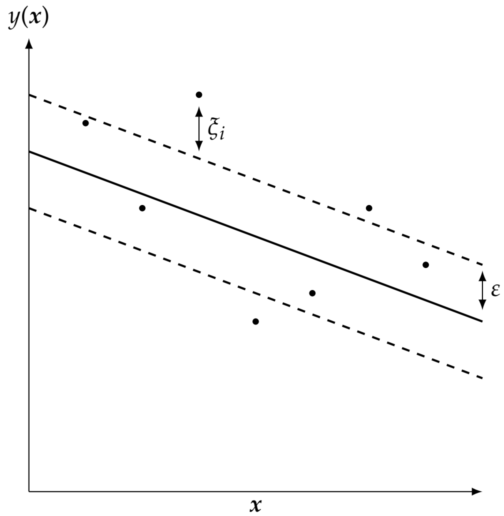

Figure. 7. Illustration of Support Vector Regression (SVR).

Increasing the regularisation parameter (C) leads to a decrease in the mean absolute error, indicating an improvement in the model's accuracy on the training data. However, beyond a certain point, increasing (C) can lead to overfitting and therefore negatively impacts the model's performance on new data. The optimal regularisation parameter is chosen as the value that maximises the number of vectors within the ε-tube while maintaining a low mean absolute error. Based on the study, the optimal regularisation parameter (C) was found to be 50,000.

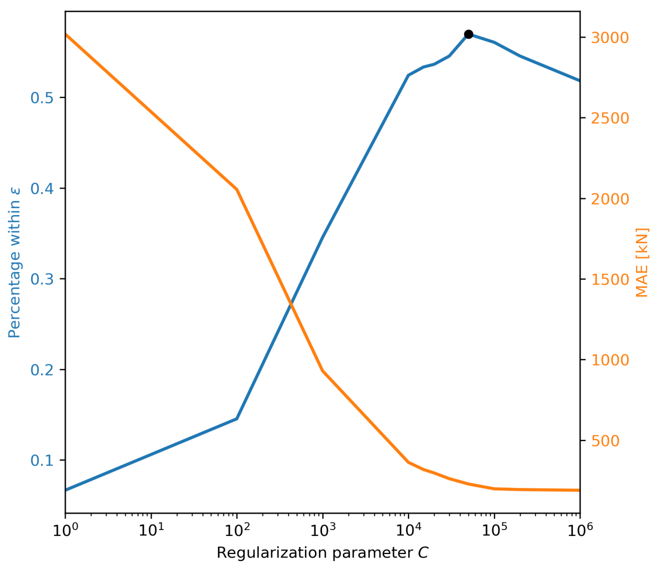

Figure. 8. Percentage of vectors within the ε-tube and mean absolute error as a function of the regularisation parameter (C).

2.3.3. Validation of Surrogate Models

Validation of the surrogate models is performed by constructing a validation set of results from the high-fidelity models. These validation sets are created using the same Design of Experiments principals previously but are due to the random sampling different from the training sets. For the validation of the surrogate models, a validation set of 72 data points was used.

Figure 9-11 presents validation of the surrogate models for the angle at padeye (α_{pad}), load reduction from the embedded chain (ΔT), and bearing capacity of the anchor (R_c). Each figure shows the surrogate predictions as a function of the validation data, with the diagonal line representing no loss of precision using the surrogate models. The coefficient of determination (R^2), the mean value (μ), and the standard deviation (σ) of the error between the validation data and predictions are presented in each figure.

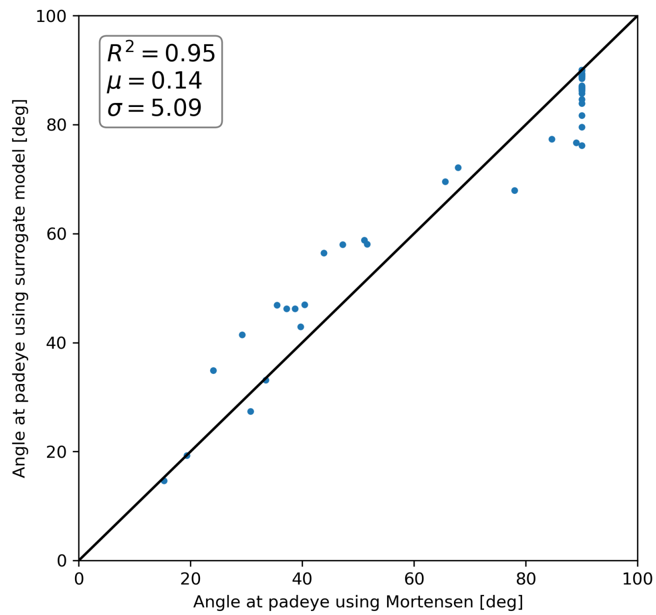

Figure. 9. Comparing between Mortensen [14] and surrogate model for the prediction of the angle at padeye (α_{pad}).

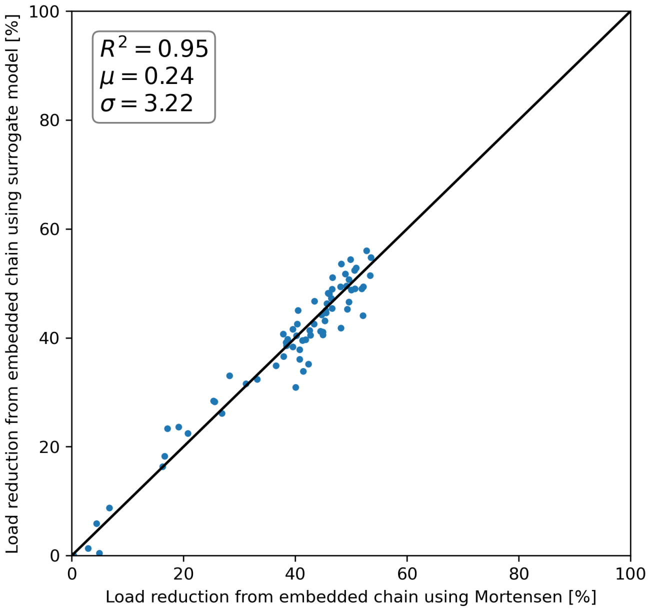

Figure. 10. Comparing between Mortensen [14] and surrogate model for the prediction of the load reduction (ΔT) from the embedded chain.

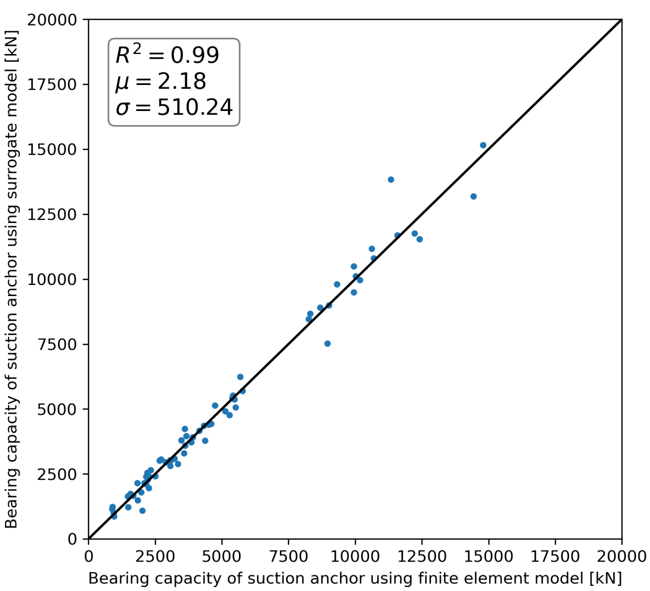

Figure. 11. Comparing between finite element results and surrogate model for the prediction pull-out force (R_c).

The results show that all surrogate models perform well on the validation data set, with coefficients of determination of 0.95, 0.95, and 0.99 for predicting the angle at padeye (α_{pad}), load reduction from the embedded chain (ΔT), and bearing capacity of the anchor (R_c), respectively. The models are generally unbiased, with low mean values of the error between validation data and surrogate predictions. The standard deviation of the error between high-fidelity models and surrogate models is generally quite small for all models. Noticeably the standard deviation of error for the anchor model corresponds to the size of the ε-tube defined in the SVR.

The overall performance of the surrogate models in predicting the various parameters of suction caisson anchors is promising, indicating their potential usefulness in design optimisation.

2.4. Monte Carlo Simulation and Optimisation Procedure

Monte Carlo simulation is a computational technique used to simulate and analyse complex systems. In the context of this study, Monte Carlo simulations are employed alongside optimisation procedures to investigate general trends in the optimal design of suction anchors, when considering the embedded chain configuration for a broad range of site and load conditions.

Figure 12 illustrates the simulation and optimisation process used in the study. 50,000 Monte Carlo simulations are conducted in the study, where each load and soil parameter is randomly generated using the Python module random, following a uniform distribution. As a result, no correlations between either load or soil parameters are considered in the simulation.

The optimisation is conducted using the SciPy optimize module, where the objective function to be minimised is the volume of the anchor given by the cost function Eq. (11). The optimisation procedure is subjected to the inequality constraint given by Eq. (12).

$$\text{Cost}(D, L) = \pi \left(\frac{D}{2}\right)^2 t + \left(\pi \left(\frac{D}{2}\right)^2 - \pi \left(\frac{D}{2} - t\right)^2\right) L \quad \textbf{(11)}$$

$$R_c(\boldsymbol{x}) \geq T_{mud} \cdot \Delta T \quad \textbf{(12)}$$

Additionally, the optimisation parameters (D, λ, z_{pad}) are given bounds as the same interval used for the construction of the surrogate models. The optimisation method applied is Sequential Least SQuares Programming (SLSQP). To address the concern of the optimisation procedure terminating in a local minimum, three different initial guesses are used, and subsequently, the most optimal result is used.

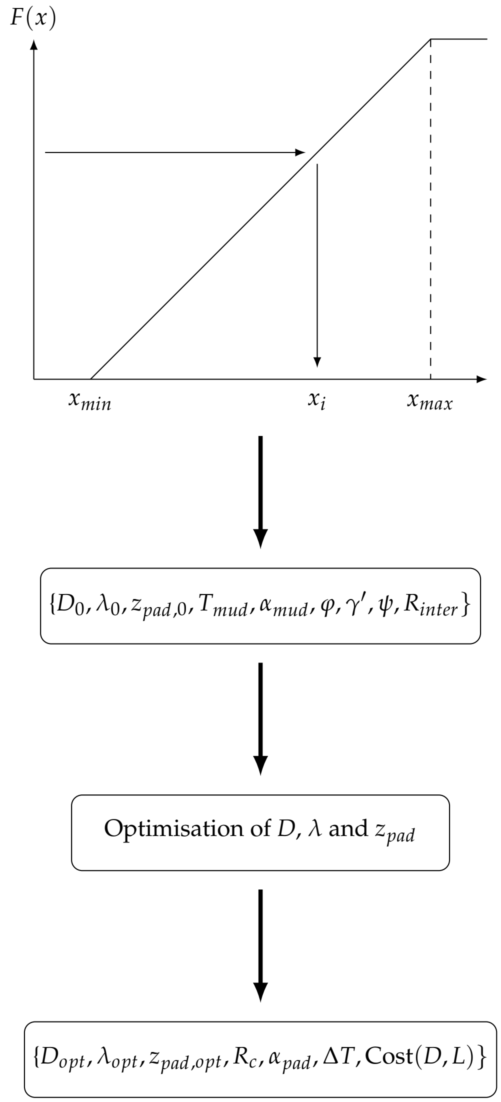

Figure. 12. Illustration of the Monte Carlo simulation and optimisation procedure.

3. RESULTS

The following section presents visualisations of the simulations and optimisations. Providing clear visualisations and presentations of high-dimensional data is a well-known challenge in the field of data analysis. As a result the result section primarily focuses on the optimised anchor design, i.e., diameter (D), aspect ratio (λ) and normalised padeye position ($\frac{z_{pad}}{L}$)

3.1. Monte Carlo Simulation and Optimisation Results

Figure 13 shows a parallel coordinate plot of the entire set of simulation results, with each blue line representing one simulation and optimisation result. The figure illustrates that each randomly simulated parameter is uniformly distributed across its axis. The optimisation procedure has resulted in optimal anchor diameter and aspect ratio covering almost the entire range of the optimisation bounds, with the exception of the large caisson diameter, being less populated. Regarding the padeye position, the general trend observed in the optimisation is that it either results in positions near the top of the range (0-0.25L) or at the bottom of the anchor, with only a small number of simulations resulting in intermediate padeye positions.

As seen in the figure, positioning the padeye at the bottom of the anchors leads to the highest load reductions and, furthermore, the highest angles at the padeye. Conversely, positioning the padeye near the top of the anchor yields the opposite effect.

The hollow cylindrical volume of the anchor ranges from approximately 2 to 15 m^3.

3.2. Optimal Anchor Design

The results of the optimisations of anchor designs are presented in Figure 14-16, which shows three violin plots of the optimised suction anchor diameter (D), aspect ratio (λ), and normalised padeye position ($\frac{z_{pad}}{L}$), respectively.

The majority of the optimisations result in anchor diameters of 3 m which is the lower bound of the optimisation process. As the objective function to be minimised is the volume of the anchor, the results indicate that it is most efficient to minimise the diameter and find the required aspect ratio, i.e., the length of the anchor, to obtain sufficient bearing capacity.

The distribution of optimal aspect ratios in figure 15 shows that the optimal suction anchor design generally has an aspect ratio in the range of 2.5-5, depending on the specific load and geotechnical conditions. A large part of the optimisation results in aspect ratios of 5, which is the upper bound of the optimisation process.

In terms of the normalised padeye position, the results show that the majority of the optimal padeye positions are at a padeye position of 0-0.25L, whereas only a very small portion of the optimisations results in other padeye positions.

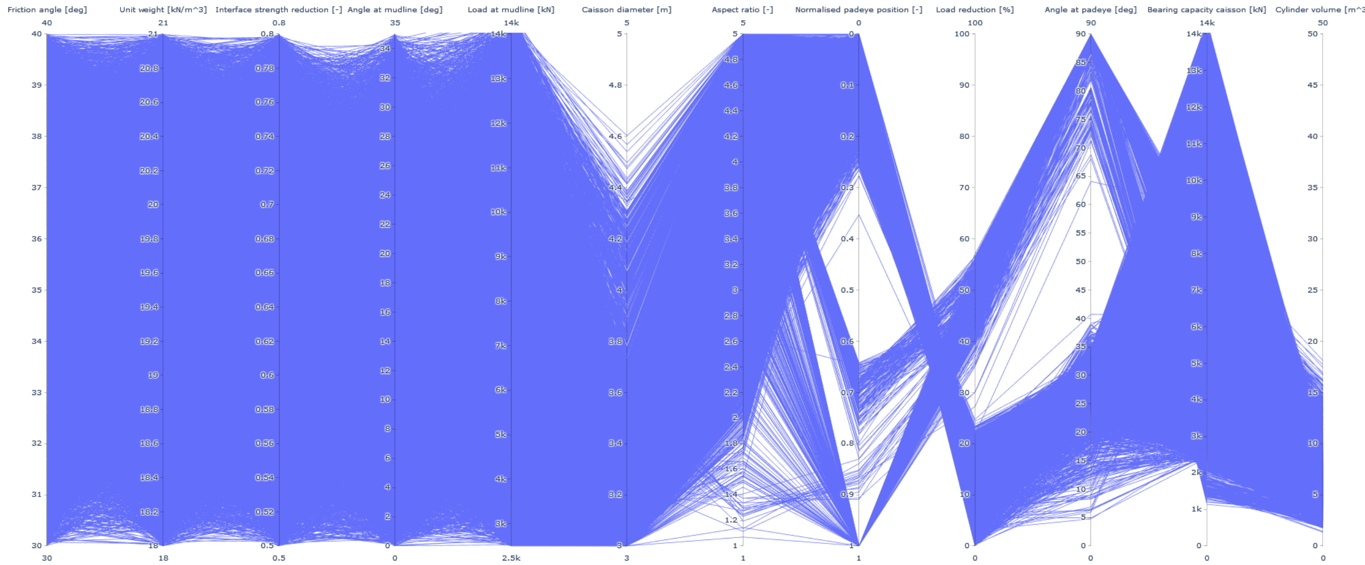

Figure. 13. Parallel coordinate plot of the Monte Carlo simulation and optimisation results.

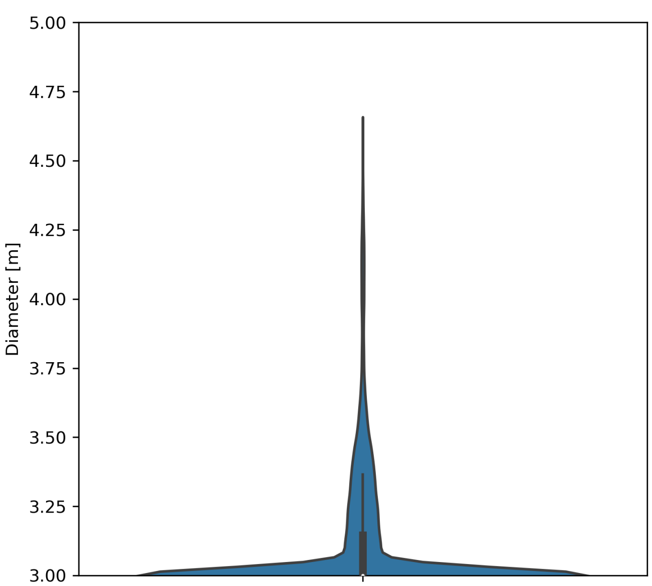

Figure. 14. Violin plots of the optimised anchor diameters.

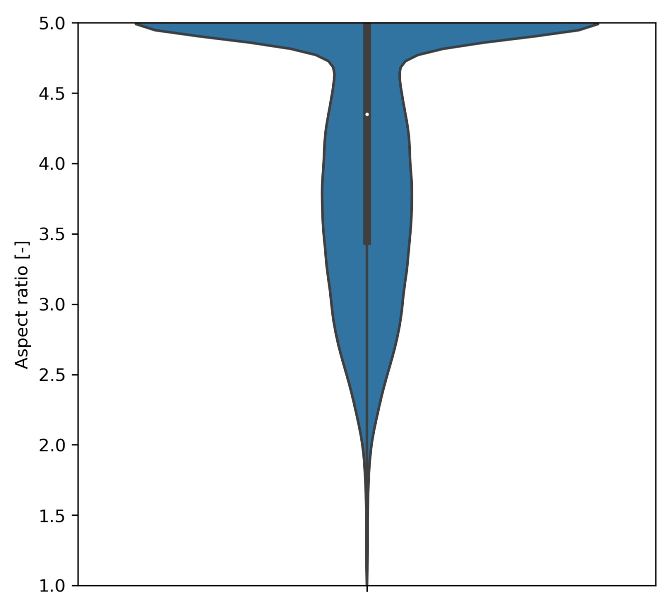

Figure. 15. Violin plots of the optimised anchor aspect ratio.

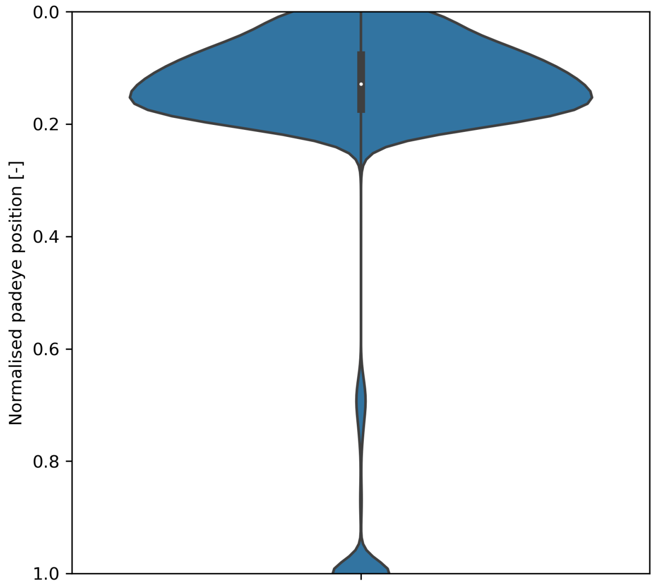

Figure. 16. Violin plots of the optimised normalised padeye positions.

3.2.1. Effect of Friction Angle

Figure 17-19 presents violin plots of the optimised suction anchor diameter, aspect ratio, and normalised padeye position for different ranges of friction angle (φ). Both figure 17 and 18 illustrates that for higher friction angle the anchor dimensions decrease. As figure 19 illustrates when the friction angles increase the normalised padeye position decreases.

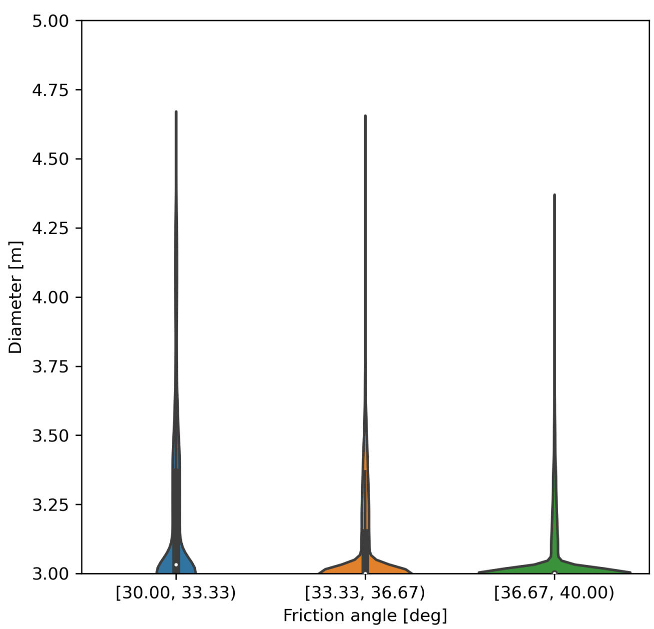

Figure. 17. Violin plots of the optimised anchor diameter divided into group based on the friction angle.

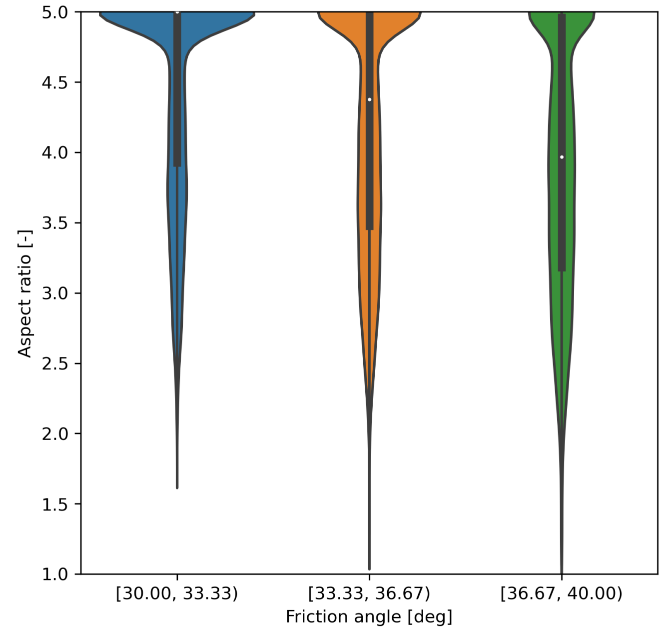

Figure. 18. Violin plots of the optimised anchor aspect ratio divided into group based on the friction angle.

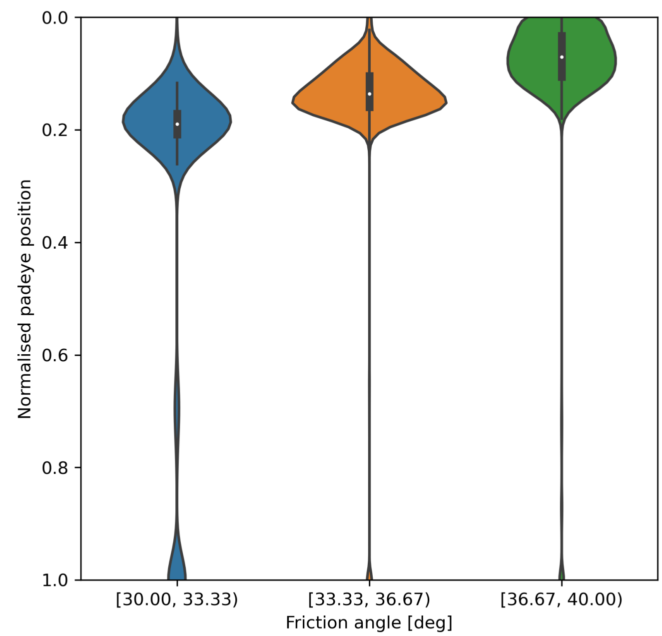

Figure. 19. Violin plots of the optimised normalised padeye position divided into group based on the friction angle.

3.2.2. Effect of Load Magnitude

To further investigate the optimised anchor design, the results are divided into ranges of the loads at the mudline (T_{mud}). Figure 20-22 presents the results of this analysis, with violin plots of the optimised suction anchor diameter, aspect ratio, and normalised padeye position for each group. The results indicate that for higher loads, the optimal aspect ratio generally increases.

Regarding the optimal normalised padeye position, figure 22 indicates that the optimal position is not significantly influenced by the load magnitude.

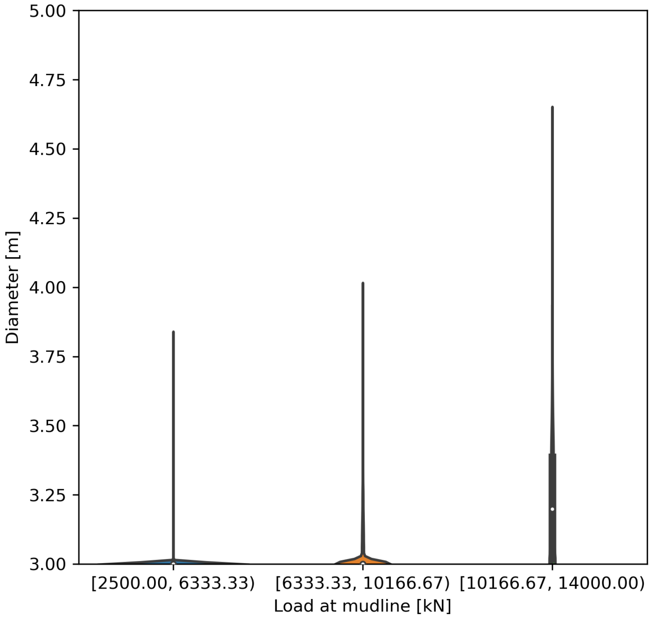

Figure. 20. Violin plots of the optimised anchor diameter divided into group based on the load at mudline.

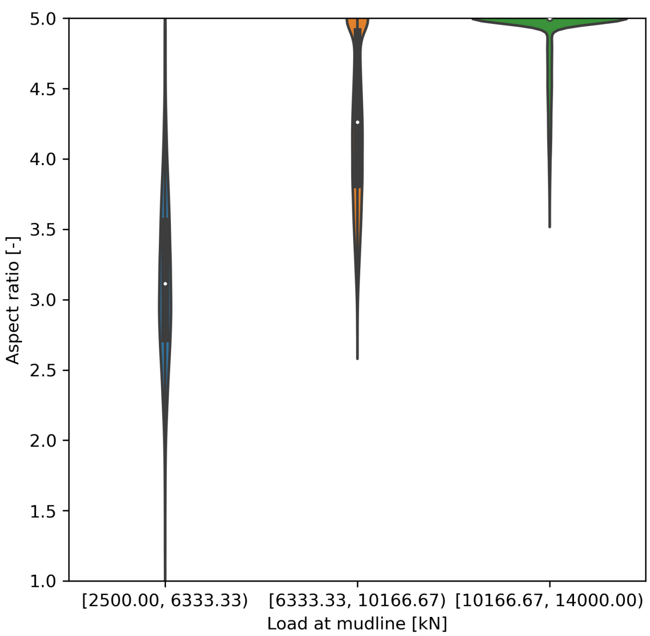

Figure. 21. Violin plots of the optimised anchor aspect ratio divided into group based on the load at mudline.

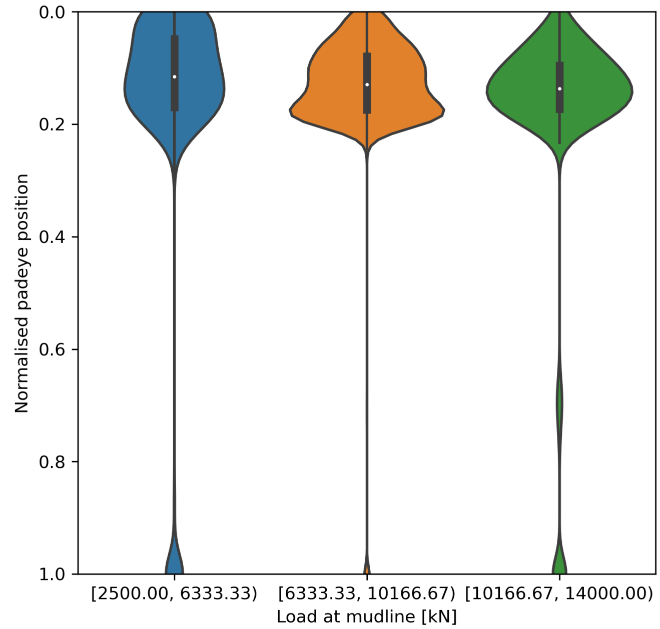

Figure. 22. Violin plots of the optimised normalised padeye position divided into group based on the load at mudline.

4. DISCUSSION

The present study investigated the accuracy and reliability of surrogate models for suction caisson anchors and identified the optimal design for different loading conditions. The findings of this study indicated that the surrogate models performed well in predicting key responses such as the angle at padeye (α_{pad}), load reduction from the embedded chain (ΔT), and bearing capacity of the anchor (R_c), with coefficients of determination of 0.95 and 0.99.

The surrogate models used in this study were found to be non-biased in their approximations of the high-fidelity models, as the mean values (μ) of the error were close to zero for all models. However, it is important to consider that the high-fidelity models themselves may be biased making either conservative or non-conservative predictions of the responses. This aspect could have a significant impact on the optimisation results, e.g., determining whether or not the load reduction from the chain exceeds the reduction in the bearing capacity of the anchor.

Additionally, the mesh generation procedure for the finite element analyses resulted in coarser meshes for suction anchors with larger aspect ratios. In general, coarser meshing tends to predict larger capacities. As a result, this could introduce some errors in the high-fidelity predictions of the bearing capacity of the anchor and consequently the surrogate model. Furthermore, it is important to note that while surrogate models approximate general trends in the training data, they do not capture the true physical behaviour as high-fidelity models do. This limitation should be considered when interpreting the results.

The installation process will have a limiting aspect ratio associated with each simulation of site conditions, as the buckling of the anchor or the inability to generate a large enough pressure difference to overcome skin friction during installation could limit the anchor geometry. Consequently, different trends in optimal design are likely to be seen if these limitations are incorporated into the optimisation procedure. The optimisations resulted for a large part of the investigated load range in optimal aspect ratios limited by the optimisation bounds, i.e., ($\lambda = 5$). As a result, the study finds the very plausible that for larger load magnitudes the optimal anchor design is limited by the factors limiting the installation.

Consequently, efforts to reduce loads from the FOWT would benefit the applicability of suction caisson anchors. Recent research has investigated the benefits of FOWT farms sharing anchors as the resulting load on the anchors are reduced [16] [7]. Furthermore, increasing the number of mooring lines could likewise reduce anchor loads.

The study's results contradicted initial expectations, as previous literature suggested that the optimal normalised padeye position would be within the range of 0.5–0.8, as this would produce the largest capacity of the suction caisson [6]. However, this study found very few optimised anchor designs with padeye positions within this range. As the study optimised the geometry by reducing material consumption, the results thus indicate that a more slender anchor is more advantageous in this regard. As a result, the padeye position should be placed at the top since, if the previous recommended range were followed, the load inclination would become most vertical. However, it is important to acknowledge that the weakness of surrogate models lies in their data-driven nature, as they do not explicitly model real physical behaviour but rather generalise trends within the data set. Future work in this field could enhance the models by incorporating more data and exploring different formulations of surrogate models. Validating the models with additional data would improve the confidence and reliability of the results.

The study identified that, for high loads, caissons with higher aspect ratios and padeye positions at the top of the anchor were generally more optimal in terms of material consumption, however limiting factors caused by installation issues could be included in the optimisation procedure to study its effect on the optimal design.

5. CONCLUSION

In conclusion, the findings of this study shed light on several important aspects of suction caisson anchor design. The study suggests that reducing loads from the Floating Offshore Wind Turbine (FOWT) would lead to a significant reduction in the optimal aspect ratio. Thus, improving the applicability of suction caisson anchors.

The surrogate-based analysis conducted in this study yielded interesting results regarding the influence of soil parameters on the optimal padeye position. Surprisingly, it was found that soil parameters have minimal impact on the determination of the optimal padeye position. Moreover, the study highlighted that the load inclination at the padeye becomes 90 degrees at relatively shallow padeye depths.

The use of surrogate models in this study proved to be an effective approach for approximating the behaviour of high-fidelity models. The surrogate models provided viable approximations for key responses, including the angle at the padeye, load reduction from the embedded chain, and the bearing capacity of the anchor. This finding emphasises the potential of surrogate models in reducing computational costs and accelerating the design optimisation process for suction caisson anchors.

Furthermore, the optimal padeye position was found to generally fall within the range of 0-0.25L. This information is crucial for engineers as it provides a guideline for determining the optimal position of the padeye early in the design process. Thus, significantly reducing the load configurations needed to be analysed.

From a bearing capacity and steel volume perspective, the study revealed that a small diameter and large aspect ratio are favourable. This design configuration can maximise the bearing capacity of the anchor while minimising the required amount of steel, leading to a more cost-effective solution. However, from an installation point of view, it was discussed that a large diameter and small aspect ratio are preferable.

In summary, this study has successfully demonstrated the accuracy and reliability of surrogate models in predicting key responses of suction caisson anchors. The findings provide valuable insights into the optimal design of these anchors, with considerations for load inclination, padeye position, aspect ratio, and diameter. These findings contribute to the development of more efficient and sustainable anchor designs in the offshore industry, ultimately leading to cost reduction and reduced environmental impact.

ACKNOWLEDGEMENTS

The authors are grateful for the guidance and constructive feedback from senior specialist Søren Dam Nielsen and leading specialist Søren Peder Hyldal Sørensen both from COWI.

The authors are grateful for not only the office space provided by COWI Aalborg but also that we could be a part of the offshore wind section during the last year of the education.

ABBREVIATIONS

DoE	Design of Experiments
FOWT	Floating Offshore Wind Turbine
LCoE	Levelized Cost of Energy
LHS	Latin Hypercube Sampling
MAE	Mean Absolute Error
OLS	Ordinary Least Squares
SLSQP	Sequential Least SQuares Programming
SVR	Support Vector Regression

SYMBOLS

C	Regularisation parameter used in the SVR
K	Kernel function used in the SVR
N_{sv}	Number of support vectors used in the SVR
N	Number of vectors in the training data used in the SVR
R^2	Coefficient of determination
Y	Response of high-fidelity model
$\boldsymbol{\beta}$	Vector of β coefficients for the surrogate model
$\boldsymbol{w}$	Vector of weight coefficient for the support vectors
$\boldsymbol{x}_i$	i^{th} support vector
$\boldsymbol{x}$	Vector of parameters or features in the design space
μ	Mean value
ν	Poisson's ratio in the Mohr-Coulomb material model
ϕ	PolynomialFeatures function used for the non-linear mapping to higher dimensional space.
σ	Standard deviation
ε	Margin of tolerance where no penalty is given to errors in the SVR
ξ_i	Slack variable that determines the degree to which samples with error more than ε are penalized.
b	biased used in the SVR
e_i	Differences between the high-fidelity and surrogate model
w_i	Weight coefficient for the i^{th} support vector
y	Response of the surrogate model
Cost	Cost function used in the optimisation
ΔT	Load reduction from mudline to padeye
α_{mud}	Load angle at mudline
α_{pad}	Load angle at padeye
α_{sand}	Ratio of the frictional and normal forces
γ'	Effective unit weight of the soil
λ	Caisson aspect ratio
ψ	Dilation angle
φ	Friction angle of the soil
A_{sand}	Empirical factor to consider the 90° rotation for each chain link
D	Caisson diameter

D_r	Relative density of soil
E_{50}^{ref}	Secant Young's modulus
$F_{current}$	Current forces
F_{wave}	Wave forces
F_{wind}	Wind forces
H	Horizontal bearing capacity
K_0	*In-situ* lateral earth pressure coefficient
L	Caisson skirt length
OCR	Over consolidation ratio
R_c	Bearing capacity of suction caisson
R_{inter}	Interface reduction factor
T_{mud}	Force at mudline
V	Vertical bearing capacity
t	Caisson wall thickness
z_{pad}	Padeye depth

REFERENCES

1. *scipy.stats.qmc.LatinHypercube - SciPy v1.10.1 Manual*. https://docs.scipy.org/doc/scipy/reference/generated/scipy.stats.qmc.LatinHypercube.html#scipy.stats.qmc.LatinHypercube. Accessed: 2023-06-05.
2. , . *sklearn.pipeline.Pipeline*. https://scikit-learn.org/stable/modules/generated/sklearn.pipeline.Pipeline.html, . Accessed: 2023-06-05.
3. , . *sklearn.preprocessing.PolynomialFeatures*. https://scikit-learn.org/stable/modules/generated/sklearn.preprocessing.PolynomialFeatures.html, . Accessed: 2023-06-05.
4. **American Petroleum Institute**, **2014**. American Petroleum Institute. *Recommended Practice for Planning, Designing and Constructing Fixed Offshore Platforms - Working Stress Design (API RP 2A-WSD), 22nd Edition*, 2014. URL https://tajhizkala.ir/doc/API/API_RP_2A_WSD_22nd_Ed_Nov_2014_Planning.pdf.
5. **Brinkgreve et al.**, **2010**. R. Brinkgreve, Erjona Engin and Harun Kürşat Engin. *Validation of empirical formulas to derive model parameters for sands*. 2010. ISBN 978-0-415-59239-0. .
6. **Cheng et al.**, **2021**. L. Cheng, M.S. Hossain, Y. Hu, Y.H. Kim and S.N. Ullah. *Failure envelope of suction caisson anchors subjected to combined loadings in sand*. Applied Ocean Research, 114, 102801, 2021. ISSN 0141-1187.
7. **Fontana et al.**, **2018**. Casey M. Fontana, Spencer T. Hallowell, Sanjay R. Arwade, Don J. DeGroot, Melissa E. Landon, Charles P. Aubeny, Brian Diaz, Andrew T. Myers and Senol Ozmutlu. *Multiline anchor force dynamics in floating offshore wind turbines*. Wind Energy, 21 (11), 1177–1190, 2018. . URL https://onlinelibrary.wiley.com/doi/abs/10.1002/we.2222.
8. **Jensen et al.**, **Jun 2023**. Christian Lykke Jensen, Stefan Rysgaard Houmann, Troels Juul Pedersen and Lars Bo Ibsen. *Chain-Soil Interactions in Cohesionless Soil under Static Loads with CPT-Data Interpretation*. Not decided for now, 2023.
9. **Jensen et al.**, **Jun 2023**. Christian Lykke Jensen, Stefan Rysgaard Houmann, Troels Juul Pedersen and Lars Bo Ibsen. *Modelling the Drained Capacity of Inclined Loaded Suction Anchors in Cohesionless Soil: A Finite Element Study*. Not decided for now, 2023.
10. **Jinbo Marine**. *Jinbo Marine*. URL https://www.jinbomarine.com/r3-offshore-studless-link-mooring-chain.html. Accessed: 2023-06-08.
11. **Lee et al.**, **2014**. Hoonyoung Lee, Dong-Soo kim and Yun Wook Choo. *Profile and Frictional Capacity of a Mooring Line Embedded in Sand via Centrifuge Model Testing*. Journal of Geotechnical and Geoenvironmental Engineering, 140(11), 04014059, 2014.
12. **Mark Randolph**, **2011**. Susan Gourvenec & David White Mark Randolph. *Offshore Geotechnical Engineering*. Taylor & Francis Ltd, 2011. ISBN 9780415477444.
13. **Montgomery**, **2021**. Douglas C. Montgomery. *Design and Analysis of Experiments*. John Wiley & Sons, Inc., Hoboken, 10th edition. edition, 2021. ISBN 9781119816959.
14. **Mortensen**, **2015**. N. Mortensen. *Chain configuration in sand, theory and large scale field testing*. Frontiers in Offshore Geotechnics III : Proceedings of the 3rd International Symposium on Frontiers in Offshore Geotechnics (ISFOG 2015), 1, 905–912, 2015.
15. **Neubecker and Randolph**, **1995**. S. R. Neubecker and M. F. Randolph. *Profile and Frictional Capacity of Embedded Anchor Chains*. Journal of Geotechnical Engineering, 121(11), 797–803, 1995.
16. **Pillai et al.**, **Dec 2022**. A.C. Pillai, T.J. Gordelier, P.R. Thies, C. Dormenval, B. Wray, R. Parkinson and L. Johanning. *Anchor loads for shallow water mooring of a 15 MW floating wind turbine — Part I: Chain catenary moorings for single and shared anchor scenarios*. Ocean Engineering, 266, 111816, 2022. . URL http://dx.doi.org/10.1016/j.oceaneng.2022.111816.
17. **Queipo et al.**, **2005**. Nestor V. Queipo, Raphael T. Haftka, Wei Shyy, Tushar Goel, Rajkumar Vaidyanathan and P. Kevin Tucker. *Surrogate-based analysis and optimization*. Progress in Aerospace Sciences, 41 (1), 1–28, 2005. ISSN 0376-0421. . URL https://www.sciencedirect.com/science/article/pii/S0376042105000102.
18. **Samui**, **01 2011**. Pijush Samui. *Prediction of pile bearing capacity using support vector machine*. International Journal of Geotechnical Engineering, 5, 95–102, 2011. .
19. **Samui et al.**, **06 2008**. Pijush Samui, Sitharam Thallak and Pradeep Kurup. *OCR Prediction Using Support Vector Machine Based on Piezocone Data*. Journal of Geotechnical and Geoenvironmental Engineering - J GEOTECH GEOENVIRON ENG, 134, 894–898, 2008. .
20. **Zhao et al.**, **2019**. L. Zhao, C. Gaudin, C. D. O'Loughlin, J. P. Hambleton, M. J. Cassidy and M. Herduin. *Drained Capacity of a Suction Caisson in Sand under Inclined Loading*. Journal of Geotechnical and Geoenvironmental Engineering, 145(2), 04018107, 2019.

Part III

Concluding Remarks

4 Summary of Articles

In the following chapter, a concise summary of the three articles is presented, highlighting their main findings. The primary objective is to provide readers with the necessary understanding to engage with the subsequent thesis discussion and conclusion.

4.1 Article 1: Chain-Soil Interactions in Cohesionless Soil Under Static Loads with CPT Interpretation

Article 1 investigated methods by Neubecker and Randolph [1995], Lee et al. [2014] and Mortensen [2015] to estimate chain-soil interactions. This includes the chain configuration, the load reduction and the change in loading angle from the mudline to the padeye of the anchor. Each method was combined with different CPT interpretation methods, namely Jamiolkowski et al. [2003] and Baldi et al. [1986] with either a depth varying lateral earth pressure coefficient ($K_0(z)$) or with a constant value ($K_0 = 1$). This was done to establish a combined method for practical implications. The combined methods were evaluated with respect to the results of a large-scale suction anchor experiment conducted in Frederikshavn, Denmark. Two tests were performed using a chain as a mooring line. The mooring lines were pulled with a hydraulic jack such that the chain configuration, load at padeye and change in loading angle could be determined.

4.1.1 Main Findings

Neubecker and Randolph [1995] and Mortensen [2015] were found to provide reasonable results compared to the large-scale test results. Both methods seemed to capture the load reduction and change in loading angle dependent on the CPT interpretation method used. The chain configuration was also estimated with some precision. Figure 4.1-4.2 presents the results of Neubecker and Randolph [1995] and Mortensen [2015] where the approaches have been combined with four different CPT methods. Figure 4.1 illustrates the methods' ability to estimate the chain configuration in comparison to the large-scale results.

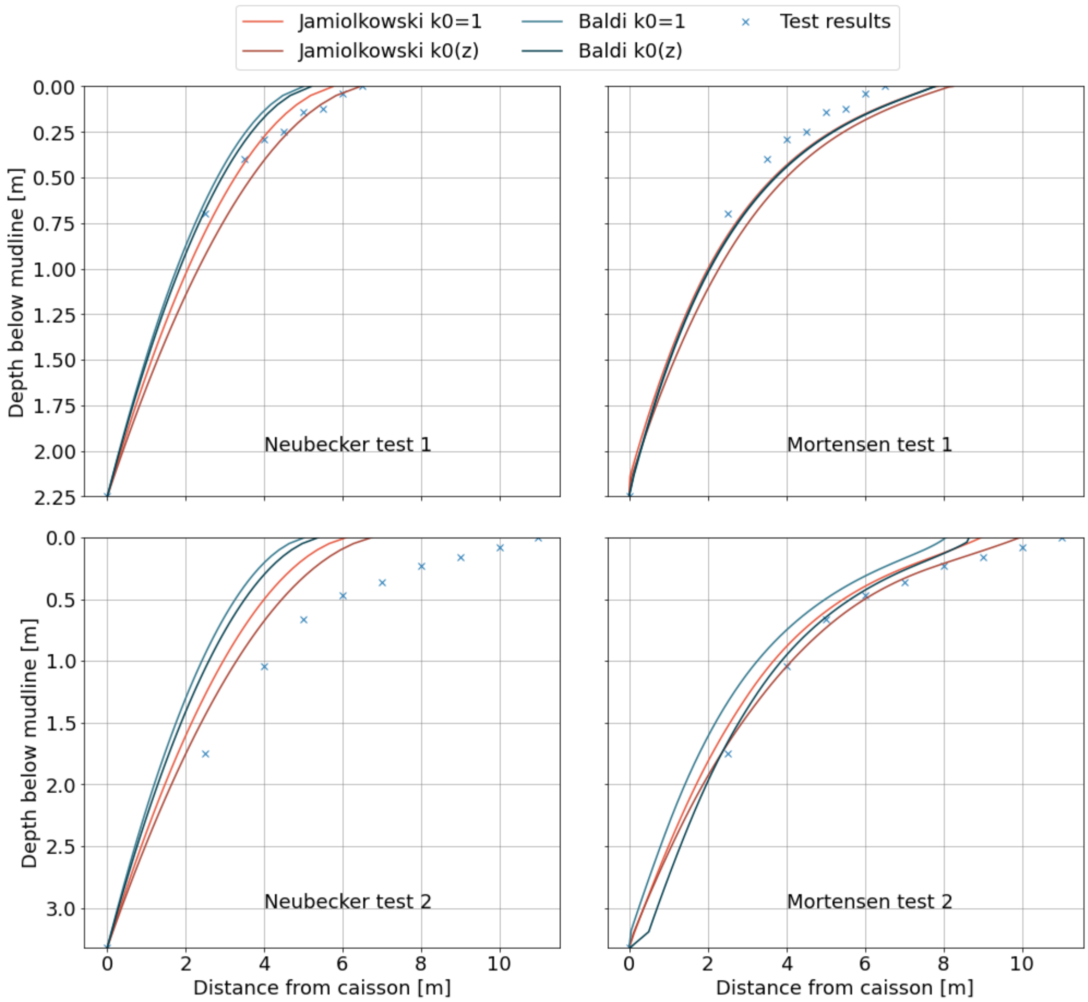

Figure 4.1. Neubecker and Randolph [1995] and Mortensen [2015] estimation of chain configuration compared to large-scale test results.

Figure 4.2 shows the determined load reduction (left) and the angle at padeye (right) also compared with the large-scale results. Even though both Neubecker and Randolph [1995] and Mortensen [2015] were deemed acceptable, the approach by Mortensen [2015] was recommended due to its ability to estimate the loading angle with a certain level of accuracy slightly higher than Neubecker and Randolph [1995].

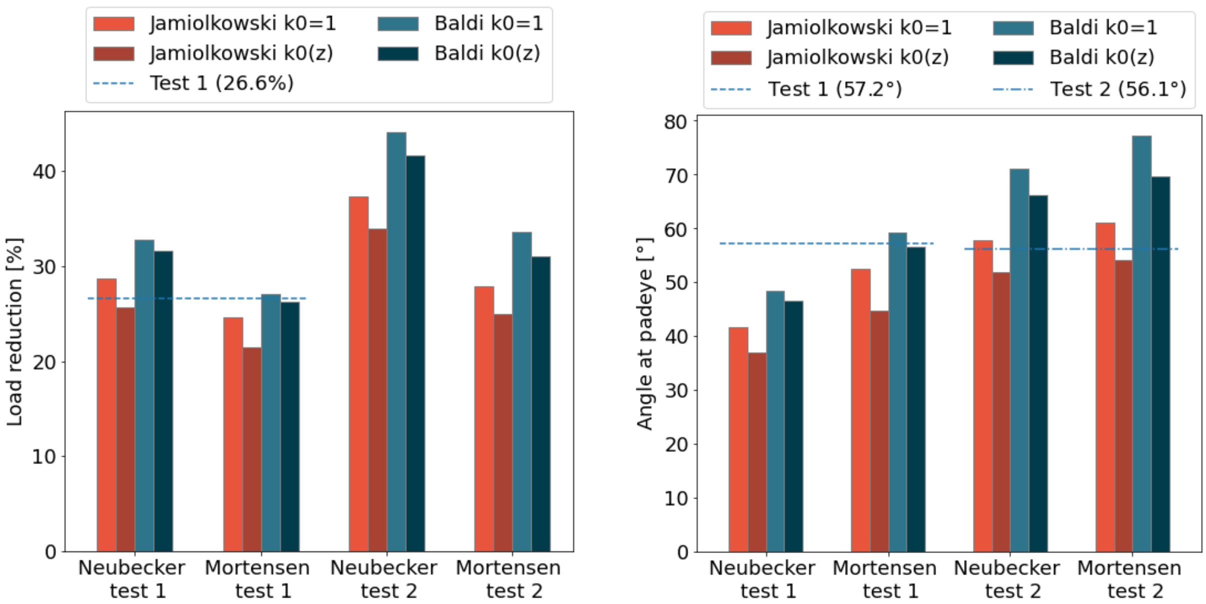

Figure 4.2. Neubecker and Randolph [1995] and Mortensen [2015] estimation of load reduction (left) and the angle at padeye (right) compared to large-scale test results.

Figure 4.3 presents a sensitivity study performed on the parameters used in the approach by Mortensen [2015]; tension at mudline (T_{mud}), angle at mudline (α_{mud}), friction angle (φ), unit weight (γ'), empirical parameter (A_{sand}) and friction coefficient (α_{sand}). The analysis revealed that the fiction angle has a large impact on the load reduction and loading angle. A small increase in friction angle resulted in a large increase in both results where a higher order effect is observed. Furthermore, it was found that the force at the mudline had the opposite effect as an increase in load resulted in a decrease of both load reduction and change in angle.

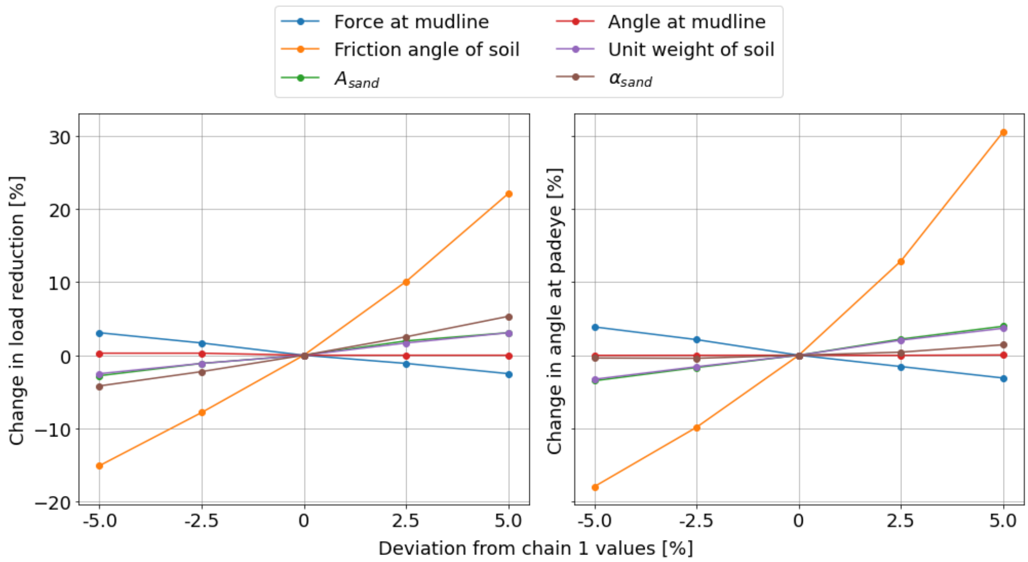

Figure 4.3. The results of the sensitivity analysis of the input parameters of the method derived by Mortensen [2015] for the load reduction and the angle at padeye.

4.2 Article 2: Modelling the Drained Capacity of Inclined Loaded Suction Caisson Anchors in Cohesionless Soil: A Finite Element Study

The second article presented a finite element study using PLAXIS 3D with a focus on different modelling techniques and soil parameters and how these would affect the bearing capacity of the anchor for different load inclinations (0°, 22 5°, 45°, 67 5°, 90°) at each padeye position on the anchor ($0.05L$, $0.25L$, $0.50L$, $0.75L$, $0.95L$).

The study found that modelling the self-weight of the anchor is necessary during the calculations, as this affects the displacement field and thereby the failure mechanisms. Consequently, the study found that modelling the anchor as a rigid body with a surface load accounting for the self-weight was sufficient.

In addition, the study considered two different material models: a Mohr-Coulomb model (MC) and a Hardening Soil model with small-strain stiffness (HSSmall). An insignificant difference was obtained using the different material models. As a result, using MC was used due to its simplicity in terms of calculations and the number of input parameters needed.

The study discovered that boundary effects were generally seen to have little effect on the pull-out force since comparing five different domain sizes showed no clear tendency on the results. Consequently, a domain size of ($\boldsymbol{X}$=$12D$, $\boldsymbol{Y}$=$6D$, $\boldsymbol{Z}$=$4L$) was found adequate.

The influence of meshing was investigated by conducting a mesh convergence for two load configurations. Generally, the pull-out force was found to decrease as the mesh coarseness decreased. Consequently, the study found that a normalised target element size ($\frac{DL}{l_e} = 3$) gave acceptable results.

The influence of the friction angle (φ), dilation angle (ψ), unit weight (γ'), lateral earth pressure coefficient (K_0) and interface reduction factor (R_{inter}) was examined and found to have a large influence on the results dependent on the load inclination and padeye position. In addition, the study that the stiffness parameters had little effect on the pull-out capacity. These results along with additional plots excluded from the article are presented in appendix B.

4.2.1 Main Findings

Figure 4.4 shows that the bearing capacity was highly sensitive to the loading type. It was found that a force-controlled procedure gave more reasonable results than a displacement-controlled procedure when compared to centrifuge tests conducted by Bang et al. [2009]. It was also found by comparing the different displacement fields in figure 4.5 that a force-controlled loading allows for more accurate displacement of the anchor. This is due to the anchor being able naturally to find the weakest failure mechanism while displacement-controlled loading restricts the anchor's movement.

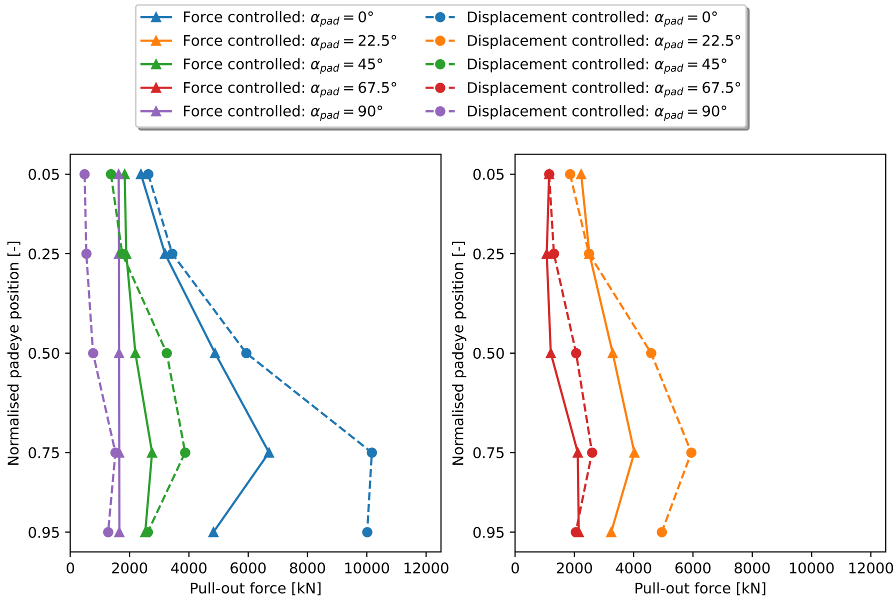

Figure 4.4. Results using force-controlled and displacement-controlled loading.

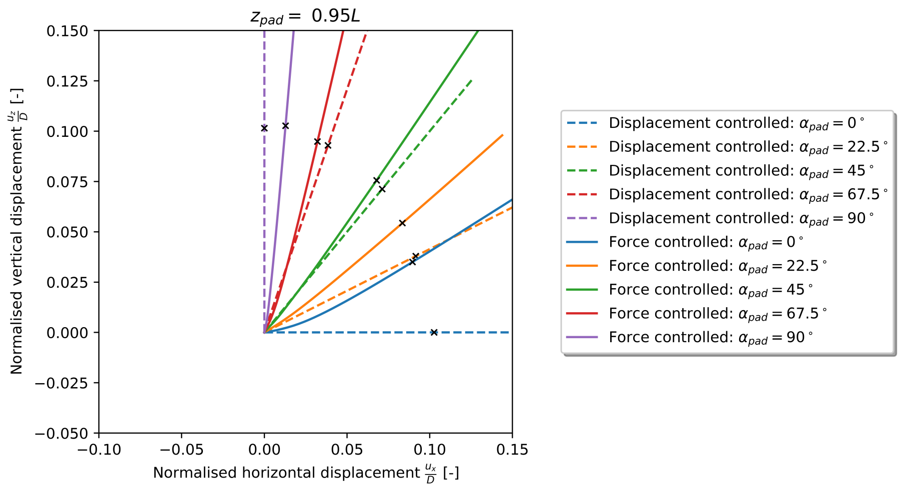

Figure 4.5. Displacement-field results with force-controlled and displacement-controlled loading for padeye position and $0.95L$.

Figure 4.6a-4.6h presents the incremental displacement (Δu_{tot}) at failure for different load configurations. Consequently, the plots illustrate how the padeye position (z_{pad}) and loading angle (α_{pad}) impact the failure mechanism of the anchor and thereby also the bearing capacity. Additional figures for the remaining load configurations are presented in B. In figure 4.6a-4.6d for padeye position (z_{pad}=0.05L) we see that for load inclinations from 0 to 45 degrees, the anchor rotates clockwise, mobilising both passive and active soil pressure. At load inclination ($\alpha_{pad} = 90°$) the anchor rotates counter-clockwise. As a result, for some intermediate load inclinations such as ($\alpha_{pad} = 67.5°$) the anchor experience little rotation and translated mostly vertically, mobilising a limited amount of soil pressure. In contrast, when the padeye position is a (z_{pad}=0.95L) the anchor rotates counter-clockwise for all load inclinations, where the point of rotation moves down as the load inclination increases.

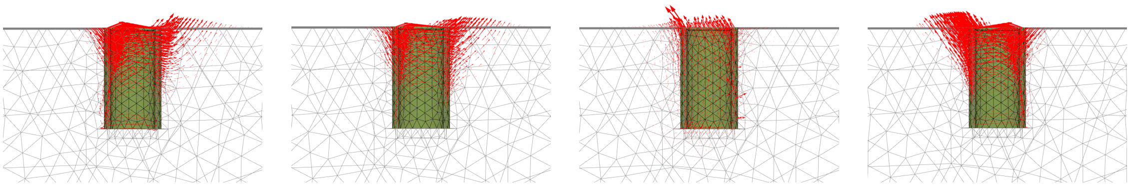

(a) $\alpha_{pad} = 0°$, $z_{pad} = 0.05L$. ***(b)*** $\alpha_{pad} = 45°$, $z_{pad} = 0.05L$. ***(c)*** $\alpha_{pad} = 67.5°$, $z_{pad} = 0.05L$. ***(d)*** $\alpha_{pad} = 90°$, $z_{pad} = 0.05L$.

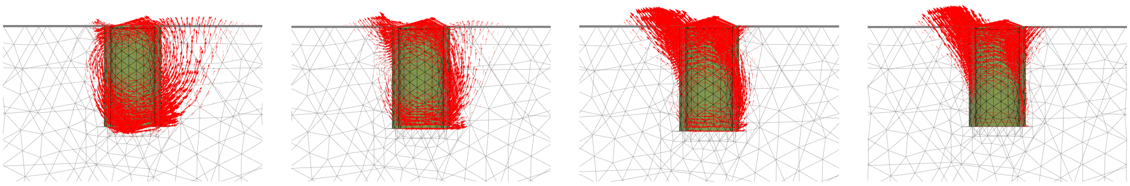

(e) $\alpha_{pad} = 0°$, $z_{pad} = 0.95L$. ***(f)*** $\alpha_{pad} = 45°$, $z_{pad} = 0.95L$. ***(g)*** $\alpha_{pad} = 67.5°$, $z_{pad} = 0.95L$. ***(h)*** $\alpha_{pad} = 90°$, $z_{pad} = 0.95L$.

Figure 4.6. Incremental displacement (Δu_{tot}) at normalised displacement ($\frac{u_{tot}}{D} = 0.1$) for different load configuration.

Soil parameters and model parameters; friction angle (φ), dilation angle (ψ), unit weight (γ'), lateral earth pressure coefficient (K_0) and interface reduction factor (R_{inter}) may have a large influence on the results. Their effect consequently depends on the failure mechanisms of the anchor whether a large soil volume is mobilised or if the skin friction dominates the bearing capacity in the case of vertical displacement. (K_0) and (R_{inter}) affects the interface strength between the anchor and the soil. Therefore, if the anchor experiences significant vertical load or displacement, these factors will have a large impact. The effect of the soil parameters, (φ), (ψ) and (γ') occurs opposite of (K_0) and (R_{inter}). This means that as more soil is mobilised, the impact of these parameters will increase accordingly.

4.3 Article 3: Surrogate-Based Optimisation of Suction Caisson Anchors with Embedded Mooring Chain

Article 3 established a combined solution to estimating the bearing capacity of the mooring system from the findings of the former two articles. The article utilised surrogate modelling to make an effective evaluation model and was thereby able to optimise the anchor design with respect to the steel volume. The surrogate models acquired are used to predict the loading angle at the padeye (α_{pad}), the load reduction of the embedded chain from the mudline to the padeye (ΔT) and the pull-out force (R_c) of the anchor. A range of values of soil, model and structural parameters are shown in table 4.1. These parameter intervals make up a design space for which the surrogate models are valid.

Table 4.1. Design space or range of parameters used to train the surrogate models.

Parameters	**Interval**	**Unit**
Load angle at mudline (α_{mud})	0 - 35	°
Tension at mudline (T_{mud})	2.5 - 14	MN
Friction angle (φ)	30 - 40	°
Unit weight (γ')	8 - 11	kN/m^3
Interface reduction factor (R_{inter})	0.5 - 0.8	-
Diameter of anchor (D)	3 - 5	m
Aspect ratio (λ)	1 - 5	-
Normalised padeye position (z_{pad})	0 - 1	-

The surrogate models were created using the training sets presented in appendix C. The training data was obtained from the chain-soil interaction approach by Mortensen [2015] and by a numerical model of the anchor in PLAXIS 3D. The performance of the surrogate models was subsequently tested against validation sets acquired in the same manner as the training sets. This is shown in figure 4.7 - 4.9 which also presents the coefficient of determination (R^2), the mean value (μ), and the standard deviation (σ) of the error between the validation data and predictions.

The coefficient of determination is between 0.95 and 0.99 for all three surrogate models. Furthermore, the mean value of the error and the standard deviation is generally quite low. However, it is noticeable that the standard deviation on the prediction of the pull-out force is relatively large. This is due to the regression method used for training the model where a margin of error (ε) is chosen. Overall the analysis indicates a satisfactory accuracy of the predictions with respect to the validations sets.

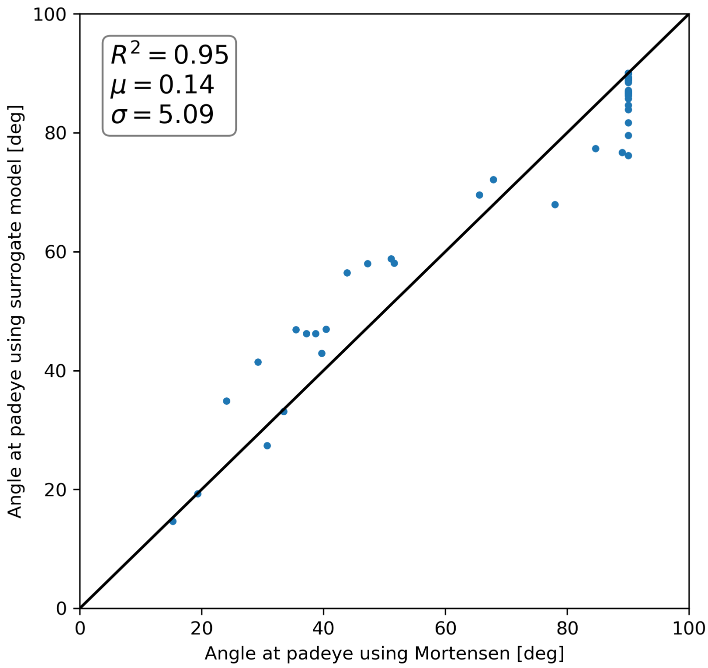

Figure 4.7. Comparison between Mortensen [2015] and surrogate model for the prediction of the angle at padeye (α_{pad}).

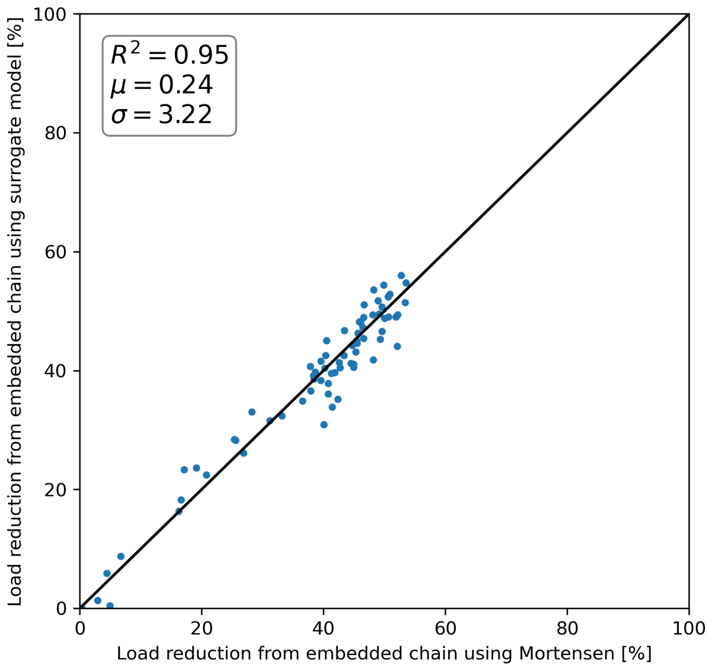

Figure 4.8. Comparison between Mortensen [2015] and surrogate model for the prediction of the load reduction (ΔT) from the embedded chain.

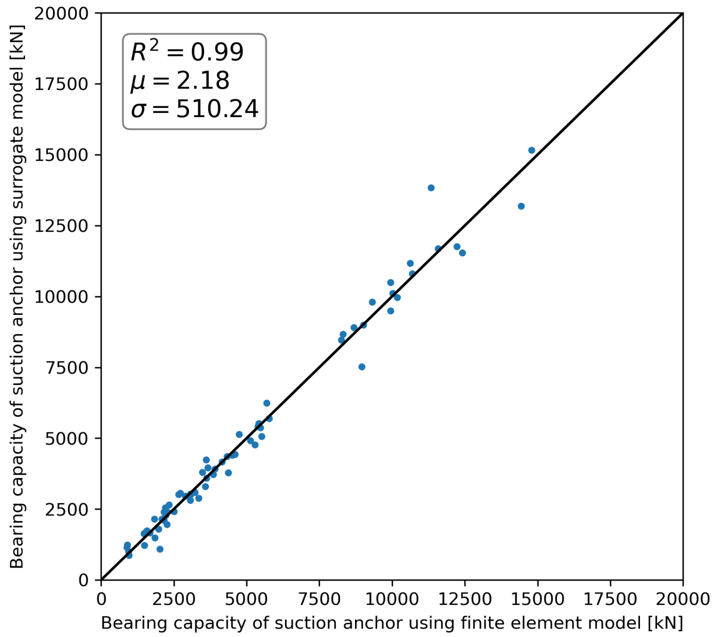

Figure 4.9. Comparison between finite element results and surrogate model for the prediction pull-out force (R_c).

The optimisation of the anchor was performed for 50,000 Monte Carlo simulations where the diameter (D), skirt length (L) and padeye position (z_{pad}) were optimised for each simulation.

4.3.1 Main Findings

It was concluded that by combining surrogate modelling with an optimisation procedure it was possible to efficiently determine general trends with respect to designing a suction caisson anchor.

Figure 4.10 shows violin plots of the optimisation results. When optimising with respect to the material consumption of the anchor it is reckoned that the diameter (D) should be minimised. The aspect ratio (λ), and thereby the skirt length (L) must be increased accordingly to obtain the required bearing capacity. The optimisation thus results in slender anchors and it is found that the padeye, in this case, should be located between $0.0L$ and $0.25L$.

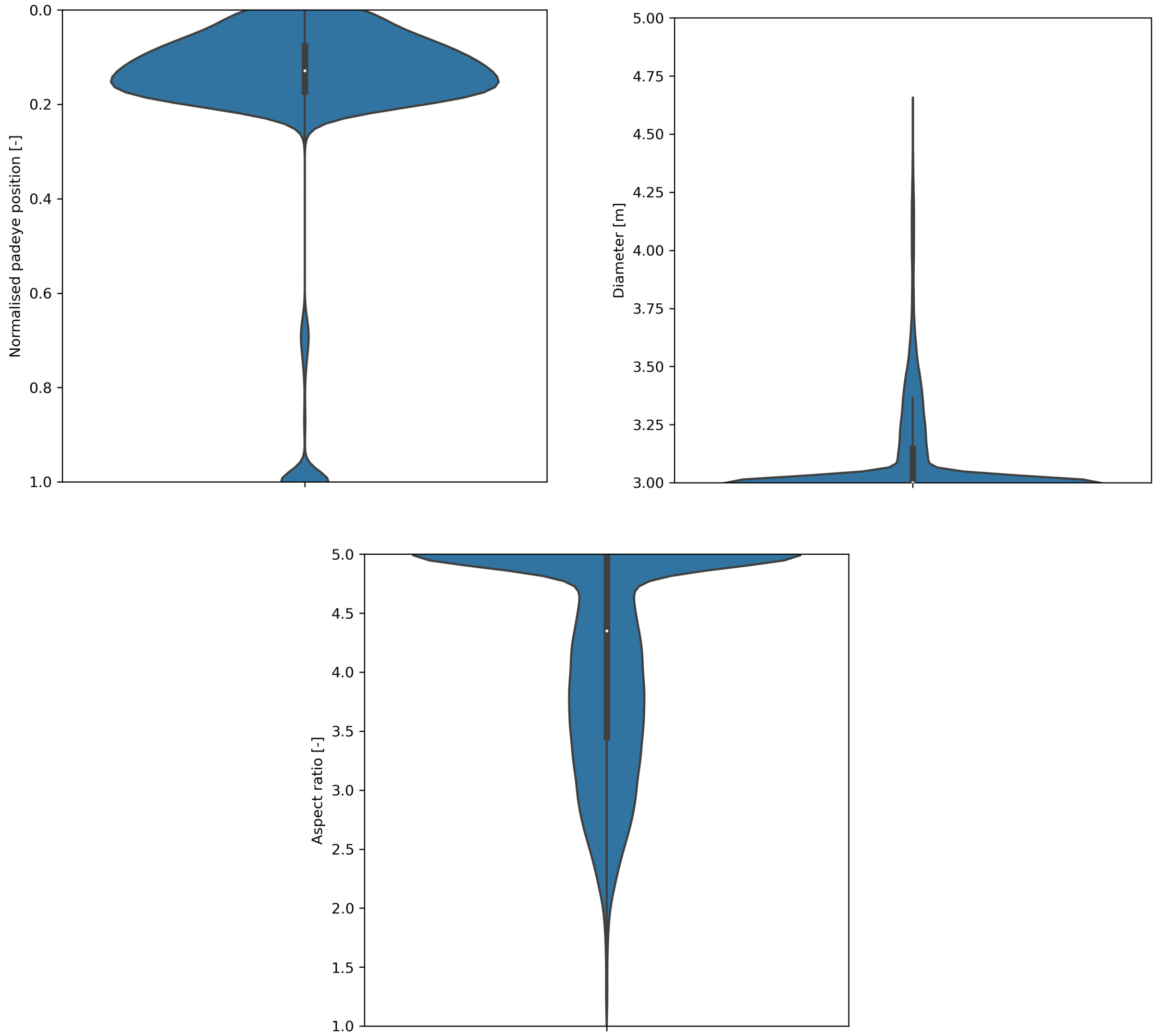

Figure 4.10. Violin plots of the optimised anchor from optimisation procedure.

5 Discussion and Future Work

The following sections present a discussion of the reliability of the results obtained in the thesis. The usability of the surrogate models is intricately tied to the decisions made regarding the numerical model and chain-soil interactions. To commence, the subsequent section discusses general aspects of surrogate modelling, where the following sections discuss the numerical model and the chain-soil interactions in relation to their effects on the surrogate models. Furthermore, the optimisation process is discussed. Lastly, based on the conducted studies, recommendations for future work are presented.

5.1 Surrogate Modelling

This thesis employs surrogate modelling as a method to evaluate and optimise the suction caisson anchor design with respect to minimising material consumption. A surrogate model is a technique used when a result of interest is complex and/or expensive to analyse, and a model of the outcome is utilised instead. The surrogate model is an approximation model that predicts the response of the high-fidelity model used, where the physical understanding of the parameters is removed. The feasibility of the surrogate model is highly dependent on the training data, such as the amount of data, the distribution of the data over the design space, and the complexity of the response from the high-fidelity model.

For a high-fidelity model that has a complex response with abrupt variations, it becomes necessary to gather an increased amount of data in these specific regions of the design space. This additional data is crucial for the surrogate model to effectively capture and reproduce such trends. The surrogate models employed in this thesis rely on training sets consisting of 330 responses, evenly distributed throughout the design space, and are validated using a data set comprising 72 responses. Conducting an analysis to determine if the amount of data is adequate and if there exist regions within the design space that are not adequately represented would enhance the reliability of the model.

The chosen design space for the surrogate models can be viewed as a limitation on the overall model. It is important to note that extrapolating the model beyond its design space is not advised. While the chosen design space serves as a practical framework for capturing the essential characteristics of the system, extrapolating may lead to unreliable predictions. Therefore, it is crucial to ensure that any conclusions drawn from the model remain within the bounds of the established design space.

5.2 Chain-Soil Interaction

This thesis investigates padeye positions at great depths. However, the chain-soil interaction method applied for the optimisation of the anchor is validated for relatively small loads and shallow padeye locations. It is therefore uncertain how well the approach performs in the design spaces examined. The chain-soil interaction method by Mortensen [2015] considers the chain to be calculated as a strip footing. However, the corresponding assumption of fully developed shear failure is not valid for all depths. For this failure mechanism to be mobilised it requires that the chain is pressed normally to the soil. A large part of the chain is assumed to be located near the mudline and develop close to horizontal. In this case, the chain is dragged parallel to the soil. The same applies in the case where the chain develops vertically along the caisson skirt, thus general shear failure does not occur. Figure 5.1 illustrates the area of the chain development where the assumption regarding the failure mechanism presumably is most accurate. Here the chain is pressed almost normally to the soil allowing for a general shear failure mechanism.

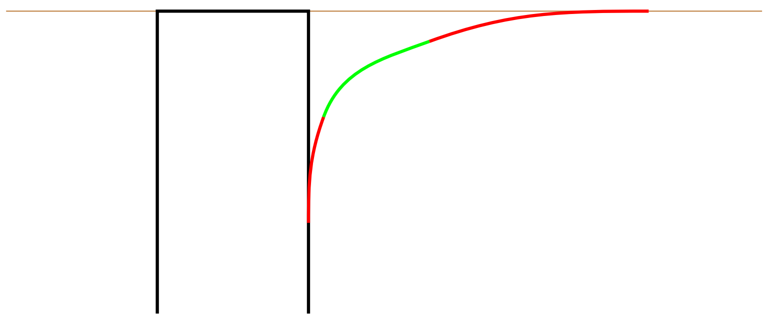

Figure 5.1. Illustration of the mooring chain part (green) where the assumption of fully developed general shear failure may hold true.

5.3 Numerical Modelling

As previously mentioned, a surrogate model merely attempts to predict the response of a more advanced model. As a result, the surrogate model used for the prediction of the pull-out capacity of the anchor includes all errors and biases present in the finite element models it is based upon.

Notably, some bias may have been introduced to the surrogate model as the finite element models were built using concepts based on a single anchor geometry. As illustrated in figure 5.2a and 5.2b, since the domain size is defined in terms of the anchor geometry as ($\boldsymbol{X}$=12D, $\boldsymbol{Y}$=6D, $\boldsymbol{Z}$=4L) different aspect ratios result in very different model domains. Consequently, the boundaries may affect the results differently. In addition, as the mesh was based on a normalised target element size ($\frac{DL}{l_e} = 3$) when the aspect ratio increased the element sizes decreased. As a result, results be overestimated for high aspect ratio models, as a coarser mesh generally predicts larger capacities.

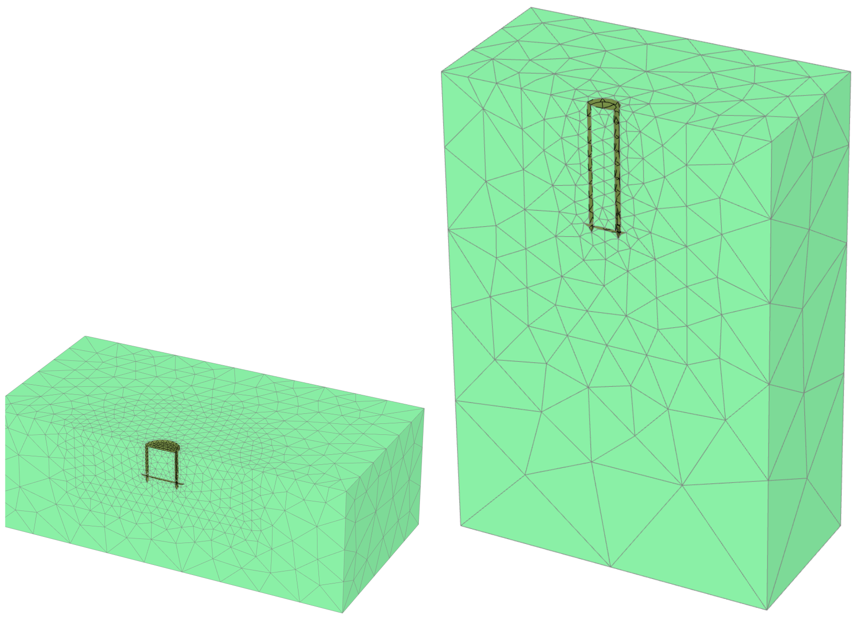

(a) Mesh used for an anchor with a aspect ratio ($\lambda = 1.03$).

(b) Mesh used for an anchor with a aspect ratio ($\lambda = 4.38$).

The finite element model of the anchor was compared to pull-out capacities from centrifuge tests performed by Bang et al. [2009]. The centrifuge tests yielded a wide spread in pull-out capacities for the same padeye positions and loading angles, thus not giving an accurate result. However, if stress/strain curves had been provided by the literature, these could have been compared to the numerical model and a possible cause of the variation assessed. Consequently, all of the uncertainties in regard to the finite element results are transferred to the surrogate model and the following optimisation results.

5.4 Optimisation of the Anchor by Considering the Chain Interaction

The design of the suction caisson anchor was in this thesis optimised in relation to the material consumption. It is in this regard evident that the steel volume depends on the diameter (D) squared, while it is linearly dependent on the skirt length (L). Consequently, this leads to the conclusion that slender anchors with small diameters (D) and high aspect ratios (λ) are preferred.

To optimise the bearing capacity of the anchor it is desirable to minimise rotation and vertical movement due to the anchor naturally mobilising larger soil volumes for horizontal translation. However, the displacement of the anchor is significantly affected by the load configuration and the padeye position.

The chain-soil interactions result in an increase in load inclination and a load reduction from the mudline to the padeye. In contrast, the pull-out force of the anchor decreases for large loading angles. Consequently, the padeye position of the anchor must depend on, if the load reduction from the chain-soil interaction with depth increases more than the anchor capacity decreases. In the optimisation procedure of the anchor, it was found reasonable to terminate the calculation of load reduction when the load inclination became 90°. This was done due to the violation of assumptions in the approach as discussed previously. Therefore, the mooring system would not benefit from placing the padeye at greater depths where the loading angle became 90°. Furthermore, the numerical analysis reckoned that the padeye position has no impact when the loading angle is 90°.

The literature examined in this thesis focused on exploring the optimal padeye position (z_{pad}) to achieve the highest bearing capacity. However, this study investigated the combination of padeye position (z_{pad}), anchor diameter (D) and aspect ratio (λ) that gives the lowest material consumption of the anchor. Consequently, this leads to contrasting conclusions regarding anchor design compared to the findings reported in the reviewed literature. For example, according to Cheng et al. [2021], the optimal padeye position (z_{pad}) was determined to be at a depth of 0.6 times to 0.7 times the length (L) of the anchor, assuming a loading angle at the padeye (α_{pad}) of 30°. In contrast, this thesis concludes that the padeye (z_{pad}) should be positioned within the range of 0 to 0.25 times the length (L) of the anchor, depending on the specific load configuration and soil conditions.

5.5 Future Work

The approach by Mortensen [2015] was assessed to give the best estimate of the chain-soil interaction and was therefore implemented in the material optimisation. The load investigated in the optimisation was significantly higher than for the large-scale tests, and thereby an analysis of how the method performs when it is scaled could be interesting. This could be done by implementing FE methods such as the Coupled Eulerian-Lagrangian (CEL) formulation, which is a numerical technique used to simulate the behaviour of materials subjected to large deformations.

The mooring line was investigated as a chain for this thesis. Alternative options such as a wire are also commonly used and could be analysed. This would mean that the optimal design would not only be based on the size of the caisson and the padeye position but also on the type of the mooring line.

The loads considered for the material optimisation of the suction caisson were determined for an anchoring system where only one anchor should resist the load and one mooring line is attached to the anchor. Different designs of the mooring system, such as more anchors in the primary loading direction or multi-line anchors, could reduce the load on the anchor. Investigations with these load conditions could improve the insight into the optimal anchoring system.

The material optimisation of the suction caisson showed that high aspect ratios of the anchor are optimal. Issues regarding the installation of the suction anchors, such as buckling, liquefaction, piping, or cavitation, are probably the limiting factors for this anchor design. The optimisation procedure could consider these phenomena to improve the feasibility of the design. Surrogate models were used to effectively capture the response of the angle at the padeye, load reduction, and bearing capacity of the caisson. A third-degree polynomial regression was employed for the angle at the padeye and load reduction, where a support vector regression with a radial basis function kernel was used for the bearing capacity of the caisson. Several other predictive modelling techniques are also available, and conducting an analysis to determine the optimal approach under these specific conditions would enhance the reliability of the optimisation process.

Conclusion 6

This thesis has been conducted with the purpose to provide insight into the geotechnical design of suction caisson anchors and embedded mooring chains for Floating Offshore Wind Turbines (FOWTs). The three questions stated below have served as a basis for three individual articles giving perspective on different aspects of the topic:

1. Which methods can be recommended for determining the embedded chain interactions and what parameters affect the load reduction and angle at padeye?
2. How can the pull-out capacity of a suction anchor be modelled using finite element analysis and what parameters affect the pull-out capacity dependent on the load configuration?
3. How can the combined bearing capacity of a suction anchor and the embedded chain be optimised efficiently and what are general tendencies in terms of an optimised design of a suction anchor?

To estimate the chain-soil interactions, three approaches were employed: Neubecker and Randolph [1995], Lee et al. [2014], and Mortensen [2015]. While the method proposed by Lee et al. [2014] did not adequately predict the load reduction, neither methods proposed by Neubecker and Randolph [1995] nor Mortensen [2015] yielded a conclusive answer on which method is most recommendable. In evaluating the chain configuration, load reduction, and the increase in loading angle from the mudline to the padeye, Mortensen [2015] method estimated reasonable results compared to the large-scale tests. Comparatively, Mortensen [2015] approach provided slightly better results than Neubecker and Randolph [1995], particularly in accurately determining the angles at the padeye. The sensitivity study highlighted that the most significant factor influencing the results was the friction angle.

The static bearing capacity of an inclined loaded suction caisson anchor was modelled in PLAXIS 3D and was analysed by exploring two different loading techniques: displacement- and force-controlled loading. From the analysis, it is recommended to use force-controlled loading since displacement-controlled loading will result in an unexpectedly high bearing capacity. As, the anchor will not be restricted to moving in a specific direction when using force-controlled loading this provides the most accurate displacement field of the two loading techniques. The suction caisson can be modelled as a rigid body but the self-weight of the anchor influences the bearing capacity depending on the padeye position and the loading angle. It is therefore assessed that it should be considered in the numerical simulation by a surface load or by applying a material type to the rigid body where the self-weight can be included.

The pull-out force of the anchor is influenced by several parameters. The observed effects are attributed to various failure mechanisms, which are dependent on the padeye position and load angle. Soil parameters, such as the interface reduction factor (R_{inter}) and the dilation angle (ψ), have a significant impact on the results and should be selected carefully considering the loading conditions, as their influence is significantly dependent on these. The thesis concluded that the pull-out force is more sensitive to variations in the friction angle (φ), unit weight (γ'), and dilation angle (ψ) as the loading angle decreases. Conversely, the sensitivity of the pull-out force to changes in the interface reduction factor (R_{inter}) increases as the loading angle increases.

By utilising surrogate modelling it was possible to acquire an efficient model to evaluate the combined bearing capacity of the suction caisson anchor and the embedded chain. This model was then used to optimise the anchor design by minimising material consumption. When optimising the anchor with respect to steel volume, the analyses show that increasing the skirt length is more beneficial than increasing the diameter.

When considering the embedded chain, it has been shown, that the loading angle increases rapidly with depth to a constant value of 90°. Furthermore, a load reduction from mudline to padeye occurs due to friction between the chain and the soil. The capacity of the anchor is largest for small loading angles. The optimal padeye position, therefore, depends on whether the load reduction from the embedded chain increases more with depth than the capacity of the anchor decreases. Previous knowledge of the mooring system expected lower load inclinations, hence the optimal padeye position was suggested to be between $0.6L$ - $0.7L$. Based on the evaluation of material consumption, it was determined in this thesis that having a padeye position at depths beyond 0.25 times the length (L) is not advantageous.

This thesis provides engineers with methods to optimise the anchor design considering the interaction effects with the mooring chain. By doing this, the overall structural integrity and load-bearing capacity can be enhanced. By considering the findings of this thesis it may help ensure stability, reliability and cost-effective solutions for the entire mooring system.

Bibliography

Ahmed and Hawlader, 2014. Sheikh Sharif Ahmed and Bipul Chandra Hawlader. *Finite Element Modeling of Inclined Load Capacity of Suction Caisson in Sand with Abaqus/Explicit.* All Days, 2014. ISOPE-I-14-191.

Baldi et al., 1986. G. Baldi, D. Bruzzi, S. Superbo, M. Battaglio and M. Jamiolkowski. *Refined Model for Interpreting Shallow Penetration CPTs in Sands.* Proceedings of the Fourth International Geotechnical Seminar, pages 143–156, 1986.

Bang et al., 07 2009. S. Bang, K.O. Kim, Y.S. Kim, Y. Cho, and K. Jones. *Centrifuge Model Tests On Suction Piles In Sand Under Inclined Loading.* International Ocean and Polar Engineering Conference, All Days, 148, 2009.

BP, 2022. BP. *bp Statistical Review of World Energy 2021*, 2022.

BP, 2023. BP. *bp Energy Outlook 2023*, 2023.

Cheng et al., 2021. L. Cheng, M.S. Hossain, Y. Hu, Y.H. Kim and S.N. Ullah. *Failure envelope of suction caisson anchors subjected to combined loadings in sand.* Applied Ocean Research, 114, 102801, 2021. ISSN 0141-1187. doi: https://doi.org/10.1016/j.apor.2021.102801. URL `https://www.sciencedirect.com/science/article/pii/S0141118721002765`.

DNVGL-RP-E303, 2017. DNVGL-RP-E303. *Recommended practice - DNVGL-RP-E303*, 2017.

Durakovic, Mar 2022. Adnan Durakovic. *Fixed, Floating, or Both? Major Offshore Wind Project Weighing Options*, 2022. URL `https://www.offshorewind.biz/2022/03/07/fixed-floating-or-both-major-offshore-wind-project-weighing-options/`.

Dutta and Degenkamp, 05 1989. A. Dutta and G. Degenkamp. *Behaviour of Embedded Mooring Chains in Clay During Chain Tensioning.* All Days, 1989. doi: 10.4043/6031-MS. URL `https://doi.org/10.4043/6031-MS`. OTC-6031-MS.

Equinor, 2022. Equinor. *Floating wind*, 2022. URL `https://www.equinor.com/energy/floating-wind`. Accessed: 2023-06-08.

Executive, 2018. The Maritime Executive. *Vryhof Contributes Mooring System for Kincardine Wind Farm*, 2018. URL https://maritime-executive.com/corporate/vryhof-contributes-mooring-system-for-kincardine-wind-farm. Accessed: 2023-06-08.

Jamiolkowski et al., 2003. M. Jamiolkowski, D. C. F. Lo Presti and M. Manassero. *Evaluation of Relative Density and Shear Strength of Sands from CPT and DMT*. pages 201–238, 2003.

Lee et al., 2014. Hoonyoung Lee, Dong-Soo kim and Yun Wook Choo. *Profile and Frictional Capacity of a Mooring Line Embedded in Sand via Centrifuge Model Testing*. Journal of Geotechnical and Geoenvironmental Engineering, 140(11), 04014059, 2014.

Mark Randolph, 2011. Susan Gourvenec & David White Mark Randolph. *Offshore Geotechnical Engineering*. Taylor & Francis Ltd, 2011. ISBN 9780415477444.

Mortensen, 2015. N. Mortensen. *Chain configuration in sand, theory and large scale field testing*. Frontiers in Offshore Geotechnics III : Proceedings of the 3rd International Symposium on Frontiers in Offshore Geotechnics (ISFOG 2015), 1, 905–912, 2015.

Neubecker and Randolph, 1995. S. R. Neubecker and M. F. Randolph. *Profile and Frictional Capacity of Embedded Anchor Chains*. Journal of Geotechnical Engineering, 121(11), 797–803, 1995. doi: 10.1061/(ASCE)0733-9410(1995)121:11(797). URL https://ascelibrary.org/doi/abs/10.1061/.

NREL, 2022. NREL. *2021 Cost of Wind Energy Review*. 2022.

RWE, 2022. RWE. *Floating Offshore Wind*, 2022. URL https://www.rwe.com/en/research-and-development/wind-power/floating-offshore-wind/floating-wind-education. Accessed: 2023-06-08.

Tethys engineering, 2022. Tethys engineering. *Fixed Offshore Wind*, 2022. URL https://tethys.pnnl.gov/technology/fixed-offshore-wind. Accessed: 2023-06-08.

United Nations, 2022. United Nations. *What is renewable energy?*, 2022. URL https://www.un.org/en/climatechange/what-is-renewable-energy?gclid=CjwKCAjw4c-ZBhAEEiwAZ105RZO4Eqsq0oDHUH6YCBmS-O2jGLOdJvLGukCV_MhxWsuNytN-250_oRoCjlgQAvD_BwE. Accessed: 2023-06-08.

Vivatrat et al., 1982. Vitoon Vivatrat, Philip J. Valent and Albert A. Ponterio. *The Influence of Chain Friction on Anchor Pile Design*. OTC Offshore Technology Conference, All Days, 1982.

Yong Bai and Wei-Liang Jin, 2016. Yong Bai and Wei-Liang Jin. *Marine Structural Design second edition*. Joe Hayton, 2016. ISBN 9780080999975.

Zhao et al., 2019. L. Zhao, C. Gaudin, C. D. O'Loughlin, J. P. Hambleton, M. J. Cassidy and M. Herduin. *Drained Capacity of a Suction Caisson in Sand under Inclined Loading*. Journal of Geotechnical and Geoenvironmental Engineering, 145(2), 04018107, 2019. doi: 10.1061/(ASCE)GT.1943-5606.0001996. URL https://ascelibrary.org/doi/abs/10.1061/%28ASCE%29GT.1943-5606.0001996.

Part IV

Appendix

CPT Results A

This appendix shows the remaining Cone Penetration Test (CPT) results used in Article 1 that investigated the chain-soil interactions. This includes graphs of the interpretations but also tables with soil parameter values applied in the different embedded chain methods that were evaluated. Figure A.1 illustrates the position of the CPTs with respect to the anchors installed for the large-scale experiment in Frederikshavn, Denmark.

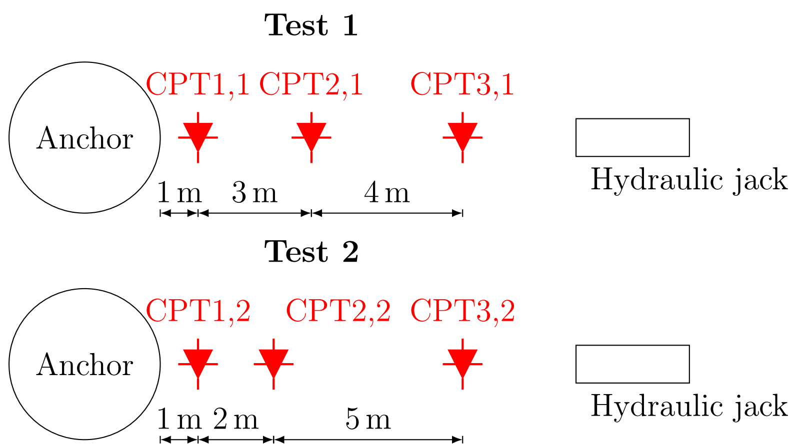

Figure A.1. A principle drawing of the two test setups seen from above, to show the distance of the CPTs from the caissons.

Figures A.2 - A.7 presents interpretations of (q_c), (D_r), (φ), (K_0) for all six CPTs.

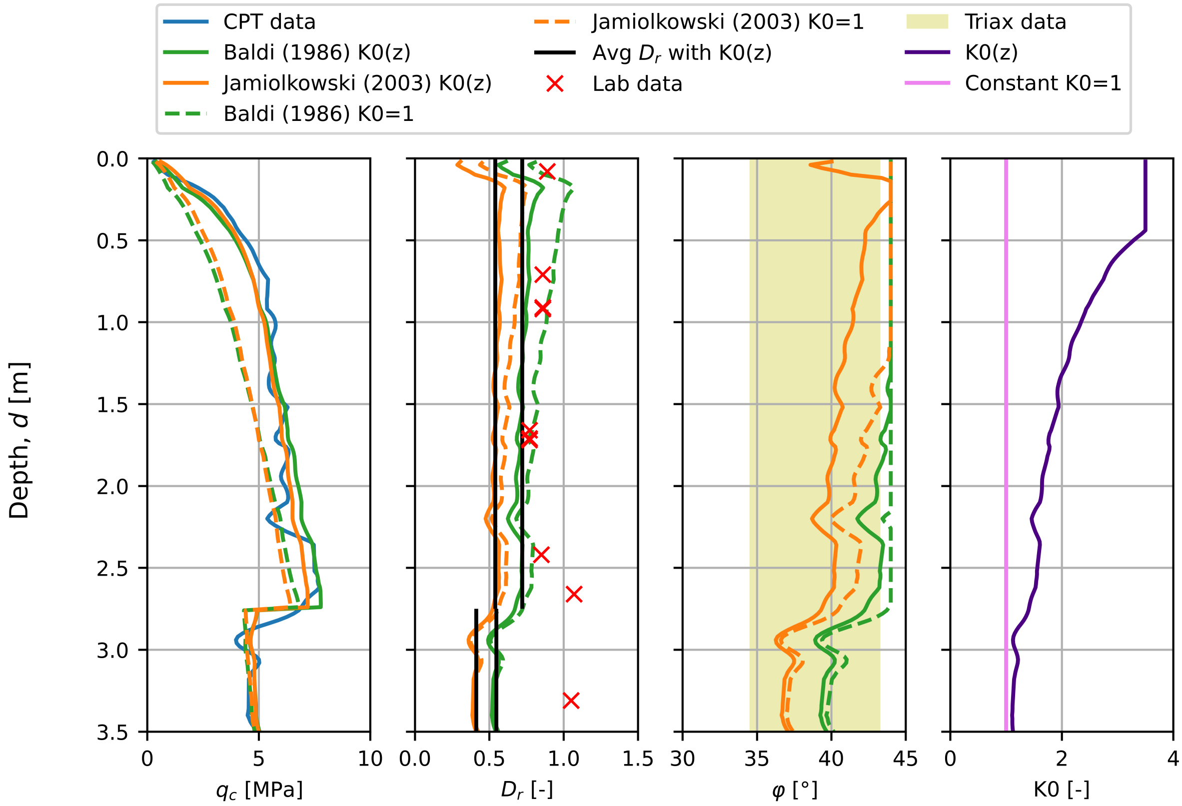

Figure A.2. Results of CPT 1,1

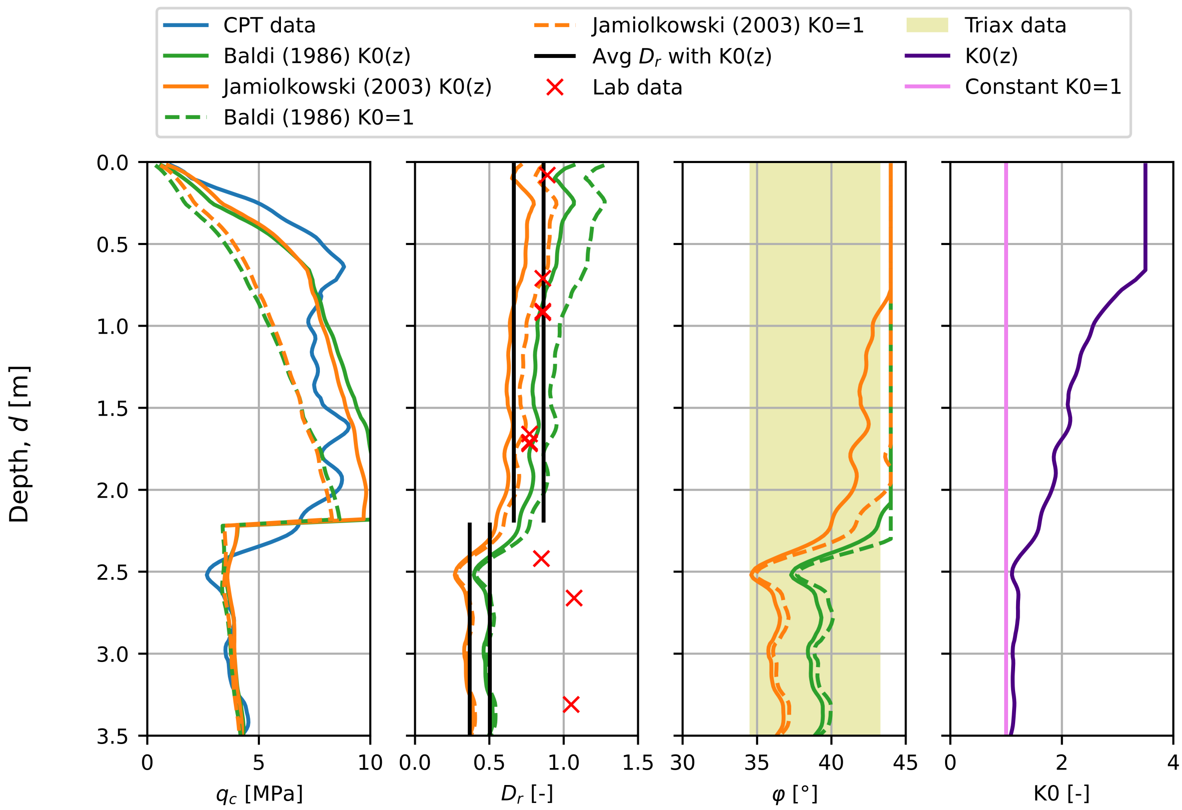

Figure A.3. Results of CPT 2,1

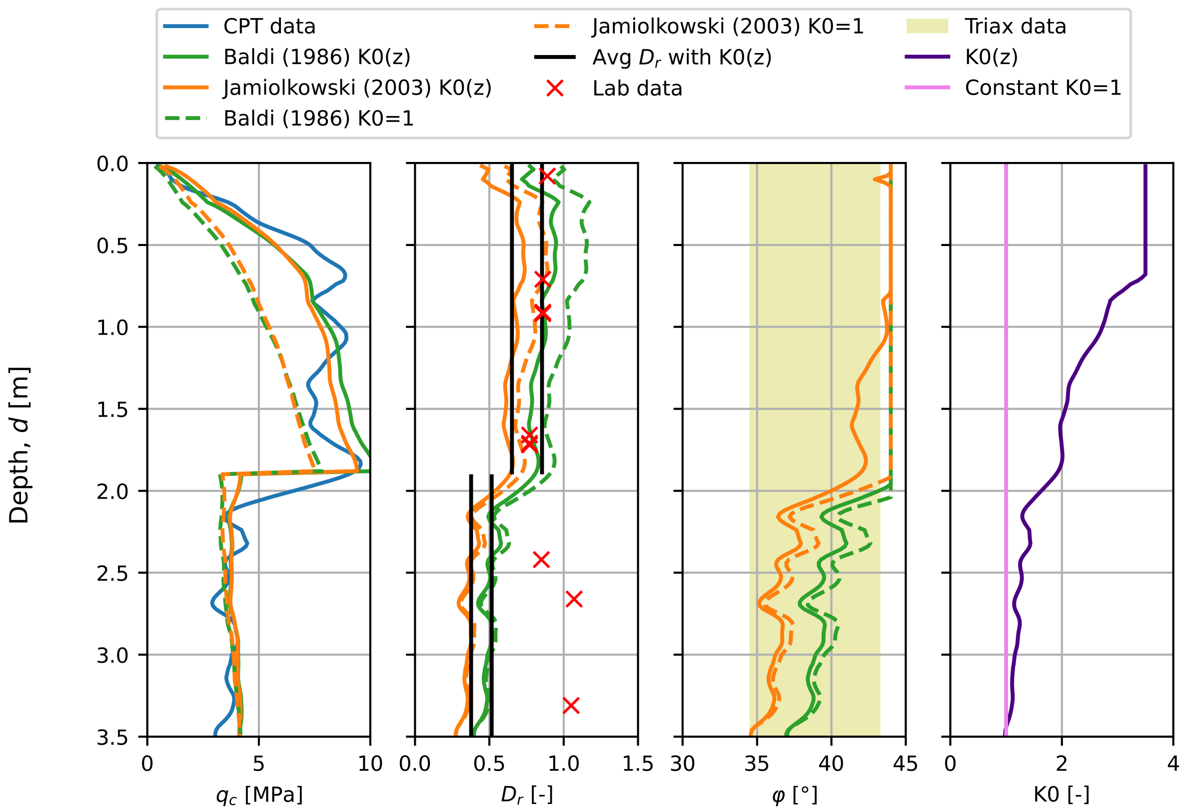

Figure A.4. Results of CPT 3,1

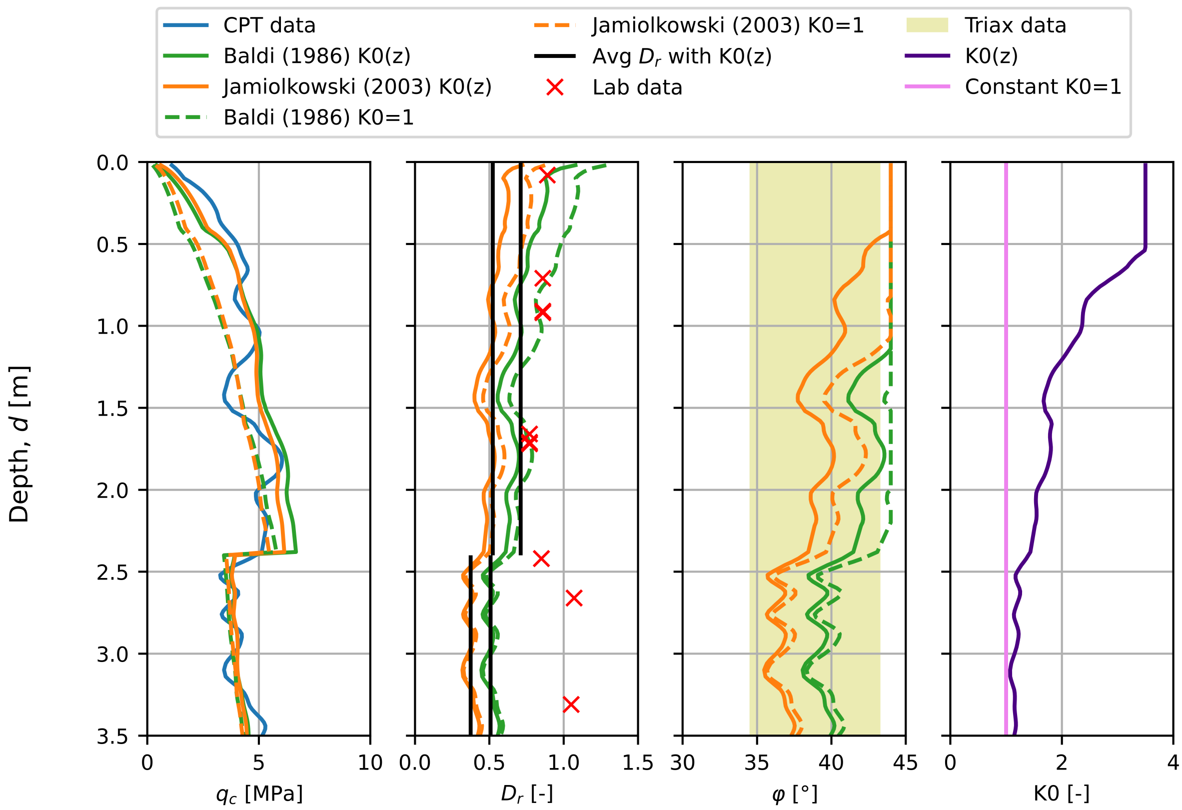

Figure A.5. Results of CPT 1,2

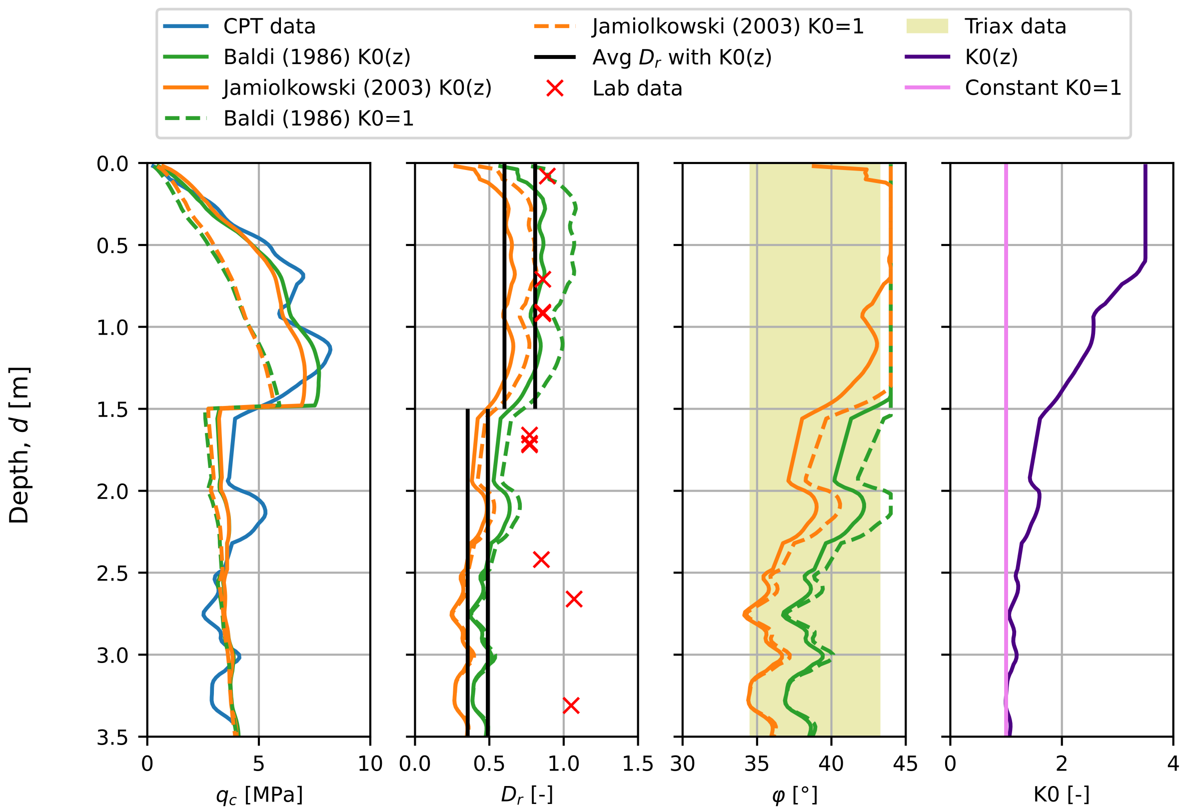

Figure A.6. Results of CPT 2,2

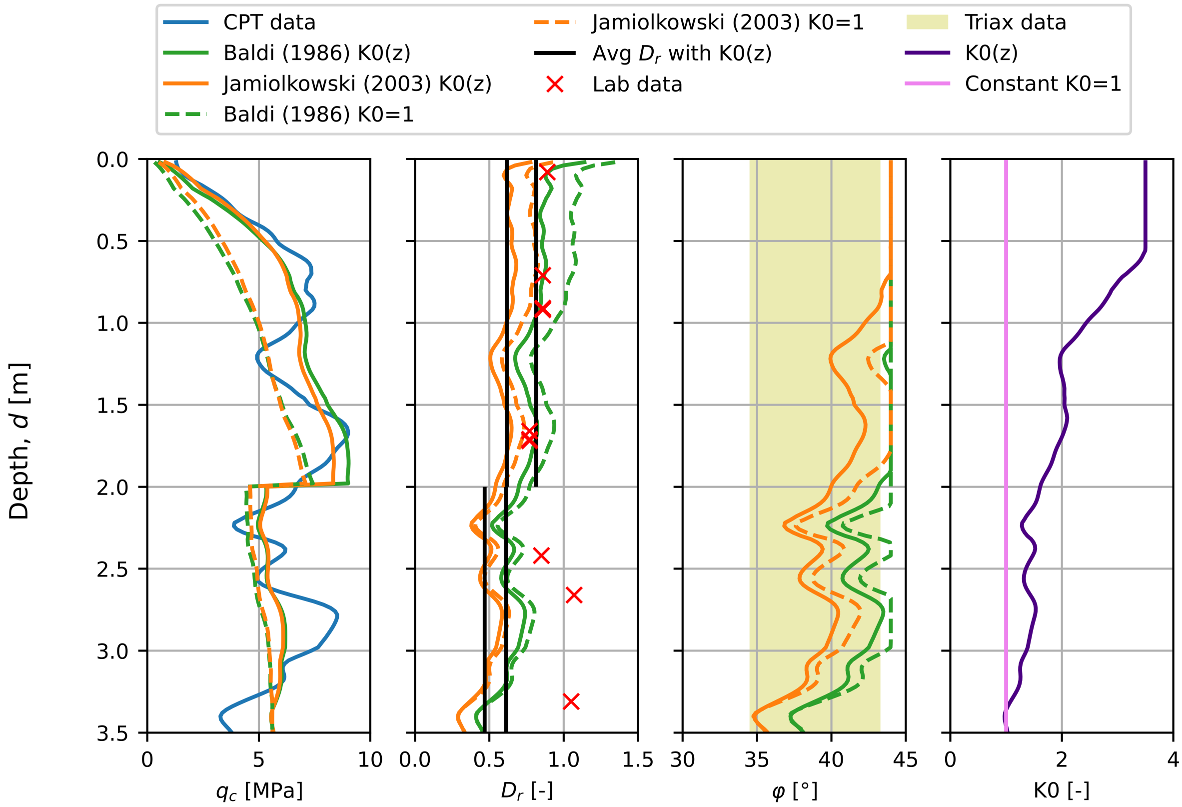

Figure A.7. Results of CPT 3,2

Table A.1 - A.5 presents all the soil parameters for the assessed methods.

Table A.1. The unit weight (γ') of the soil used for the chain-soil interaction methods.

Depth [m]	CPT 1,1 [kPa]	CPT 2,1 [kPa]	CPT 3,1 [kPa]	CPT 1,2 [kPa]	CPT 2,2 [kPa]	CPT 3,2 [kPa]
0.00-0.25	7.5	7.5	7.4	5.9	6.7	7.0
0.25-0.50	7.5	7.5	7.4	5.9	6.7	7.0
0.50-0.75	7.5	7.5	7.4	5.9	6.7	7.0
0.75-1.00	7.8	7.9	8.0	6.8	7.4	7.9
1.00-1.25	8.0	8.2	8.4	7.3	8.2	8.4
1.25-1.50	8.0	8.3	8.4	7.3	8.4	8.2
1.50-1.75	8.1	8.4	8.3	7.3	8.1	8.3
1.75-2.00	8.3	8.6	8.7	7.8	7.4	8.9
2.00-2.25	8.4	8.6	8.2	7.8	7.7	9.0
2.25-2.50	8.4	8.2	7.4	7.9	8.1	8.4
2.50-2.75	8.6	7.3	7.1	7.8	7.2	8.3
2.75-3.00	8.5	7.6	7.3	7.6	7.3	8.6
3.00-3.25	8.2	7.5	7.4	7.7	7.5	8.9
3.25-3.50	8.2	7.8	7.5	8.0	7.6	8.5
3.50-3.75	8.4	7.9	7.2	8.3	7.9	8.1
3.75-4.00	8.5	8.3	7.0	8.4	7.9	8.3

Table A.2. The friction angle (φ) determined by the use Jamiolkowski et al. [2003] with ($K_0(z)$).

Depth [m]	CPT 1,1 [°]	CPT 2,1 [°]	CPT 3,1 [°]	CPT 1,2 [°]	CPT 2,2 [°]	CPT 3,2 [°]
0.00-0.25	42.3	44.0	43.8	44.0	43.0	34.6
0.25-0.50	43.0	44.0	44.0	43.8	44.0	43.4
0.50-0.75	42.1	44.0	44.0	42.0	43.9	43.3
0.75-1.00	41.5	43.5	43.7	40.5	42.3	43.3
1.00-1.25	41.1	42.6	43.2	40.3	42.8	41.9
1.25-1.50	40.4	42.1	41.9	38.1	41.1	40.0
1.50-1.75	40.3	42.2	41.6	39.4	38.7	41.5
1.75-2.00	40.0	41.5	41.8	39.8	37.3	41.6
2.00-2.25	39.4	40.6	37.7	38.8	38.7	39.9
2.25-2.50	39.8	37.4	37.1	37.5	37.1	37.8
2.50-2.75	39.9	35.7	35.9	36.3	35.3	38.4
2.75-3.00	37.5	36.2	36.6	36.5	35.4	39.9
3.00-3.25	37.2	36.0	35.9	36.0	35.4	39.1
3.25-3.50	36.8	36.7	35.5	37.2	35.3	37.2
3.50-3.75	37.3	36.3	33.2	37.1	35.3	35.5
3.75-4.00	36.6	39.8	33.7	37.2	36.6	37.4

Table A.3. The friction angle (φ) determined by the use Jamiolkowski et al. [2003] with (K_0=1).

Depth [m]	CPT 1,1 [°]	CPT 2,1 [°]	CPT 3,1 [°]	CPT 1,2 [°]	CPT 2,2 [°]	CPT 3,2 [°]
0.00-0.25	44.0	44.0	44.0	44.0	44.0	38.9
0.25-0.50	44.0	44.0	44.0	44.0	44.0	44.0
0.50-0.75	44.0	44.0	44.0	44.0	44.0	44.0
0.75-1.00	44.0	44.0	44.0	43.9	44.0	44.0
1.00-1.25	43.9	44.0	44.0	43.2	44.0	43.9
1.25-1.50	43.0	44.0	44.0	40.1	43.5	42.4
1.50-1.75	42.5	44.0	44.0	41.5	40.5	43.8
1.75-2.00	42.0	43.9	43.7	41.8	38.6	43.7
2.00-2.25	40.9	42.5	38.8	40.3	40.1	41.5
2.25-2.50	41.4	38.4	38.0	38.4	38.0	38.7
2.50-2.75	41.3	36.2	36.5	36.8	35.7	39.4
2.75-3.00	38.2	36.7	37.2	37.0	35.7	41.2
3.00-3.25	37.7	36.3	36.3	36.3	35.6	40.0
3.25-3.50	37.1	37.1	35.7	37.6	35.4	37.6
3.50-3.75	37.7	36.5	33.0	37.5	35.2	35.5
3.75-4.00	36.7	40.8	33.5	37.4	36.7	37.8

Table A.4. The friction angle (φ) determined by the use Baldi et al. [1986] with ($K_0(z)$).

Depth [m]	CPT 1,1 [°]	CPT 2,1 [°]	CPT 3,1 [°]	CPT 1,2 [°]	CPT 2,2 [°]	CPT 3,2 [°]
0.00-0.25	44.0	44.0	44.0	44.0	44.0	39.9
0.25-0.50	44.0	44.0	44.0	44.0	44.0	44.0
0.50-0.75	44.0	44.0	44.0	44.0	44.0	44.0
0.75-1.00	44.0	44.0	44.0	44.0	44.0	44.0
1.00-1.25	44.0	44.0	44.0	43.7	44.0	44.0
1.25-1.50	43.9	44.0	44.0	41.6	43.9	43.5
1.50-1.75	43.6	44.0	44.0	42.8	42.0	44.0
1.75-2.00	43.3	44.0	44.0	43.1	40.4	44.0
2.00-2.25	42.5	43.6	40.8	42.0	41.8	43.0
2.25-2.50	43.0	40.4	40.0	40.4	40.0	40.7
2.50-2.75	43.0	38.4	38.7	39.1	38.1	41.3
2.75-3.00	40.3	39.0	39.4	39.2	38.1	42.9
3.00-3.25	39.9	38.7	38.6	38.6	38.0	41.9
3.25-3.50	39.4	39.3	38.1	39.9	37.8	39.8
3.50-3.75	39.9	38.8	35.6	39.7	37.7	37.9
3.75-4.00	39.1	42.5	36.0	39.7	39.1	40.0

Table A.5. The friction angle (φ) determined by the use Baldi et al. [1986] with (K_0=1).

Depth [m]	CPT 1,1 [°]	CPT 2,1 [°]	CPT 3,1 [°]	CPT 1,2 [°]	CPT 2,2 [°]	CPT 3,2 [°]
0.00-0.25	44.0	44.0	44.0	44.0	44.0	42.6
0.25-0.50	44.0	44.0	44.0	44.0	44.0	44.0
0.50-0.75	44.0	44.0	44.0	44.0	44.0	44.0
0.75-1.00	44.0	44.0	44.0	44.0	44.0	44.0
1.00-1.25	44.0	44.0	44.0	44.0	44.0	44.0
1.25-1.50	44.0	44.0	44.0	43.9	44.0	44.0
1.50-1.75	44.0	44.0	44.0	44.0	43.9	44.0
1.75-2.00	44.0	44.0	44.0	44.0	42.1	44.0
2.00-2.25	43.9	44.0	42.1	43.9	43.7	44.0
2.25-2.50	44.0	41.5	41.3	41.7	41.2	42.0
2.50-2.75	44.0	39.1	39.5	39.8	38.7	42.6
2.75-3.00	41.2	39.6	40.2	39.9	38.5	43.9
3.00-3.25	40.6	39.1	39.0	39.1	38.3	43.0
3.25-3.50	39.8	39.8	38.3	40.5	37.9	40.3
3.50-3.75	40.4	39.1	35.2	40.2	37.7	37.9
3.75-4.00	39.2	43.1	35.8	40.1	39.3	40.4

Numerical Modelling B

This appendix includes additional investigations not shown in Article 2 regarding numerical modelling. Furthermore, it presents the remaining failure mechanisms that were excluded from the article.

B.1 Effect of Young's Modulus and Poisson's Ratio

As mentioned in the article concerning the numerical modelling of the suction caisson anchor, the Young's modulus had an insignificant effect on the pull-out force. Figure B.1a presents the pull-out force for different padeye depths (z_{pad}) and load inclinations (α_{pad}) using a Young's modulus of 36 000 kPa, with a shaded area indicating the effect of varying the modulus by 5%. As illustrated by the results, the pull-out force appears to be non-sensitive to small changes in the modulus. A similar analysis is conducted for the Poisson's ratio with similar results, as illustrated in figure B.1b. Consequently, these stiffness parameters were not included in the surrogate model as they presumably have little effect on the capacity.

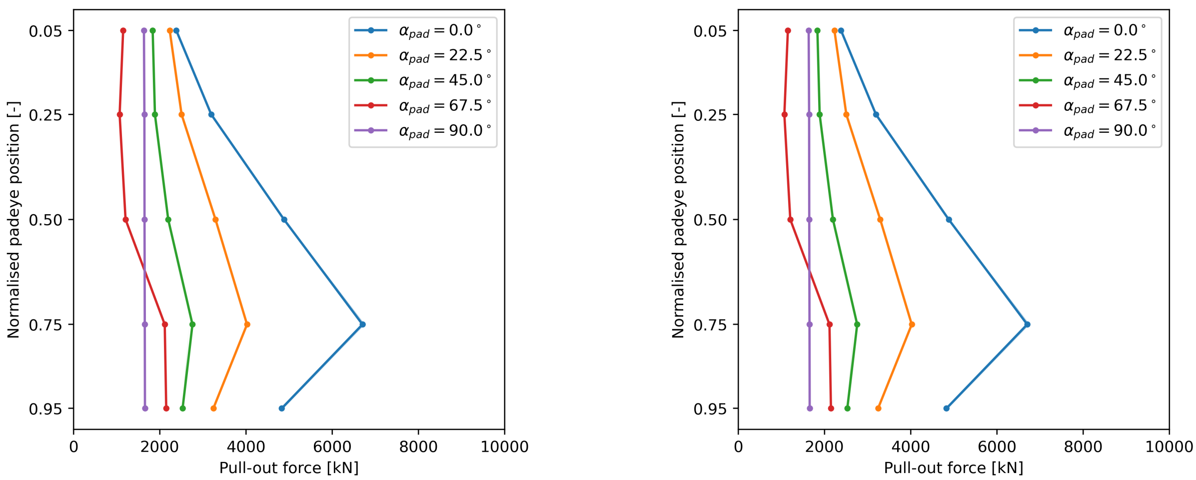

(a) Young's Modulus sensitivity on the pull-out force.

(b) Poisson's ratio sensitivity on the pull-out force.

Figure B.1. Young's Modulus and Poisson's ratio sensitivity on the pull-out force at various normalized padeye positions ($\frac{\mathrm{ZP}}{\mathrm{L}}$) for various load inclinations (α_{pad})

B.2 Failure Mechanisms

Figure B.2 - B.6 illustrates the failure mechanisms of the anchor for each padeye position ($0.05L$, $0.25L$, $0.50L$, $0.75L$, $0.95L$) and load inclination (0°, 22 5°, 45°, 67 5°, 90°) examined in Article 2.

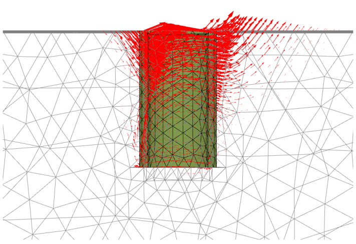

(a) $\alpha_{pad} = 0°$, $z_{pad} = 0.05L$.

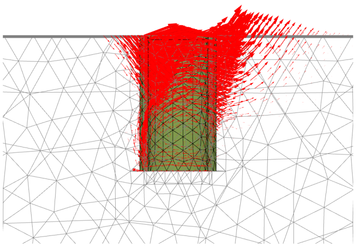

(b) $\alpha_{pad} = 22.5°$, $z_{pad} = 0.05L$.

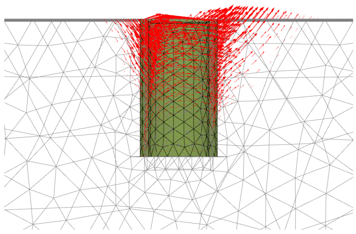

(c) $\alpha_{pad} = 45°$, $z_{pad} = 0.05L$.

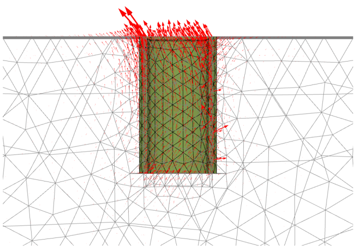

(d) $\alpha_{pad} = 67.5°$, $z_{pad} = 0.05L$.

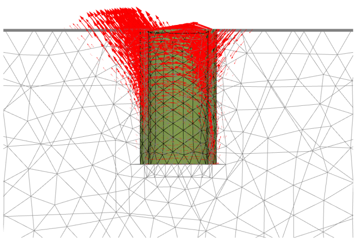

(e) $\alpha_{pad} = 90°$, $z_{pad} = 0.05L$.

Figure B.2. Incremental displacement (Δu_{tot}) at normalised displacement ($\frac{u_{tot}}{D} = 0.1$) for all loading angles investigated at padeye position $0.05L$

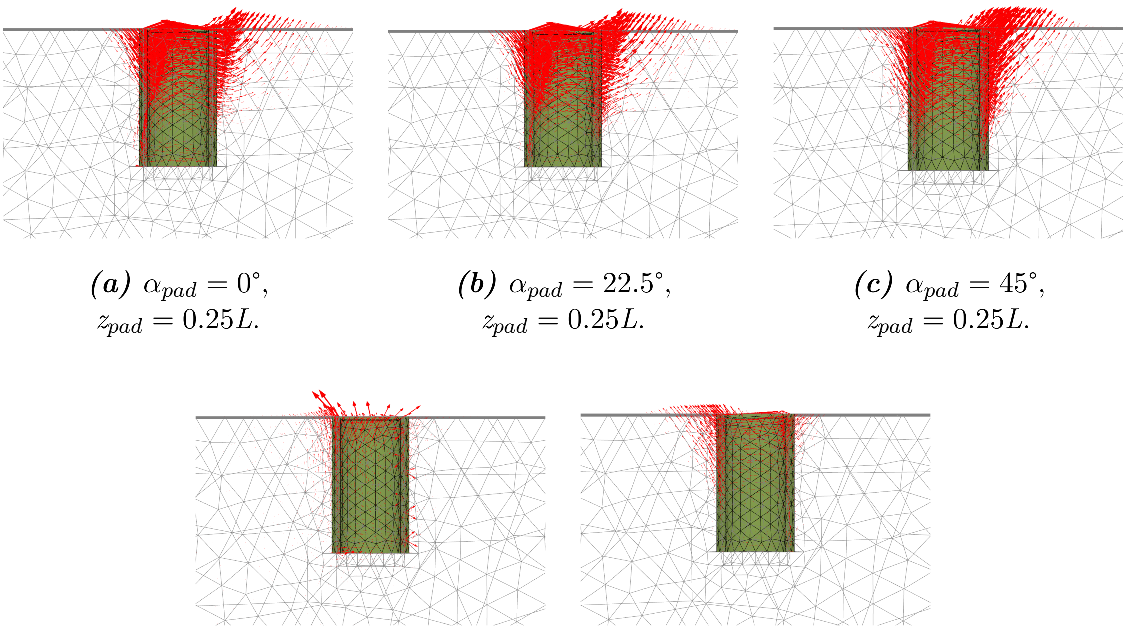

(a) $\alpha_{pad} = 0°$, $z_{pad} = 0.25L$.

(b) $\alpha_{pad} = 22.5°$, $z_{pad} = 0.25L$.

(c) $\alpha_{pad} = 45°$, $z_{pad} = 0.25L$.

(d) $\alpha_{pad} = 67.5°$, $z_{pad} = 0.25L$.

(e) $\alpha_{pad} = 90°$, $z_{pad} = 0.25L$.

Figure B.3. Incremental displacement (Δu_{tot}) at normalised displacement ($\frac{u_{tot}}{D} = 0.1$) for all loading angles investigated at padeye position $0.25L$

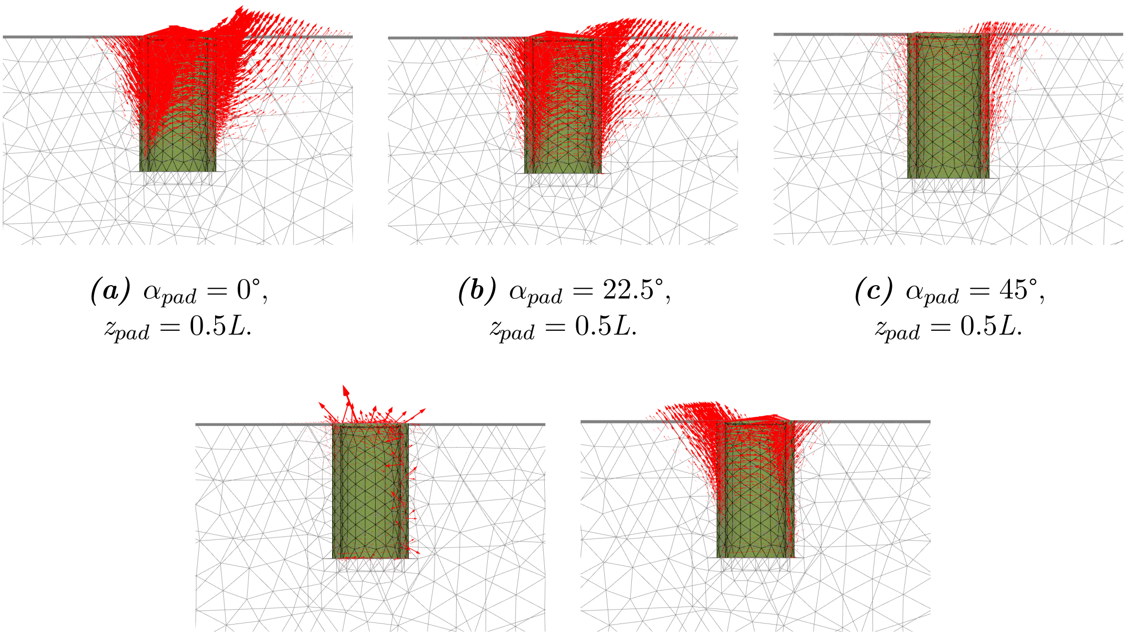

(a) $\alpha_{pad} = 0°$, $z_{pad} = 0.5L$.

(b) $\alpha_{pad} = 22.5°$, $z_{pad} = 0.5L$.

(c) $\alpha_{pad} = 45°$, $z_{pad} = 0.5L$.

(d) $\alpha_{pad} = 67.5°$, $z_{pad} = 0.5L$.

(e) $\alpha_{pad} = 90°$, $z_{pad} = 0.5L$.

Figure B.4. Incremental displacement (Δu_{tot}) at normalised displacement ($\frac{u_{tot}}{D} = 0.1$) for all loading angles investigated at padeye position $0.5L$

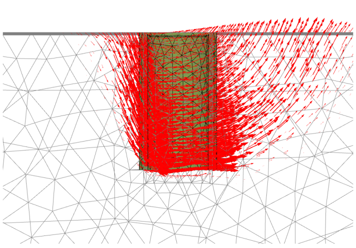

(a) $\alpha_{pad} = 0°$, $z_{pad} = 0.75L$.

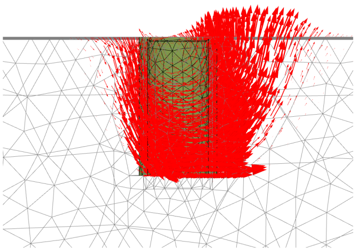

(b) $\alpha_{pad} = 22.5°$, $z_{pad} = 0.75L$.

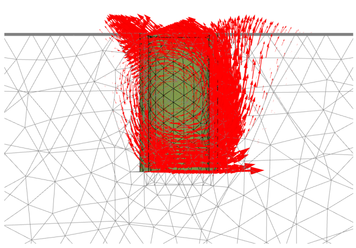

(c) $\alpha_{pad} = 45°$, $z_{pad} = 0.75L$.

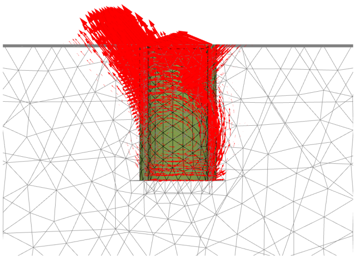

(d) $\alpha_{pad} = 67.5°$, $z_{pad} = 0.75L$.

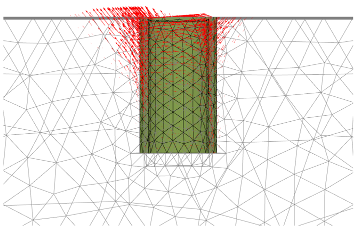

(e) $\alpha_{pad} = 90°$, $z_{pad} = 0.75L$.

Figure B.5. Incremental displacement (Δu_{tot}) at normalised displacement ($\frac{u_{tot}}{D} = 0.1$) for all loading angles investigated at padeye position $0.75L$

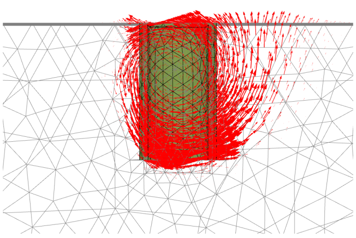

(a) $\alpha_{pad} = 0°$, $z_{pad} = 0.95L$.

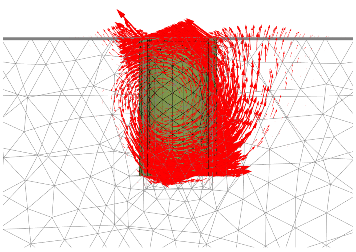

(b) $\alpha_{pad} = 22.5°$, $z_{pad} = 0.95L$.

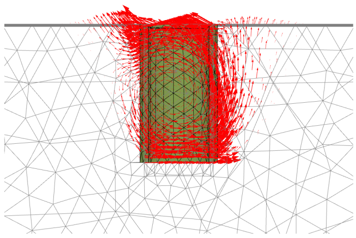

(c) $\alpha_{pad} = 45°$, $z_{pad} = 0.95L$.

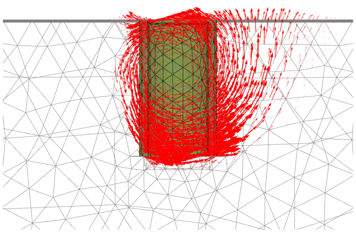

(d) $\alpha_{pad} = 67.5°$, $z_{pad} = 0.95L$.

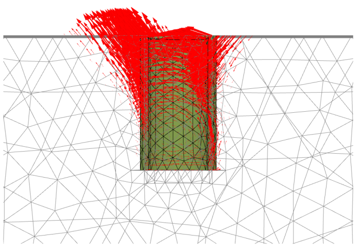

(e) $\alpha_{pad} = 90°$, $z_{pad} = 0.95L$.

Figure B.6. Incremental displacement (Δu_{tot}) at normalised displacement ($\frac{u_{tot}}{D} = 0.1$) for all loading angles investigated at padeye position $0.95L$

B.3 Force-Displacement Curves

Figure B.7-B.11 presents pull-out force as a function of a normalised total displacement $(\frac{u_{tot}}{D})$ for different load inclinations and padeye positions.

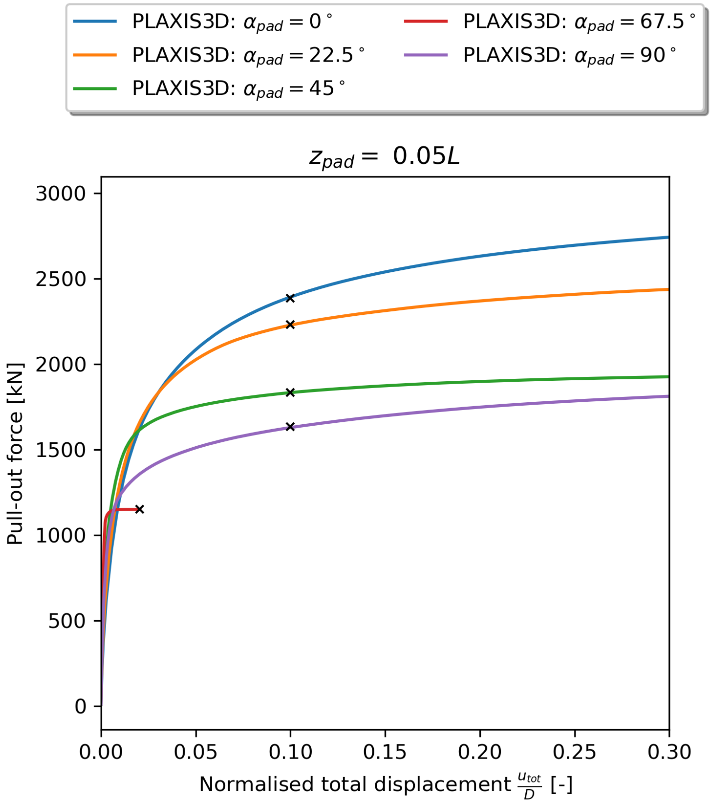

Figure B.7. Force-displacement curves for padeye position ($z_{pad} = 0.05L$).

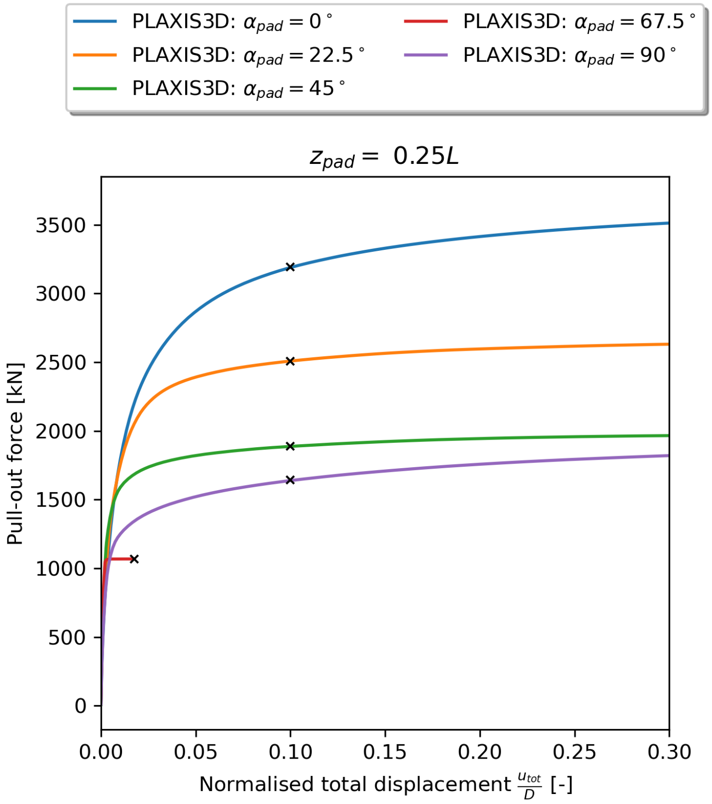

Figure B.8. Force-displacement curves for padeye position ($z_{pad} = 0.25L$).

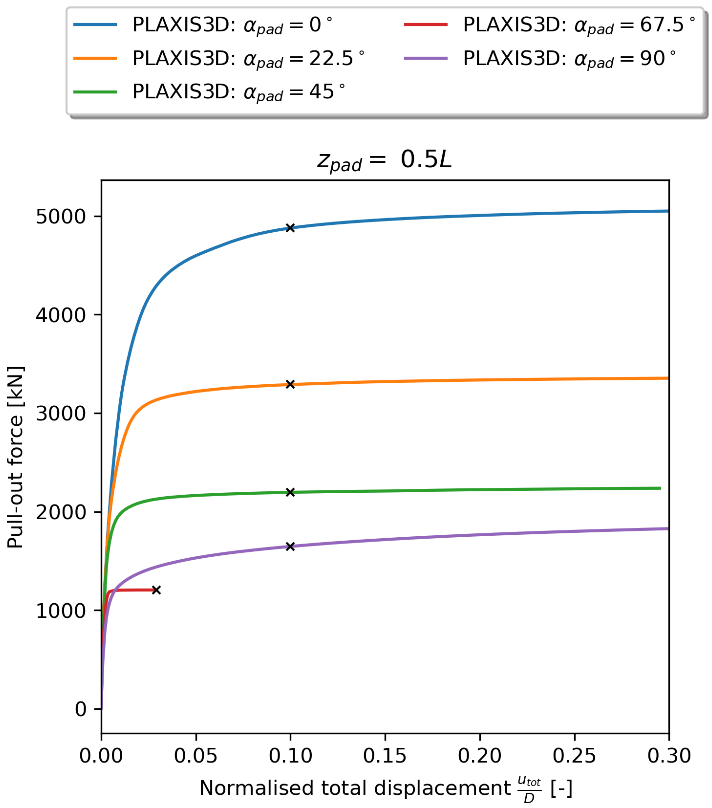

Figure B.9. Force-displacement curves for padeye position ($z_{pad} = 0.5L$).

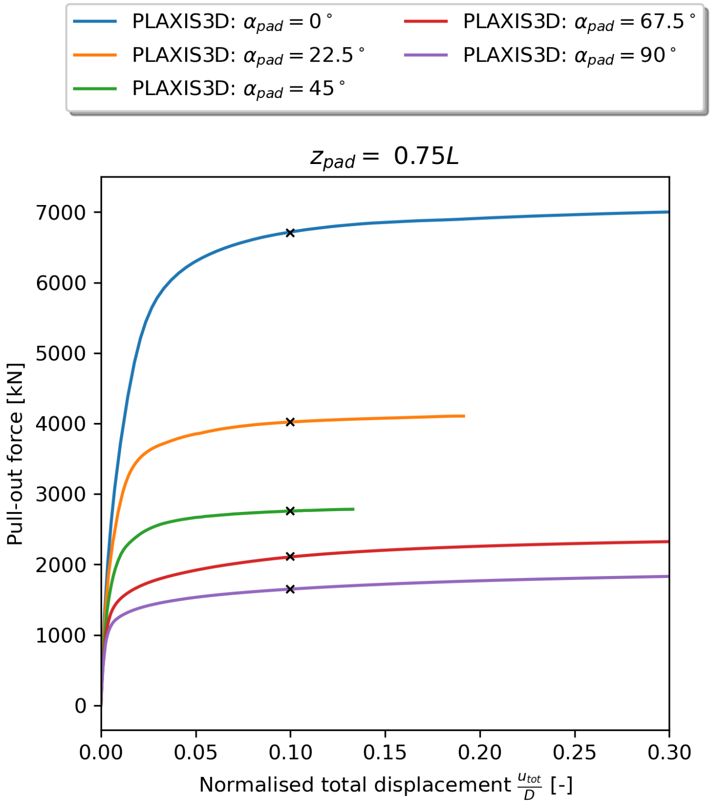

Figure B.10. Force-displacement curves for padeye position ($z_{pad} = 0.75L$).

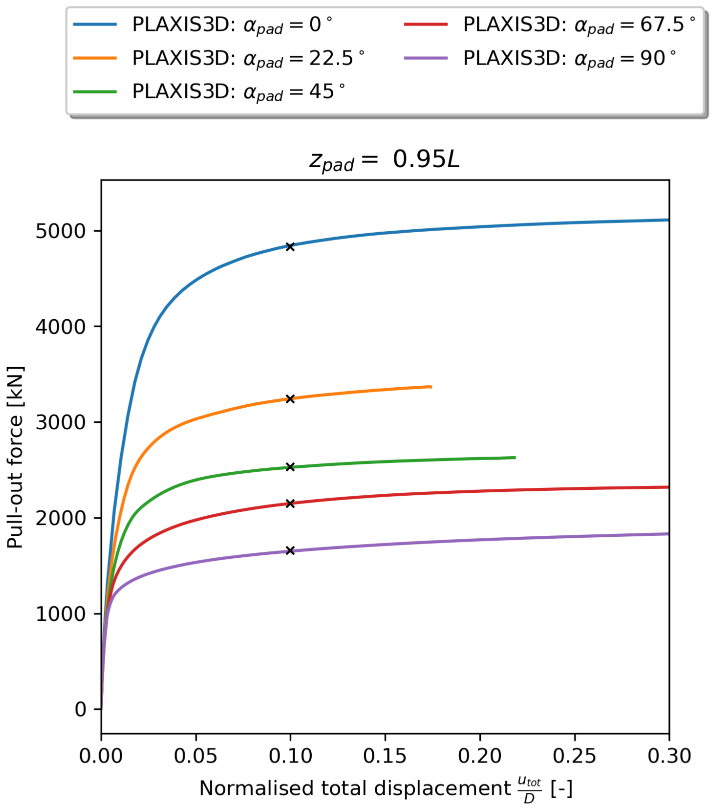

Figure B.11. Force-displacement curves for padeye position ($z_{pad} = 0.95L$).

B.4 Displacement Fields

Figure B.12-B.16 presents the displacement field for different load inclinations and padeye positions.

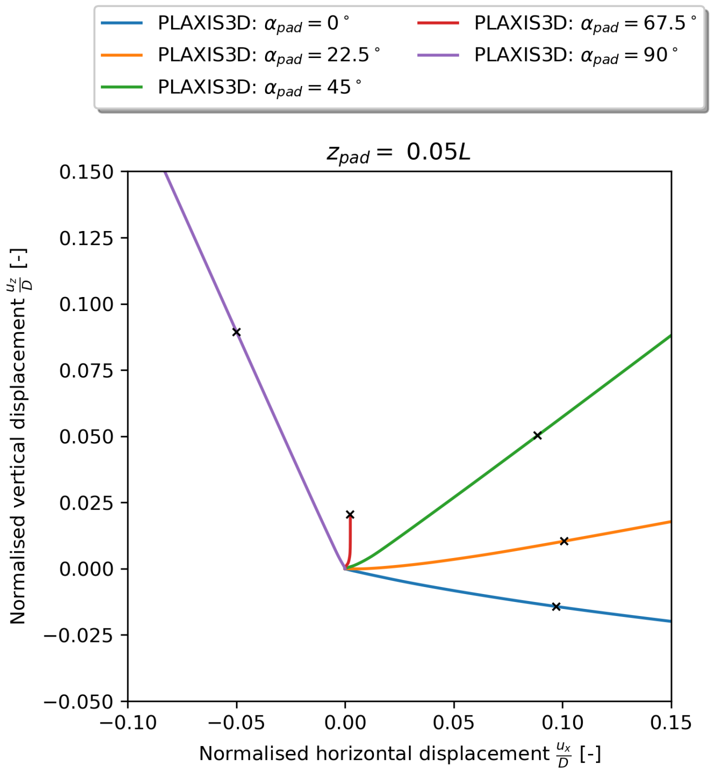

Figure B.12. Displacement field for padeye position ($z_{pad} = 0.05L$).

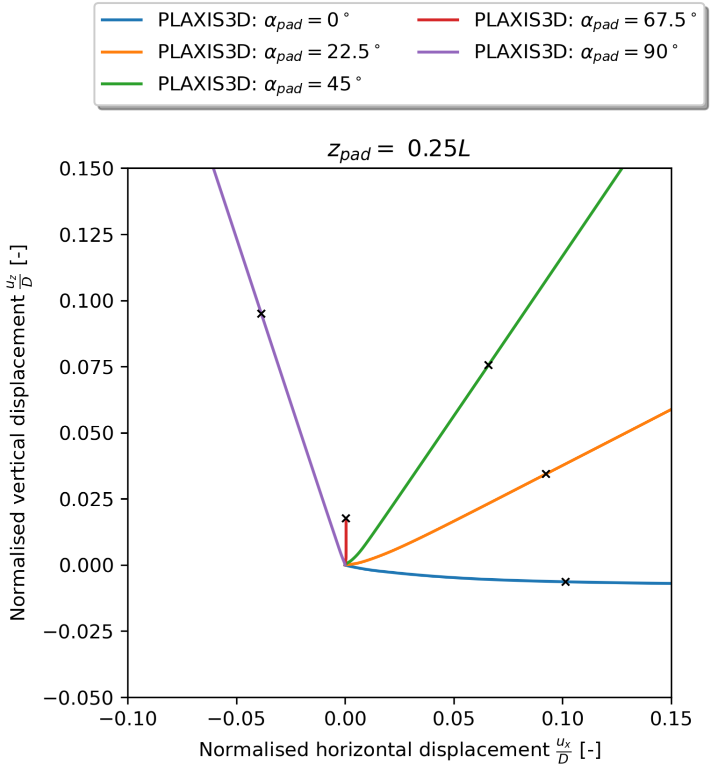

Figure B.13. Displacement field for padeye position ($z_{pad} = 0.25L$).

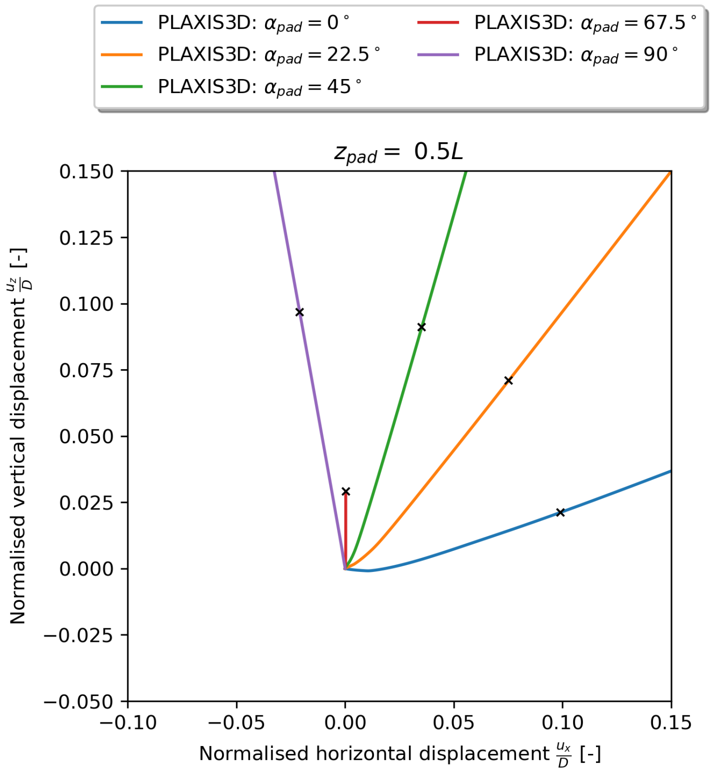

Figure B.14. Displacement field for padeye position ($z_{pad} = 0.5L$).

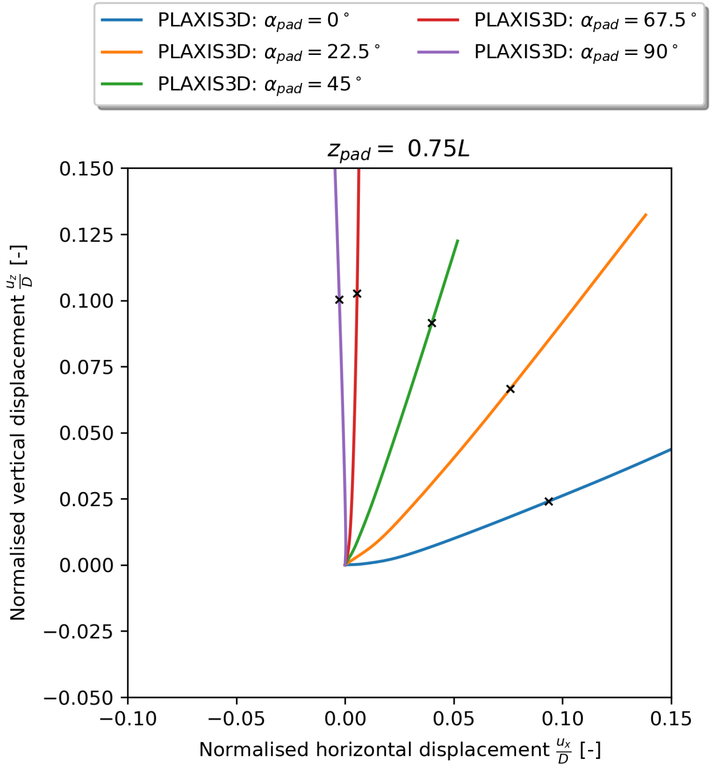

Figure B.15. Displacement field for padeye position ($z_{pad} = 0.75L$).

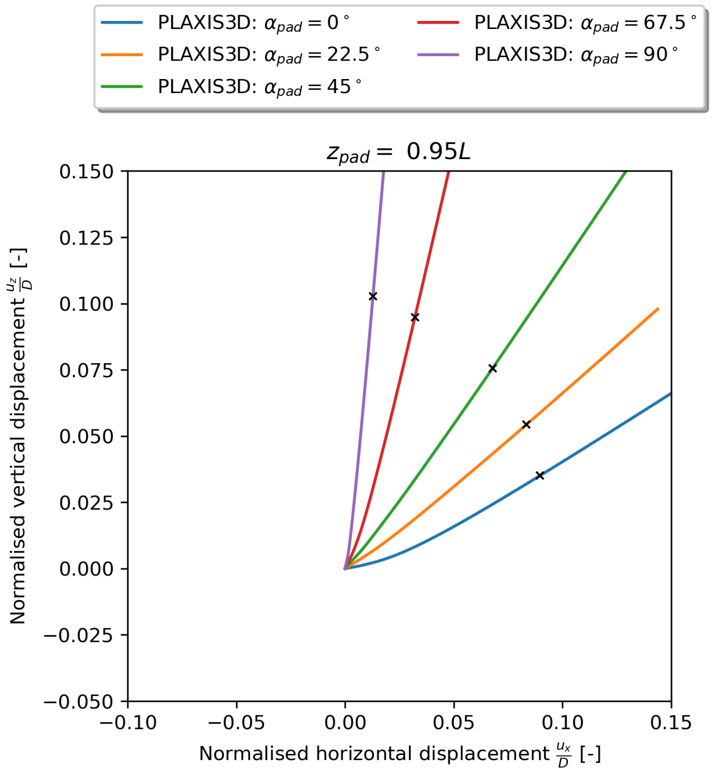

Figure B.16. Displacement field for padeye position ($z_{pad} = 0.95L$).

Surrogate Models C

The test plans, validation sets and the β-coefficients for the surrogate models used in the thesis are presented in the following sections.

C.1 Load Reduction and Angle at Padeye Models

Table C.1. The β-coefficients of the load reduction (ΔT) model.

Features	β-coefficients	Features	β-coefficients	Features	β-coefficients
β_0	-242.167	$T_{mud} z_{pad}$	0.0	$\gamma'^2 T_{mud}$	-0.0
φ	215.222	${z_{pad}}^2$	-0.856	$\gamma'^2 z_{pad}$	-0.002
γ'	-359.495	φ^3	0.021	$\gamma' {\alpha_{mud}}^2$	-0.0
α_{mud}	7.172	$\varphi^2 \gamma'$	0.039	$\gamma' \alpha_{mud} T_{mud}$	0.0
T_{mud}	-0.009	$\varphi^2 \alpha_{mud}$	-0.0	$\gamma' \alpha_{mud} z_{pad}$	0.0
z_{pad}	24.394	$\varphi^2 T_{mud}$	-0.0	$\gamma' {T_{mud}}^2$	-0.0
φ^2	-2.898	$\varphi^2 z_{pad}$	0.0	$\gamma' T_{mud} z_{pad}$	-0.0
$\varphi \gamma'$	-11.189	$\varphi \gamma'^2$	0.205	$\gamma' {z_{pad}}^2$	-0.001
$\varphi \alpha_{mud}$	-0.064	$\varphi \gamma' \alpha_{mud}$	0.007	${\alpha_{mud}}^3$	-0.0
φT_{mud}	-0.0	$\varphi \gamma' T_{mud}$	0.0	${\alpha_{mud}}^2 T_{mud}$	0.0
φz_{pad}	-0.509	$\varphi \gamma' z_{pad}$	0.014	${\alpha_{mud}}^2 z_{pad}$	-0.001
γ'^2	28.73	$\varphi {\alpha_{mud}}^2$	-0.0	$\alpha_{mud} {T_{mud}}^2$	-0.0
$\gamma' \alpha_{mud}$	-0.797	$\varphi \alpha_{mud} T_{mud}$	-0.0	$\alpha_{mud} T_{mud} z_{pad}$	-0.0
$\gamma' T_{mud}$	0.0	$\varphi \alpha_{mud} z_{pad}$	-0.001	$\alpha_{mud} {z_{pad}}^2$	0.001
$\gamma' z_{pad}$	-0.315	$\varphi {T_{mud}}^2$	-0.0	${T_{mud}}^3$	-0.0
${\alpha_{mud}}^2$	0.034	$\varphi T_{mud} z_{pad}$	-0.0	${T_{mud}}^2 z_{pad}$	-0.0
$\alpha_{mud} T_{mud}$	-0.0	$\varphi {z_{pad}}^2$	0.006	$T_{mud} {z_{pad}}^2$	-0.0
$\alpha_{mud} z_{pad}$	0.045	γ'^3	-0.612	${z_{pad}}^3$	0.013
${T_{mud}}^2$	0.0	$\gamma'^2 \alpha_{mud}$	0.015		

Table C.2. The β-coefficients of the angle at padeye (α_{pad}) model.

Features	β-coefficients	Features	β-coefficients	Features	β-coefficients
β_0	-380.466	$T_{mud}z_{pad}$	0.001	$\gamma'^2 T_{mud}$	-0.0
φ	297.546	${z_{pad}}^2$	-1.307	$\gamma'^2 z_{pad}$	-0.047
γ'	-460.12	φ^3	0.033	$\gamma' {\alpha_{mud}}^2$	-0.001
α_{mud}	0.352	$\varphi^2\gamma'$	0.031	$\gamma'\alpha_{mud}T_{mud}$	0.0
T_{mud}	-0.026	$\varphi^2\alpha_{mud}$	-0.004	$\gamma'\alpha_{mud}z_{pad}$	-0.002
z_{pad}	11.164	$\varphi^2 T_{mud}$	-0.0	$\gamma' {T_{mud}}^2$	-0.0
φ^2	-3.879	$\varphi^2 z_{pad}$	-0.002	$\gamma' T_{mud}z_{pad}$	-0.0
$\varphi\gamma'$	-16.593	$\varphi\gamma'^2$	0.357	$\gamma' {z_{pad}}^2$	-0.002
$\varphi\alpha_{mud}$	0.3	$\varphi\gamma'\alpha_{mud}$	0.001	${\alpha_{mud}}^3$	-0.0
φT_{mud}	0.0	$\varphi\gamma' T_{mud}$	0.0	${\alpha_{mud}}^2 T_{mud}$	0.0
φz_{pad}	-0.455	$\varphi\gamma' z_{pad}$	0.016	${\alpha_{mud}}^2 z_{pad}$	-0.001
γ'^2	38.129	$\varphi{\alpha_{mud}}^2$	-0.001	$\alpha_{mud}{T_{mud}}^2$	-0.0
$\gamma'\alpha_{mud}$	-0.84	$\varphi\alpha_{mud}T_{mud}$	-0.0	$\alpha_{mud}T_{mud}z_{pad}$	-0.0
$\gamma' T_{mud}$	0.0	$\varphi\alpha_{mud}z_{pad}$	-0.001	$\alpha_{mud}{z_{pad}}^2$	0.003
$\gamma' z_{pad}$	1.552	$\varphi {T_{mud}}^2$	-0.0	${T_{mud}}^3$	-0.0
${\alpha_{mud}}^2$	0.073	$\varphi T_{mud}z_{pad}$	-0.0	${T_{mud}}^2 z_{pad}$	-0.0
$\alpha_{mud}T_{mud}$	0.0	$\varphi {z_{pad}}^2$	0.008	$T_{mud}{z_{pad}}^2$	-0.0
$\alpha_{mud}z_{pad}$	0.05	γ'^3	-0.856	${z_{pad}}^3$	0.021
${T_{mud}}^2$	0.0	$\gamma'^2\alpha_{mud}$	0.023		

Table C.3. The test plan for the two chain models (ΔT, α_{pad}).

Test	φ [°]	γ' [kPa]	α_{mud} [°]	T_{mud} [kN]	z_{pad} [m]	ΔT [%]	α_{pad} [°]
1	38.03	9.97	3.34	7610.05	17.16	52.67	90.0
2	34.19	8.91	21.03	8109.9	2.37	8.53	31.33
3	31.58	9.17	9.4	4647.27	20.07	50.35	90.0
4	36.01	9.54	6.2	2926.59	14.4	50.99	90.0
5	37.19	8.32	0.55	10741.56	20.33	52.44	90.0
6	30.17	9.25	9.29	9413.26	10.51	49.66	90.0
7	32.38	8.78	15.3	12833.79	23.31	45.35	90.0
8	35.33	8.33	24.45	4749.57	19.65	42.8	90.0
9	36.88	10.85	14.48	10111.53	21.39	47.73	90.0
10	35.81	8.11	21.57	10927.58	7.57	44.79	90.0
11	38.45	9.53	19.12	6765.49	6.49	44.6	90.0
12	38.83	9.3	21.64	5252.39	9.46	43.14	90.0
13	31.33	8.76	13.82	10490.39	10.58	48.76	90.0
14	37.67	9.59	21.35	3307.41	19.15	43.41	90.0
15	34.71	10.64	1.9	6621.79	24.09	52.41	90.0
16	34.57	8.47	11.36	3634.24	18.57	49.38	90.0

Test	φ [°]	γ' [kPa]	α_{mud} [°]	T_{mud} [kN]	z_{pad} [m]	ΔT [%]	α_{pad} [°]
17	36.25	9.6	19.5	9271.27	22.74	45.52	90.0
18	30.88	9.08	24.86	7697.97	21.03	43.37	90.0
19	39.04	10.94	11.65	8531.24	19.55	48.04	90.0
20	39.53	9.07	24.17	11141.8	0.79	2.26	26.79
21	33.34	9.27	25.22	5578.46	23.19	41.84	90.0
22	35.11	7.99	2.5	13243.58	1.31	9.2	13.49
23	35.23	8.56	7.68	8290.91	24.29	50.72	90.0
24	30.19	8.66	22.65	11154.43	24.76	42.8	90.0
25	32.09	8.1	14.68	7278.02	23.93	46.18	90.0
26	32.27	10.74	7.96	6284.17	3.37	20.7	34.96
27	35.06	10.04	24.33	9137.73	9.06	40.92	90.0
28	30.1	10.84	19.59	3066.74	17.9	45.96	90.0
29	35.99	8.61	33.41	6039.02	16.69	38.8	90.0
30	30.82	8.0	26.81	9669.91	12.95	42.23	90.0
31	31.74	9.1	9.99	9721.58	19.2	48.19	90.0
32	32.23	9.26	0.69	6360.53	16.63	53.7	90.0
33	36.83	8.7	11.33	3360.91	11.36	49.5	90.0
34	33.72	9.46	4.24	8519.61	3.19	21.52	32.45
35	34.43	9.41	4.02	13024.58	24.47	52.87	90.0
36	32.2	8.88	21.19	4807.53	22.39	44.17	90.0
37	37.75	9.37	16.44	13014.41	0.18	0.32	16.79
38	33.76	8.73	9.95	4931.23	15.81	48.89	90.0
39	32.95	8.95	26.72	3840.81	17.32	41.4	90.0
40	31.61	10.61	20.75	3253.63	24.36	44.34	90.0
41	36.88	10.26	11.49	5474.37	10.8	48.63	90.0
42	34.24	8.71	6.3	10707.97	8.84	50.96	90.0
43	30.14	8.39	18.21	5439.32	2.15	5.87	25.09
44	31.23	10.27	5.46	11869.67	5.24	28.36	44.7
45	39.88	8.69	18.94	11679.21	21.26	46.38	90.0
46	31.99	9.7	30.86	3969.88	10.05	39.58	90.0
47	35.67	9.4	32.97	3789.89	5.98	37.41	90.0
48	36.56	10.59	3.92	6412.55	1.06	9.15	14.93
49	33.0	8.2	30.25	9972.08	23.33	41.28	90.0
50	31.81	10.89	0.76	11432.46	11.74	54.37	90.0
51	35.14	9.98	13.2	3765.17	22.67	48.92	90.0

Test	φ [°]	γ' [kPa]	α_{mud} [°]	T_{mud} [kN]	z_{pad} [m]	ΔT [%]	α_{pad} [°]
52	35.25	8.83	28.71	8355.05	20.39	40.06	90.0
53	34.12	10.41	21.85	13297.56	8.14	44.15	90.0
54	36.5	8.43	24.53	12312.67	12.49	42.96	90.0
55	31.55	8.07	33.16	11790.82	19.84	39.19	90.0
56	33.91	8.51	5.34	5736.62	18.98	50.51	90.0
57	37.42	8.6	8.15	9595.95	3.84	29.06	49.41
58	30.62	9.33	17.36	6125.94	4.07	17.0	39.0
59	38.98	10.17	10.54	8733.92	3.63	31.3	56.46
60	35.28	9.11	1.15	13362.28	8.53	52.2	90.0
61	34.03	9.18	25.47	7424.36	6.59	36.07	80.18
62	30.93	10.5	8.71	8196.39	17.41	50.98	90.0
63	31.67	9.13	31.51	3122.98	7.98	38.57	90.0
64	32.74	10.32	14.55	2966.7	8.65	48.03	90.0
65	37.16	9.36	16.25	4406.04	7.27	45.22	90.0
66	33.24	8.43	28.41	4240.87	4.9	25.23	62.9
67	36.77	10.3	26.08	4791.66	4.58	32.71	74.45
68	37.25	8.9	9.73	11579.08	9.93	47.25	90.0
69	31.17	8.29	20.89	6374.79	22.19	43.85	90.0
70	33.07	9.67	10.62	11874.53	24.1	47.85	90.0
71	36.1	10.42	30.48	13716.95	18.73	39.85	90.0
72	38.08	7.96	17.48	12736.57	18.02	43.37	90.0
73	34.33	9.23	28.09	13230.29	18.18	42.04	90.0
74	31.87	8.79	30.44	7091.7	11.26	39.4	90.0
75	39.33	8.31	25.02	12008.25	21.58	40.52	90.0
76	33.86	9.99	32.6	8069.78	19.35	40.24	90.0
77	36.2	10.15	0.33	9954.81	10.23	53.81	90.0
78	38.35	10.87	2.36	3747.52	9.25	52.72	90.0
79	36.43	9.85	17.11	2522.27	1.68	11.02	30.65
80	36.23	8.16	9.49	7640.92	20.62	49.98	90.0
81	32.92	10.53	34.72	6928.64	7.59	37.03	90.0
82	38.62	10.36	0.5	10800.29	0.65	8.32	10.45
83	32.1	8.92	16.19	7570.28	9.22	46.86	90.0
84	36.14	9.76	1.02	2750.17	23.6	51.85	90.0
85	38.26	10.35	15.71	8922.11	22.23	44.47	90.0
86	36.36	8.24	13.42	4550.83	9.15	48.23	90.0

Test	φ [°]	γ' [kPa]	α_{mud} [°]	T_{mud} [kN]	z_{pad} [m]	ΔT [%]	α_{pad} [°]
87	30.39	8.49	2.56	7124.14	12.17	51.56	90.0
88	30.6	8.85	15.4	3653.05	22.27	47.57	90.0
89	33.09	10.82	32.8	11184.68	14.54	39.19	90.0
90	39.85	10.04	11.97	9765.02	19.24	46.43	90.0
91	30.77	9.71	15.88	10173.71	6.96	31.97	61.9
92	38.6	10.56	3.57	12166.91	21.84	49.16	90.0
93	33.5	9.83	15.55	8752.23	7.0	40.76	79.77
94	31.71	8.98	14.17	6805.22	8.93	46.47	90.0
95	36.92	9.15	24.06	11103.23	21.15	40.66	90.0
96	34.28	8.24	4.67	2655.63	20.95	51.94	90.0
97	30.79	8.27	25.33	3145.52	1.93	4.95	31.12
98	31.53	10.08	20.18	12445.84	7.68	34.22	71.0
99	34.35	7.99	18.79	5292.86	16.88	44.94	90.0
100	30.97	8.68	18.74	4999.59	7.44	40.15	80.37
101	36.31	9.95	18.58	11355.44	3.5	18.67	43.16
102	39.29	9.1	14.07	6535.61	11.03	44.89	90.0
103	39.68	10.75	9.14	13120.55	15.22	47.34	90.0
104	34.11	10.73	33.33	11615.54	19.48	37.15	90.0
105	31.35	10.21	16.74	3421.32	0.52	0.79	17.62
106	30.06	9.31	34.22	10593.78	7.16	23.37	65.83
107	35.57	10.47	2.71	5744.85	2.79	24.73	35.98
108	30.29	9.65	9.65	9068.45	6.01	30.02	51.77
109	38.75	8.74	14.8	12068.26	1.84	10.44	27.71
110	30.03	9.96	26.39	6668.7	15.29	43.09	90.0
111	33.84	7.98	13.35	7774.59	1.58	5.76	20.12
112	37.7	8.89	32.33	9256.37	5.57	34.04	84.77
113	34.76	9.73	34.63	9613.09	24.89	36.59	90.0
114	39.92	9.89	30.17	4066.01	20.14	38.83	90.0
115	31.96	10.84	19.28	7901.31	7.74	42.14	86.39
116	35.95	9.06	1.33	7380.41	5.38	45.05	74.65
117	34.69	8.95	3.02	8243.81	16.09	52.09	90.0
118	31.9	9.44	33.59	8887.06	15.87	38.74	90.0
119	35.91	9.22	19.9	11766.78	19.02	45.12	90.0
120	33.62	9.13	19.95	11239.85	8.94	45.45	90.0
121	39.66	8.29	3.63	8154.61	11.15	49.54	90.0

Test	φ [°]	γ' [kPa]	α_{mud} [°]	T_{mud} [kN]	z_{pad} [m]	ΔT [%]	α_{pad} [°]
122	35.0	10.47	16.96	11387.83	15.72	44.99	90.0
123	32.05	10.16	27.55	10785.07	18.84	41.17	90.0
124	37.49	10.88	28.89	12038.38	7.2	38.97	90.0
125	31.08	9.34	1.49	13977.95	18.52	51.73	90.0
126	38.76	10.5	19.41	4360.64	2.55	20.56	46.86
127	33.56	10.7	23.78	5142.77	3.69	18.74	48.2
128	37.59	10.1	34.07	5610.6	14.6	37.05	90.0
129	38.47	8.93	7.95	8994.09	10.37	48.53	90.0
130	31.49	9.94	23.45	10291.39	10.14	44.25	90.0
131	37.24	9.86	24.68	11493.65	15.12	43.42	90.0
132	38.9	10.61	24.73	10162.37	7.36	41.22	90.0
133	37.93	8.87	7.52	9849.61	2.07	15.67	27.49
134	35.89	10.19	4.69	10553.25	2.21	16.2	25.24
135	33.53	10.12	11.74	9102.86	13.16	49.66	90.0
136	30.66	10.64	4.33	9450.33	4.34	24.45	36.96
137	35.16	8.18	27.18	6709.09	1.09	2.11	29.59
138	34.04	8.03	29.56	8440.99	8.39	38.83	90.0
139	31.84	8.99	22.3	12141.23	2.61	6.46	29.95
140	39.77	8.5	1.66	5787.33	8.45	52.55	90.0
141	37.09	8.22	4.84	11488.13	2.68	20.23	31.4
142	35.39	10.22	8.87	10958.28	12.27	48.16	90.0
143	39.25	9.91	30.66	6056.04	21.94	39.43	90.0
144	38.11	8.23	34.52	7057.63	13.98	37.37	90.0
145	37.33	10.28	34.39	4685.1	5.82	38.83	90.0
146	37.01	10.54	31.26	7666.22	0.95	2.02	33.58
147	30.24	8.04	19.06	12675.1	13.8	45.0	90.0
148	33.22	10.43	13.52	11049.65	24.81	47.89	90.0
149	39.55	10.45	31.91	12695.25	6.27	40.11	90.0
150	37.64	10.69	27.6	7906.48	21.36	41.2	90.0
151	36.07	9.03	26.48	13611.14	11.64	39.97	90.0
152	38.72	7.97	4.13	4312.14	4.8	51.31	90.0
153	36.97	9.44	28.85	13149.34	11.48	38.01	90.0
154	39.61	7.95	25.83	5196.87	22.58	40.78	90.0
155	30.49	10.18	28.62	7261.96	22.89	41.05	90.0
156	30.46	10.07	6.01	7749.07	14.83	51.36	90.0

Test	φ [°]	γ' [kPa]	α_{mud} [°]	T_{mud} [kN]	z_{pad} [m]	ΔT [%]	α_{pad} [°]
157	32.81	8.35	20.95	13743.67	6.85	29.39	62.91
158	30.89	10.02	27.05	12394.29	8.22	32.73	75.14
159	37.91	8.8	31.76	5691.84	22.54	39.07	90.0
160	32.33	10.24	22.16	10516.83	22.02	42.4	90.0
161	35.71	9.16	13.97	4301.11	23.06	47.72	90.0
162	30.42	8.19	12.57	10270.92	3.12	10.99	25.91
163	36.71	8.09	33.83	4276.99	13.28	37.03	90.0
164	32.87	9.38	18.08	8477.08	12.97	44.46	90.0
165	38.8	8.17	5.9	8658.23	15.47	51.68	90.0
166	38.51	8.48	15.13	3195.11	15.96	46.25	90.0
167	32.33	8.54	3.09	12482.03	9.71	52.88	90.0
168	34.97	9.92	30.64	11939.44	2.43	6.73	38.72
169	36.68	8.31	23.21	6840.45	0.39	0.53	23.8
170	30.74	9.64	27.32	8423.66	22.85	41.14	90.0
171	37.99	9.04	0.24	4618.61	16.8	53.29	90.0
172	36.3	10.09	33.69	11284.62	3.78	15.57	53.91
173	30.53	10.81	6.94	2901.55	21.12	51.58	90.0
174	35.45	9.74	14.91	8962.28	1.24	4.47	20.14
175	38.53	8.41	29.69	8610.95	9.35	41.71	90.0
176	37.43	9.52	23.64	13312.85	5.14	30.25	68.59
177	32.42	9.19	6.68	6307.08	6.32	41.26	70.63
178	33.48	10.82	13.02	5565.71	18.43	47.05	90.0
179	38.4	8.13	26.99	3534.78	4.95	42.88	90.0
180	31.25	10.4	33.87	5527.35	22.96	39.51	90.0
181	35.87	9.55	31.32	6880.5	11.79	38.37	90.0
182	39.11	10.58	23.28	2863.14	7.87	43.92	90.0
183	34.42	9.58	11.07	12430.34	3.99	21.98	40.41
184	38.14	10.66	20.59	13554.93	10.19	44.55	90.0
185	38.38	10.32	21.28	5345.38	17.72	44.38	90.0
186	36.46	10.01	16.12	6440.54	21.6	47.51	90.0
187	31.46	9.63	27.87	4486.99	4.15	16.82	49.36
188	33.14	9.0	12.14	13436.5	16.29	46.65	90.0
189	39.82	9.78	29.23	6017.66	2.89	20.01	56.26
190	32.97	9.39	4.55	3298.28	0.87	5.6	11.08
191	34.73	8.58	17.59	10457.67	4.51	22.82	48.4

Test	φ [°]	γ' [kPa]	α_{mud} [°]	T_{mud} [kN]	z_{pad} [m]	ΔT [%]	α_{pad} [°]
192	38.02	9.29	6.81	12630.7	3.06	23.67	39.06
193	38.19	9.79	16.51	8118.25	5.46	43.75	90.0
194	35.46	8.46	5.06	12277.36	20.56	51.37	90.0
195	30.98	9.72	6.76	4451.94	14.85	50.32	90.0
196	38.32	9.03	26.87	7492.9	12.0	42.79	90.0
197	35.78	8.51	27.94	13618.65	18.19	41.46	90.0
198	37.05	10.48	8.45	7026.56	24.97	48.14	90.0
199	38.16	8.45	12.34	5907.55	5.01	43.84	84.68
200	31.42	9.33	1.74	6920.79	24.63	51.65	90.0
201	36.59	10.38	17.89	9533.44	20.25	45.32	90.0
202	34.25	9.24	22.84	2731.97	6.17	43.05	90.0
203	34.79	9.82	22.48	3714.44	17.43	42.57	90.0
204	38.24	10.71	16.57	12551.23	23.98	47.06	90.0
205	32.88	8.1	5.78	3587.56	11.4	50.91	90.0
206	38.56	9.99	8.58	3566.17	6.79	48.9	90.0
207	31.04	8.55	24.24	7965.41	14.24	42.4	90.0
208	32.57	8.62	33.21	12348.96	0.6	0.35	33.58
209	35.82	9.87	19.82	6111.18	13.54	44.91	90.0
210	39.22	7.95	30.86	7142.61	12.28	40.35	90.0
211	32.58	8.44	34.32	8262.94	7.09	29.88	77.12
212	31.93	9.5	19.63	5046.77	1.17	2.57	22.56
213	35.5	9.01	29.12	3052.98	3.31	19.26	54.35
214	34.6	10.39	18.29	7802.73	13.86	46.04	90.0
215	34.94	10.51	10.21	5415.97	9.63	50.48	90.0
216	32.47	10.44	22.96	12240.7	17.2	44.18	90.0
217	33.41	10.86	21.49	6159.74	20.51	43.01	90.0
218	39.46	8.67	28.17	11332.57	6.44	41.91	90.0
219	34.38	10.9	18.4	7458.95	1.46	4.86	24.11
220	35.59	8.03	14.4	13950.48	14.75	47.48	90.0
221	37.97	8.57	31.44	11706.81	24.57	38.23	90.0
222	33.39	9.91	0.1	11641.91	0.15	2.04	2.35
223	39.94	10.67	5.7	7520.16	5.35	48.23	90.0
224	34.92	8.61	32.11	9877.63	9.79	39.27	90.0
225	39.32	9.08	34.9	10371.58	14.93	37.28	90.0
226	34.49	10.23	20.12	11259.35	10.75	45.36	90.0

Test	φ [°]	γ' [kPa]	α_{mud} [°]	T_{mud} [kN]	z_{pad} [m]	ΔT [%]	α_{pad} [°]
227	31.0	9.9	12.66	13480.76	16.4	48.03	90.0
228	34.83	10.77	27.47	10411.7	18.34	39.73	90.0
229	39.08	10.57	28.46	2830.02	15.37	39.81	90.0
230	33.44	9.8	2.04	8875.29	11.09	53.05	90.0
231	35.35	10.9	13.73	11021.96	6.1	39.31	75.79
232	32.62	8.83	4.38	8694.38	15.63	50.63	90.0
233	32.65	9.52	2.81	11812.15	12.61	52.27	90.0
234	30.34	8.4	11.24	12922.46	21.5	48.09	90.0
235	34.54	8.92	30.1	4860.81	23.84	40.15	90.0
236	33.73	10.06	11.8	3893.01	6.73	47.53	90.0
237	36.97	8.82	2.21	2783.73	8.07	53.66	90.0
238	35.73	9.2	0.88	7194.86	4.22	35.83	53.78
239	36.54	10.92	29.45	8571.77	0.01	0.01	29.47
240	30.27	9.49	32.39	5967.44	2.33	4.52	37.65
241	37.82	9.61	27.75	9561.91	10.44	40.1	90.0
242	36.42	8.28	31.94	2585.81	19.42	37.89	90.0
243	39.5	10.33	13.58	13807.12	11.89	47.33	90.0
244	39.99	9.56	7.6	6206.89	19.77	50.81	90.0
245	35.04	9.68	10.44	9388.49	23.48	48.03	90.0
246	30.57	9.63	32.21	12795.06	20.16	39.94	90.0
247	36.61	8.4	12.26	6253.3	16.99	49.18	90.0
248	33.16	8.35	21.81	9704.25	3.9	15.14	41.01
249	37.81	10.22	6.12	13673.77	22.48	51.81	90.0
250	33.05	9.75	17.67	13393.03	15.06	43.82	90.0
251	33.99	8.84	7.19	11960.04	9.9	51.61	90.0
252	37.12	8.59	20.54	3907.32	1.64	8.33	30.62
253	38.86	9.0	17.22	10851.47	20.79	45.23	90.0
254	32.72	8.36	9.0	10879.75	7.93	44.18	80.49
255	35.61	10.72	34.03	3385.43	20.9	38.6	90.0
256	33.95	10.78	8.32	13929.68	4.69	27.88	47.42
257	33.66	9.23	28.23	9339.97	16.31	40.85	90.0
258	39.45	9.62	4.95	7862.06	12.74	51.2	90.0
259	32.27	8.12	29.35	13875.77	4.43	12.73	45.26
260	30.69	8.38	1.2	10676.98	13.06	53.91	90.0
261	32.85	10.79	23.92	10011.5	19.94	42.29	90.0

Test	φ [°]	γ' [kPa]	α_{mud} [°]	T_{mud} [kN]	z_{pad} [m]	ΔT [%]	α_{pad} [°]
262	37.38	9.41	10.3	10969.32	13.21	48.89	90.0
263	34.18	10.1	25.73	12518.06	22.07	41.85	90.0
264	38.66	10.05	2.89	6735.8	20.75	50.13	90.0
265	33.19	8.02	6.47	2696.65	5.72	46.54	81.54
266	31.2	9.48	20.34	4902.88	13.71	44.38	90.0
267	39.19	8.74	8.69	3471.5	24.2	50.45	90.0
268	38.94	9.05	33.05	9188.91	23.52	35.96	90.0
269	39.14	8.26	17.95	13538.03	5.64	40.1	84.46
270	37.33	8.86	23.35	5088.52	12.87	44.56	90.0
271	31.29	10.66	26.53	10089.61	4.26	13.81	43.87
272	31.64	10.3	29.91	13450.92	2.01	3.26	33.65
273	34.61	9.93	8.25	4151.56	6.59	49.9	90.0
274	36.18	9.28	5.2	10311.18	21.68	50.32	90.0
275	34.46	8.64	31.18	6486.09	1.75	4.13	36.0
276	39.8	9.84	25.64	10624.92	16.02	42.33	90.0
277	39.38	8.53	10.79	10053.74	3.45	28.07	50.85
278	30.43	10.53	15.61	12863.7	10.63	47.57	90.0
279	36.65	9.68	9.76	10408.33	14.39	47.41	90.0
280	37.63	9.15	12.42	4069.25	3.0	25.9	48.06
281	35.54	9.72	12.82	12760.38	5.83	35.96	67.77
282	36.04	10.48	26.22	8329.23	13.59	41.97	90.0
283	32.77	9.57	15.04	10223.48	18.33	47.5	90.0
284	33.32	10.15	29.7	5273.45	14.06	40.81	90.0
285	32.03	10.55	7.23	13775.94	10.92	51.34	90.0
286	37.29	9.77	0.2	9321.21	18.1	54.12	90.0
287	39.03	9.47	15.2	3953.39	17.59	45.89	90.0
288	38.28	9.5	29.92	9916.66	15.57	40.42	90.0
289	30.02	10.12	10.84	4707.79	0.35	0.47	11.35
290	39.16	9.88	32.75	12909.19	0.74	1.42	34.38
291	30.32	8.97	31.7	13181.98	16.14	38.41	90.0
292	33.81	8.14	16.99	9194.93	16.94	46.46	90.0
293	39.6	10.25	5.3	3998.51	9.61	51.75	90.0
294	32.5	9.85	32.46	2609.32	12.7	40.2	90.0
295	34.87	8.81	26.17	12201.62	14.25	42.85	90.0
296	30.71	10.2	29.04	2554.13	11.95	40.53	90.0

Test	φ [°]	γ' [kPa]	α_{mud} [°]	T_{mud} [kN]	z_{pad} [m]	ΔT [%]	α_{pad} [°]
297	36.39	8.63	18.53	7361.14	15.4	45.57	90.0
298	39.75	8.25	20.46	9801.19	18.94	45.64	90.0
299	32.13	8.65	7.84	11554.15	17.51	49.79	90.0
300	35.19	10.35	25.38	9017.77	8.29	42.16	90.0
301	37.85	10.13	23.07	6611.15	16.49	44.71	90.0
302	37.76	10.76	22.2	7343.88	10.86	41.81	90.0
303	35.4	9.67	23.72	5652.23	8.78	44.53	90.0
304	38.94	9.31	13.11	13835.92	19.86	48.25	90.0
305	31.76	10.29	2.23	4107.11	18.66	52.39	90.0
306	37.56	10.8	10.93	4557.81	14.09	48.61	90.0
307	31.15	10.73	14.28	6567.33	12.56	47.81	90.0
308	36.73	10.68	1.98	12581.54	14.66	50.33	90.0
309	34.88	8.07	9.11	4939.93	12.1	49.77	90.0
310	32.54	10.63	25.93	8775.71	2.82	8.61	36.34
311	33.89	10.92	30.99	3475.84	13.48	38.5	90.0
312	35.66	10.6	7.1	5011.28	16.53	51.69	90.0
313	36.81	8.77	34.89	12970.82	4.77	21.02	63.59
314	32.16	10.37	3.47	4448.76	23.67	52.95	90.0
315	38.67	9.43	16.78	2993.73	21.77	44.44	90.0
316	39.4	9.21	22.55	7973.3	12.37	41.49	90.0
317	34.64	10.43	15.94	5854.11	9.53	46.15	90.0
318	33.6	8.72	17.78	3201.47	13.37	45.09	90.0
319	34.07	9.46	1.46	5810.94	13.73	52.67	90.0
320	32.68	9.81	10.14	6963.08	1.41	5.84	16.98
321	31.38	8.05	3.72	9479.08	17.78	53.16	90.0
322	32.45	8.52	12.89	5919.17	23.14	48.79	90.0
323	33.69	10.03	6.43	12088.39	17.81	50.93	90.0
324	37.48	8.08	22.74	8823.79	11.57	43.99	90.0
325	37.54	8.15	5.6	13060.0	23.72	50.94	90.0
326	37.1	9.35	22.02	7210.86	24.45	41.73	90.0
327	31.43	8.21	7.36	8032.48	5.18	28.07	46.0
328	31.12	8.76	3.27	5174.61	0.28	1.12	4.5
329	39.71	8.96	12.06	5377.33	8.62	47.86	90.0
330	33.3	8.37	25.06	4201.73	17.06	42.86	90.0

Table C.4. The validation set for the two chain models (ΔT, α_{pad}).

Test	φ [°]	γ' [kPa]	α_{mud} [°]	T_{mud} [kN]	z_{pad} [m]	ΔT [%]	α_{pad} [°]
1	36.76	8.15	2.13	5781.42	18.25	52.15	90.0
2	36.44	8.5	25.55	5692.7	5.84	40.02	89.01
3	35.38	8.36	17.26	11792.78	3.47	16.61	38.67
4	38.56	8.69	32.96	10206.71	19.51	38.6	90.0
5	39.41	9.46	31.73	7109.39	8.16	39.57	90.0
6	36.27	8.77	18.16	8001.69	13.95	46.4	90.0
7	33.72	9.58	1.54	3372.7	11.38	53.56	90.0
8	37.86	8.01	28.08	11544.58	22.81	39.51	90.0
9	37.65	10.89	16.89	6775.37	12.58	46.66	90.0
10	31.86	9.68	6.64	10465.15	22.22	49.55	90.0
11	36.01	9.12	33.12	4822.31	0.35	0.31	33.46
12	32.56	8.21	20.66	13676.84	15.05	44.89	90.0
13	32.64	9.0	17.83	3133.72	5.16	33.13	65.54
14	34.8	9.91	24.04	6132.58	6.81	41.43	90.0
15	35.47	8.06	22.71	4978.9	14.55	44.52	90.0
16	39.5	9.73	20.12	5099.68	22.54	44.89	90.0
17	32.33	9.62	24.84	2923.33	20.44	42.72	90.0
18	32.12	9.9	32.2	12179.04	17.58	37.88	90.0
19	35.03	10.43	28.62	9851.37	23.62	41.24	90.0
20	37.4	9.06	30.33	2534.86	15.66	40.37	90.0
21	37.34	10.38	8.39	8651.04	15.98	48.94	90.0
22	37.11	8.24	6.97	3239.44	2.81	26.87	43.85
23	30.79	10.19	21.79	7568.77	19.06	45.27	90.0
24	39.0	10.66	22.03	11972.02	17.87	42.34	90.0
25	39.61	8.96	24.57	13359.94	13.15	43.37	90.0
26	31.79	10.54	23.27	6645.24	6.3	31.13	67.89
27	31.1	10.11	29.29	5514.15	15.43	41.83	90.0
28	34.03	10.75	19.26	9182.75	0.07	0.06	19.32
29	36.95	10.3	12.33	9507.36	5.48	40.8	77.99
30	34.2	8.91	11.55	13761.79	18.46	49.55	90.0
31	31.13	9.41	18.89	13106.01	24.08	45.49	90.0
32	31.31	7.94	12.68	7913.59	8.52	44.7	84.64
33	35.89	10.09	14.33	13853.39	10.67	46.58	90.0
34	30.3	8.53	31.09	4074.21	10.92	40.49	90.0

Test	φ [°]	γ' [kPa]	α_{mud} [°]	T_{mud} [kN]	z_{pad} [m]	ΔT [%]	α_{pad} [°]
35	35.27	10.52	34.39	4098.89	14.89	37.83	90.0
36	39.99	9.32	5.59	8912.2	17.28	48.11	90.0
37	30.01	9.96	4.14	6360.53	13.45	50.9	90.0
38	30.92	9.27	13.68	4332.85	3.44	17.12	35.43
39	37.96	9.72	10.09	11730.83	0.84	4.39	15.24
40	39.21	8.43	4.54	12353.37	11.83	48.21	90.0
41	33.22	10.93	11.07	4558.52	20.52	49.12	90.0
42	33.42	9.55	33.92	13414.82	2.43	4.91	39.7
43	32.03	8.11	10.67	6219.36	21.08	49.26	90.0
44	30.54	8.33	16.1	9235.49	19.33	46.06	90.0
45	32.84	10.59	6.03	12558.13	4.37	25.32	40.4
46	35.6	9.39	5.33	7437.7	7.03	52.08	90.0
47	33.77	9.29	26.04	8794.82	16.81	42.55	90.0
48	32.95	9.15	27.11	8332.73	20.02	40.2	90.0
49	32.46	8.47	2.73	9746.16	4.13	25.6	37.2
50	39.77	10.44	3.38	5867.76	1.35	16.22	24.06
51	34.96	8.85	7.39	4729.53	21.68	50.02	90.0
52	34.62	8.72	23.4	10621.96	4.56	20.75	51.09
53	38.07	9.04	16.01	9604.33	9.15	45.63	90.0
54	37.54	10.82	29.89	12730.14	7.8	38.43	90.0
55	36.6	9.2	9.37	10798.34	24.7	50.57	90.0
56	30.66	8.8	8.25	12602.5	6.04	28.19	47.21
57	38.88	8.08	21.11	8540.45	1.51	6.74	29.22
58	36.16	10.65	31.42	7697.23	24.5	38.35	90.0
59	35.76	10.25	3.79	12929.87	21.3	50.65	90.0
60	34.14	8.29	34.57	7247.78	10.21	36.51	90.0
61	38.68	10.03	26.37	3500.68	2.6	19.12	51.62
62	34.55	10.73	8.99	2661.73	10.04	49.87	90.0
63	31.63	8.86	29.04	11040.47	9.39	40.73	90.0
64	39.03	8.58	11.97	3767.29	16.42	46.56	90.0
65	33.56	8.61	1.08	6827.24	23.17	53.35	90.0
66	30.25	10.33	27.39	10021.13	1.88	2.93	30.74
67	36.83	9.82	19.48	11143.21	12.4	43.45	90.0
68	38.35	9.79	0.46	8233.41	7.4	51.89	90.0
69	38.33	10.15	15.04	3903.64	23.36	45.41	90.0

Test	φ [°]	γ' [kPa]	α_{mud} [°]	T_{mud} [kN]	z_{pad} [m]	ΔT [%]	α_{pad} [°]
70	31.51	10.78	0.56	10876.81	13.85	52.71	90.0
71	34.38	9.49	13.27	11394.02	11.58	45.88	90.0
72	33.16	10.0	15.26	5271.76	8.76	48.14	90.0

C.2 Suction Anchor Model

Table C.5. The test plan for the anchor model (R_c). The grey rows are the support vectors with the Weight coefficient (w_i).

Test	φ [°]	γ' [kPa]	D [m]	λ [-]	$\frac{z_{pad}}{L}$ [-]	R_{inter} [-]	α_{pad} [°]	R_c [kN]	w_i
1	39.43	9.01	4.17	1.03	0.53	0.6	38.66	1944	-
2	30.52	10.23	3.23	4.42	0.36	0.62	41.98	6322	-
3	30.82	10.54	3.76	1.63	0.03	0.63	15.11	1817	4921
4	39.28	9.03	4.83	2.61	0.78	0.53	90.0	3591	-
5	31.57	9.53	4.9	1.07	0.06	0.64	5.01	2126	-4057
6	34.76	9.59	3.91	2.55	0.0	0.53	14.59	5023	-
7	36.35	9.51	4.91	4.73	0.79	0.73	90.0	13171	10267
8	31.76	8.28	3.99	1.47	0.75	0.57	59.92	1215	-
9	37.49	8.93	3.54	2.46	0.04	0.71	24.36	4719	-
10	36.55	8.67	3.56	2.22	0.61	0.72	84.88	1545	-49608
11	36.88	10.03	4.01	4.61	0.2	0.5	59.75	7178	-50000
12	36.04	9.57	4.79	2.2	0.69	0.68	90.0	3678	-2361
13	30.67	10.5	3.6	1.96	0.15	0.57	33.36	2199	-
14	37.37	10.7	4.67	3.11	0.25	0.72	50.68	13723	44749
15	35.58	8.79	3.03	2.87	0.58	0.53	66.22	1059	-4728
16	32.44	9.48	3.33	2.13	0.19	0.66	13.53	2652	-
17	33.23	9.78	3.85	1.65	0.4	0.74	33.12	2651	-
18	35.36	10.12	3.39	3.44	0.04	0.68	14.71	7111	-
19	36.38	8.41	3.87	4.84	0.9	0.54	90.0	4939	-9245
20	32.4	10.31	4.11	3.8	0.86	0.5	90.0	4522	-
21	32.75	9.33	4.84	2.07	0.88	0.58	90.0	2748	-8074
22	31.36	8.43	4.29	2.95	0.3	0.74	30.12	8458	-
23	33.91	10.38	3.41	2.36	0.41	0.56	47.21	1836	-2943
24	34.1	9.74	4.59	2.3	0.61	0.62	82.16	2998	-
25	30.07	9.26	3.64	4.27	0.5	0.59	63.79	4163	24263
26	30.74	9.94	4.66	2.38	0.98	0.66	90.0	3594	-
27	32.58	8.13	3.11	1.58	0.1	0.78	27.0	996	2408
28	37.15	9.64	3.65	1.94	0.96	0.64	90.0	1458	-
29	31.99	8.31	4.02	2.08	0.22	0.6	16.6	3822	-
30	31.81	10.76	3.8	2.97	0.52	0.7	61.14	3403	-

Test	φ [°]	γ' [kPa]	D [m]	λ [-]	$\frac{z_{pad}}{L}$ [-]	R_{inter} [-]	α_{pad} [°]	R_c [kN]	w_i
31	30.6	8.32	3.96	1.71	0.19	0.53	22.42	2096	-
32	39.64	9.6	3.17	3.22	0.71	0.68	90.0	1830	-
33	39.8	10.07	4.54	4.89	0.95	0.6	90.0	10012	-
34	39.21	9.82	3.4	1.68	0.93	0.75	90.0	1827	-
35	33.1	8.89	3.27	3.9	0.18	0.53	29.77	6094	-
36	34.97	9.49	3.68	3.15	0.92	0.55	90.0	2318	9427
37	37.21	8.45	4.77	4.58	0.11	0.7	45.88	27232	50000
38	36.89	10.13	4.92	3.14	0.2	0.63	51.15	13589	-
39	39.08	9.73	3.3	2.44	0.75	0.62	90.0	1273	-
40	38.44	9.63	5.0	1.15	0.46	0.75	40.88	3809	-
41	34.44	10.85	3.37	1.35	0.44	0.7	32.18	1603	-
42	30.98	8.81	4.1	4.12	0.14	0.69	23.05	10161	-50000
43	37.04	9.37	4.47	2.69	0.24	0.61	35.2	10400	-
44	32.78	10.49	3.45	4.18	0.25	0.71	39.98	9181	14642
45	33.87	8.59	4.69	3.85	0.5	0.61	90.0	6996	-
46	34.63	8.28	4.17	3.81	0.24	0.62	44.59	11104	-
47	34.84	10.52	3.66	1.48	1.0	0.77	69.98	1818	6
48	35.19	8.81	3.68	2.58	0.87	0.56	90.0	1594	9862
49	35.91	9.65	3.59	1.01	0.08	0.52	21.25	967	-349
50	32.69	10.9	3.05	2.16	0.62	0.73	44.56	1770	-
51	37.47	10.09	4.25	1.53	0.78	0.7	73.17	2891	50000
52	37.67	10.36	4.18	3.04	0.14	0.67	25.18	13283	-50000
53	35.28	9.95	3.06	2.94	0.39	0.78	41.21	3826	-
54	35.63	9.81	4.16	4.1	0.56	0.51	90.0	5155	-
55	32.56	9.66	3.58	4.78	0.55	0.63	90.0	4775	-
56	30.04	8.56	4.37	2.86	0.1	0.69	23.62	5600	-43258
57	39.86	8.88	3.53	2.02	0.88	0.66	90.0	1434	-
58	37.09	8.51	3.08	4.68	0.3	0.59	55.09	3630	-24431
59	36.91	9.29	3.9	4.56	0.52	0.6	90.0	5425	-
60	39.58	9.59	4.0	2.52	0.64	0.73	90.0	2960	-
61	36.13	10.51	4.33	4.3	0.87	0.54	90.0	7108	-
62	37.88	9.73	4.43	3.55	0.09	0.72	24.81	20162	50000
63	33.37	9.89	4.23	2.63	0.73	0.76	90.0	3647	-
64	30.72	9.79	3.42	2.29	0.31	0.76	23.55	3235	-
65	31.75	8.75	3.61	3.01	0.96	0.58	90.0	1977	-

Test	φ [°]	γ' [kPa]	D [m]	λ [-]	$\frac{z_{pad}}{L}$ [-]	R_{inter} [-]	α_{pad} [°]	R_c [kN]	w_i
66	34.47	8.12	3.83	1.82	0.45	0.64	37.02	2635	-
67	39.53	9.45	4.54	4.38	0.48	0.7	90.0	9267	-24222
68	30.4	10.88	4.46	3.65	0.91	0.55	90.0	5996	-
69	34.55	8.89	4.87	3.37	0.14	0.7	38.73	16288	-25248
70	39.73	10.75	4.41	1.3	0.6	0.56	54.31	1519	-32953
71	34.12	9.3	4.73	1.56	0.11	0.6	34.57	3615	-9651
72	30.24	10.2	4.51	2.8	0.77	0.61	90.0	3991	-
73	35.17	9.12	3.11	3.45	0.34	0.55	55.7	2006	-
74	35.91	10.65	3.82	2.18	0.63	0.57	71.43	1636	-
75	36.02	8.26	4.89	4.1	0.43	0.79	90.0	10027	-
76	30.13	9.38	4.95	4.13	0.8	0.52	90.0	8523	1144
77	38.92	10.26	4.34	1.73	0.36	0.79	50.87	3782	5347
78	31.43	9.25	4.42	2.4	0.13	0.51	35.93	4974	50000
79	38.35	9.84	3.82	2.48	0.52	0.56	74.65	1756	34422
80	36.08	8.03	3.34	4.08	0.92	0.76	90.0	2961	-
81	30.5	9.97	3.77	1.16	0.87	0.6	29.18	1297	-
82	36.2	10.68	3.43	1.74	0.81	0.52	63.55	988	-
83	37.79	10.92	4.13	2.41	0.03	0.66	8.67	8592	-
84	39.42	8.08	3.29	3.95	0.02	0.68	34.38	9070	2545
85	39.77	10.6	4.95	2.23	0.18	0.68	31.41	13220	25382
86	34.26	9.03	4.98	2.82	0.35	0.72	48.46	10457	-
87	30.78	8.53	4.16	3.28	0.59	0.62	71.67	3705	7983
88	35.07	8.07	4.64	2.92	0.94	0.65	90.0	4117	-341
89	30.64	10.52	4.52	1.18	0.85	0.73	52.15	1945	-17248
90	34.38	9.89	4.8	3.5	0.25	0.69	48.49	15750	50000
91	38.49	9.35	3.7	2.65	0.54	0.55	90.0	1735	-25229
92	36.67	8.4	3.01	3.34	0.36	0.79	44.27	4180	-
93	38.2	10.78	4.31	3.34	0.44	0.5	90.0	4231	-
94	39.38	8.65	3.14	1.12	0.97	0.58	54.32	740	-7495
95	37.58	9.68	3.37	3.7	0.03	0.73	29.19	9040	-50000
96	38.05	8.87	4.63	1.52	0.32	0.76	41.58	3620	-6973
97	33.48	8.64	3.62	2.85	0.43	0.51	58.12	1868	-
98	37.25	10.14	4.62	1.59	0.62	0.77	62.0	3011	-
99	38.24	9.22	4.49	2.28	0.5	0.64	80.29	2704	-
100	30.86	9.71	3.08	4.99	0.62	0.56	90.0	3006	-

Test	φ [°]	γ' [kPa]	D [m]	λ [-]	$\frac{z_{pad}}{L}$ [-]	R_{inter} [-]	α_{pad} [°]	R_c [kN]	w_i
101	35.4	9.46	4.25	4.81	0.71	0.76	90.0	9020	-
102	38.42	10.0	4.13	1.92	0.86	0.51	90.0	1454	-4784
103	32.03	8.7	3.44	3.99	0.09	0.57	9.99	5836	-
104	35.06	10.61	3.93	3.74	0.76	0.66	90.0	4779	-
105	32.61	10.59	4.56	3.67	0.16	0.76	24.37	16916	-48026
106	37.57	8.6	4.3	3.63	0.65	0.52	90.0	4148	-
107	31.62	8.06	4.27	4.75	0.8	0.67	90.0	7058	-31897
108	33.18	9.58	4.87	3.07	0.99	0.51	90.0	4943	-
109	35.56	9.28	4.89	1.42	0.77	0.7	70.74	3334	28053
110	39.18	8.95	3.96	3.66	0.66	0.74	90.0	4515	-
111	32.27	8.66	4.28	2.57	0.41	0.65	40.61	6011	50000
112	34.91	8.33	4.27	2.32	0.87	0.61	90.0	2176	-
113	33.45	10.41	4.5	2.55	0.01	0.79	23.25	8389	843
114	39.35	8.62	4.11	3.13	0.47	0.78	90.0	4245	-
115	30.56	10.01	3.48	3.08	0.5	0.69	47.27	3572	-50000
116	36.97	10.64	3.52	2.91	0.33	0.71	59.34	2897	-
117	39.15	8.77	3.35	3.4	0.22	0.56	35.68	7179	1353
118	31.08	10.48	3.15	1.68	0.51	0.59	28.6	1769	-
119	32.84	9.54	3.26	2.66	0.76	0.61	68.48	1465	-
120	38.54	8.97	4.38	1.88	0.28	0.77	34.88	5447	-50000
121	34.54	8.76	3.2	1.29	0.08	0.55	11.86	943	-16481
122	35.7	9.37	3.98	3.24	0.41	0.53	63.1	3183	-
123	31.17	10.08	3.14	4.4	0.74	0.51	90.0	2548	-6274
124	38.32	8.17	4.86	1.95	0.2	0.54	30.85	7158	22717
125	39.47	8.35	3.19	3.6	0.94	0.73	90.0	2113	-
126	36.26	10.09	3.12	3.86	0.47	0.68	79.36	2413	50000
127	34.67	9.93	3.58	1.54	0.45	0.78	28.22	2420	-3571
128	31.01	8.62	3.89	2.24	0.23	0.8	29.87	3653	30993
129	35.5	8.74	4.56	2.01	0.64	0.56	90.0	2057	-9871
130	33.29	9.27	3.78	4.57	0.21	0.74	41.96	13133	50000
131	34.04	8.54	3.69	2.48	0.26	0.74	37.28	4037	-
132	32.24	10.66	4.75	4.33	0.37	0.51	90.0	9067	-
133	30.29	9.52	3.9	1.93	0.93	0.78	64.76	2427	-
134	32.17	9.77	3.88	3.09	0.67	0.62	90.0	2959	-
135	34.6	10.55	4.45	2.88	0.45	0.79	66.41	5255	-50000

Test	φ [°]	γ' [kPa]	D [m]	λ [-]	$\frac{z_{pad}}{L}$ [-]	R_{inter} [-]	α_{pad} [°]	R_c [kN]	w_i
136	38.26	10.33	3.72	1.72	0.68	0.71	61.31	1720	-
137	38.77	9.05	3.06	3.05	0.15	0.52	30.51	4566	-
138	31.83	10.15	3.02	2.64	0.05	0.75	10.74	2439	-
139	31.38	10.67	4.04	2.07	0.57	0.8	41.41	4858	50000
140	30.91	10.0	4.49	4.8	0.32	0.66	64.22	11275	-50000
141	36.64	10.82	3.19	4.51	0.57	0.74	90.0	3895	-23331
142	31.23	9.13	3.5	1.14	0.43	0.66	32.01	1046	-
143	38.13	10.79	3.81	3.8	0.76	0.72	90.0	4903	-7418
144	37.18	8.68	4.44	1.37	0.94	0.7	80.19	2331	-
145	37.44	9.75	3.69	4.17	0.85	0.79	90.0	5103	-
146	33.74	8.94	3.92	4.2	0.98	0.6	90.0	4638	-
147	38.82	9.44	3.67	1.32	0.24	0.71	36.84	1515	-
148	36.51	10.39	3.61	1.04	0.21	0.65	21.85	1235	-
149	31.92	9.42	3.05	4.04	0.99	0.56	90.0	2047	-
150	37.34	9.88	3.77	4.28	0.42	0.56	90.0	4444	-
151	38.99	9.99	4.48	4.5	0.07	0.77	26.15	32757	50000
152	31.21	8.8	4.86	4.41	0.42	0.64	90.0	9682	-
153	36.74	9.36	4.46	2.12	0.51	0.55	75.4	2085	50000
154	39.72	8.05	4.68	2.45	0.3	0.54	48.72	4221	-50000
155	32.88	8.91	3.26	4.03	0.68	0.66	90.0	2666	-
156	37.09	9.41	3.42	3.19	0.46	0.58	68.88	1972	50000
157	31.42	9.7	3.74	1.21	0.73	0.64	38.9	1430	-
158	33.36	9.87	3.49	2.68	0.23	0.56	22.15	4730	-
159	32.34	9.81	3.97	3.17	0.11	0.76	26.39	7888	-
160	36.95	8.2	3.32	1.46	0.74	0.57	43.6	1152	10374
161	38.65	10.57	3.31	3.98	0.96	0.66	90.0	3143	-1292
162	34.28	10.24	4.36	2.17	0.35	0.6	40.46	5669	50000
163	37.63	9.11	4.94	2.49	0.79	0.65	90.0	4349	-12337
164	31.26	8.3	3.28	1.35	0.37	0.72	14.83	1194	-2786
165	32.19	8.6	3.07	1.09	0.53	0.75	36.2	658	-10710
166	38.85	10.96	3.85	3.58	0.38	0.52	90.0	3493	-6315
167	37.78	10.35	4.39	3.47	0.66	0.52	90.0	4846	-
168	35.24	9.92	3.86	3.88	0.18	0.61	31.51	13046	-
169	35.8	9.56	3.39	2.93	0.92	0.75	90.0	2125	-
170	38.8	9.4	4.63	3.43	0.04	0.59	29.57	18467	-

Test	φ [°]	γ' [kPa]	D [m]	λ [-]	$\frac{z_{pad}}{L}$ [-]	R_{inter} [-]	α_{pad} [°]	R_c [kN]	w_i
171	30.21	10.73	3.23	1.98	0.89	0.76	52.05	1884	-
172	36.42	10.8	4.97	2.74	0.94	0.62	90.0	5573	-
173	38.58	8.49	3.03	4.47	0.67	0.71	90.0	2578	-
174	35.54	10.19	4.52	1.56	0.16	0.55	12.63	4624	-
175	38.08	8.27	3.61	4.29	0.56	0.58	90.0	3588	21988
176	35.67	10.89	3.46	4.6	0.31	0.73	56.88	7554	-25729
177	37.83	10.47	3.18	2.62	0.1	0.57	16.85	4742	-12857
178	37.65	8.15	4.08	3.69	0.57	0.65	90.0	4133	-
179	35.68	8.92	3.94	1.78	0.7	0.69	73.17	1741	-
180	35.75	9.09	3.93	2.53	0.84	0.58	90.0	1976	-
181	39.32	10.41	3.64	4.82	0.37	0.77	90.0	6740	37319
182	33.94	9.1	4.92	4.02	0.82	0.77	90.0	11028	50000
183	32.02	9.96	4.19	2.71	0.97	0.73	90.0	3526	-
184	31.47	8.96	3.74	3.57	0.39	0.6	61.43	3431	50000
185	32.5	10.74	3.36	4.92	0.03	0.52	18.02	7928	-16616
186	38.89	9.67	4.05	3.31	0.9	0.56	90.0	3425	-
187	38.69	8.71	4.77	4.48	0.52	0.79	90.0	11454	-
188	33.41	8.63	4.34	4.65	0.6	0.67	90.0	7677	-
189	33.59	9.06	3.29	1.78	0.15	0.68	18.09	1844	-
190	33.7	10.45	3.25	4.44	0.48	0.64	90.0	3462	-
191	36.27	8.44	4.64	1.69	0.05	0.7	5.99	5260	-
192	31.31	8.14	4.59	2.79	0.61	0.71	86.76	3968	-
193	32.52	10.17	4.33	2.51	0.84	0.65	90.0	3124	-
194	38.11	10.62	3.01	1.61	0.64	0.62	58.62	678	-19332
195	39.17	10.43	4.08	2.1	0.48	0.56	65.74	1768	-
196	34.87	8.68	4.2	3.63	0.8	0.79	90.0	5441	-50000
197	38.37	8.55	3.55	1.99	0.75	0.67	76.74	1382	-8710
198	38.02	9.18	4.76	4.74	0.39	0.59	90.0	10068	-34613
199	37.22	9.14	3.22	1.29	0.57	0.68	32.96	1342	-
200	33.78	8.42	3.31	2.05	0.97	0.66	73.84	1468	8881
201	36.83	10.81	4.88	1.44	0.38	0.67	39.56	4610	-
202	34.08	10.04	3.63	3.32	0.72	0.7	90.0	3106	-
203	37.75	8.86	3.56	4.63	0.82	0.51	90.0	3625	-
204	31.3	10.72	3.32	3.22	0.69	0.5	90.0	1800	-18938
205	35.36	9.31	3.34	2.26	0.6	0.77	48.91	2107	-4548

Test	φ [°]	γ' [kPa]	D [m]	λ [-]	$\frac{z_{pad}}{L}$ [-]	R_{inter} [-]	α_{pad} [°]	R_c [kN]	w_i
206	33.07	9.84	4.55	4.87	0.98	0.72	90.0	11227	12732
207	35.78	10.33	4.73	3.78	0.12	0.59	27.58	20855	50000
208	36.48	9.0	4.37	1.22	0.99	0.74	76.99	1967	-23606
209	33.67	8.2	4.85	2.35	0.02	0.79	18.18	7790	-
210	34.01	9.39	3.1	1.39	0.33	0.57	24.29	1105	-
211	30.61	8.93	4.7	3.42	0.62	0.8	90.0	7262	-
212	30.96	8.58	3.95	3.26	0.93	0.55	90.0	2777	-
213	36.59	8.38	4.31	2.99	0.79	0.75	90.0	4062	-27602
214	36.54	8.1	4.19	4.79	0.4	0.64	90.0	6603	-
215	36.11	9.85	4.24	2.04	0.22	0.72	34.34	5401	-30000
216	32.08	9.16	4.51	3.89	0.49	0.62	90.0	6527	-
217	33.51	9.29	4.62	4.44	0.75	0.73	90.0	9901	-
218	33.03	8.46	4.81	1.64	0.47	0.53	45.74	2261	-50000
219	39.82	9.34	3.86	4.38	0.85	0.64	90.0	5357	-
220	39.97	10.91	3.13	3.49	0.29	0.75	72.04	2336	-
221	33.99	10.12	4.35	3.36	0.7	0.62	90.0	4943	-
222	37.71	8.21	4.05	2.11	0.71	0.78	90.0	3531	50000
223	39.11	10.68	4.03	2.99	0.91	0.73	90.0	3986	-
224	32.7	10.63	4.07	3.99	0.47	0.77	77.81	6586	23184
225	33.32	8.48	3.83	4.95	0.83	0.63	90.0	5491	-
226	34.75	9.86	4.75	2.15	0.59	0.76	70.44	3750	-15009
227	33.64	10.25	3.54	2.77	0.74	0.79	90.0	2502	-
228	35.83	8.82	4.15	1.05	0.13	0.77	19.09	1655	-
229	30.31	9.68	4.29	1.86	0.27	0.58	19.81	3901	-
230	37.97	8.01	4.72	2.9	0.13	0.63	23.26	14566	5403
231	36.79	10.21	4.08	2.33	0.38	0.61	48.83	3350	-50000
232	33.54	10.87	3.44	1.23	0.84	0.59	37.12	1354	16740
233	38.3	10.11	4.57	3.97	0.58	0.78	90.0	9723	15022
234	39.92	10.56	4.05	2.84	0.41	0.71	83.93	3404	-
235	32.87	10.85	4.71	4.16	0.65	0.58	90.0	9105	-
236	34.8	9.17	4.4	1.79	0.07	0.67	28.52	4140	-
237	31.58	9.43	4.22	3.82	0.21	0.72	41.26	11500	-31144
238	31.87	8.57	4.0	1.11	0.77	0.68	31.23	1455	-47153
239	30.36	10.71	3.98	4.23	0.29	0.74	41.39	11939	-
240	36.63	9.21	3.1	1.66	0.78	0.58	59.0	816	-

Test	φ [°]	γ' [kPa]	D [m]	λ [-]	$\frac{z_{pad}}{L}$ [-]	R_{inter} [-]	α_{pad} [°]	R_c [kN]	w_i
241	36.17	9.76	4.32	2.77	0.32	0.57	51.67	4596	-50000
242	35.88	10.77	3.72	4.7	0.73	0.75	90.0	6621	-
243	35.43	10.18	3.28	3.94	0.81	0.71	90.0	3112	-
244	30.22	10.05	4.09	1.6	0.28	0.62	35.32	2373	-
245	38.15	9.25	4.21	4.31	0.99	0.75	90.0	7617	-
246	34.7	9.61	3.17	4.86	0.63	0.73	90.0	3857	-
247	34.42	10.4	4.14	4.53	0.95	0.53	90.0	6515	-
248	33.82	10.95	3.79	1.0	0.27	0.54	17.02	1296	-
249	38.63	10.22	3.22	1.75	0.23	0.54	38.84	1930	18035
250	32.13	10.03	3.48	4.84	0.61	0.61	90.0	4483	-
251	32.21	10.31	4.83	1.84	0.89	0.72	82.51	3778	-
252	34.9	10.98	4.02	4.08	0.34	0.63	68.24	6316	-50000
253	33.92	10.98	3.21	2.6	0.9	0.63	90.0	1404	-
254	32.65	9.21	3.75	1.38	0.68	0.71	40.39	2015	47090
255	35.33	9.07	4.25	3.06	0.01	0.57	6.63	8835	13761
256	34.51	8.49	3.04	4.67	0.49	0.65	90.0	2586	-
257	39.05	8.23	3.57	2.27	0.44	0.71	59.92	1467	-
258	33.26	8.34	3.16	3.48	0.84	0.77	90.0	2024	-
259	34.19	10.06	3.51	3.61	0.91	0.58	90.0	2809	-
260	31.67	10.28	3.66	4.72	0.06	0.79	28.95	10315	-50000
261	34.22	8.37	4.45	4.36	0.06	0.53	15.26	14712	-464
262	37.54	10.29	3.13	4.54	0.64	0.67	90.0	3276	-
263	37.0	10.43	4.72	3.77	0.89	0.79	90.0	9683	-
264	37.29	8.18	3.88	2.76	0.17	0.8	41.65	6342	-1003
265	34.36	9.19	3.46	3.53	0.68	0.52	90.0	2185	-
266	37.98	9.8	3.5	4.14	0.16	0.6	35.25	12179	33371
267	32.93	8.84	4.99	4.2	0.95	0.65	90.0	9918	-
268	31.14	9.1	3.36	3.93	0.83	0.75	90.0	3084	-
269	30.81	9.49	4.82	4.62	0.19	0.64	41.91	19532	-
270	37.41	10.92	3.09	2.42	0.81	0.53	90.0	958	-
271	31.11	9.04	3.79	3.1	0.79	0.78	90.0	3145	-
272	39.56	10.54	3.98	4.25	0.01	0.64	26.99	20235	15286
273	32.31	8.01	4.23	1.13	0.72	0.54	36.94	1715	-
274	31.95	8.02	3.55	3.51	0.86	0.69	90.0	2587	20585
275	36.72	9.52	4.22	4.34	0.12	0.78	32.82	22400	50000

Test	φ [°]	γ' [kPa]	D [m]	λ [-]	$\frac{z_{pad}}{L}$ [-]	R_{inter} [-]	α_{pad} [°]	R_c [kN]	w_i
276	39.27	8.47	3.75	2.0	0.08	0.52	24.87	3801	-
277	34.68	10.45	4.66	4.35	0.54	0.67	90.0	10158	-
278	35.98	10.34	3.92	1.27	0.55	0.63	42.61	1547	-
279	32.37	8.99	4.38	1.81	0.58	0.5	39.18	2508	-737
280	31.9	9.91	4.12	3.54	0.07	0.54	26.79	8284	-36333
281	37.94	8.51	4.71	2.31	0.96	0.52	90.0	2534	-
282	39.62	10.84	4.78	4.98	0.7	0.57	90.0	12448	24119
283	33.14	8.52	3.5	2.73	0.02	0.67	9.48	3632	50000
284	30.37	8.04	3.38	4.69	0.25	0.53	43.95	5612	25099
285	36.24	8.74	4.61	4.22	0.0	0.59	27.46	18401	-50000
286	34.99	10.7	4.19	1.26	0.17	0.75	34.93	2303	3689
287	37.88	9.94	3.19	1.9	0.17	0.63	27.3	2403	-
288	35.27	10.28	4.98	4.93	0.26	0.54	89.06	12765	50000
289	32.1	9.23	4.39	3.86	0.44	0.77	82.24	6982	21170
290	36.77	9.32	3.53	3.69	0.54	0.69	90.0	3141	-
291	37.31	8.36	3.73	1.51	0.29	0.63	24.52	2314	-
292	31.71	9.55	4.59	1.25	0.31	0.5	18.39	2729	-10645
293	34.32	9.07	4.06	4.96	0.34	0.7	75.33	7487	-
294	33.05	10.93	4.36	4.96	0.12	0.59	33.45	20856	50000
295	39.03	10.16	4.96	3.2	0.42	0.6	90.0	6574	-
296	32.8	8.85	4.93	1.2	0.65	0.6	35.54	3581	45148
297	32.94	8.37	3.84	4.47	0.49	0.51	90.0	4089	-
298	30.46	8.23	4.67	4.65	0.67	0.78	90.0	10024	-
299	36.43	8.4	4.8	3.16	0.65	0.51	90.0	4388	-
300	31.05	9.72	4.69	3.75	0.27	0.69	51.5	12459	-
301	39.96	8.78	4.12	1.4	0.4	0.64	44.07	2333	50000
302	38.7	9.96	4.91	4.04	0.67	0.67	90.0	10309	-
303	32.99	10.83	4.42	1.84	0.05	0.55	21.75	4261	-11564
304	30.12	8.08	3.25	2.38	0.56	0.59	41.67	1576	-38303
305	30.45	8.73	4.95	1.89	0.34	0.74	39.12	5016	-
306	33.84	8.17	4.44	3.73	0.33	0.65	59.98	6539	-50000
307	38.48	8.11	4.48	4.05	0.83	0.61	90.0	6151	-9286
308	35.1	8.1	4.58	1.44	0.89	0.55	64.8	2193	-
309	30.03	8.31	3.47	3.4	0.7	0.73	80.77	2461	-
310	39.49	8.25	4.53	3.28	0.74	0.65	90.0	4837	-

Test	φ [°]	γ' [kPa]	D [m]	λ [-]	$\frac{z_{pad}}{L}$ [-]	R_{inter} [-]	α_{pad} [°]	R_c [kN]	w_i
311	33.57	8.24	4.03	1.85	0.46	0.69	43.24	2800	25244
312	35.01	8.16	3.7	4.25	0.09	0.71	15.36	11599	-50000
313	35.47	10.94	4.99	3.02	0.55	0.66	90.0	7135	-
314	30.9	10.97	4.26	4.52	0.53	0.68	90.0	8586	-
315	30.16	9.46	3.0	3.73	0.12	0.69	20.96	3445	50000
316	38.57	9.19	3.24	1.19	0.11	0.8	7.05	1341	-3145
317	39.69	9.62	3.8	4.76	0.31	0.58	90.0	5277	-
318	36.31	10.58	3.65	3.59	0.21	0.62	36.45	10027	-
319	31.53	11.0	4.79	3.38	0.82	0.67	90.0	7674	-
320	38.74	8.7	3.43	4.88	0.24	0.77	69.84	4996	-42733
321	32.48	8.98	3.16	2.7	0.35	0.66	37.95	2982	-
322	39.89	8.98	4.55	3.91	0.27	0.54	90.0	6244	-
323	33.21	10.58	4.85	1.48	0.51	0.53	35.11	3757	-
324	34.17	10.37	4.65	1.33	0.59	0.74	49.71	2635	-50000
325	38.95	10.46	4.6	1.07	0.88	0.69	70.66	2342	-
326	33.62	10.21	3.71	3.3	0.08	0.61	31.11	7031	-
327	35.14	8.83	3.91	4.91	0.16	0.76	31.55	19265	17127
328	31.49	10.8	4.81	2.2	0.28	0.74	33.9	8126	10889
329	31.68	10.27	4.75	2.82	0.72	0.55	90.0	4467	-
330	35.96	9.15	3.4	3.24	0.38	0.59	55.56	2491	-

Table C.6. The validation set for the anchor model (R_c).

Test	φ [°]	γ' [kPa]	D [m]	λ [-]	$\frac{z_{pad}}{L}$ [-]	R_{inter} [-]	α_{pad} [°]	R_c [kN]
1	37.07	9.21	4.89	2.13	0.89	0.65	90.0	3474
2	31.77	8.09	4.75	3.63	0.61	0.57	90.0	5775
3	38.41	8.58	4.44	1.78	0.26	0.62	37.7	4518
4	38.96	10.0	3.04	1.89	0.72	0.63	63.91	879
5	32.66	10.87	4.55	1.88	0.49	0.53	53.02	2325
6	38.31	9.24	3.62	3.26	0.63	0.73	90.0	2892
7	35.11	10.38	4.78	2.74	0.13	0.51	22.35	12411
8	31.46	9.05	3.76	4.54	0.43	0.78	87.4	5513
9	34.16	9.96	3.7	3.61	0.02	0.68	19.62	8255
10	34.76	11.0	3.84	3.38	0.84	0.71	90.0	4153
11	30.04	9.11	4.23	3.15	0.9	0.6	90.0	3623

Test	φ [°]	γ' [kPa]	D [m]	λ [-]	$\frac{z_{pad}}{L}$ [-]	R_{inter} [-]	α_{pad} [°]	R_c [kN]
12	37.09	10.3	4.33	4.46	0.1	0.77	39.28	25163
13	30.95	8.81	3.08	3.3	0.25	0.53	22.21	3660
14	39.04	9.32	3.51	1.43	0.05	0.68	9.96	2233
15	34.47	8.35	4.33	1.57	0.69	0.57	63.22	1468
16	30.46	8.04	4.1	1.47	0.17	0.62	18.76	1847
17	39.22	8.42	4.59	2.9	0.77	0.75	90.0	4747
18	34.7	9.03	4.96	4.79	0.99	0.65	90.0	12229
19	35.27	9.36	4.38	1.09	0.15	0.79	15.33	2166
20	36.83	9.71	3.91	4.19	0.31	0.61	90.0	5125
21	38.65	8.31	3.58	2.98	0.93	0.64	90.0	1975
22	36.25	8.61	3.33	3.9	0.18	0.8	31.79	9319
23	36.52	9.5	4.99	2.35	0.54	0.56	84.95	3573
24	33.83	8.74	4.52	1.32	0.53	0.59	43.02	1836
25	35.49	10.15	4.39	3.08	0.97	0.54	90.0	3912
26	30.4	10.35	3.66	4.72	0.54	0.67	90.0	5473
27	33.71	10.46	4.57	4.85	0.3	0.58	80.97	10174
28	34.3	10.53	3.19	2.51	0.64	0.66	56.61	1571
29	30.76	9.39	4.47	4.39	0.06	0.71	14.19	11342
30	37.92	10.56	4.69	4.65	0.67	0.54	90.0	10020
31	39.86	10.1	4.63	3.75	0.56	0.73	90.0	8305
32	32.33	9.27	3.16	4.07	0.62	0.54	90.0	2204
33	37.86	8.64	3.46	2.22	0.33	0.52	33.45	3351
34	31.92	10.8	3.44	1.76	0.12	0.65	7.01	2091
35	39.51	8.92	4.87	4.25	0.37	0.68	90.0	9949
36	37.36	9.68	4.01	2.08	0.59	0.78	71.52	2270
37	36.62	8.21	4.19	3.88	0.75	0.62	90.0	5284
38	30.99	8.4	4.93	3.95	0.45	0.73	90.0	9014
39	32.95	8.7	4.71	3.04	0.08	0.64	15.68	10684
40	30.64	10.25	3.48	2.82	0.57	0.6	55.98	2161
41	35.92	8.46	3.28	4.72	0.66	0.63	90.0	3214
42	33.35	10.75	3.6	4.3	0.81	0.59	90.0	4329
43	35.38	9.84	4.05	1.99	0.47	0.55	40.95	2721
44	34.01	8.78	3.81	2.27	0.71	0.74	61.92	2248
45	38.19	10.46	4.74	1.7	0.76	0.71	90.0	4364
46	32.03	9.93	4.81	2.64	0.38	0.67	56.4	5684

Test	φ [°]	γ' [kPa]	D [m]	λ [-]	$\frac{z_{pad}}{L}$ [-]	R_{inter} [-]	α_{pad} [°]	R_c [kN]
47	39.39	10.88	3.87	2.71	0.41	0.64	90.0	2657
48	36.21	10.7	3.73	1.18	0.14	0.55	26.97	1504
49	33.6	9.62	3.4	1.01	0.4	0.77	30.04	942
50	31.38	8.53	3.92	1.61	0.86	0.74	49.34	2262
51	31.67	9.53	3.19	2.41	0.01	0.59	32.36	2018
52	38.81	9.76	4.06	3.82	0.09	0.56	41.43	14435
53	32.8	8.91	3.12	2.02	0.42	0.76	40.62	1678
54	37.74	10.2	3.78	1.15	0.87	0.57	57.26	1492
55	35.7	8.14	3.03	1.23	0.5	0.69	25.88	962
56	34.34	10.07	4.28	3.2	0.28	0.77	43.26	10612
57	37.47	9.88	3.26	4.91	0.48	0.6	90.0	3848
58	34.94	8.22	3.99	4.37	0.03	0.52	21.29	11582
59	36.1	8.28	4.48	3.41	0.2	0.7	36.22	14793
60	35.64	9.56	3.09	4.02	0.92	0.7	90.0	2503
61	31.16	10.58	4.84	2.47	0.22	0.79	28.0	9944
62	38.58	10.64	3.24	4.13	0.22	0.72	51.1	8956
63	32.47	9.81	4.17	3.69	0.71	0.69	90.0	5415
64	30.25	9.65	4.64	1.38	0.79	0.66	41.76	3071
65	37.54	8.03	3.69	2.59	0.28	0.72	42.87	4595
66	39.68	8.98	3.33	2.3	0.97	0.5	90.0	898
67	36.76	9.45	4.13	4.97	0.83	0.75	90.0	8681
68	32.13	10.76	3.37	3.46	0.81	0.78	90.0	3069
69	33.26	9.14	3.54	3.55	0.35	0.51	47.39	3604
70	39.86	10.93	4.26	2.84	0.35	0.52	76.38	3070
71	33.19	10.29	4.21	1.52	0.95	0.76	78.11	2218
72	32.53	8.84	3.96	4.61	0.88	0.58	90.0	5381